Making a MESS: a Multi-Experiment Spectral Suite for studying hydrated electrons

ALEXANDRA LOUISE TYSON

Durham University

Department of Chemistry

Making a MESS:

a Multi-Experiment Spectral Suite to study hydrated electrons

Alexandra Louise Tyson

A thesis submitted for the degree of Doctor of Philosophy

2018

DECLARATION

The research described herein was conducted at the Department of Chemistry, Durham University between October 2015 and December 2018. All of the work is my own, except where otherwise stated. No part has been submitted previously for a degree at Durham, or any other, university.

STATEMENT OF COPYRIGHT

ABSTRACT

In this work, the design and implementation of a Multi-Experiment Spectral Suite (MESS) is described. The MESS currently contains two time-resolved experiments - Transient Absorption (TA), and Second Harmonic Generation (SHG) – but has been designed with a view to expansion. The primary species of interest to be studied is the hydrated electron. As an electron is generated during water ionization, its hydrated form is significant within many scientific processes including, but not limited to, biological chemistry and tissue damage, atmospheric chemistry and nuclear chemistry. However, the majority of what is known about the hydrated electron is its behaviour in a bulk solvation environment with little understanding known about its behaviour at interfaces where it reacts in most instances. The MESS provides the ability to build a bottom up picture of solvation environment on molecular dynamics in going from the bulk (TA) to the interface (SHG).

SHG enables the study of interfacial dynamics due to its inherent surface sensitivity. The method described here is an improvement on a previous phase-sensitive SHG technique that varied the phase of the interference between the SHG from a sample ($\mathbf{E}_{SHG}$) and a local oscillator ($\mathbf{E}_{LO}$) manually by incrementally changing the distance between the sample and reference sample. The new technique presented here is able to record the entire interference pattern in a single shot by using a phase varying unit comprised of a Reference Surface sandwiched between two glass wedges. The technique is characterised in this work by studying the excited state dynamics of malachite green at the air/water interface, exhibiting excellent phase stability and sensitivity and comparatively short acquisition times.

In comparison, the TA technique presented is experimentally simpler than SHG. The excited state dynamics of molecules are studied in which a pump pulse induces an excitation which is then probed by a white light pulse spanning 520-950 nm continuously. In combination with 30 kHz modulation of the laser, shot-to-shot pump-probe measurements are presented for both SHG and TA techniques.

"If I have seen further it is by standing on the shoulders of giants"

~ Isaac Newton

ACKNOWLEDGMENTS

The eloquent words of Sir Isaac Newton express more succinctly the way I feel towards those I love than I could ever possibly compose. I therefore apologise for the feeble attempt that follows, which in no way does justice to those without whom this thesis would not have been possible.

First and foremost I must thank supervisor, Professor Jan Verlet. Thank you for encouraging me, advising me and never shying away from my tears over the last 7 years. I cannot imagine working for someone I admire more and your guidance has not only made me a better scientist (hopefully…) but a better, more confident person, for which I will be forever grateful.

In the same vain I must also thank my project predecessors: Dr David 'let me say something inappropriate' Woods and Dr Paweł 'let me say as little as possible' Nowakowski. Without you, the start of this project would have been (even more) daunting and I owe most of what I know to the pair of you.

Next I would like to thank the other members of tribe Verlet, both past and present, as well as all my other friends in the department. Although there are too many of you to name I would particularly like to thank Golda, Aude, Jess, James, Meera, and Jacquie. You have all provided invaluable and never-ending support, much needed coffee breaks, laughter, fun and friendship and I am significantly richer for having you all in my life. Thank you for all the small moments that made the days more bearable and have meant everything to me.

To Christian, thank you for being my champion and my strongest ally. Thank you reminding me there is more to life than work as without you I would have surely driven myself crazy working all hours god sends (and probably forgotten to eat in the process). I know the next step will be hard but I am so excited for the life that awaits us.

To my brother Nicholas, thank you for being so gorgeous and always providing laughter in even the most mundane situations. You are my favourite person and I am honoured to be your big sister.

To my sister Ruth, thank you for understanding me above all others, checking up on me and providing love and support when I needed it most. You are my best friend with strength and determination that is truly inspirational. I am lucky to have you as a little sister.

Finally, to my parents, my successes are entirely your fault and I blame you for everything. You have been my loudest cheerleaders, strongest critics, and most positive educational influences. Your faith in me has been unwavering, even when I have doubted myself. Thank you for pushing me to succeed without pushing so hard that I did not need to develop my own motivation. Without you I would not be here, something for which I will be forever indebted. You are quite simply my heroes.

I love you.

CONTENTS

List of Abbreviations

CTTS	**Charge-Transfer-To-Solvent**
DFT	**Density Functional Theory**
ESA	**Excited State Absorption**
GSB	**Ground State Bleach**
GVD	**Group Velocity Dispersion**
HD	**Heterodyne Detected**
LHM	**Liquid Height Monitor**
LO	**Local Oscilator**
MD	**Molecular Dynamics**
MQC	**Mixed Quantum Classical**
PD	**Phase Delay**
PES	**Photo-Electron Spectroscopy**
PRS	**Pump Reference Spot**
PSU	**Phase Shifting Unit**
PVU	**Phase Varying Unit**
RS	**Reference Sample**
SEM	**Stimulated Emission**
SFG	**Sum Frequency Generation**
SHG	**Second Harmonic Generation**
TA	**Transient Absorption**
TD DFT	**Time Dependent DFT**
TDM	**Transition Dipole Moment**
VDE	**Vertical Detachment Energy**
VSFG	**Vibrational Sum Frequency Generation**

1. INTRODUCTION

1.1. ULTRAFAST SPECTROSCOPY

With the discovery of photosynthesis in 1779, and the development of the photographic process in 1839, the initiation of chemical processes by light has been a long established and well-known phenomenon.[1,2] However, it was not until the seminal work of the 1967 Nobel laureates, Norrish and Porter, that the capacity to study the dynamics of such chemical processes occurring on nanosecond timescales came to fruition.[3] Before 1967, dynamics of chemical reactions were being studied using a technique called "stopped flow" where time resolution was determined by the rate at which solutions could be mixed and therefore limited to the regime of tens of microseconds. In contrast, Norrish and Porter conceived a new method of flash photolysis in 1947 that disturbed an equilibrium using high intensity flashes of light and allowed the observation of short lived intermediates for the very first time.[3,4]

Over the next half of the 20th century, technological development saw the replacement of flash lamps with lasers, which quickly advanced from nanosecond pulses through to the femtosecond regime, far beyond the realm thought possible in the 1950s. At the frontier of this ultrafast world was the seminal work of Zewail, for which he was awarded the 1999 Nobel Prize in chemistry.[4,5] In his Nobel

lecture Zewail states that with femtochemistry "the ephemeral transition states, denoted in the past by square brackets ([TS‡]) for their elusiveness, can now be clocked as molecular species TS‡.".[6]

Today, ultrafast femtosecond lasers are commercially available and have been used extensively to study molecular dynamics on ultrashort timescales, allowing full characterisation of excited state processes such as isomerisation, bond cleavage and electron transfer. In all of these studies, a pump-probe scheme is employed in which a sample is excited from its ground equilibrium state at a specific instance in time. In optical spectroscopy, this process is usually arises through the absorption of an ultrashort light pulse, termed the pump pulse. The evolution of this excited state is then monitored using a probe at different time intervals from the excitation event. In gas phase experiments, the probe can take the form of detection of molecular fragments or electrons at different time intervals, whereas in the condensed phase a change in absorbance of a second pulse of light, or the emission of light, after excitation can be used to monitor the excited state dynamics.[7]

The information yielded from time-resolved experiments is dependent on the final state chosen to be studied by the probe pulse. Experiments conducted on liquid samples tend to utilise broadband probes because of their generality and ability to follow changes in the excited states. As a consequence, transient absorption (TA) and nonlinear wave mixing experiments have become very popular in studying solution phase molecules and reactions.[5]

1.1.1. ABSORPTION OF RADIATION

When light interacts with a material there are generally two things that can happen; absorption and scattering. Absorption of radiation by a species is a frequency dependent process in which the electric field of an incident wave of light induces an oscillation in a molecules electron density. As a consequence of quantum mechanics, the total energy of a species is quantized with contributions from many forms of internal energy: translational, rotational, vibrational, and electronic. If the energy of the induced oscillation equals the energy difference

between the ground and a higher lying excited state, the wave functions of the two states are coupled and excitation may occur via absorption.[8–10] The probability of an excitation however is dependent on more than simply matching the energy of the transition, it must also satisfy electric dipole selection rules (i.e. the selection rules governing the transitions that occur through the interaction with the electric vector of the radiation).[8–10]

If the incoming photon is not resonant with an excited state or transitions to the energetically accessible states are forbidden by selection rules, then a process called *non-resonant scattering* occurs. In this process the electromagnetic field drives an oscillation in the electron cloud of the material which remains in its electronic ground state. This process is accompanied by an oscillating dipole moment that instantaneously radiates light at the same frequency as the incoming light. Scattering is therefore an elastic process of absorption and re-emission with no alteration to the light wave other than its direction. If the incident light is un-polarized, the light will be scattered in random directions. The processes of transmission, reflection and refraction are therefore the observable macroscopic consequence of scattering at the atomic level.

Due to the small energy difference between rotational and vibrational states, absorption of low energy wavelengths in the microwave and infrared only results in transitions between these states. However, the energy of visible and UV photons is comparable to that of electronic transitions in which the distribution of electrons in a species is changed. An electronically excited state of a species can differ significantly in its reactivity from that of the ground state, especially if an electron is moved between bonding, non-bonding and antibonding molecular orbitals resulting in the nature and strength of bonding varying considerably. Electronic excitation can also make reaction pathways accessible that are improbable from the ground state due to a large activation barrier. As the distribution of electrons in a molecule is fundamental to its reactivity, understanding how changes in the spatial distribution affect molecules' reactivity is of pivotal importance.[9]

1.1.1.1. SELECTION RULES AND TRANSITION INTENSITIES

The transition dipole moment (TDM), R^{nm}, describes the strength of the electric dipole moment associated with the change from the ground state, *m*, to the excited state, *n*, in all three Cartesian coordinates:[8]

$$R^{nm} = \langle \psi_n^* | \mu | \psi_m \rangle, \tag{1}$$

where μ is the electric dipole moment operator. Thus, the first selection rule for any transition is that the transition probability $|R^{nm}|^2$ is non-zero. The remaining rules are specific to the type of transition that occurs and the quantum numbers that describe the states.[8,9]

In atoms, electronic selection rules can be defined in their entirety by the quantum numbers available to describe the states. In diatomic molecules, one or two symmetry properties are needed in addition to the quantum numbers, depending on whether the diatomic is homo- or heteronuclear in nature. For non-linear polyatomic molecules, the quantum numbers are no longer easy to define, and as such only the spin selection rule remains:

$$\Delta S = 0. \tag{2}$$

This rule holds unless there is strong spin-orbit coupling between states with different spin multiplicities.[8,9]

As both the ground and excited states possess their own set of vibrational levels, an electronic excitation is (generally) accompanied by a change in vibrational state. However, unlike vibrational transitions within the same state, which have a selection rule of $\Delta v = \pm 1$, Δv can hold any value when the transition is coupled with an electronic excitation. Such transitions are thus termed vibronic transitions.[8,9]

However, these selection rules merely describe whether a transition is allowed or forbidden, and not the strength of the TDM or intensity of the transition. For a

vibronic transition, the dipole moment, and therefore equation (1) can be rewritten in terms of the vibrational, *v*, and electronic, *e*, components:

$$R_{ev} = \langle \psi_e'^* \psi_v'^* | \mu | \psi_e'' \psi_v'' \rangle, \tag{3}$$

where ψ' and ψ'' represent the upper and lower wavefunctions respectively. Integration first over the electronic coordinates and then considering the electronic TDM, R_e, as a constant with respect to the internuclear distance yields the following expression:[8]

$$R_{ev} = \langle \psi_e'^* | \mu | \psi_e'' \rangle \langle \psi_v'^* | \psi_v'' \rangle = R_e \langle \psi_v'^* | \psi_v'' \rangle \,. \tag{4}$$

These approximations are valid as a consequence of the Frank Condon principle in which nuclear motion is considered to be frozen within the time scale of light absorption. The term $\langle \psi_v'^* | \psi_v'' \rangle$ then describes the overlap integral between the vibrational wave functions in the ground and excited state. The square of this term is called Franck-Condon factor.[8,9]

1.1.1.2. OSCILLATOR STRENGTH

Experimentally, the strength of a transition can be determined by integrating across an absorption peak, yielding the absorption coefficient, $\mathcal{A}$:

$$\mathcal{A} = \int \varepsilon(\nu) d\nu \,, \tag{5}$$

where $\varepsilon(\nu)$is the frequency dependent molar absorption coefficient. $\mathcal{A}$ provides a useful connection between quantum mechanical theory and experimental observations through a unitless quantity called the oscillator strength, f_{nm}:

$$f_{nm} = \left[\frac{4\varepsilon_0 m_e c^2 \ln(10)}{N_\mathrm{A} e^2} \right] \mathcal{A} \,, \tag{6}$$

where ε_0 is the vacuum dielectric permittivity, m_e is the electron mass, c is the speed of light, N_A is Avogadro's number, and e is the electron charge. This

measures the strength of a transition whereby transitions comparable to that of a free electron oscillating in three dimensions have a value approaching unity.[10]

1.1.2. MOLECULAR PHOTOPHYSICS

Compared to the ground state, an excited state is much less stable and will undergo a number of processes to 'lose' the excess energy: emission, internal conversion, intersystem crossing, ionisation, energy transfer to another molecule, isomerization, dissociation, direct reactions to generate chemically new species, and so on. The most common process however is collisional quenching whereby collisions between molecules result in the energy being transferred to random motion and thermal energy before emission can take place. This is then known as *dissipative absorption* and occurs in all materials to some extent. As a consequence, the lifetime of excited states is typically very short with full and detailed discussion of all of the possible processes found in any standard undergraduate physical chemistry textbook. The following brief overview is based on the works of Gilbert,[10] Hollas,[8] Brückner,[11] and Wayne.[9]

In the absence of an intermolecular interaction, there are many intramolecular processes by which an excited species may return back down to the ground state. These processes are schematically represented in the Jablonski diagram shown in Figure 1, and may be radiative (straight line arrows) or non-radiative (curved arrows) in nature. There are three radiative transitions accessible between electronic states within a molecule; absorption, stimulated emission and spontaneous emission. As already discussed, absorption between states of the same spin multiplicity is allowed (equation (2)). Stimulated emission is the equal opposite to absorption and occurs when an excited state interacts with an incident photon inducing a transition of the same energy to a lower energy state. Spontaneous emission is the process by which an excited state spontaneously emits a photon to transition back to a lower energy level. The probability of spontaneous emission is directly proportional to ν^3, where ν is the energy of the emitted photon (and therefore the transition energy). As such, spontaneous emission between vibrational levels has a very low probability and non-radiative processes dominate. There are two types of spontaneous emission represented in

Figure 1; fluorescence (shown in green) and phosphorescence (shown in red) which only differ by the fact that they are spin allowed and spin forbidden processes respectively. Due to the violation of the spin selection rule, the rate of phosphorescence is typically much slower than fluorescence.

As shown in Figure 1, absorption from the ground state often results in a vibrationally hot excited state as a consequence of the Frank-Condon principle. In the condensed phase, this extra vibrational energy is lost on the timescale of diffusion via vibrational relaxation (VR) through collisions with solvent molecules until the excited state is degraded to its ground vibrational energy level. It is only once the excited state is vibrationally relaxed that it may undergo other processes such as spontaneous emission, intersystem crossing (ISC) or internal conversion (IC). The latter two processes are both non-radiative and represented on Figure 1 by horizontal arrows to show the electronic energy exchange occurs with no loss in the total energy of the system. Whereas IC is a spin allowed conversion, ISC is spin forbidden and produces an excited state of a different spin multiplicity and therefore ISC usually precedes phosphorescence.

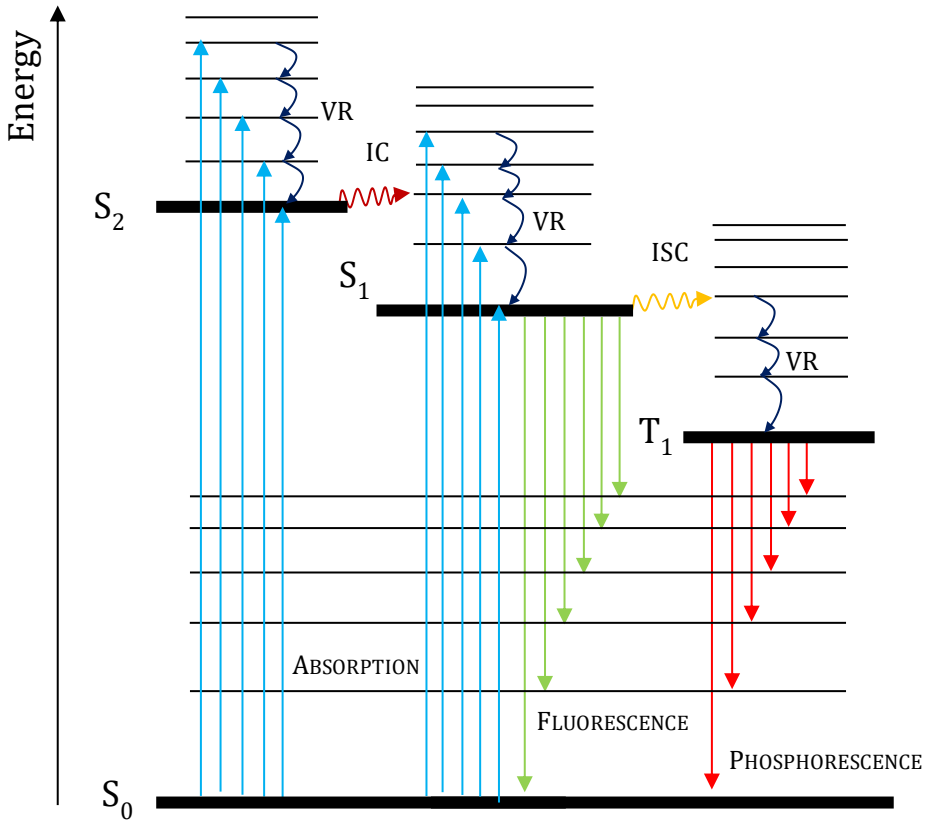

Figure 1 shows schematically the formation of spin allowed excited states (S_1 and S_2) from the ground state (S_0) via absorption and the intramolecular processes by which an excited state may lose this excess energy. Radiative process are represented with straight line arrows and non-radiative transitions are represented by curved arrows where IC = internal conversion, ISC = intersystem crossing, and VR = vibrational relaxation.

1.2. HYDRATED ELECTRONS

In 1808, Humphry Davy observed a "beautiful metallic appearance" and "fine blue colour" when potassium was heated in ammonia vapour.[12] A century later, Charles A. Kraus published a series of impressive studies on the conductivity of alkali metals dissolved in liquid ammonia that suggested the existence of "electrons surrounded by an envelope of ammonia".[13,14] Soon after, Gibson and Argo published the optical absorption of a series of alkali metals dissolved in ammonia, all of which exhibit the same strong blue colour observed by Davy.[15,16] From this work, the blue colour was shown to be independent from the metal identity and therefore not consistent with the assumption that the only species present in solution are solvated metal atoms.[16] Consequently, the concept of a solvated electron as an independent chemical species was established, displacing all preceding theories and cementing Davy's extraordinary contribution to science as the first person to observe the solvated electron more than 100 years prior.[17]

This thesis will focus primarily on the specific case of the solvated electron in water, e_{aq}^-, hereafter referred to as the hydrated electron. In 1952, it was suggested that such a species could be a product of the radiolysis of aqueous solutions,[18] however the significantly shorter lifetime of the hydrated electron compared to the equivalent species in ammonia results in an absence of the characteristic blue colour on dissolving alkali metals in water.[19] It was therefore ten years later, in 1962, before the first absorption spectrum of the hydrated electron (Figure 2) was recorded by Hart *et al.* using pulsed radiolysis of aqueous solutions, a result that was then reproduced independently by Keene.[20,21]

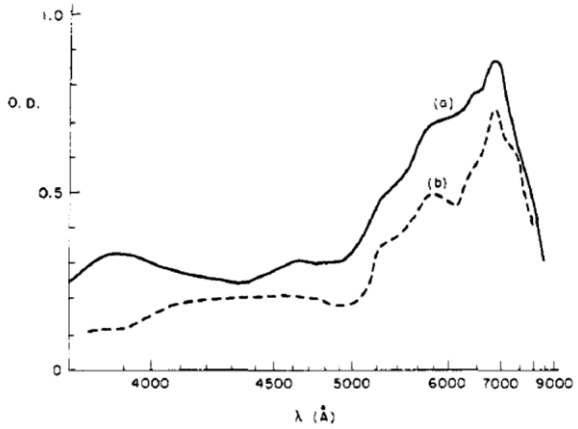

Figure 2 shows the absorption band of the hydrated electron in (a) 0.05 M solution of Na_2CO_3 and (b) pure water. Reprinted with permission from Hart and Boag (1962). Copyright (2018) JACS.

Since its discovery, the hydrated electron has been studied extensively, primarily due to its fundamental role in multiple areas of chemistry including, but not limited to radiation chemistry,[22,23] biological chemistry[24–26], atmospheric- and astro-chemistry[27–29], biochemistry[30–33] and its significance as a reducing agent in aqueous chemistry cannot be overstated.[22] In essence, the hydrated electron can be considered as the most fundamental quantum solute and an archetypal system to model many dynamical processes including solvation relaxation dynamics, electron delocalisation and autoionisation.[34,35]

Absorption of high energy radiation is known to potentially result in many forms of damage to living cells, including mutagenesis and DNA breakage.[36] However, recent work has shown that it is the hydrated electron product, and not the OH radical, from the radiolysis of water that inflicts the most damage.[26,36–38] In vacuum it has been shown that electrons with energies ranging from 3 – 20 eV are able to promote both single and double strand helix breaks with the DNA ionization threshold estimated to range from 7-10.5 eV.[24] A study by Simons[39] which was later supported by the experimental work by Martin *et al.* further showed that electrons with energies as low as 0.1 eV were capable of inducing covalent bond breakage in DNA.[40] Furthermore it has been shown that the energetically unfavourable attachment of an electron to nucleobases in a vacuum is significantly reduced on addition of only a few water molecules.[41,42] As such, it is reasonable to expect that a fully solvated aqueous environment may result in significant enhancement of the electron attachment to DNA.[17] Although the dissociative electron attachment mechanism of DNA breakage (which has been proposed to involve resonances with a $\pi \rightarrow \pi^*$ transition[39,43]) will not be discussed here, it is clear that gaining a full description of the mechanisms of formation and reactivity of the hydrated electron in different solvation environments is very important for understanding its role in the chemistry of all these fields.[35]

1.2.1. STRUCTURE AND PROPERTIES

1.2.1.1. ABSORPTION SPECTRUM

Considering the discovery of the hydrated electron primarily stemmed from the colour of metallic solutions, it is perhaps unsurprising that its most studied feature is its electronic absorption spectrum. Due to its characteristic asymmetric shape, (shown in Figure 3 by the black line)[44] with Gaussian functionality on the red edge and Lorentzian functionality on the blue edge, it has become the primary observable used to detect the species.[17,45,46]

The main Gaussian part of the absorption spectrum is very well characterised by a particle-in-a-box model using time-dependent density functional theory (TD DFT) with atomistic transitional orbitals and quantum numbers. From these many-electron simulations the lowest energy transitions are associated with excitation from the 1*s* ground state to the three 1*p* localised and orthogonal excited states. When combined with transitions to higher lying bound excited states, the main Gaussian part of the spectrum is accounted for almost in its entirety. The breadth of the band can be explained by the TD DFT cavity being both non-spherical and fluxional, inducing heterogeneous broadening and non-degeneracy in the *p*-states.[17,46,47] However, the low energy Lorentzian tail is not accounted for. As the

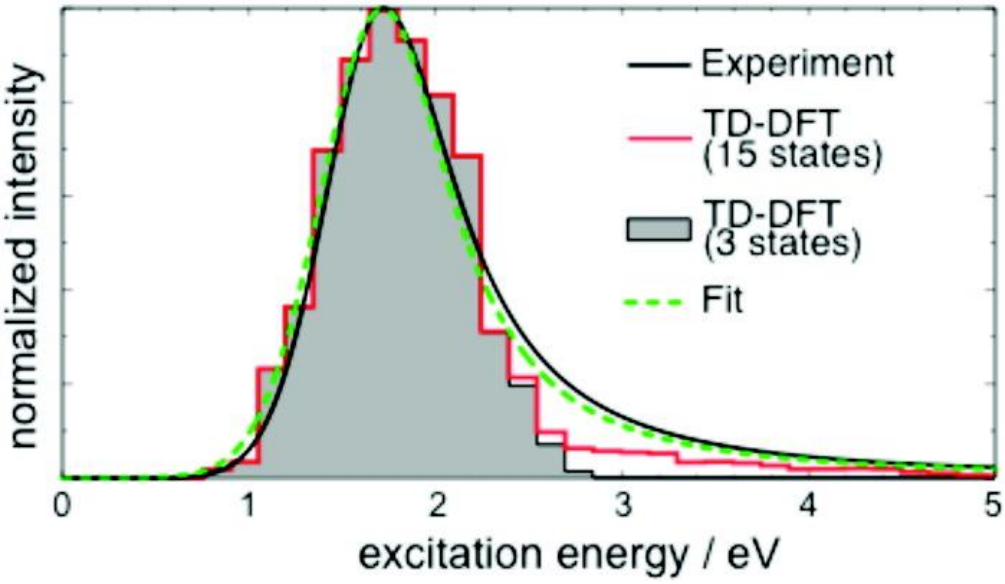

Figure 3 compares the results of the experimentally measured absorption spectrum of the hydrated electron to the results of TD DFT calculations that incorporate different numbers of excited states. Image reprinted with permission from Herbert and Jacobson, Copyright (2018) American Chemical Society.

blue tail overlaps with the low energy edge of the photoelectron spectrum, a long established thought is that it arises from transitions from the bound state to the continuum.[48–50] However, theoretical calculations that are capable of characterising continuum states do not reproduce such a feature in the simulated absorption spectrum. This suggests that the structure is not adequately described by such states and there is a greater complexity needed.[17,44,51]

In 2010, Herbert and Jacobson published a theoretical model that accounts for the optical absorption spectrum. Two different methodologies were employed; the first utilised a one-electron model that incorporates many-body electron-water polarization, and the second is a many-electron time-dependent density functional theory method with long range corrections to account for electron binding energies in water clusters. Although neither reproduces the quantitative intensities observed on the blue side of the spectrum, the improvement on previous studies is significant. The quasi-continuum states are shown to extend far into the water envelope and considered to be bound in nature due to energies that lie well below the vacuum level. In fact, the TD DFT results that incorporate the first 15 excited states (accounting for >99% of the oscillator strength) is able to generate absorption intensity corresponding to the blue tail, as shown in Figure 3.[44] This picture is interesting when compared to a measured oscillator strength of 1.14, as a value greater than 1 implies that in the excitation some intensity is borrowed from electrons on the water molecules surrounding it.[52]

1.2.1.2. VERTICAL DETACHMENT ENERGY

Since their first generation in 1981, finite water clusters, $(H_2O)_n^-$, up to n=200 have been studied by photoelectron spectroscopy (PES).[53–55] As small clusters are capable of being well characterised by electronic structure calculations, comparison of experimental results to theory provides great insight as to how an electron can be accommodated by water molecules within a cluster.[17,53,56] Initially, the primary focus of many computational studies was to catalogue the isomers of a cluster and attempt to elucidate the isomers responsible for the PES spectra. However, the number of isomers possible with a cluster, many of which have strongly overlapping peak signatures, makes this process non-trivial – especially

as cluster size is increased – placing great restriction on the incisiveness of simulations that simply catalogue the possible isomers.[17] Furthermore, the complexity of assignment is compounded by the fact that the process of electron attachment to water clusters is accompanied by energy transfer, resulting in the study of potentially non-equilibrium species or promotion of auto detachment pathways that would not be reproduced by the minimised energy structures generated in theoretical simulations.[17,57]

As such, a more useful measure may be the comparison of the vertical detachment energies (VDE), the magnitude of which indicates the strength of electron association with the cluster, and therefore its potential position of localisation. In early studies, the dependence of the VDE on the size of the cluster is shown experimentally to vary linearly as a function of $n^{-1/3}$. This is in agreement with the theory of solvation and therefore used to validate the extrapolation of the VDE to infinite cluster sizes to obtain values for the bulk phase of 3.3 eV.[54,58,59] Yet, Verlet *et al.* challenged this picture in which different electron binding positions were

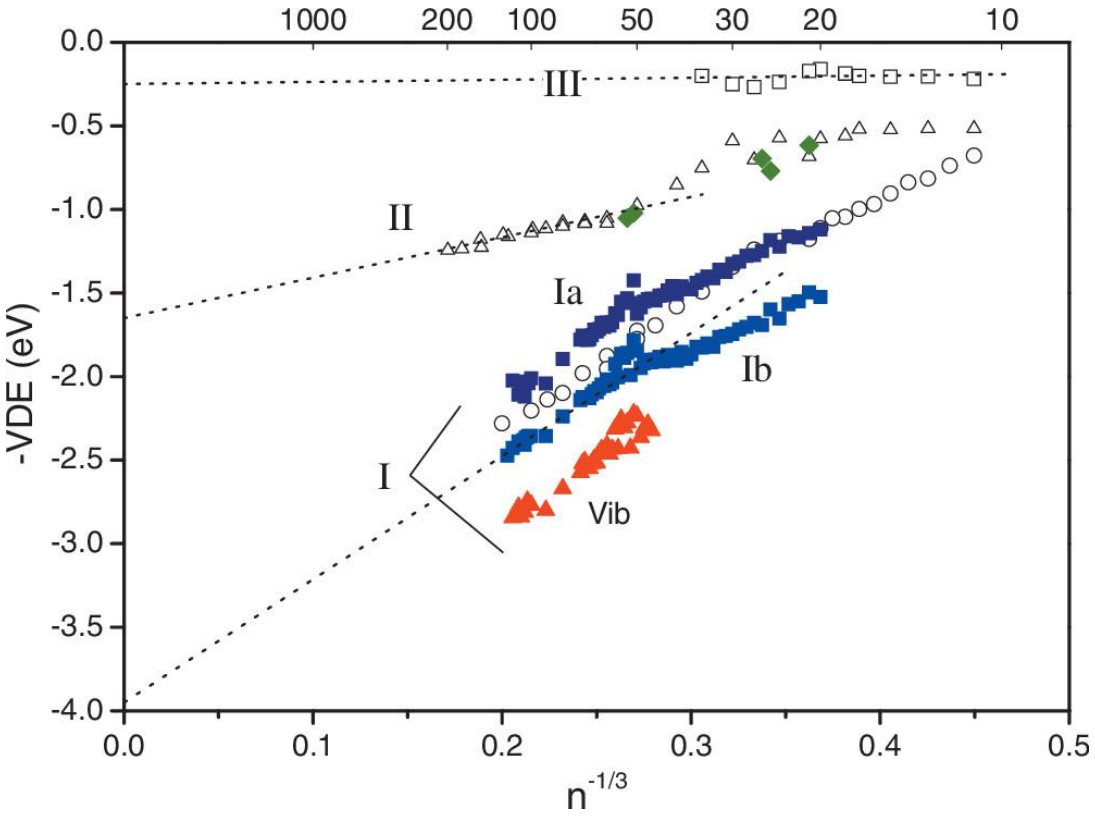

Figure 4 shows the positions of the peaks in the photoelectron spectra of clusters as a function of the cluster radius. The filled symbols show the results and assignments of Ma *et al, J Chem Phys,*2009, **131**, 144303*;* the empty symbols show the results and assignments of isomers I, II, and III made by Verlet *et al.* Reprinted with permission from Ma *et al.* (2009). Copyright (2018) AIP.

observed dependent on the pressure conditions, and therefore the local temperature, of the clusters on formation. From this work three isomers, associated with surface bound and internal states of the electron were proposed; assignments that were supported by molecular dynamic simulations that both predate and supersede the experimental work.[53,60,61] Furthermore PES studies of clusters thermalized at 10 K in a cold ion trap postulated full internalisation of the electron being increasingly favoured from n = 25 and being dominant at n = 46. The results from both these studies are shown in Figure 4 with the work of Ma *et al.* further sub-categorising isomer I to different internally solvated states, which they argue were previously unresolved due to the lack of thermal characterisation.[55]

Given these experimental results, computational interest was reignited in cluster structure. Using a new pseudopotential that treated both the water-water and electron-water polarization self-consistently, Jacobson and Herbert were able to identify four distinct isomers shown in Figure 5.[47,62] Analysis of the temperature dependence revealed unambiguous agreement of Isomer III with that of a dipole-bound state with a low VDE correlating to weak binding interactions. Isomer II was found to quantitatively agree with the picture of a surface-bound electron, with increased internalisation leading to a fully internalised cavity state through a partially embedded state corresponding to Isomers Ib and Ia respectively.[17,62]

The discussion thus far, however, assumes that extrapolation of cold gas-phase cluster data is representative of hydrated electrons in ambient liquid water. In 2010, four different groups questioned this assumption and independently focused efforts to directly measure the VDE of liquid water through PES of microjets. On the whole, the values reported were both consistent with each other (ranging from 3.3 – 3.6 eV) as well as the extrapolated results from cluster experiments (3.3 – 3.4 eV).[56,63–66] As well as a peak at 3.3 eV, the study by Siefermann *et al.* reported a distinct feature at 1.6 eV with a lifetime >100 ps. They assigned this peak to originate from a hydrated electron localised at the surface in accordance with the soft X-ray's sensitivity to the surface.[64] However, no other studies to date have reproduced peak at this intensity with a comparable lifetime.

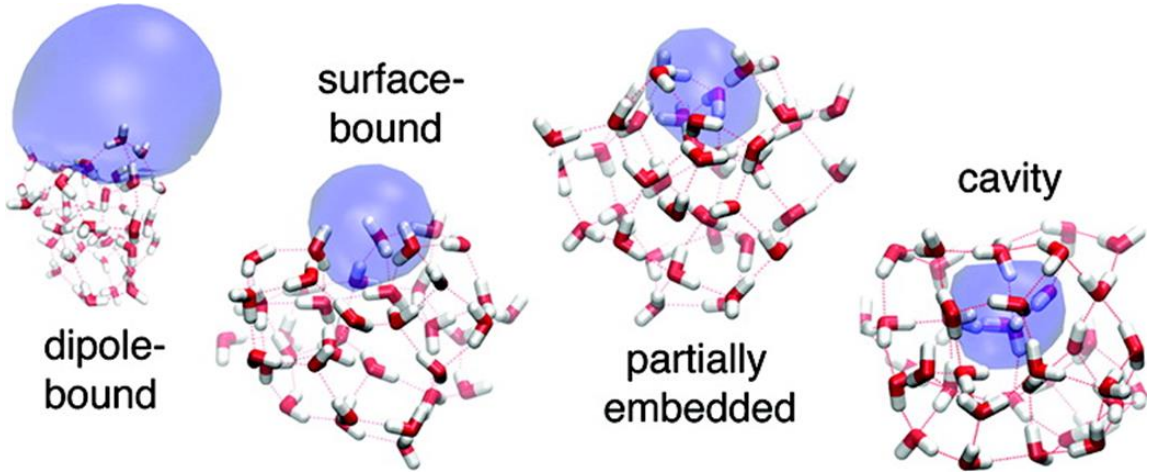

Figure 5 shows the four isomer structure types observed for the cluster $(H_2O)_{40}^-$. Reprinted with permission from Jacobson and Herbert (2011). Copyright (2018) ACS.

More recently it has been proposed that the wavelength dependence of the photoemission of hydrated electron is indicative of only internal solvated states, with inelastic scattering diminishing the energy of electrons before detection. In soft X-ray PES this electron-electron scattering would be large and thus is proposed to explain the nature of the previously observed long lived peak at 1.6 eV.[66] Furthermore, recent ab initio studies predict a VDE of 3.1-3.2 eV for interfacial electrons, and 3.3-3.4 eV for bulk species.[67] This therefore places doubt on the capacity of PES studies to distinguish between such species.[67] Consequently within the available experimental arsenal, PES is potentially the least insightful technique in elucidating binding structure.[17] However, a model that is unable to quantitatively reproduce experimental VDE trends will be significant and thus, PES and VDE is vitally important when evaluating the feasibility of proposed structures.[62]

1.2.1.3. THEORETICAL MODELS

With no experimental technique available to directly probe the hydrated electron structure on the molecular level, computational chemistry has a paramount role. Within the theoretical world, there are two main approaches taken to study the hydrated electron system; static and statistical. In the static approach the potential energy landscape governing hydrated electron geometry is probed using increasingly complex techniques ranging from continuum and semi-continuum

methods, through to high level ab initio approaches and density functional theory (DFT). The main limitations of this approach are two-fold: firstly, system sizes that generate precise and meaningful results are severely restricted; and secondly, the calculation of stationary points along a surface gives no information regarding the statistical or dynamics of a system as a whole. In contrast, statistical approaches look at the averaged ensemble properties through classical techniques and are therefore able to study time-evolution of the hydrated electron under different thermodynamic conditions.[61] As the quantum nature of an excess electron cannot be characterised purely classically, a mixed quantum-classical (MQC) is applied in which a subset of the system (at the very least the electron) is described by quantum mechanics, whilst the rest of the system is described classically in Monte Carlo or molecular dynamics (MD) techniques.[68] Due to one-electron models being computationally significantly less expensive than many-electron models such as DFT and ab initio calculations, most studies on e_{aq}^- are based on one-electron MQC MD simulations in which the classical and quantum mechanical components are coupled via pseudopotentials. The nature of these pseudopotentials is important and can have drastic effects on the properties of the output hydrated electron picture.[69]

Latent in the discussion of the hydrated electron thus far is the assumption that the electron itself occupies a region of excluded volume, henceforth referred to as a cavity, within the hydrogen bonded water network. The reason for this assumption is the overwhelming predilection for the cavity model in the literature since the 1950's; yet this paradigm has not been without challenge.[59] The following will therefore first discuss the cavity model before turning to the main models that have been developed in response to its failings. Computational details and parameters will not be discussed here but can be found both in the original literature, and summarised comprehensively in a review by Turi *et al*..[68]

CAVITY MODEL

The first description of an electron solvated by ammonia (an analogous system to water) in the 1950's proposed a spherical like cavity in which the electron is trapped by polarization it induces in the surrounding liquid continuum.[70]

Comparison of the solvation of an electron with that of an anion, such as the halides, soon led to the development of a more molecular solvation cavity by Natori and Watanabe in which the electron is surrounded by a cage of water molecules, with the hydrogens pointing towards the electron centre.[71] Comparison of this molecular structure with experimental electron spin resonance (ESR) data revealed coordination numbers of less than 4 were inconsistent with the line shape which was later supported by Kevan in 1981 who proposed an octahedral 6-coordinate structure is glassy water.[72–74]

Since the 1980's the cavity model was extensively developed and refined to consider the electron quantum mechanically with a rigid water structure encasing it. Using pseudopotentials to describe the electron-water interactions, MQC MD simulations of the absorption spectra were attempted semi-successfully, reproducing both the position and width but lacking the asymmetrical blue tail (as discussed in section 1.2.1.1).[75–77] It should however be noted that in most modern models, the cavity is considered to be highly fluxional and non-spherical in nature.[47,78] In more recent years, the dynamics of solvation under different thermodynamic conditions has been probed, observing a collapse of the electron wave function as the water reorganises to spontaneously form a cavity on a ~1 ps timescale.[35,47,67,79,80]

The sustained attention on the cavity model is not a simple consequence of a lack of other suitable descriptions. Extensively it has been shown to well characterise experimental features even with one-electron models, as long as polarizable water molecules are included.[17] A recent study by Kumar *et al.* for example demonstrated that cavity forming DFT calculations on minimal 4 water tetrahedral structures are able to quantitatively reproduce essentially all of the available experimental evidence including solvation energy, radius of gyration (from absorption spectra width), and the ~200 cm^{-1} redshift for OH stretching frequency in Raman spectra.[81] Furthermore, many experimental results that are not perfectly characterised, such as the hydrated electron diffusion coefficient and its temperature dependence, are reproduced in semi-quantitative fashion.[78] Even the Lorentzian tail of the absorption spectrum, which had evaded previous cavity

model simulations and initiated much debate regarding its suitability as a consequence, is now reasonably well characterised using TD DFT.[44]

NON-CAVITY MODEL

To satisfy the Pauli-exclusion principle between the electrons on the water molecules and the hydrated electron itself, the pseudopotentials employed in cavity forming models tend to be highly repulsive.[82] However, in 2010 Larsen, Glover and Schwartz (LGS) revaluated the balance between attractive and repulsive forces and proposed a new pseudopotential that resulted in a hydrated electron structure in which the water molecules impregnate the wave function of the hydrated electron, yielding a region of increased water density and no excluded volume at the position of e_{aq}^-.[83] This is a unique feature of the LGS pseudopotential and is justified by the authors as being aligned with prior measurements of e_{aq}^- having a negative partial molar volume, $\bar{V}_e$.[69]

The LGS model is however extremely controversial, receiving immediate criticism, primarily due to the lack of agreement with established experimental benchmarks, such as the VDE which is significantly overestimated.[69,84–86] In fact, the experimental features that the LGS model reproduces well, such as the diffusion coefficient and radius of gyration, are also well characterised in the cavity models.[69] Furthermore, when compared to the exact solution of the Schrödinger equation of an excess electron in a field of water the pseudo-orbital calculated by the LGS potential is significantly lowered in energy, suggesting a potential that is far too attractive.[86] In fact, even the justification for the enhanced water density has been undermined by the reported value of $\bar{V}_e$ being misquoted, with the original literature only quoting a range without conclusively stating the sign.[69,87]

The non-cavity model is far from being entirely disregarded. Although cavity models have now reproduced the absorption spectrum blue tail, an oscillator strength greater than unity (as discussed in section 1.2.1.1) can only be explained by a non-cavity picture.[52] What's more, the cavity model almost completely fails to reproduce the observed absorption spectrum temperature dependence where the LGS model reproduces the results almost quantitatively. Consequently, the long-

running debate between the non-cavity and cavity models remains unquenched.[82,88]

With the reality of modern day pseudopotentials, it is likely that the 'real' structure of the hydrated electron lies somewhere on the continuum between the cavity and non-cavity models. In a study by Uhlig *et al.,* ab initio MQC MD calculations implied a complex structure containing a large cavity contribution (containing 41% of the spin density) as well as a diffuse function that extends far into the solvating water structure and echoes that of a non-cavity structure (24% overlapping with the water molecules, and a ~35% diffuse contribution beyond the first solvation shell).[46,89] This work proved to be the springboard from which the study by Kumar *et al.* is based, that incorporates diffuseness into the cavity model, and successfully reproduces many experimental features, as discussed above.

1.2.2. FORMATION

Consistent with the hydrated electron's importance there is a plethora of literature and comprehensive reviews dedicated to its formation.[17,19,22,90,91] In the original 1962 study, the hydrated electron was generated through pulsed radiolysis via interaction of 1.8 MeV electrons with aqueous solutions. Consequently much of what is known about the hydrated electron originates from experiments involving the radiolysis of water. Yet, the ionising radiation in radiolysis experiments typically has a very large distribution of high excitation energies, and therefore generates electrons with a broad range of kinetic energies and ejection distances.[92] This is further exacerbated by the generated electrons having sufficient energy to cause at least one secondary ionising event, resulting in a lack of homogeneity in the distribution of excitation events called "spurs".[22,93] Hydrated electrons have therefore also been formed by sonolysis; two-photon excitation of pure water; and photo detachment of a donor species such as I^- and CN^- via a charge-transfer-to-solvent (CTTS) states.[17] However, as the initiation process is known to have a large impact on the solvation dynamics, the hydrated electrons generated by different techniques are not equivalent.[94]

The advent of ultrafast spectroscopy has seen a large array of photolysis studies on the hydrated electron.[94] In contrast to radiolysis, the excitation energy from a laser is much lower with a narrower spectral distribution. This results in a much narrower range of kinetic energies amongst the hydrated electron products, with a more uniform distribution across the sample.[92,93] All the work presented in this thesis utilises femtosecond time-resolved spectroscopy techniques. As such, the remainder of this section will be dedicated to the mechanisms by which the hydrated electron is generated through the absorption of light.

1.2.2.1. IONISATION OF LIQUID WATER

Before photolysis experiments became the vogue, pulsed radiolysis experiments in alcohols suggested multiple stages of solvation.[95–97] However only dynamics occurring from 30 ps onwards were able to be studied.[93,98] Due to the comparatively sub-picosecond solvation dynamics in water, such shifts in the hydrated electron absorption spectrum were not observed until 1986. In this study by Migus *et al.,* a transient localised state was attributed to the non-equilibrium 'hot' electron, e_{NE}, with absorption in the IR is observed to have been established within 110 fs. This band then decays with a lifetime of 240 fs and the growth of the characteristic hydrated electron peak at 720 nm.[34,99] This blue shift in the frequency of the $s \rightarrow p$ absorption is entirely consistent with the picture of the hydrated electron as a simple particle-in-a-box, in spite of the oversimplification of its nature. From this model, the absorption is a direct consequence of the extent of delocalisation with the shift arising from solvent relaxation. In a study by Savolaninen *et al.* the initial frequency of the absorption peaks at ~1.5 THz, when combined with MD simulations, indicates an instantaneous size of approximately 40 Å.[35]

The importance of the precursor states to the hydrated electron extends beyond the observation of solvent relaxation however. In multiple studies over the last decade, it has been shown that precursors to the hydrated electron are very reactive, with different solvation dynamics, reaction rates and products, observed in comparison to e_{aq}. These pre-hydrated states have also been shown to be the

species that induce reductive damage to DNA, and not that of the fully hydrated state.[26,94,100,101] Figure 6 summarises these experimental approaches use to study the hydrated electron of which there are two main types: multiphoton ionisation of liquid water and optical excitation of excess electrons. In all the studies, the nature of the precursors formed as well as the solvation dynamics are shown to be highly dependent on the mechanism of generation and the energy of excitation.[34]

In 1996, Crowell and Bartels found that there are three mechanisms by which an electron is generated by photons in the range between 3.0 and 5.0 eV. At low photon energies (3.02 – 3.47 eV) a direct (3+1) Resonance Enhanced Multi-Photon Ionisation mechanism, shown in Figure 6(a), promotes a water molecule to some excited state which is then excited above the ionisation potential to form a highly delocalised conduction band, $e_{CB'}$, with high kinetic energy.[34,102] Low energy photons access optically excited states of the equilibrated ground state. Conduction band electrons lying above the VDE may be accessed by one or two photon excitation as shown in Figure 6(e) and (f) respectively. At lower excitation energies e_P is accessed which is comprised of a set of three nondegenerate p-like states, shown in Figure 6(d).[34,103] Although the conduction band electrons in Figure 6 are distinguished by their designation ($e_{CB'}$, $e_{CB''}$ and $e_{CB'''}$), all are delocalised over

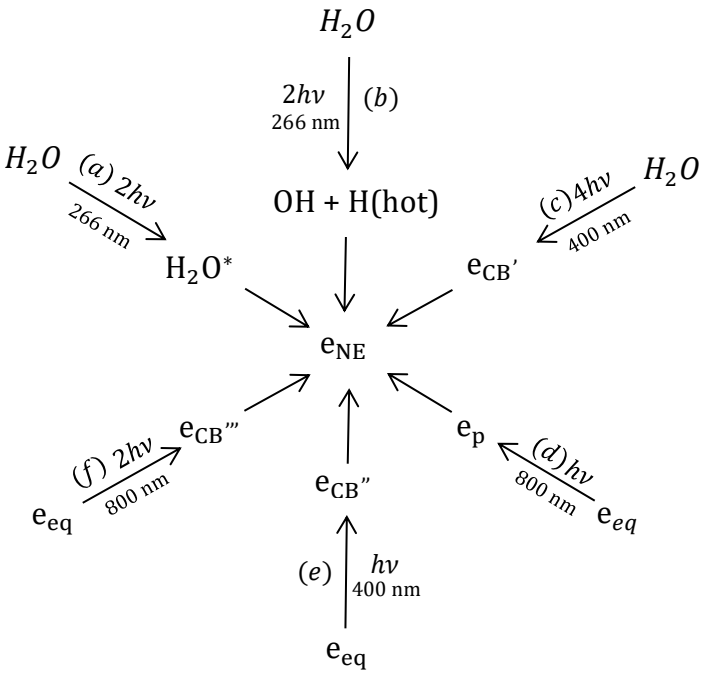

Figure 6 shows the many experimental techniques that have been utilised to study the hydrated electron and its precursors.

tens of angstroms and short lived, localised in a different solvent site to that of the original donor in less than 100 fs. In fact, the structure and dynamics are likely to be very similar across all three with the subscripts merely included to highlight the different mechanisms of generation.[104]

As photon energy is increased (above 3.85 eV), two photon absorption dominates which has been explored in a number of recent studies.[102,105–107] There are two proposed two-photon mechanisms: exciton decay Figure 6(a) and direct dissociation Figure 6(b), both of which occur at energies below the ionisation potential of water and electron separation occurs via nuclear rearrangement.[35,108] Once formed, the hydrated electron can either react with other products, such as OH and H_3O^+, in a process called diffusional geminate recombination or relax via solvation to the equilibrated hydrated electron, e_{aq}^-. The recombination probability is directly proportional to the distance between the ejection distance of the electron on creation, and therefore the separation between the geminate ion pair. The further the ion is ejected, the greater the chance that the hydrated electron will be long lived. As the kinetic energy imparted to the electron is proportional to the distance from the positive ion counterpart, the greater the total excitation energy, the lower the product yield from geminate recombination. [34,93,102,105–107]

1.2.2.2. PHOTODETACHMENT VIA CTTS

Although it may sound appealing to study the hydrated electron in pure solvent, the molecular cross-section for multiphoton absorption is significantly smaller than the cross-sections responsible for single photon absorption. Photo-detachment of electrons from donor species by single photon absorption is experimentally much simpler, resulting in a higher e_{aq}^- yield. These transitions in aqueous anions have been extensively studied both experimentally and theoretically with the energy of the transition shown to be highly dependent on solvent, temperature, and environment.[108–114] These bands, that are not observed in gas phase studies, are therefore assigned as CTTS transitions, with energies that lie below the detachment energy of the donor.[108] Iodide is a long standing

prototype for the CTTS state transition resulting in the generation of the hydrated electron in high yields.[108,110]

In 2002 Bradforth and Jungwirth provided a qualitative picture of the CTTS state of anions in bulk solutions in which it is proposed that the hydrated electron is formed by relaxation within the first solvation sphere, in close proximity to the now neutral parent radical, forming a solvated contact pair, $I^0{:}e^-$, with electron ejection driven by the solvent rearrangement.[109,111,115] This is in strong contrast to the ionisation of water discussed above as well as other donor anions such as cyanide ions from $[Fe(CN)_6]^{4-}$ in which the ejection length far exceeds that of the first solvation shell.[109]

Across the low energy CTTS excitation described above, there is no change in the geminate recombination yield or the dynamics suggesting that the primary mechanism at these energies is through a common excited state with the same mechanism of ejection. However, as the energy increases above the VDE (~7.1 eV for Iodide)[116] two main channels have been identified: a minor pathway leading to direct photo detachment and a relaxation pathway through the CTTS manifold which is dominant. [108,112,115,117]

Although Iodide has been extensively studied, hydrated electrons have also been generated from other aqueous inorganic anions, such as Ferrocyanide ions,[100,108,118–120] and organic molecules with acidic moieties such as indole and phenol.[121–124]

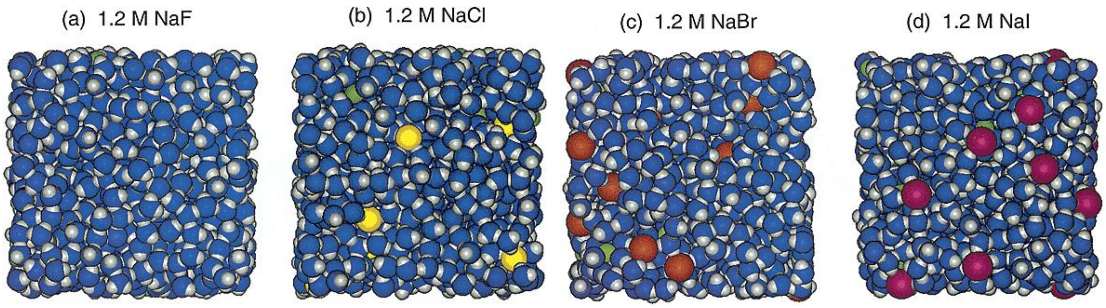

Figure 7 shows the MD simulation results from Jungwirth and Tobias of the surface concentration of 1.2 M sodium halide solutions as viewed down onto the surface. Reprinted with permission from Jungwirth and Tobias (2002). Copyright (2018) AIP.

1.2.3. SURFACE OR BULK?

The fundamental question as to whether ions exist at an interface is crucial to both physics and chemistry. For the hydrated electron in particular there are many features of solvation at surfaces that remain unclear; where does the electron solvate; how does its structure and properties differ from bulk species; and what role do the surface electrons play in chemistry?[125]

In 2002, Jungwirth and Tobias developed a new comprehensive picture of how ions are distributed across an interface. The MD results, shown in Figure 7, are represented as looking down onto the surface and indicate that an anion's surface propensity is increased proportionally with its polarizability.[126,127] As has been previously discussed, the equilibrated hydrated electron (with its highly diffuse wave function) is polarizable and may be expected to have at least some surface affinity – especially if it was generated via a CTTS from an ion already prevalent at the surface.

However, experiments on liquid microjets (conducted in an attempt to validate the extrapolation of cluster data to the bulk) in which hydrated electrons were generated from I^- only yields one VDE peak at 3.4 eV considered to be from a bulk

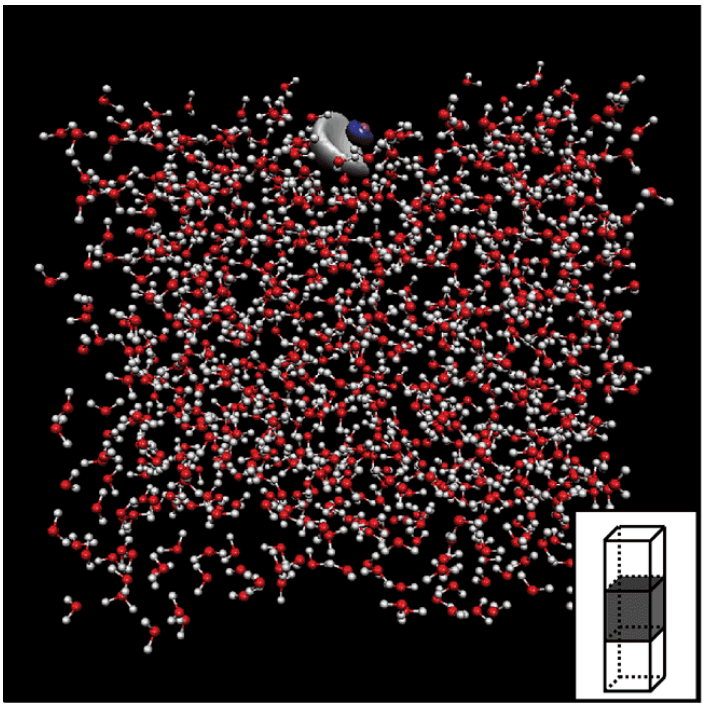

Figure 8 shows the shape of the CTTS triplet state for iodide at the air-water interface. Iodide is purple and at the surface. Reprinted with permission from Bradforth and Jungwirth (2002). Copyright (2018) American Chemical Society

species. All of these studies however probe the electron at times >100 ps and at ambient liquid temperatures, the thermal energy is considered great enough that surface bound electrons would have undergone a full transition to internal states within this timescale. MD simulations on pure water interfaces suggests complete quenching of surface states within 10 ps.[128] Furthermore, time-resolved PES revealed no angular anisotropy for I^- or an electron generated via its CTTS. This is interpreted as being indicative of bulk solvated species with significant elastic scattering of the photo-emitted electrons removing the angular dependence.[129,130]

In contrast, a parallel study on 1,4-diazabicyclo[2,2,2]octane (DABCO) observed anisotropy from DABCO indicating a surface state, and yet the hydrated electron generated from DABCO only exhibited isotropic angular distributions. Thus, even if a molecule itself is found at a surface, the CTTS transition appears to eject the electron into the bulk phase, generating an internally solvated state.[66,130] This picture is consistent with the MD simulations by Bradforth and Jungwirth in which the HOMO of the CTTS for iodide at the air-water interface is shown to be pointing directly into the bulk phase, as shown in Figure 8.[109]

As previously mentioned, the hydrated electron's absorption spectrum is highly dependent on the radius of gyration, which in turn is determined by solvation structure. At an interface, there is disruption of the hydrogen bonding network

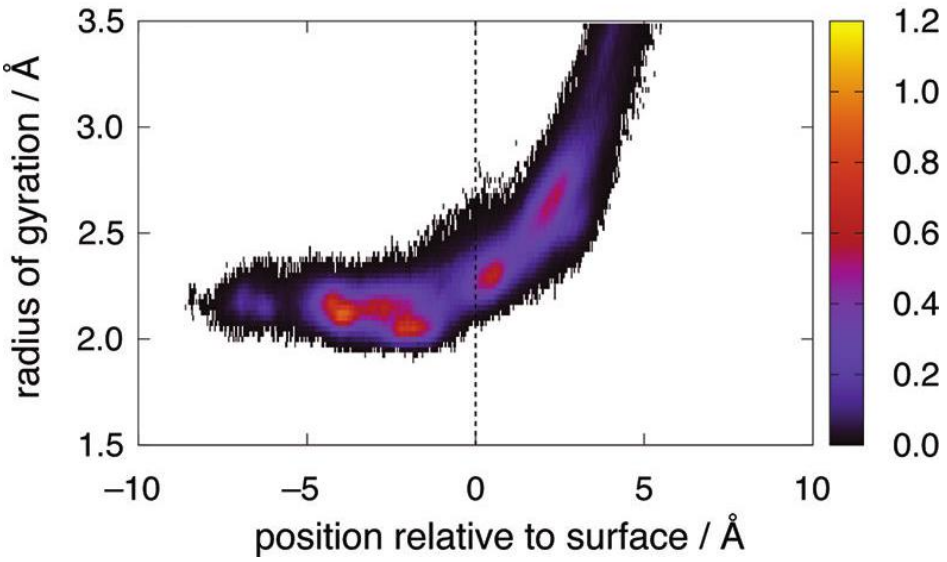

Figure 9 shows the simulated probability distribution of the electron radius of gyration as a function of the relative position to the surface. Adapted, with permission, from Jacobson and Herbert, copyright 2018 American Chemical Society.

which could change the structural properties of the electron, and therefore its radius of gyration with respect to the bulk. Figure 9 shows that MD simulations suggest a rapid change in the radius of gyration towards a size not dissimilar to that of the bulk species as the interface is traversed (with the positive to negative direction being from the gas phase towards the bulk).[62] As even partial solvation has drastic effects on the radius of gyration, it is perhaps unsurprising that the MD simulated absorption spectra for the bulk and surface bound electron appear virtually indistinguishable from one another.[46,67] However, the absorption spectrum at the interface has not been measured experimentally and considering the plethora of contradictory theoretical results regarding the hydrated electron's structure, differences, or lack thereof, between the surface and internal states cannot be confirmed without experimental verification.

In section 1.2.1.2, the PES has been used extensively to show that the position of a hydrated electron has a complex dependence on cluster size and temperature. Yet a consensus regarding how this information can be extrapolated to the bulk phase has not been attained. A clearer picture of electron localisation arises by studying ice deposited on metal surfaces (acting as the electron source) through both time and angle resolved two photon photoelectron spectroscopy. The results show that the solvation dynamics of amorphous wetting layers do not change with increased layers or adsorption of Xe (shown to quench the electron signal), indicating an absence of surface bound states. Furthermore, on amorphous ice the lifetime of solvation occurs on the fs to ps regime,[131,132] a rate comparable to that reported in liquid water surfaces.[111,133] Yet the opposite is seen for crystalline ice layers, with long lived surface localisation observed on the order of minutes.[132] These experimental results are particularly enlightening when coupled to the DFT study by Bhattacharya *et al.* who present results indicating crystalline ice shows a significant surface preference over bulk, even when the latter has defects within the hydrogen bonding network, whereas both sites are equally energetically favourable for amorphous ice. In both instances, the electrons occupy vacuous space within the solvent network indicating that electrons are primary trapped at pre-existing defect sites before solvation occurs via nuclear rearrangement.[133,134]

Yet ice studies at ~40 K suffer from the same criticism as cluster studies – the conditions are not representative of ambient systems.

The interrogation of air/water interfaces under atmospheric conditions is possible using a surface specific technique called Second Harmonic Generation (SHG) which is only active in a non-centrosymmetric environment such as at an interface. This method has been utilised by our group to study the interfacial hydrated electron with a variant called Sum Frequency Generation (SFG) being utilised by other groups in similar studies. Full discussion of SHG and its relation to SFG can be found in Chapter 4, with its application to the interfacial hydrated electron being the focus of section 4.2.4.

1.3. THE MULTI-EXPERIMENT SPECTRAL SUITE (MESS)

An overarching theme in the Verlet group's research focus has been the study of molecular dynamics in different solvation environments. Before now, this was explored using three standalone experiments that probe molecules in solvent free gas phase environments, in partially solvated cluster environments (both of which use PES), and at a liquid-air ambient interface using SHG. However, until recently the group had no ability to study the changes in molecular dynamics in going from a surface to bulk solvation environments. To fill this gap, the Multi-Experiment Spectral Suite (MESS) has been designed.

The work in this thesis describes the design and implementation of the MESS which incorporates multiple time-resolved spectroscopy experiments on one optical table, with the capacity to switch easily between them. At present, the MESS contains two experiments: Transient Absorption (TA) and a newly designed SHG experiment that builds on the previous setup. However the interchangeability gives the potential to expand the MESS further to incorporate more experiments.

The remainder of this thesis will therefore be structured as followed; first the components of the MESS that are interchangeable and common across both experiments will be introduced; then each experimental technique will be discussed in turn, detailing the experimental setups and key results for each.

2. GENERAL COMPONENTS OF THE MESS

2.1. LASER SYSTEMS

The light source for the MESS is a single unit, ultra-compact Yb-Doped Potassium Gadolinium Tungstate (Yb:KGW) laser system (Carbide, Light Conversion) with full output characteristics detailed in Table 1. As will be discussed in Chapter 4, the signal intensity is proportional to the square of the input field intensity in the SHG experiment. As such these features provide an effective compromise between pulse duration (and therefore time resolution) and pulse energy due to the high repetition rate and output power, optimising signal intensities.

The 1030 nm fundamental wavelength offers the possibility of generating a supercontinuum spanning from 500 nm through to the near IR (1000 nm), without the spectral gap typically of 100 nm width centred at ~800 nm that arises in commonly used Ti:Sapphire driven continuum. This is important as many molecules of scientific interest possess interesting features at this near IR-visible boundary. This includes the hydrated electron whose bulk absorption maximum is well documented to exist at 720 nm.[21,135]

All three MESS experiments are time-resolved in nature, utilising an optical pump-probe scheme as described in section 1.1. The following sections describe the generation of the pump and probe frequencies utilised in each experiment within the MESS components with reference to Figure 10.

Table 1 the output characteristics of the new CARBIDE laser output purchased from Light Conversion.

	Carbide
Output wavelength / nm	1030
Repetition rate / kHz	60
Output power / W	5
Pulse width / fs	~250
Pulse energy / µJ	~84

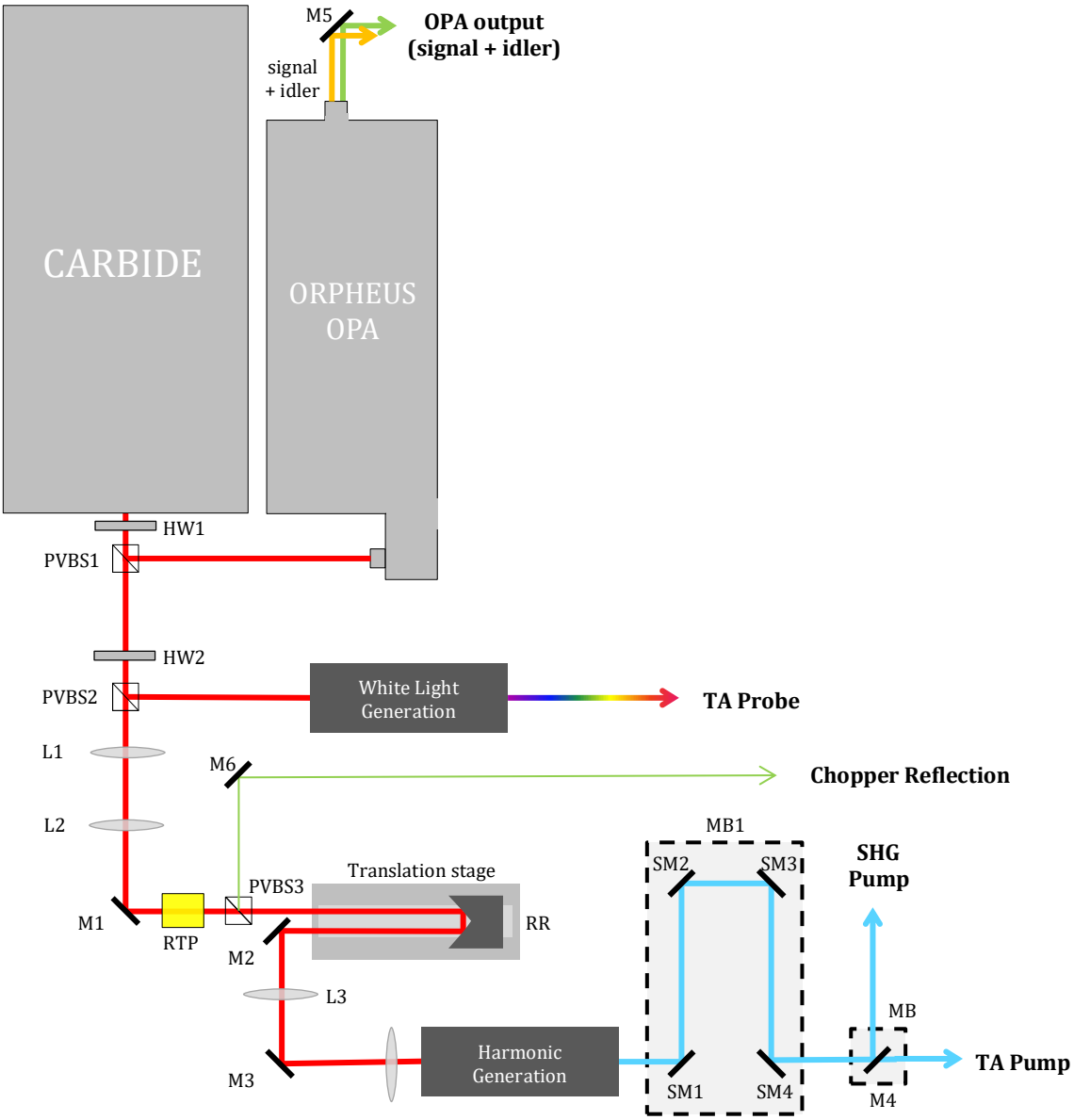

Figure 10 shows the optical configuration for the generation of the pump and probe pulses used in all three MESS experiments where M = cold mirror, SM = selective mirror, HW = half waveplate, VPBS = variable polarising beam splitter, P = polarisor, RR = retroreflector, MB = magnetic base, AS = aspheric lens, AC = achromatic lens, F = filter, RTP = RTP pockels cell and I = iris.

2.1.1. PROBES

The CARBIDE output is directed through a half-waveplate into a polarising variable beam splitter (PVBS1) which reflects 1.8 W and transmits 3.2 W of the CARBIDE output. The reflected 1.8 W is used to seed an optical parametric amplifier (OPA) (Orpheus, Light Conversion), the output of which is used as the probe for the SHG experiment.

The transmitted portion of the CARBIDE output is directed through a second half wave plate (HW2) and polarising beam splitter (PVBS2). Using HW2 the majority of the beam is set to be horizontally polarized and therefore transmitted through PVBS2 and used as the pump beam. Approximately 5% of the 3.2 W output is reflected by the beam splitter cube and directed into a white light (WL) generation stage which will be described in detail in section 3.3.2.2. The output white light then forms the probe for the TA experiment.

2.1.2. PUMP

The beam transmitted from PVBS2 is directed through a rubidium titanyl phosphate (RTP) crystal (the purpose of which will be discussed in section 2.1.2.1) onto a retroreflector on a motorized delay stage. This allows fine control of the arrival of the pump pulse in relation to the probe. The reflected light is then directed through the harmonic generation stage (described in full in section 2.1.2.2) in which the second, third, fourth or fifth harmonic of the 1030 nm fundamental is generated. Once generated, the desired harmonic frequency is separated from the fundamental beams by using a series of selective mirrors (SM1-4). These mirrors are located on an interchangeable series of kinematic magnetic bases (MB1) which allow the selective mirrors for the desired harmonic to be put in place without jeopardising alignment and stability each time the pump frequency is changed. The pump pulses are used in all three experiments in the MESS with a second magnetic base (MB2) placed after the selective mirrors to allow the pump beam path to be easily redirected into the different experimental set ups. When the top plate of MB2 is present, a cold mirror (M4) directs the beam into the SHG experiment. When the top plate is removed, there is no mirror to alter

the pumps path and the beam instead travels directly into the TA and reflectance set ups.

2.1.2.1. 30 KHZ PUMP MODULATION

Pump modulation uses a physical moving component (such as a chopper wheel or shutter), but other methods are possible such as an acousto-optic or electro-optic modulator. Ideally the frequency of this modulation is set to half the laser repetition rate allowing shot-to-shot background subtraction and therefore lower levels of noise. This is discussed further in section 3.2.

Immediately after PVBS2, the beam has a diameter of 2 mm and a maximum possible power of 3.2 W (with no light reflected into the WL generation stage), thus yielding a pulse energy of 54 μJ at 60 kHz and a potential incident intensity of 6.9 GW cm^{-2} on the crystal. The *x*-cut RTP is quoted by the supplier to have a damage threshold of 1 GW cm^{-2} for 1 ns pulses. As pulse length scaling laws break down below the ps regime, upon consultation, an appropriate threshold limit for the femtosecond regime is considered to be 2 GW cm^{-2}. A magnifying Galilean telescope, constructed from a divergent lens (L1, $f = -100$ mm) and a focusing lens (L2, $f = 50$ mm), is therefore placed before the RTP cell, reducing the intensity to 1.7 GW cm^{-2}. To optimise frequency conversion in the harmonic generation stage, the beam size is then reduced using a Keplerian telescope with a 500 mm lens (L3) and 150 mm lens (L4).

Figure 11 represents the three tier triggering sequence required to generate the 30 kHz chopped pump train. Initially the rising edge of the 60 kHz digital laser output shown in Figure 11(a) is used to trigger a digital delay generator (T560 Highland Technology) which divides the signal by two. This outputs a train of 30 kHz pulses with a programmable width (W) and delay (D) with respect to the rising edge of the trigger, shown in Figure 11(b), both of which are used to optimise the temporal overlap between the arrival of the laser output pulses and the chopper signal. The rising edge of this 30 kHz pulse train then triggers a pulser (homemade with a 100 W power supply), which generates two outputs that are each attached to a separate pin across the RTP cell, as shown in Figure 12. The first output, shown by

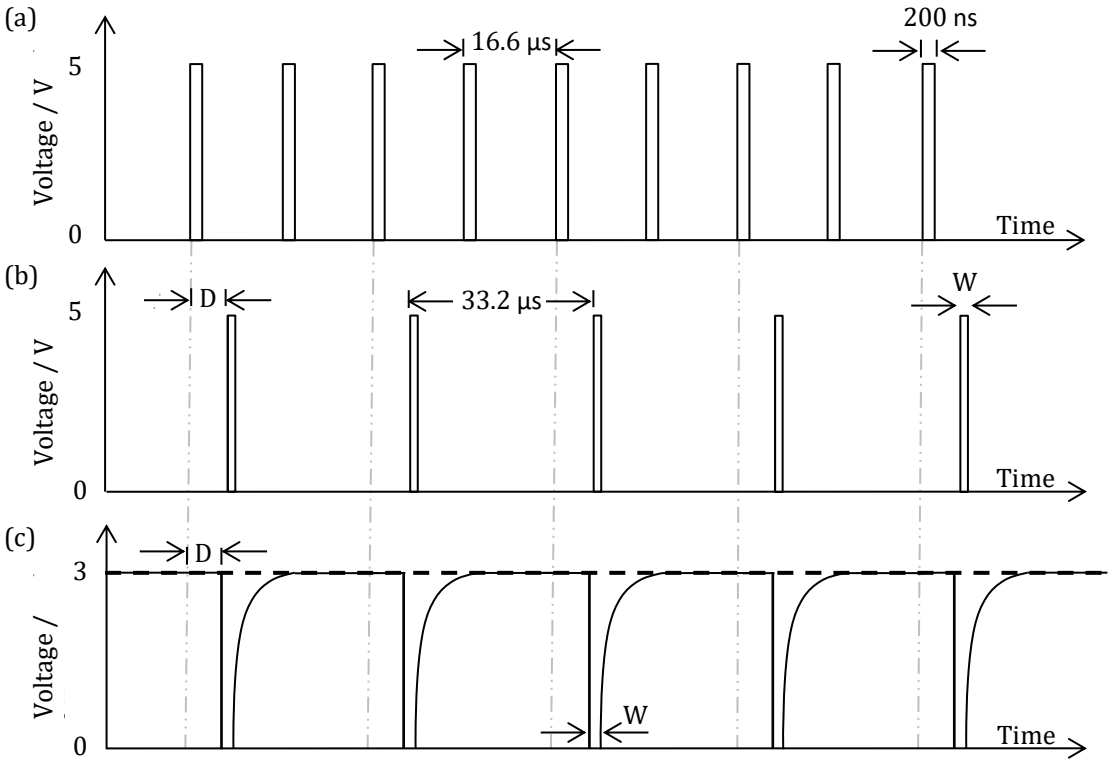

Figure 11 represent schematically the signal inputs required to trigger the RTP chopper whereby (a) represents the 60 kHz digital laser output used to trigger the T560 Highland Technology Digital Delay Generator which divides the signal by two and outputs a train of 30 kHz pulses with a defined width (W) and delay (D) with respect to the laser, as shown in (b). This 30 kHz pulse train then triggers a homemade pulser (100 W power supply) which has two outputs, each attached to a pin either side of the RTP crystal. The first output, shown as the dashed black line in (c), is a constant DC High voltage output held at 3 kV. The second output, shown by the black trace, drops its voltage from 3 kV to 0 when triggered by the rising edge of (b), thus generating a 3 kV potential difference across the RTP cell pulsed at 30 kHz.

the dashed black line in Figure 11(c) is a constant DC high voltage held at a high voltage (HV). The second output, shown by the solid trace, pulses its voltage from HV to 0 V when triggered by the delay generator output. When these two outputs are each attached to the cell pins, it generates a pulsed potential difference (up to 3 kV with optimum modulation observed at 2.05 kV) across the crystal pulsed at 30 kHz, which has the consequence of rotating the polarization of the input beam by 90° when the potential difference is present, thus generating a train of pulses with alternating polarisations. This train of pulses then passes through PVBS3 which transmits the vertically polarized pulses, resulting in a 30 kHz pulse train. Thus, by switching the input polarization before the harmonic stage, the pump will be chopped at the same rate that the RTP electrical pulse is driven. This is significantly faster than a mechanical chopper that can be locked to an external

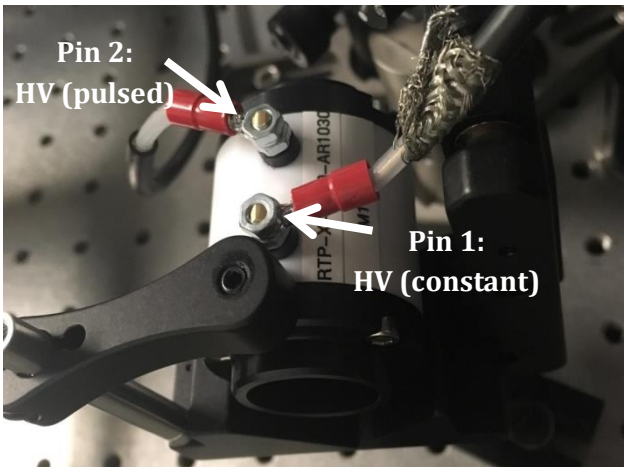

Figure 12 shows the RTP crystal in its housing with the two pins across which the potential difference generated by the pulser is applied.

clock. The reflected pulse train from PVBS3 (which contains a small amount of SHG light generated within the crystal) is then used to separate pump on from pump off signals in TA and Reflectance experiments, as discussed in detail in section 3.3.2.3.

2.1.2.2. HARMONIC GENERATION

Figure 13 describes the harmonic generation stage used to frequency convert the CARBIDE 1030 nm output. The boxed panel shows all the components that are included in the harmonic generation state. The configurations beneath show the component combinations required to generate the second (SHG, 515 nm), third (THG, 343 nm), fourth (FHG, 257 nm) and fifth (5HG, 206 nm) harmonics of the fundamental. The circles and arrows show a horizontal and vertical polarization respectively with all frequencies designed to have the same polarization on output. The colours represent the different harmonic frequencies where red = 1030 nm, green = 515 nm, purple = 343 nm, dark blue = 257 nm and light blue = 206 nm. The relative positions of the circles/arrows show the delay between the pulses of different frequencies. Frequency conversion is optimised by a Keplerian telescope (L3 = 500 mm, L4 = 150 mm), as shown in Figure 10.

SECOND HARMONIC (515 NM) GENERATION

A Type 1 BBO crystal (θ= 23.4° and ϕ= 90°, Eksma Optics) frequency doubles the 1030 nm fundamental. The 515 nm is then filtered from the fundamental using the selective mirrors (SM1-4 on MB). A half wave plate (HWP) is included before the

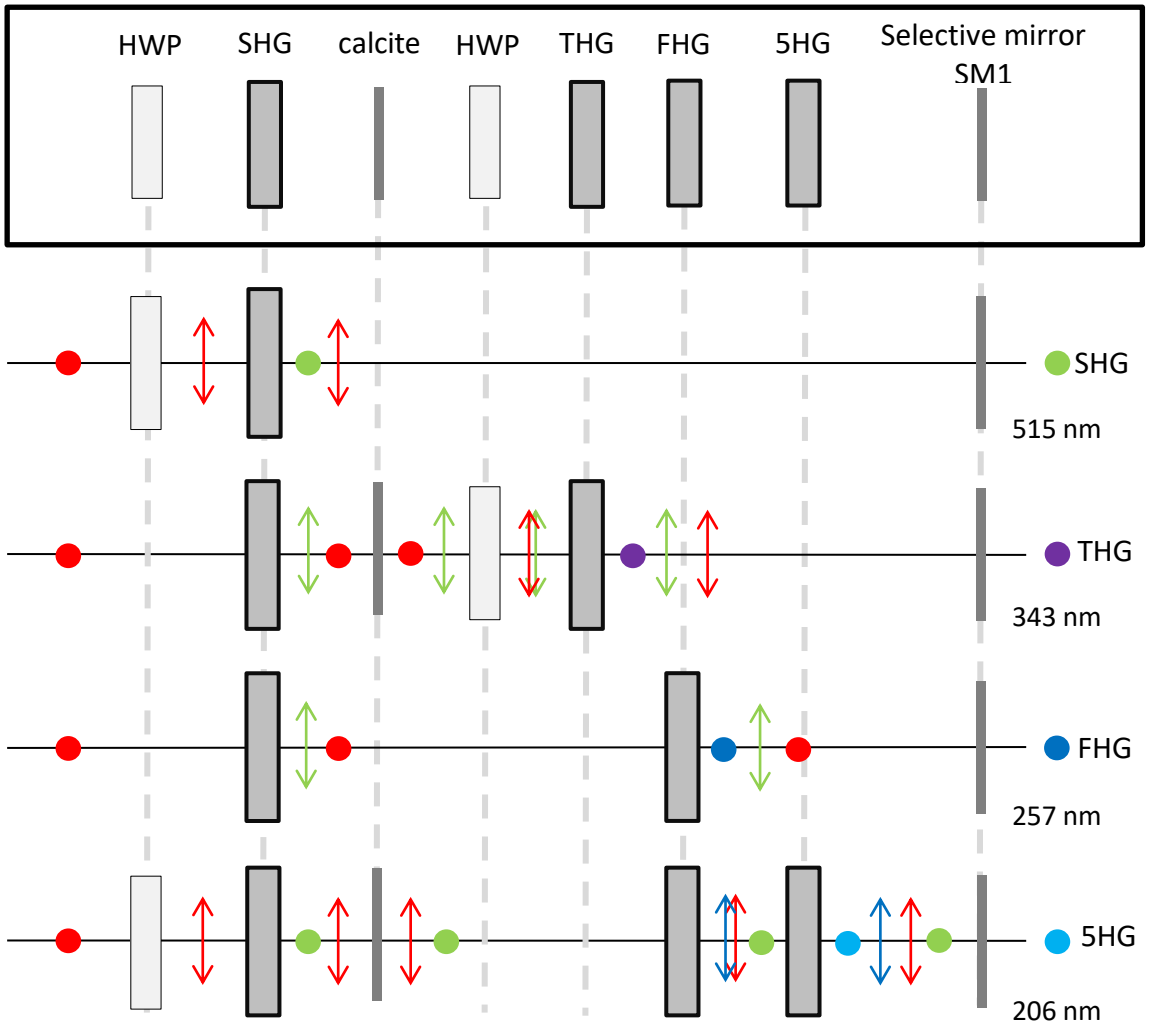

Figure 13 shows the configurations of the harmonic generation stage to access the second (SHG, 515 nm), third (THG, 343 nm), fourth (FHG, 257 nm) and fifth (5HG, 206 nm) harmonics of the fundamental. The top boxed panel shows all the possible components in the harmonic stage, with the configurations beneath showing the components necessary for the generation of each harmonic frequency. The filled circles show a horizontal polarization and the arrows show a vertical polarization. The different colours of the circles/arrows represent the different wavelengths; red = 1030 nm, green = 515 nm, purple = 343 nm, dark blue = 257 nm, and light blue = 206 nm. The dark grey boxes represent the BBO crystals.

crystal to ensure that the output polarisation from the harmonic generation stage is the same for all frequencies. On output, the 515 nm measures 3.4 μJ pulse^{-1} with 20% conversion efficiency from 1030 nm measured to be 18 μJ pulse^{-1}.

THIRD HARMONIC (343 NM) GENERATION

The output from the SH crystal (515 and residual 1030 nm) is used to generate THG frequencies using a Type 1 BBO crystal (θ= 32° and ϕ= 90°, Crysmit). For Type 1 harmonic generation, the 1030/515 nm pulses need to be both temporally overlapped and have the same polarisation. A half waveplate (HWP) is used to

rotate the polarisation of the 1030 nm light by 90° whilst preserving the polarisation of the 515 nm light. However, the 515 nm radiation propagates more slowly through the HWP than the 1030 nm, further increasing the temporal delay between the 1030/515 nm pulses. To compensate for this, the output from the SH crystal first propagates through a calcite (birefringent) plate that acts as a variable delay compensator (250 – 600 fs) before passing through the HWP. Rotation of the calcite plate tunes the temporal overlap of the 1030/515 nm pulses in the THG crystal maximising the conversion to 343 nm. The 343 nm output is filtered from the 1030/515 nm using the selective mirrors (SM1-4 on MB). On output the 343 nm measures 2.2 μJ pulse^{-1} with 64% conversion efficiency of 515 nm.

FOURTH HARMONIC (257 NM) GENERATION

The output from the SH crystal (515 and residual 1030 nm) is used to generate FHG by frequency doubling the 515 nm pulse in a Type 1 BBO crystal (θ= 51° and ϕ= 90°, Eksma Optics). The 257 nm is then separated from the 1030/515 nm using the elective mirrors (SM1-4 on MB). On output the 257 nm measures 1.3 μJ pulse^{-1} with 37% conversion efficiency from 515 nm.

2.2. SAMPLE SET UP

All the samples studied by the MESS are liquids. Due to the high pulse power and repetition rate output from the CARBIDE, sample degradation was observed on the experimental timescale. As such, all samples are constantly moved to prevent photodecomposition. Details regarding each experiment's sample set up can be found in the corresponding experiment chapters.

3. TRANSIENT ABSORPTION

3.1. ABSORPTION AND EMISSION OF RADIATION

As described in section 1.1.1, if light incident on a species matches the defined energy difference between the current energy state and some higher energy state, the molecule can absorb the quanta of energy and become excited. The absorption of a species is characterised by the Beer-Lambert Law,[136]

$$I = I_0 e^{-\varepsilon(\lambda)cl}\,, \tag{7}$$

where I is the measured light intensity after transmission through the sample, I_0 is the incident light intensity, c is the sample concentration, l is the path length through the sample, and $\varepsilon(\lambda)$ is the molar extinction coefficient of the molecule of interest. The absorbance, A, of a sample can be defined as[8]

$$A(\lambda) = \varepsilon(\lambda)cl = -\log_{10}\left(\frac{I(\lambda)}{I_0(\lambda)}\right), \tag{8}$$

and describes the optical density of a sample.

3.1.1. POLARISATION CONSIDERATIONS

As well as incident light energy, the polarisation of light plays an important role. When light interacts with a molecule, a transition dipole moment (TDM) is induced along a molecular coordinate. Maximal absorption arises when the TDM and

polarization are parallel (and zero absorption when they are orientated perpendicular to one another). In an isotropic medium, molecular orientation is random with all measured properties, such as orientation, being that of the ensemble.[136]

Once excited, a molecule may emit light, and that light is also emitted with a polarization. If the molecule has rotated in the plane perpendicular to detection between absorption and emission, then the emitted polarisation will be different to that of the incident polarization. This is the polarisation anisotropy, r :

$$r = \frac{3}{5}(\cos^2\theta - 1) \tag{9}$$

where θ is the angle relating the polarisation of the incident light and the TDM. To remove this angular dependence, a polarization anisotropy value of zero is necessary, occurring at the average orientation angle of an isotropic medium known as the magic angle of 54.7°. Therefore all Transient Absorption (TA) experiments in this thesis are performed under magic angle conditions whereby the pump and probe polarizations differ by 54.7°.[137]

3.1.2. TIME RESOLVED ABSORPTION SPECTROSCOPY

TA spectroscopy is a pump-probe technique that monitors the change in absorption of a molecule in the bulk solvation environment as a function of time. In brief, a sample is excited by a temporally short laser pulse, promoting a small proportion of molecules from the ground to an excited state which is then probed by another laser pulse. By changing the delay between the two pulses and plotting a difference absorption (DA) TA spectrum, the variation in optical density, $\Delta OD(\lambda, t)$, of the excited state can be revealed with respect to wavelength and time:

$$\Delta OD(\lambda, t) = -\log_{10}\left(\frac{I(\lambda, t)}{I_0(\lambda)}\right), \tag{10}$$

where $I(\lambda, t)$ represents the pump-probe signal, and $I_0(\lambda)$ the pump blocked ground state background.[138] $\Delta OD(\lambda, t)$ therefore contains dynamic processes that

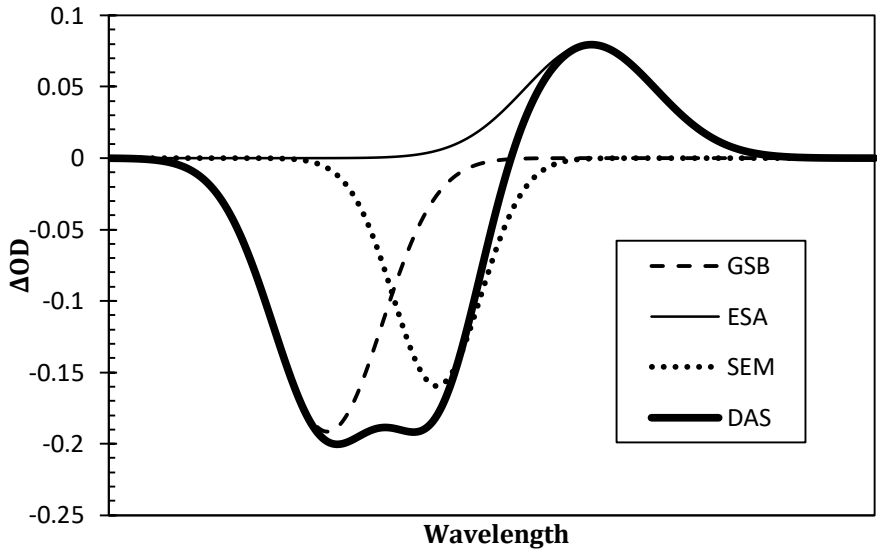

Figure 14 shows the contributions to the difference absorption spectrum: ground state bleach, GSB, (dashed line), excited-state absorption, ESA, (thin solid line), stimulated emission, SEM, (dotted line) and the total difference absorption spectrum, DAS, which is a sum of all the contributing parts (solid thick line).

occur within the excited species generated such as, but not limited to, proton transfer, energy migration and relaxation, isomerisation and the generation of a new photoproduct. The following sections will discuss the main contributions to a TA spectrum with reference to Figure 14.

3.1.2.1. GROUND STATE ABSORPTION

As the difference spectrum is calculated by subtracting the ground state absorption spectrum (as shown in equation (10)), the first contribution to a DA spectrum is a ground state bleach, GSB. As a small amount of the molecules in the ground state have been excited to an excited state, the concentration of molecules in the ground state has been reduced. As such, the absorbance of the ground state after excitation is less than that in the background pump blocked reference, and consequently the signal will be negative in the DA spectrum. This is demonstrated by the dashed line in Figure 14.[138]

3.1.2.2. EXCITED STATE EMISSION

The next contribution to the DA spectrum is stimulated emission (SEM). As already discussed, a molecule that has been excited can radiatively decay back to the ground state by stimulated or spontaneous emission. As the excited state is often

vibrationally hot, the emission from the excited state back to ground state has a Stokes shift to longer wavelengths, with respect to the GSB, as the excited state first vibrationally relaxes before emission. SEM results in an increase in light intensity incident on the detector and consequently $I(\lambda) > I_0(\lambda)$, so the signal is negative. This is shown in the dotted line in Figure 14 with a reasonably large Stokes shift. Many chromophores however have such a small stokes shift that the SEM and GSB overlap.[138]

3.1.2.3. EXCITED STATE ABSORPTION

The third contribution to the DA spectrum, shown in Figure 14, is excited-state absorption (ESA). Just as absorption can occur from the ground state, once generated, the excited state can absorb the probe wavelengths to even higher energy levels. As a consequence, the ESA peak is positive in the DA spectrum as the probe light intensity is reduced at the detector at the wavelengths absorbed. This is shown as the thin solid line in Figure 14.[138]

3.1.2.4. PRODUCT ABSORPTION

The final possible contribution to a DA spectrum is the absorption by long lived states such as photoproducts, triplet states or isomers that are accessed via the excitation. The absorption of such a state will be positive in the DA spectrum, with a long lived GSB at wavelength(s) that access this product pathway.[138]

3.1.2.5. TRANSIENT ABSORPTION SPECTRA

As the delay between the pump and probe is varied, the change in optical density with respect to time can be plotted, revealing the dynamics and lifetimes of the excited states. Figure 15 shows a simplified DA evolution with respect to time that models the decay of an excited state back to the ground state without generation of photoproducts. Before $t_{0,}$ the DA spectrum is flat, as the signal is measuring the ground state absorption referenced to the ground state absorption. After excitation, GSB, SEM and ESA are all present and at their most intense when the excited state is in its highest concentration, immediately after excitation. As the

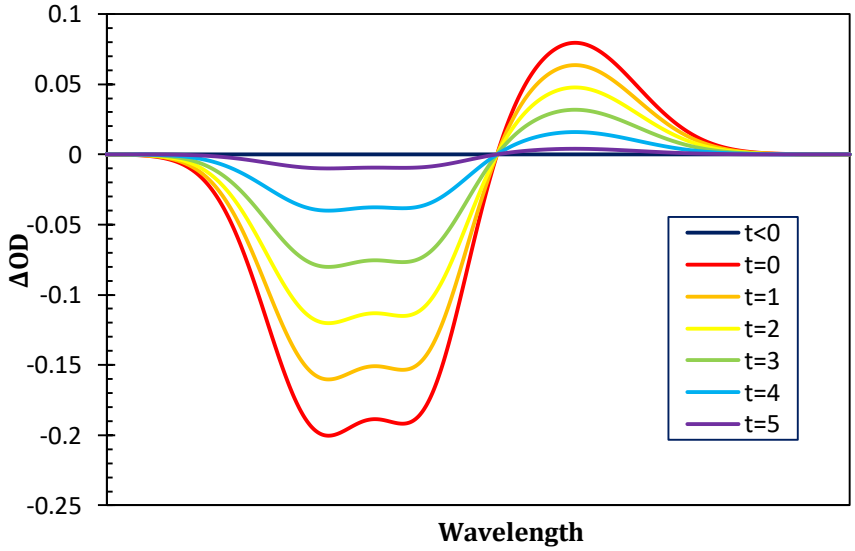

Figure 15 shows the variation in the DA spectrum with respect to time as the excited state relaxes back to its ground state. The time scale is used to represent increments in time with respect to t_0.

probe is delayed more with respect to the excitation event, the concentration of the excited state decreases (as the ground state is established) and the peaks weaken in intensity until the ground state is entirely repopulated.

3.2. TECHNIQUE APPLICATIONS

Traditionally TA experiments involved ultrafast lasers with low repetition rates. However, the advent of modern lasers and amplification systems has seen systems with high repetition rates and sufficient peak power becoming readily available. As a consequence, applications of TA in the literature are vast and the variations in experimental design and instrumentation extensive. In essence, all optical TA absorption techniques are comprised of a laser system that generates the pump and probe pulses, a detector and a mechanism to modulate the pump (and sometimes the probe). Generating the 'pump off' background reference is typically achieved via one of two mechanisms: pump modulation or a second reference detection line.

Pump modulation is experimentally much more common and typically uses a physical moving component (such as a chopper wheel or shutter), but other methods are possible such as an acousto-optic or electro-optic modulator. Ideally

the frequency of this modulation is set to half the laser repetition rate, resulting in every alternate detected signal being assigned as a reference.[119,139–141] Mechanical chopper modulation is straightforward at low laser repetition rates, but as repetition rates increase, they become less stable, introduce phase jitter to an external reference and require very small apertures.[141,142] Alternatively each probe pulse can be split into two paths, conventionally by a beamsplitter, one which intersects with the excited volume of the sample, and one that does not. Both can then be detected simultaneously on two separate detectors.[143–145] Disregarding the cost of second detection line, identical 50:50 splitting of a pulse using commercially available beamsplitters is non-trivial and thus introduces signal offsets and noise to the ΔOD signal that cannot be considered to be constant functions and therefore removed in post-processing. If the mechanism of pump modulation is ignored however, broadly speaking all TA techniques can be differentiated in terms of laser repetition rates (i.e. low or high) and the mechanism of detection: traditional monochromatic detection or dispersed broadband multichannel detection.

The most traditional form of TA experiments had monochromatic probe pulses detected on single channel detectors. In contrast a broadband multichannel detection technique utilises the full supercontinuum spectrum to capture continuous absorption changes across a range of wavelengths in a single shot. In essence, this is achieved by dispersing the probe through a prism or grating onto a multichannel detector (either a CCD or array of photodiodes). However, multichannel detectors are limited by comparatively slow readout rates in relation to commercially available laser systems (unlike single channel detection which are available with rates in the GHz regime). This results in shot-to-shot signal acquisition becoming increasingly difficult as repetition rates exceed those of commercially available and affordable cameras.

This is not to say that faster repetition rate lasers have not been utilised in dispersion TA techniques, but the mismatch in rates results in the spectra being effectively measured as a steady state signal and thus many probe pulses contributing to one image – typically reducing the photon efficiency and increasing noise due to the lack of enhanced energy correlation of successive laser pulses. The

lack of photon efficiency and consequent increase in noise due to the lack of shot-to-shot measurements results in dispersed detection technique conventionally being used only with laser repetition rates that can be matched by commercially available detectors, ranging from tens of Hertz,[119,145,146] through to 1-5 kHz lasers.[88,107,119,140,144,147]

Although signal to noise ratio (SNR) of low repetition rate experiments benefit from the ability to easily perform shot-to-shot background referencing, in general low repetition rate lasers have poor SNR due to the power spectral density which is inversely related to the repetition frequency f_{rep} – otherwise known as 'pink noise'. Thus, increasing the repetition rate favourably improves the SNR. With both MHz laser repetition rates and fast photodiodes commercially available, the potential to extend the traditional single channel detection into the hundreds of kHz to MHz regime became attractive in the 90s and 00s.[148–151] Yet the time intensiveness of scanning wavelengths (either by OPAs or by filtering white light) is non-trivial and not substantially offset by the reduction in 'active' acquisition time i.e. the time it takes to record one time point. Thus recent literature over the last decade has seen a shift to develop broadband shot-to-shot techniques at fast repetition rates which effectively compromise between data acquisition time, SNR and experimental stability.

An elegant technique developed to address broadband spectroscopy at higher repetition rates is the recent work of Cerullo's group using a Fourier Transform (FT) TA set up. FT-TA has been utilised very successfully to perform shot-to-shot data acquisition at lower repetition rates,[35,152] and in 2016 Cerullo's group extended this into the 20 MHz regime using an acousto-optic modulator.[153] In brief, the technique utilises a birefringent wedge pair to generate two delayed 'replicas' polarized normal to each other, each containing an interferogram (due to the interference between the two replicas). The two replicas are separated by a Wollaston prism and detected by a photodiode. By translating one of the wedge pairs the delay between the replicas can be altered and the signal as a function of wedge position can be Fourier transformed to yield signal in the frequency domain. The results are extremely sensitive ($<10^{-6}$) without compromising broadband detection and thus form a gold standard for TA techniques.

Although it is unlikely that a dispersed broadband will be able to compete with the SNR ratio offered by experiment developed by FT-TA, the instantaneous feedback of a 'traditional' frequency dispersed technique is still alluring experimentally. Thus other groups, including our own, have focused on methods that find a compromise between detecting the broadband dispersed signal in the frequency domain whilst increasing repetition rates beyond the few kHz regime.

Kanal *et al.* published one such technique that can operate shot-to-shot with a fast 100-kHz camera.[142] Unusually, the experimental set up still uses a chopper wheel to modulate the pump which, as discussed earlier, is conventionally considered only to be applicable to a few kHz. By combining very small slits with a fast repetition rate, the study shows that 50 kHz modulation is possible. At low repetition rates, the chopper is conventionally triggered by a laser output. However, at such high motor turning speeds as to induce chopping above 100 kHz, the jitter of rotation is no longer insignificant and synchronisation to the laser becomes critical. To combat this challenge, Kanal *et al.* present a method by which the chopper instead drives the laser. Although it is undeniable that the sensitivity presented in the results is a significant enhancement on any other dispersed techniques, the sophistication of the electronics required to drive the laser should not be underestimated in its experimental complexity. This drives the motivation of the work presented in the remainder of this chapter in which we have strived to maintain traditional TA techniques, whilst increasing repetition rates to 60 kHz without adding the significant experimental complexity presented by both Kanal *et al.* and the work of Cerullo.

3.3. EXPERIMENTAL

3.3.1. SAMPLE

A commercial demountable 1" flow cell (Harrick, DLC-M25) was utilised to hold the TA sample with a path length of 950 μm enclosed between two 1 mm thick CaF_2 windows (Crystran). To prevent sample degradation, approximately 200 cm^3 of sample is circulated through a flow system by a magnetically driven centrifugal pump (MarchMay, AC-2CP-MD). The focus of the pump (particularly at 257 nm) however, resulted in burning of the cell windows on relatively short timescales (<24 hours). Consequently, the flow cell was mounted on a motorized stage that horizontally translates the sample cell horizontally in the perpendicular axis to the incident pump and probe.

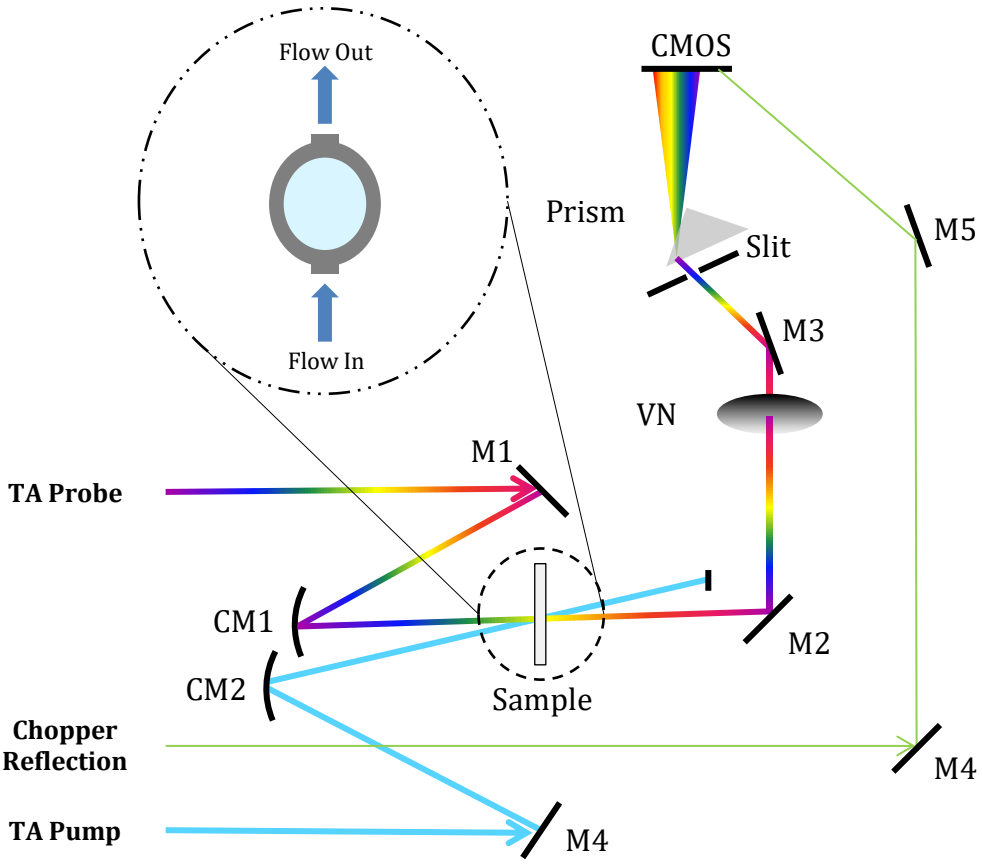

Figure 16 shows a schematic representation of the pump-probe experimental set up of the TA experiment where M = cold mirror, F = filter, CM = curved mirror, VND = variable neutral denisty filter and BB = spatial beam block. The blue and multi-coloured beam paths represent the pump and probe beams respectively. The origin of the pump and probe inputs prior to M1 and M4 are shown in Figure 10. The inset shows the sample cell (HARRICK) through which the sample is flowed.

3.3.2. PUMP-PROBE

Figure 16 shows the TA experimental set up as viewed from above the optical table. The pump and probe inputs are an immediate continuation from the paths shown in Figure 10.

3.3.2.1. PUMP SET UP

As discussed in section 2.1.2, the desired pump is generated through a harmonic generation stage and then filtered using selective mirrors. The pump beam is then directed onto a curved mirror (CM2) by mirror M4 which focuses the pump beam within the sample flow cell. After the flow sample cell the pump beam is blocked by a spatial beam block (BB).

3.3.2.2. PROBE SET UP

To generate the WL probe a portion of the CARBIDE output (as described in section 2.1.1) is directed into a white light generation stage consisting of an aperture, an aspheric lens, a sapphire window (acting as the supercontinuum medium), an achromatic doublet lens, and an aperture to select the central portion of the output WL beam. Once generated, the WL passes through a filter to remove the remaining fundamental 1030 nm seed before being directed onto a curved mirror, CM1, which acts to tightly focus the beam into the sample flow cell to overlap spatially with the pump spot.

After transmittance through the sample, the probe is directed through variable neutral density filter (VND) to protect the camera from saturation. To tune the spectral resolution, the probe is passed through a variable slit by M3 before being dispersed by a prism onto a line scan camera (Lightwise Allegro, Imaging solutions group) which has a maximum line rate of 80 kHz and a single line of 2048 pixels with a bit depth of 11 bit and a size of 10×200 μm.

3.3.2.3. CHOPPER REFLECTION

To distinguish between pump on and pump off the reflected pulse train from PBVS3 (Figure 10) is directed onto the camera by M4 and M5 in Figure 16 to generate a pump reference spot, PRS. As this beam is a 30 kHz train of pulses, the PRS is only present on every other line when the camera is set to a line rate of 60 kHz to match the repetition rate of the laser. The LabVIEW program (discussed in the next section) is then able to use the presence of this spot to distinguish between pump on signal (PRS absent) and pump off signal (PRS present) as shown in Figure 17.

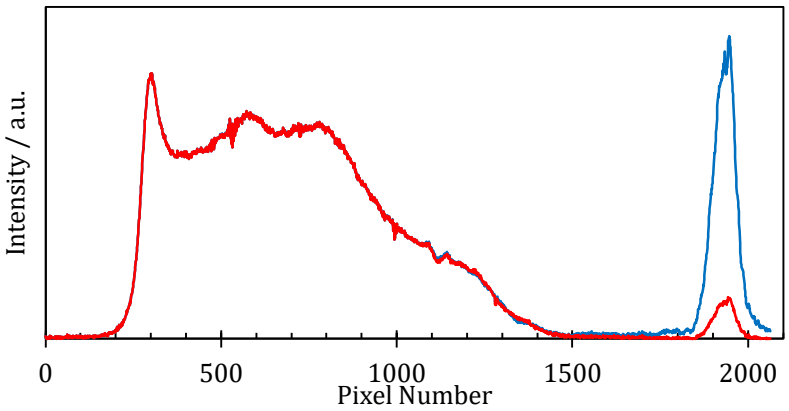

Figure 17 shows pump on signal (red) and pump off signal (blue) which are distinguished by the presence or absence of a reference peak (PBS) at pixel numbers > 1900

3.3.3. EXPERIMENTAL CONTROL

The TA experiment is controlled by a program (represented in Figure 18) written in LabVIEW. Outside of the first loop the camera parameters are set, the delay stage is configured and the time file containing the times to be interrogated are read. The program then moves inside the first loop and the delay stage is moved to the first time from the time file. Once at the correct position on the delay stage, the camera acquisition is triggered in which a 1 x 2048 pixel image is transferred to the camera's on-board Field Programmable Gate Array at a line rate of 60 kHz. Once 4092 images have been stored, the FPGA transfers a 2048 x 4092 array via USB to the computer, and read into LabVIEW. The use of an FPGA eliminated the need to advanced camera interfacing using specialised Framegrabbers and dual CameraLink interfaces.

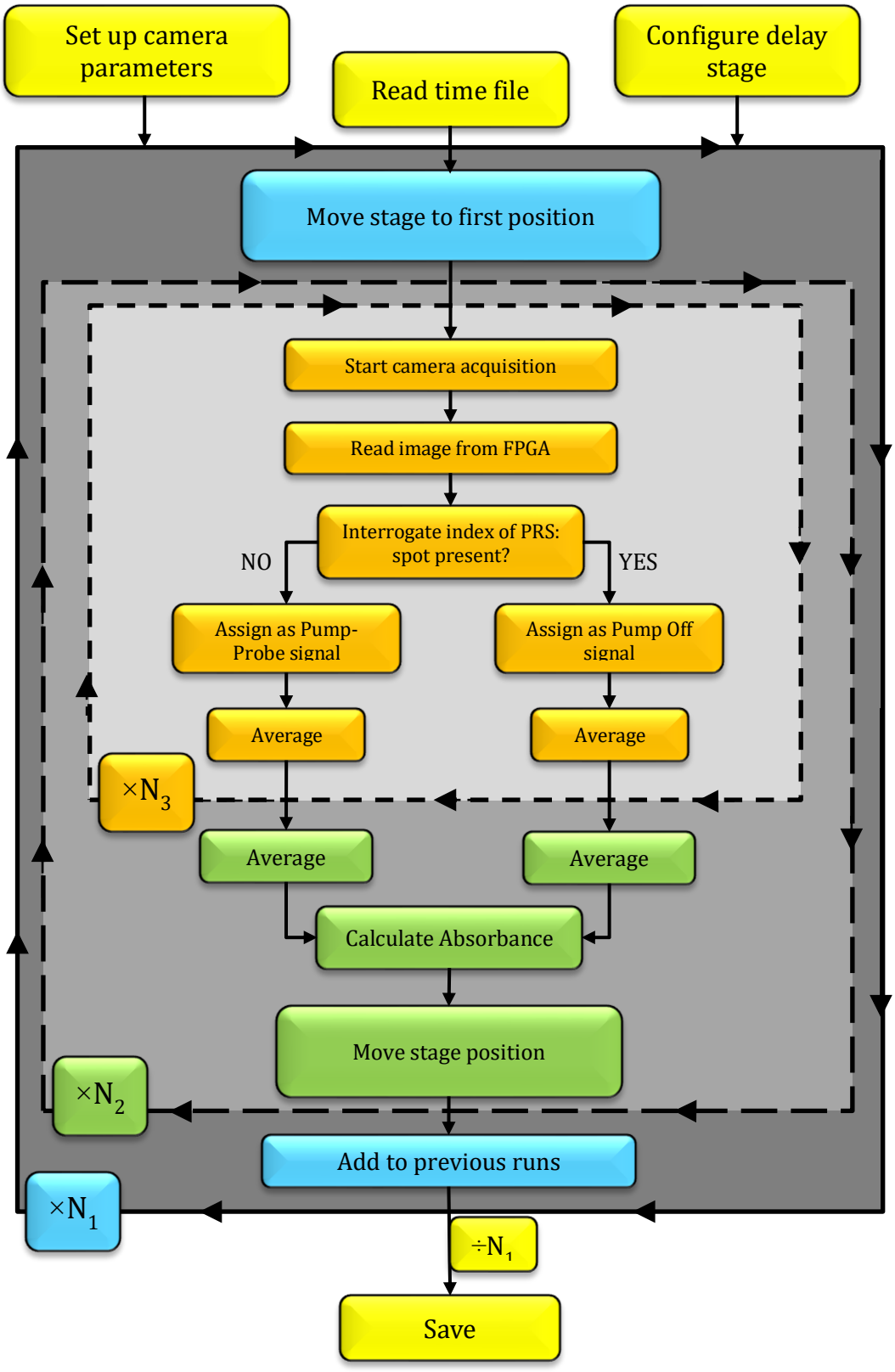

Figure 18 shows a flow diagram schematic representation of the LabVIEW program that controls the TA experiment. Each set of coloured boxes represents operations within the same loop that repeat N times where N_3 is the number of spectra to average per time point, N_2 is the number of time points per scan, and N_1 is the number of delay stage scans per experiment.

At this point, each of the 4092 images are assigned as either Pump-Probe spectra or Pump Off spectra by interrogating the index at which the PRS is located. Once separated, the 2046 spectra assigned to each of the two signals are averaged. This loop is then repeated N_3 times. After the required number of spectra per time point has been recorded, the data is averaged and the absorbance is calculated using equation (10). The stage is then moved to the next time point and the acquisition loop is repeated until the delay stage has scanned through all the time points from the time file (where N_2 is the number of time points). This process is repeated N_1 times. The experiment then leaves the loop, the spectra are averaged by the number of runs, N_1, and the data is saved in the desired file location.

3.3.3.1. FINDING TEMPORAL OVERLAP

To find and optimise temporal overlap at the sample between the pump and probe pulses a version of the program shown in Figure 18 is used in which the first while loop has been removed. This generates a 'live' and constantly updating absorbance spectrum which can be manually scanned through time points using buttons that trigger a movement of the stage. By using a sample with a strong absorption or emission in the visible wavelengths and a transition that can be accessed by the pump wavelengths, the appearance of signal can be used to find t_0, and the overlap can be optimised by trying to maximise this signal. There are many samples suitable for this purpose including laser dyes such as DCM, and fluorescein.

The data shown in Figure 19 shows the evolution of the 515 nm pumped TA signal of DCM (4-Dicyanomethylene-2-methyl-6-(4-dimethylaminostyryl)-4H-pyran) as the delay stage is scanned through. Using this data t_0 can be attributed to be at the second time position shown (t_2) as this is the first point at which signal can be seen (shown by the orange arrow). As time evolves from t_2 the signal can be seen to 'grow in'. This is due to the temporal delay between the shorter and longer wavelengths of the white light, called chirp which will be discussed fully in section 3.3.4.2. All spectra have a baseline centred at an absorbance of 0 and are shifted relative to each other for clarity. DCM has been successfully used to find t_0 for 515 nm and 343 nm pump wavelengths. Fluorescein was more suitable for 257 nm pump.

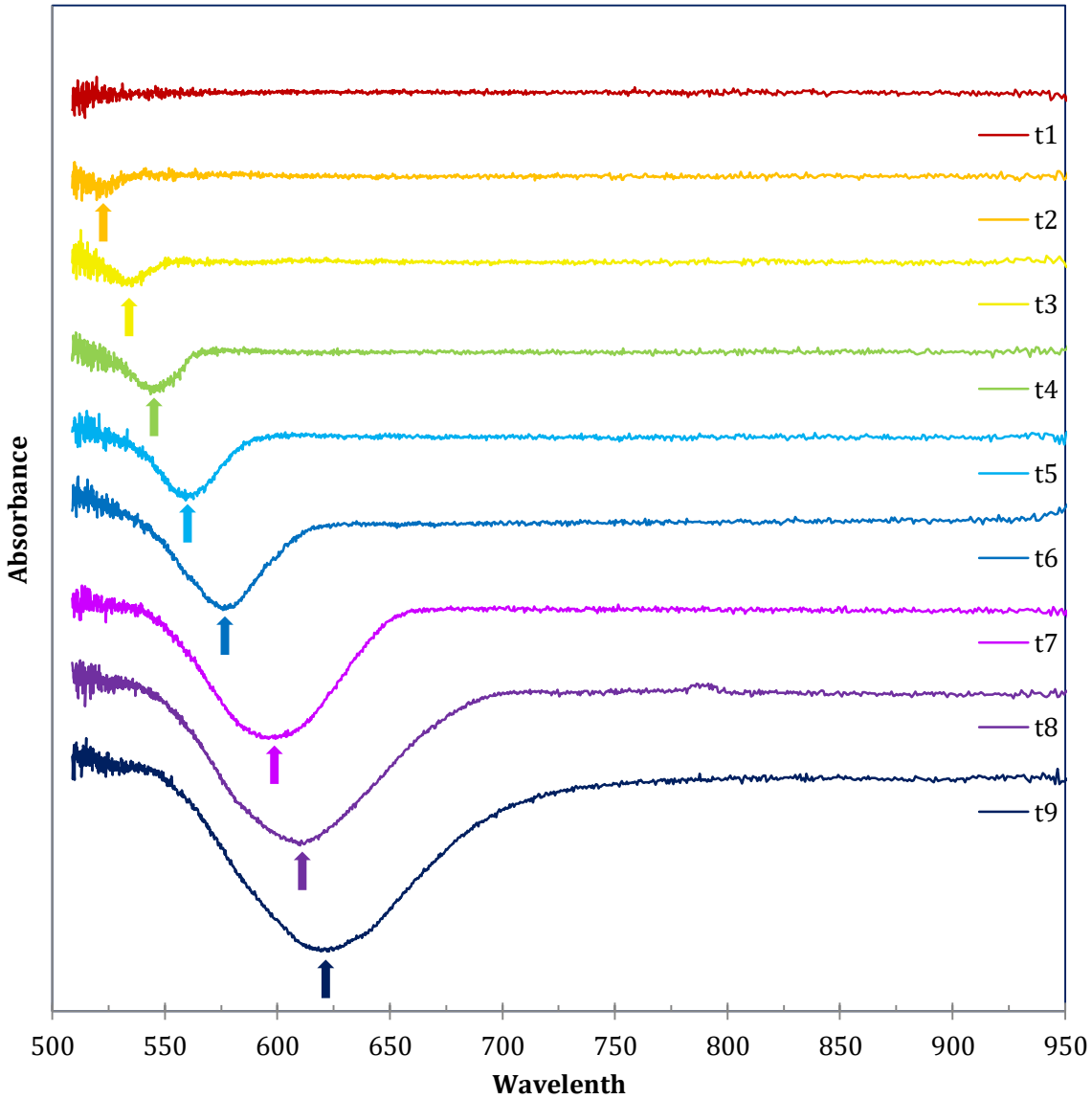

Figure 19 shows the change in the DCM TA signal (pumped at 515 nm) as the delay stage is changed from before t_0 (red, t_1), through t_0 (orange, t_2) and past t_0 into the positive time regime (t_3-t_9). The arrows shown indicate the peak maximum at each time position. The spectra have been shifted relative to each other for clarity with all spectra baselines being centred at an absorbance of 0.

3.3.4. POST PROCESSING

Once an experiment has completed there are two very important post-processing procedures that take place. At the point of saving, the array holds the average spectra at each time point as a function of the sensor pixel number. The calibration processing step then determines the relationship between pixel and wavelength to yield spectra as a function of wavelength. The second processing step corrects for the temporal chirp observed across the WL probe pulse.

3.3.4.1. CALIBRATION

A commercial filter with a characteristic transmission profile (ThorLabs, FGB67) is used to calibrate pixel to wavelength. The transmission spectrum provided by the supplier (validated using a UV-vis spectrometer) is shown by the green trace in Figure 20(a).

By selecting the positions of the characteristic peaks as a function of the camera pixel number (from a recorded spectrum taken with the filter placed in the probe beam path before the camera), and plotting them as a function of the desired wavelength (taken from the transmission spectrum at the same points), a fourth

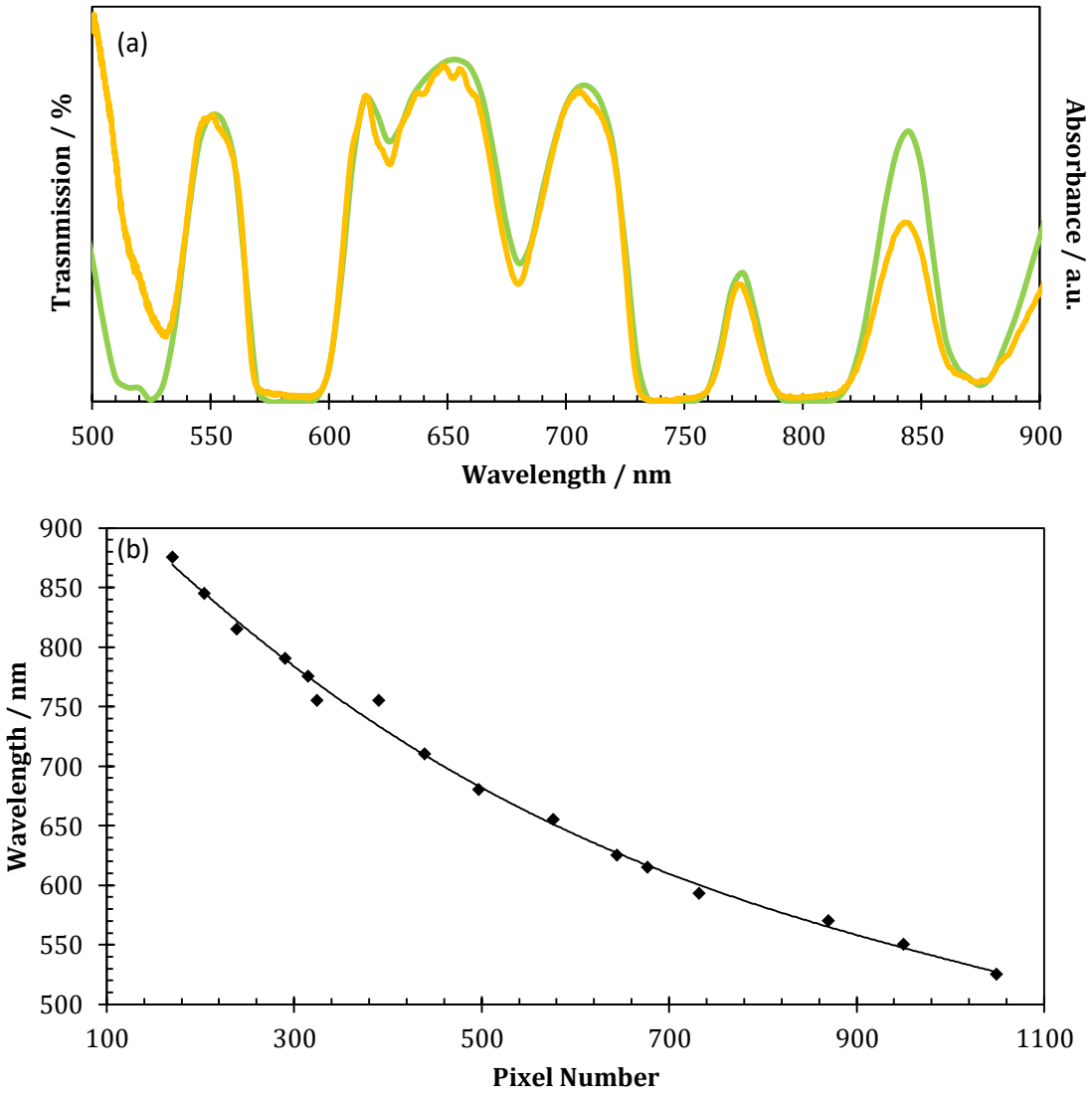

Figure 20 shows the transmission spectrum provided by ThorLabs (green line) and the experimental spectrum recorded when the filter is placed in the probe beam path before the camera

order polynomial can be fitted. This calibration curve is shown in Figure 20(b) and characterises wavelength as a function of pixel number. By applying this fit across the entire spectrum, the spectrum can be replotted as a function of wavelength. The orange trace in Figure 20 shows the excellent agreement between the processed experimental data and the reference spectrum from Thorlabs.

3.3.4.2. CHIRP CORRECTION

When WL is generated, not all wavelengths are generated at the same moment in time due to the intensity profile of the Gaussian beam.[154,155] This is then further exacerbated by group velocity dispersion (GVD) as different wavelengths of light travel through any medium (except a vacuum) at different speeds. As such, a pulse containing different wavelengths will broaden in time the further it travels.[146,156] It should be noted that GVD and chirp can be corrected for experimentally using specialised optics, but this is expensive and may change with different experimental configurations. Considering the desired interchangeable nature of the MESS, it is more desirable to correct for the chirp in post-processing.

To characterise the chirp, a pump-probe experiment is performed with pure solvent as the sample. This produces a non-resonant signal for each wavelength of the probe at the instance in time that it is temporally (and spatially) overlapped with the pump pulse. This signal can be attributed to the $\chi^{(3)}$non-resonant two-photon processes of stimulated Raman scattering and impulsive stimulated Raman scattering.[145] By extracting the points of maximum intensity across the wavelengths, a calibration curve can be fitted to give the time as a function of wavelength.[140] This function is then applied to the wavelength calibrated data array to give a time-shift for each wavelength. As the chirp is a property of the WL probe, the functionality of the chirp in a system will be independent of the pump wavelength.

The data shown in Figure 21 has been taken using the TA experiment at 515 nm pump excitation where panel (a) shows the raw pure solvent signal, (b) the calibration curve between wavelength and time, and (c) the chirp corrected spectrum. It can be seen from Figure 21(c) that there is a temporal width

associated with the signal which indicates the cross correlation of the pump and probe pulses when they are spatially overlapped.[157]

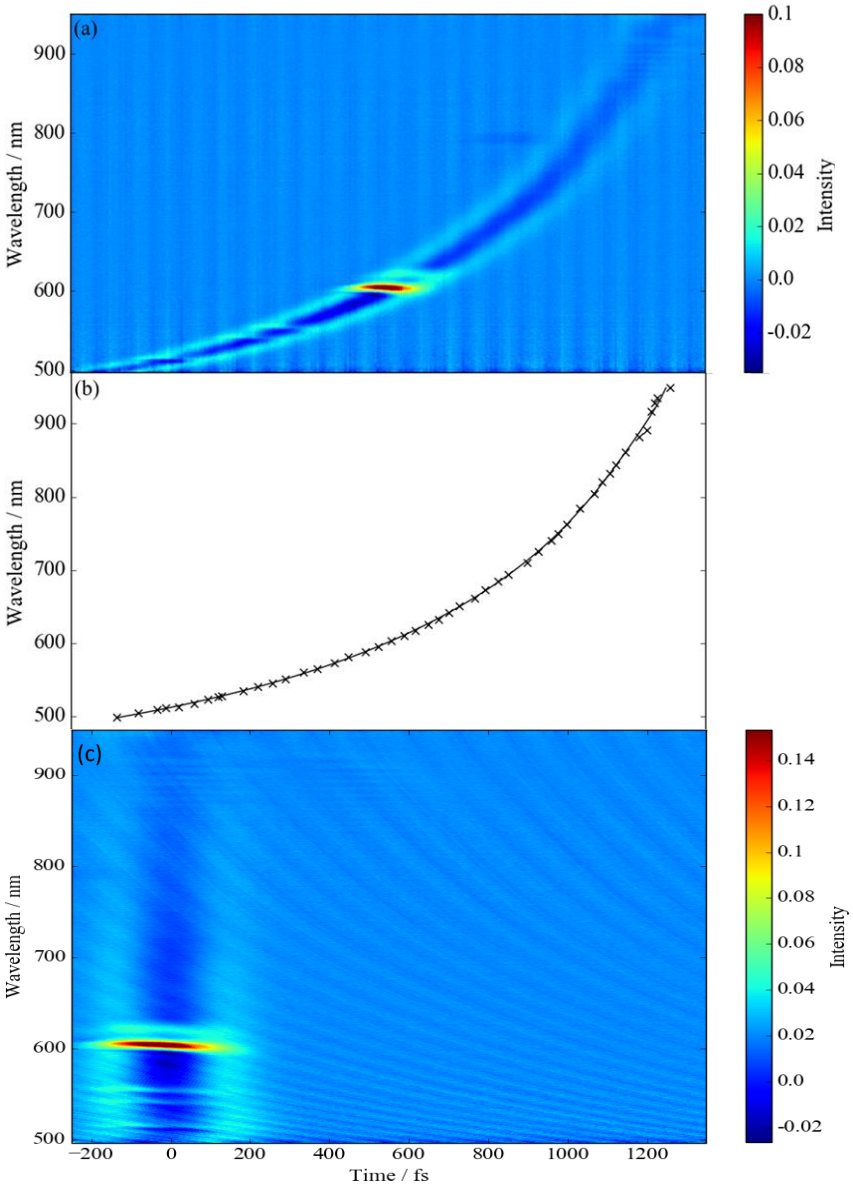

Figure 21 shows the pump-probe measurements with 515 nm excitation on pure methanol with (a) showing the uncorrected absorbance intensities, (b) the extracted signal maxima points and a fit, and (c) the corrected spectrum. The time axis is set to the corrected t0 value.

3.4. RESULTS

3.4.1. FLUORESCEIN SODIUM SALT

As a proof of concept for the TA experiment, a study was conducted on fluorescein which has a well-documented $S_1 \leftarrow S_0$ absorption centred at 490 nm and emission at 515 nm.[158,159] The results presented here use the 515 nm (1.2 μJ pulse^{-1}) pumping regime and a 3 mM solution of fluorescein sodium salt (Sigma Aldrich) in high purity water. When experiments were initially conducted, a constant offset was observed before t_0 even in the absence of a pump pulse. The magnitude of this offset was substantially reduced when the 30 kHz chopping regime was introduced, but not eliminated. The origin of this 'signal' is unknown but it is

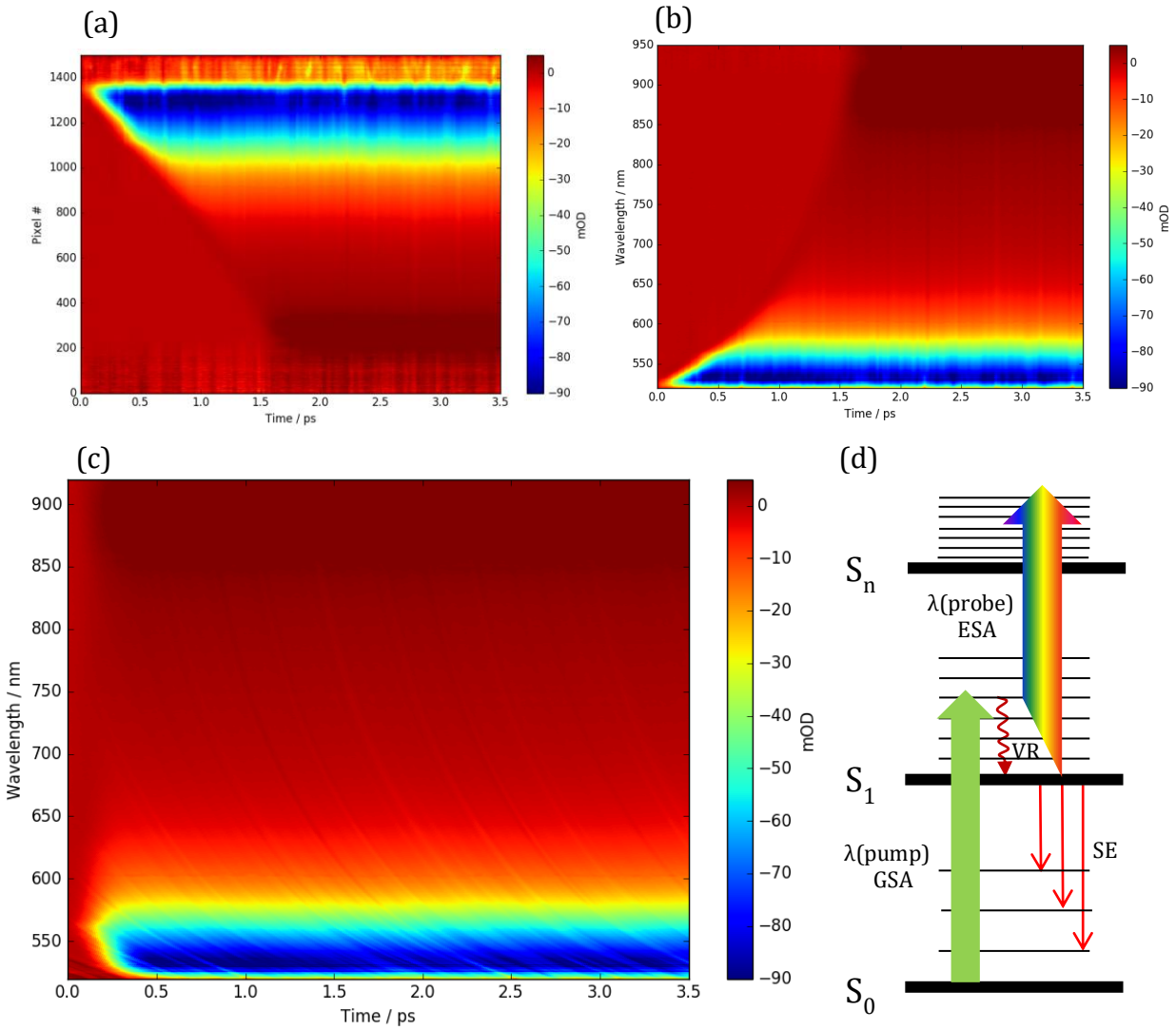

Figure 22 shows TA data for fluorescein with (a) showing the raw data as a function of pixel number, (b) showing the wavelength calibrated data, (c) showing the wavelength and chirp corrected data and (d) showing a schematic of the dynamics represented in (c).

suspected that it arises from nonlinear optical processes induced by the probe and sample flow turbulence.[160,161] To correct for this, an additional processing step was introduced to background subtract the constant offset before t_0.

The TA results for fluorescein are shown in Figure 22 where (a) shows the background subtracted data as a function of pixels, (b) shows the wavelength calibrated data, (c) shows the chirp corrected TA signal and (d) shows a schematic of the observed dynamics shown in (c). Within the first 400 fs the GSB signal exhibits a small blue shift from 560 to 530 nm consistent with vibrational relaxation (VR) of the hot S_1' state to its ground vibrational state, S_1. After the complete relaxation, SEM to the ground S_0 state dominates the TA signal at short wavelengths. In conjunction with the blue-shift, the negative peak shows a signal broadening consistent with shorter SE transitions becoming accessible with increasing VR.

In addition to the negative GSB signal, a positive ESA signal can be seen to grow and red-shift from 560 to 880 nm with the same lifetime as VR. The origin of this redshift arises from the interplay of the SE and ESA signal intensities. Immediately after formation, the hot S_1 state can either vibrationally relax or absorb/emit a photon. At early times the ESA is effectively outcompeted by VR and SE, resulting in increasing ESA signal intensity as VR is completed and the probability of ESA is increased from the longer lived S_1 ground state.

3.4.1.1. NOISE LEVEL ANALYSIS

Before the introduction of the 30 kHz chopping regime, the pump beam was modulated using a mechanical wheel at a 1 kHz chopping rate. To quantify the reduction in noise with the increased chopping rate, two experiments were conducted on fluorescein at 30 kHz and 1 kHz respectively, whilst keeping other experimental parameters constant, including camera integration rate (meaning both data sets were recorded in the same time frame). The results are shown in Figure 23 with panel (a) run at 30 kHz and (b) at 1 kHz. The kinetic traces for the two TA peaks are presented in Figure 23(c) and clearly show the reduction in noise as repetition rate is increased from 1 kHz (grey) to 30 kHz (red/blue).

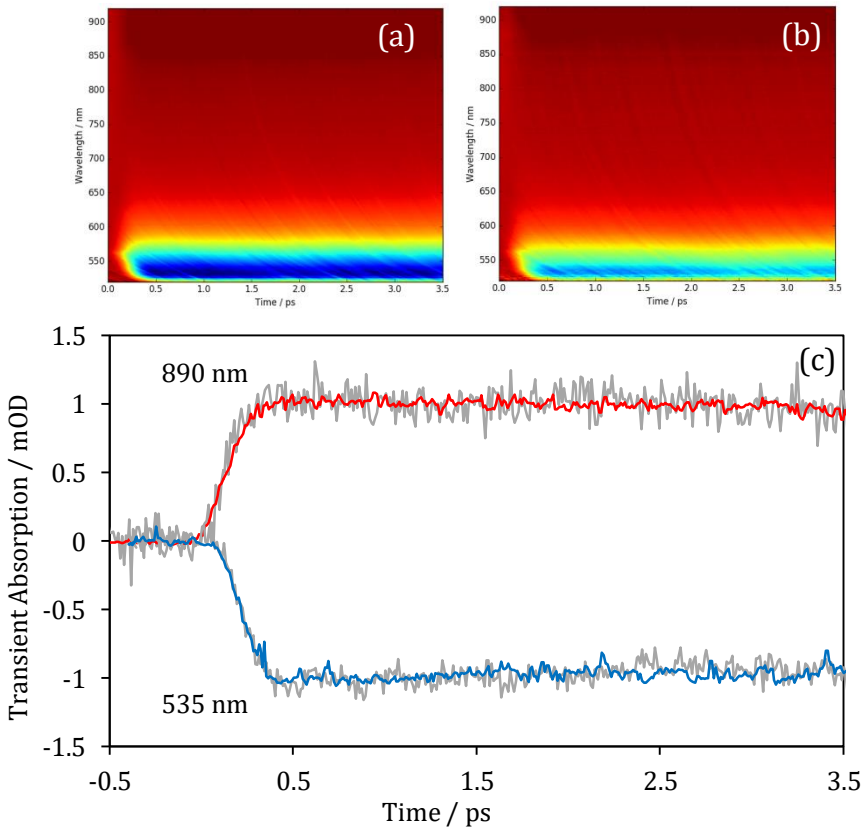

Figure 23 shows TA measurements on fluorescein run at a laser repetition rate of (a) 30 kHz and (b) 1 kHz with panel (c) showing the kinetic traces of both peaks at 890 nm (grey = 1 kHz and red = 30 kHz) and 535 nm (grey = 1 kHz and blue = 30 kHz).

3.4.2. DYNAMICS OF PHOTO-INDUCED CHARGE-TRANSFER-TO-SOLVENT (CTTS) REACTIONS

Although the results on fluorescein validated the principles of the TA experiment, no time resolved studies could be found for comparison of the kinetics. As such a second set of preliminary experiments was conducted to provide confidence in the new experimental set up. The hydrated electron has both a characteristic absorption spectrum and plethora of time-resolved studies dedicated to studying the photo detachment dynamics from small inorganic anions and was therefore identified as a perfect candidate to validate the dynamics of the new TA experiment.

The ferrocyanide anion, $[Fe(CN)_6]^{4-}$, has been extensively studied as a source of electron generation in high yield after photo detachment with UV light (1,2,3).[162–164] The photo detachment pathway had previously been associated with a CTTS transition,[118] with relaxation to the hydrated electron through a precursor or pre-

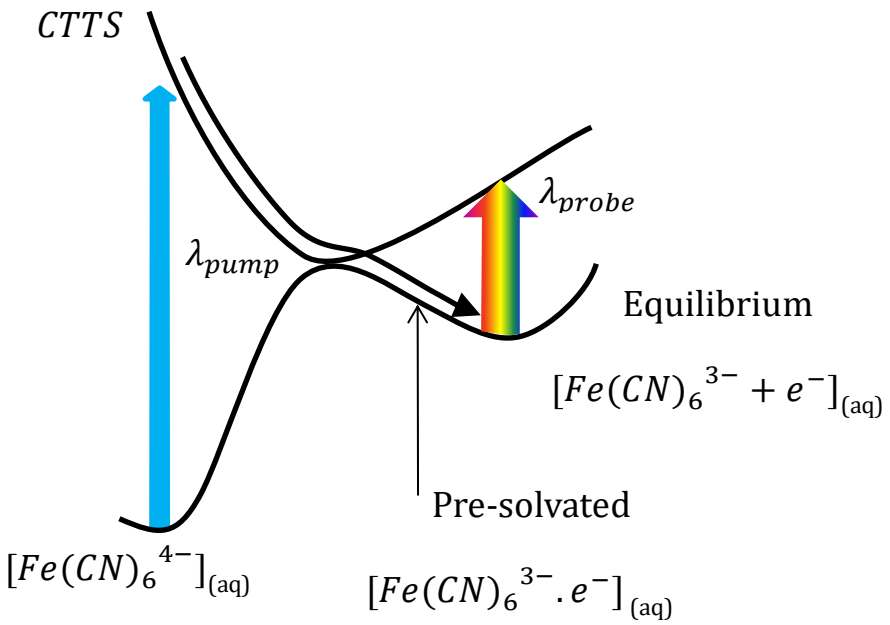

Figure 24 shows a schematic to represent the pump-probe regime for the generation of electrons from the ferrocyandie anion.

hydrated state.[99] The results presented here utilise a 257 nm pump pulse (0.6 μJ pulse^{-1}) and a white light probe, as represented schematically in Figure 24, and a 0.5 M solution of potassium ferrocyanide (Sigma Aldrich) in high purity water.

The TA results are shown in Figure 25. Figure 25(a) focuses on the early time dynamics and shows the appearance of a broad absorption peak immediately after excitation followed by a spectral blue shift, which is completed within the first 3 ps. After these initial dynamics, the absorption band shows a constant decay across all wavelengths, as shown in Figure 25(b). To confirm the presence of the hydrated electron a spectral slice at 500 ps is taken and fit to the Coe formula,[45] which has been centred at 715 nm, and is shown by the black and red traces in Figure 25(c). Although the hydrated electron is commonly reported to have an absorption band centred at 720 nm, a study of the temperature dependence of the hydrated electron absorption spectrum by Jou and Freeman reveals an absorption value at 715 nm would correspond to a local temperature of 21°C, which is entirely consistent with our laboratory temperature.[165]

In an attempt to validate our TA experiment, the results are compared to a similar study by Lenchenkov *et al.* in which various concentrations of ferrocyanide are excited by 265 nm.[166] Analysis of the early time dynamics is conducted by crudely fitting the dynamics up to 3 ps to two exponentials and a convolution function. The

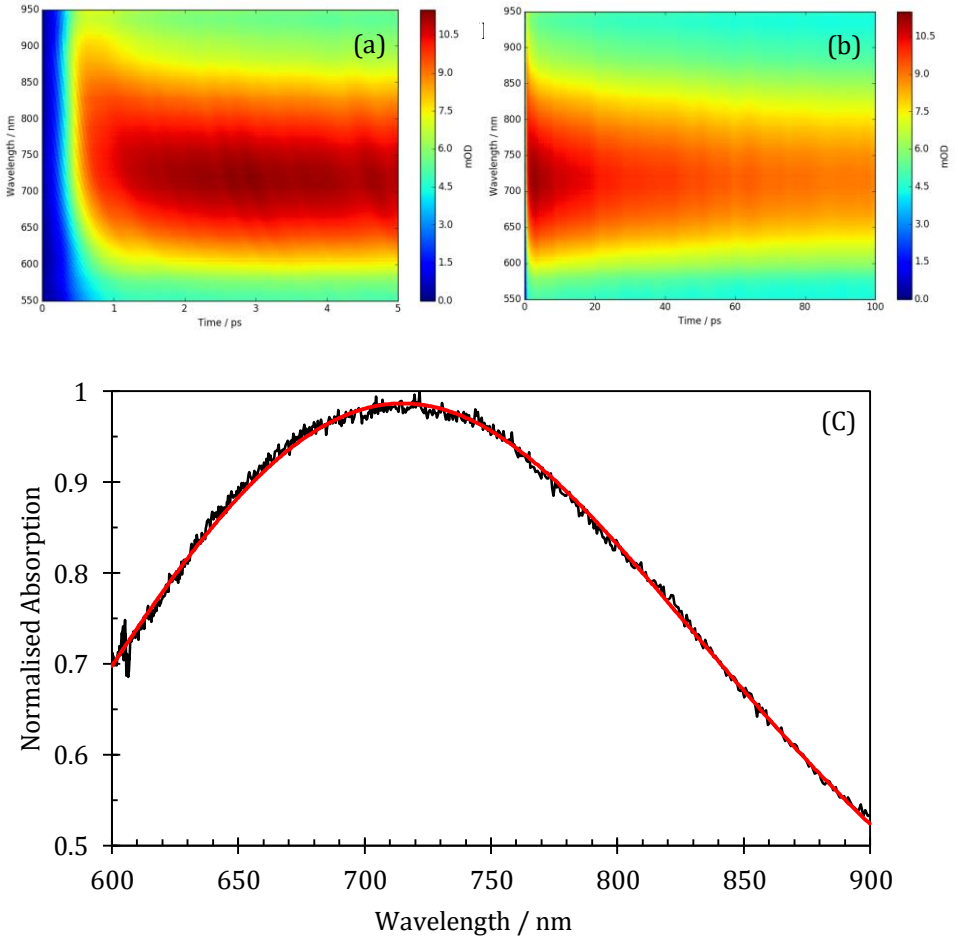

Figure 25 shows the TA results for 0.5 M ferrocyanide with (a) showing early time dynamics, (b) long time dynamics, and (c) showing the spectral profile of the TA peak at 500 ps (black) fitted to the hydrated electron spectrum centred at 715 nm (red).

data and corresponding fits are shown in Figure 26(a). The fastest rise time of ~250 fs is observed for 950 nm with the slowest rise time of ~650 fs observed for 550 nm. This is consistent with the results of Lenchenkov *et al.* who observe the same trend, as shown in Figure 26(b), with a rise time of 180 fs at 1000 nm and 550 fs at 500 nm. The slightly longer rise times at all wavelengths may be a consequence of the higher excitation energy in our experiment, which leads to higher kinetic energies of the ejected electron and possibly longer solvation times as more energy needs to be dissipated. At higher wavelength, there is also a decay of absorbance (see Figures 2 and 3). From 950 to 800 nm, lifetimes increase from 550 fs to 1 ps, which is in agreement with Lenchenkov *et al.*.

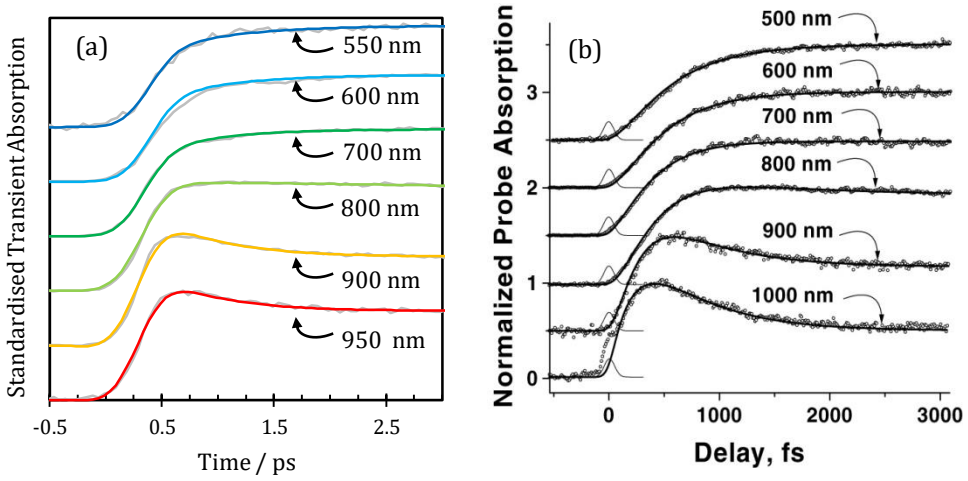

Figure 26 (a) shows the early time dynamics from this experiment (grey traces) with corresponding fits (coloured traces) and (b) shows the equivalent data from Lenchenkov *et al.* Reprinted with permission from Lenchenkov (2001). Copyright (2018) JPL.

The main conclusion of the study by Lenchenkov *et al.*, is that the relaxation dynamics of electrons generated from $[Fe(CN)_6]^{4-}$ are similar to that observed from multiphoton ionisation of water rather than those from iodide. This is rather surprising as electrons detached from iodide are also generated via a CTTS transition.[167] To show that the $[Fe(CN)_6]^{4-}$ dynamics represented in Figure 25 do not represent those of iodide, a corresponding study was conducted on a 0.1 M NaI solution. Once detached from iodide, a radical-electron contact pair is formed which after equilibration follows kinetics predicted by Staib and Borgis.[168,169] Using this analysis, the rate of electron production, k_p, occurs faster for the CTTS reaction from iodide than that shown in Figure 26 for ferrocyanide at all wavelengths. This conclusion was one of the main findings of the study by Lenchenkov *et al.*. The reason for the discrepancy is related to the ejection distance of the electron. For iodide, a contact pair is formed which is a short range electron ejection distance.

Figure 27 shows the long-time dynamics at three characteristic wavelengths across the electron absorption spectrum for both ferrocyanide (red) and iodide (black) data sets. Across all wavelengths, the survival probability at long times is much higher for ferrocyanide than iodide which shows the characteristic decay associated with geminate recombination of a contact pair.[167] The absence of this decay in ferrocyanide, which exhibits much slower kinetics, is consistent with the

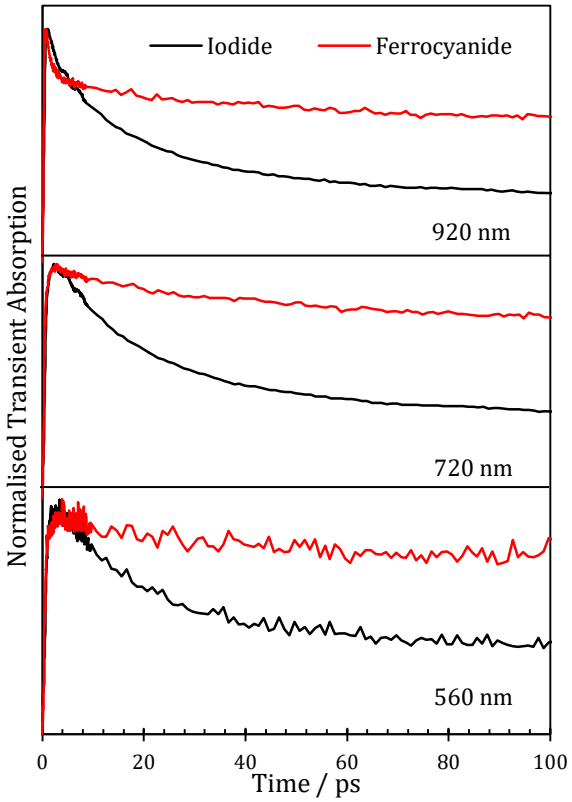

Figure 27 shows the long-time dynamics of electrons photo-detached from iodide (black) and Ferrocyanide (red) at 920 nm, 720 nm and 560 nm.

fact that there is no contact pair formed due to the Coulombic repulsion between $[Fe(CN)_6]^{3-}$ and the emitted electron, resulting in longer ejection distances and reduced geminate recombination compared to iodide. It is, however, interesting to note that at times < 10 ps, ferrocyanide exhibits a faster decay than iodide at 920 nm. The timescales at which this occurs corresponds to the blue-shifting of the absorption band corresponding to relaxation to the equilibrated electron state which for iodide is nearly twice as slow, reaching completion within 6 ps.[167]

Although the long-time dynamics have not been quantified here, the good agreement with the results of this study and that of Lenchenkov *et al.* and Vilchiz *et al.* for iodide provides confidence that the newly developed TA experiment is performing as expected with excellent SNR.

3.4.3. HYDRATED ELECTRONS FROM THE PHENOLATE ANION

Photo-oxidation is commonly observed following excitation of solute anions in the ultraviolet (UV) spectral range. For small inorganic ions, distinctive absorption bands appear in the UV that result in charge injection into the solvent. These so-called CTTS bands have been extensively studied in the literature.[111,116,117,170,171] Perhaps the most commonly studied photo-oxidation system is the CTTS of iodide in water. With ultrafast time-resolution, the evolution of the CTTS state can be probed directly[111,172] as well as the subsequent solvation of the electron and radical iodine atom.[108,173] The accepted view is that, following excitation of the lowest CTTS band, a contact pair is formed which subsequently thermalizes and then decays either by geminate recombination or dissociation to form a free hydrated electron, $e^-_{(aq)}$. At higher excitation energies, the electron can be injected into the solvent at longer range.[9] Similar overall dynamics are observed for other small aqueous inorganic anions such as $Fe(CN)_6^{4-}$, for which no contact pair is formed.[118,166] In contrast, most organic molecules lack the characteristic CTTS absorption bands, but nevertheless undergo photo-oxidation,[122,124,174] and a question arises about how electron loss occurs in these molecules. Here we probe the photo-oxidation of aqueous phenolate, $Ph^-_{(aq)}$, as a representative component of many bioactive chromophores. Using transient absorption spectroscopy, we show that, despite the absence of a CTTS band, very similar dynamics to typical CTTS processes are observed with the formation of a contact pair and subsequent dissociation and geminate recombination.

The phenolate chromophore is a common part in bioactive chromophores. For example, in photoactive proteins such as the green fluorescent protein and the photoactive yellow protein, local excitation of the Ph^- $\pi^* \leftarrow \pi$ transitions define some of the higher-lying electronic states in the UV spectral range. These have been extensively probed in the gas-phase, where very fast autodetachment has been observed.[175,176] In solution and proteins, photo-oxidation of many bioactive chromophores occurs following UV excitation suggesting that the same phenolate-localised $^1\pi\pi^*$ states lead to electron loss despite the presence of a solvent or a protein.[177–182] Here, we take a bottom-up approach and probe the photo-oxidation

of the simple Ph^- in an aqueous solution in an attempt to understand the photochemistry of this simple chromophore as a basis to understanding the photo-oxidation of more complex bioactive molecules. Specifically, we use transient absorption in the 550-950 nm spectral range to directly probe the electron loss channel through the production of a hydrated contact pair, which has a strong electronic transition around 720 nm that corresponds to its extensively studied p ← s transition.[21,165]

Ph^- has previously been studied by transient absorption. Early studies with 27 ps time-resolution, showed that $e^-_{(aq)}$ generation was essentially instantaneous.[183] More recently, the photo-oxidation of $Ph^-_{(aq)}$ has been studied in detail by the Bradforth group following excitation at 266 nm.[147] In their experiment, they probed the dynamics in the $290 < \lambda < 700$ nm range. While the study by Chen *et al*. was sensitive to the $Ph^0_{(aq)}$ radical product, the sensitivity to the hydrated electron was limited because their probe only partially overlapped with that p ← s transition of $e^-_{(aq)}$ and did not access its peak. Nevertheless, they were able to deduce remarkable insight through extensive analysis and fitting of their transient data. The key conclusion from their work was that the dynamics following excitation to the S_1 $^1\pi\pi^*$ state of Ph^- did not resemble that of a typical CTTS state. Instead, a slow growth of the absorption band due to the $[Ph^0{:}e^-]_{(aq)}$ contact pair was observed, indicating a relatively slow emission of the electron from the S_1 state. In the present study, the photo-oxidation event was initiated at 257 nm (instead of 266 nm) and the resultant dynamics appear very different and similar to CTTS dynamics, implying an extreme sensitivity to excitation energy. Our results allow us to extend the interpretation provided by Chen *et al*. [147] and provide a consistent explanation of the observed discrepancies between the two experiments.

All of the results presented used a 100 mM aqueous solution of phenolate prepared by dissolving phenol (Sigma Aldrich) in water that was adjusted to pH = 13 using of NaOH. For iodide experiments, a 100 mM solution of NaI (Sigma Aldrich) in water was used. The water in all experiments was taken from a filtration unit (Millipore Milli-Q Gradient A10, 18.2 MΩ). The solution's temperature was equilibrated to that of the room at 21 °C (294 K).

3.4.3.1. RESULTS AND ANALYSIS

The transient absorption spectra of $Ph^-_{(aq)}$ excited at 257 nm are shown in Figure 28. Figure 28(a) focusses on the short timescales (<5 ps) and shows the appearance of a broad absorption peak following excitation, with a spectral shape that shifts toward shorter wavelength as time evolves. The spectrum then appears to narrow on a few-picosecond timescale and decays at longer timescales as shown in Figure 28(b). The absorption spectrum at 100 ps peaks at 715 nm and can be assigned to the characteristic absorption band of $e^-_{(aq)}$.[7]

To assist analysis of the fast dynamics, kinetic slices of the transient absorption data in Figure 28 have been taken at a series of wavelengths; these are shown in Figure 29. Inspection of this data reveals two key features. The transient absorption signal across the wavelength range probed appears after ~200 fs and then peaks between approximately 1 and 2 ps, depending on the wavelength, with longer wavelengths peaking earlier (consistent with the observed blue-shift at early times in Figure 28). The overall dynamics are reminiscent of those observed for $I^-_{(aq)}$.[108,173] To explore this further, experiments on $I^-_{(aq)}$ photoexcited to its CTTS state at 257 nm were also performed. Figure 30 shows the transient absorption kinetics at three representative wavelengths for $I^-_{(aq)}$ and $Ph^-_{(aq)}$. Each kinetic trace has been normalised to its maximum absorption for comparison purposes. The overall kinetics following photo-oxidation of $I^-_{(aq)}$ and $Ph^-_{(aq)}$ are strikingly similar. In particular, the dynamics are very similar for short probewavelengths and deviate somewhat as λ increases as exemplified by the λ = 920 nm probe in Figure 30.

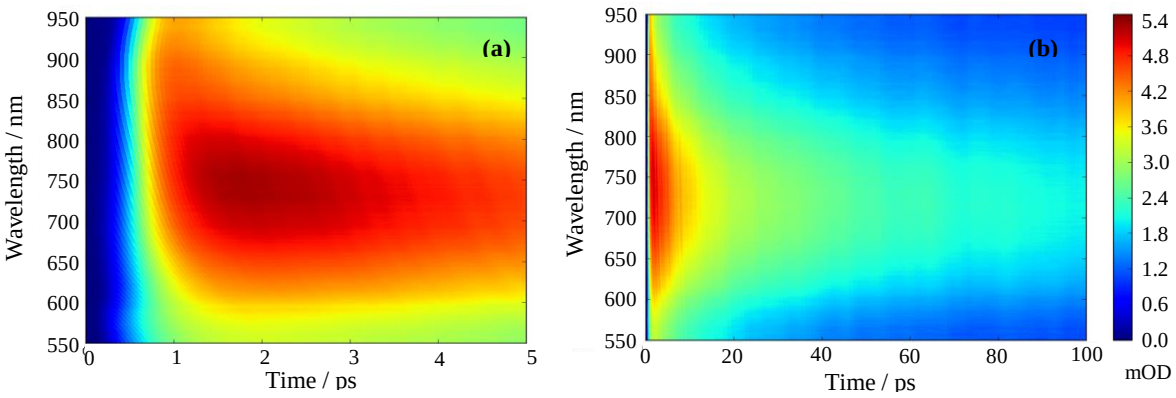

Figure 28 shows the transient absorption spectra of Ph^- excited at 257 nm, focussing on (a) dynamics at early times (5 ps) and (b) longer times (up to 100 ps).

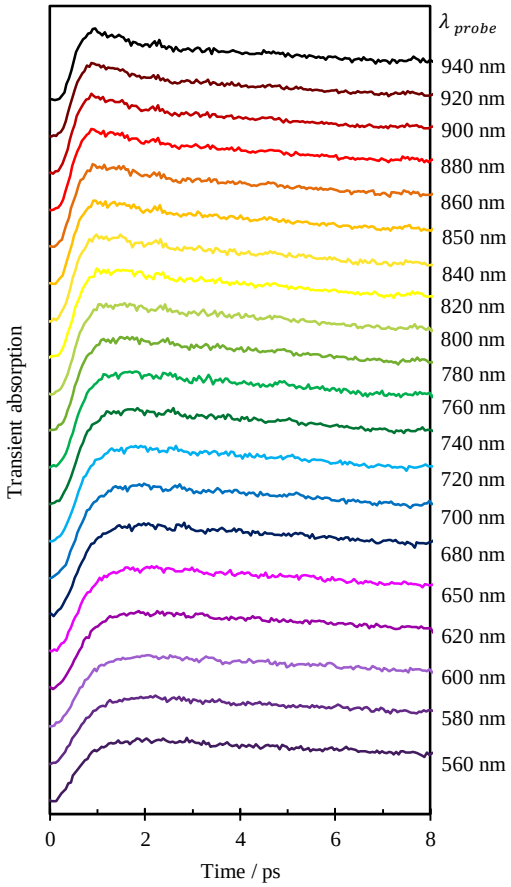

Figure 29 shows the kinetic traces of the transient absorption following photo-oxidation of Ph^- at a range of probe wavelengths.

Because of the overall similarity between the photo-oxidation dynamics of $I^-_{(aq)}$ and $Ph^-_{(aq)}$, we employ the model by Staib and Borgis[168,169] that has previously been used to explain the kinetics following CTTS from $I^-_{(aq)}$.[108,173] In this model, an electron is ejected from the solute with a rate constant k_p. The electron is initially located in close proximity to the radical parent species forming a contact pair. The surrounding solvent rearranges to accommodate the altered charge distribution. Once thermalized, the contact pair can either reform the anion by nonadiabatic reverse electron transfer (geminate recombination) with rate coefficient k_n, or it can dissociate to form the neutral radical and $e^-_{(aq)}$ with a rate coefficient k_d. The contact pair and free hydrated electron are assumed to have indistinguishable absorption spectra so that the transient absorption signal can be modelled as the number density $N(t)$ of both:

$$N(t) = \frac{k_d}{k_d + k_n} + \frac{k_p}{k_d + k_n - k_p}\left(\frac{k_p - k_d}{k_p}\exp\left(-k_p t\right) - \frac{k_n}{k_n - k_d}\exp\left(-(k_d + k_n)t\right)\right). \quad (11)$$

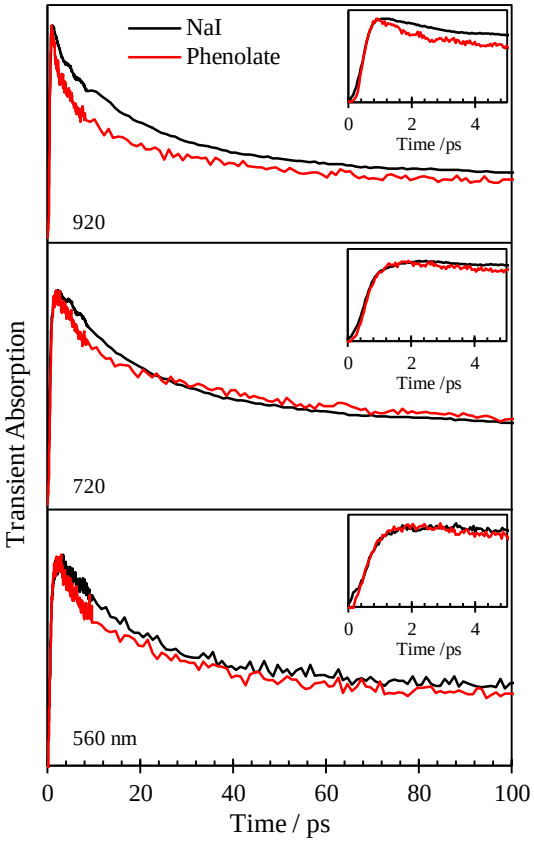

Figure 30 shows normalised kinetic traces of the tranisent absorption at three representative probe wavelengths for following the photo-oxidation of Ph^- (red lines) and I^- (black lines). The insets show the fit to the first 5 ps of the kinetics.

In order to fit this expression to the data in Figure 29, a convolution with the instrument response, $C(t)$, (assumed to be Gaussian with FWHM = 250 fs) was performed. We have used this to fit the photo-oxidation dynamics of both $I^-_{(aq)}$ and $Ph^-_{(aq)}$ at the three representative probe wavelengths in Figure 30, with the results shown in Table 2. Our results for $I^-_{(aq)}$ are in good agreement with to those obtained by Bradforth and coworkers who obtained rate coefficients of k_n = (33 ps)$^{-1}$ and k_d, = (70 ps) $^{-1}$ at a probe wavelength of 255 nm.[173] Overall, the kinetics for $Ph^-_{(aq)}$ fit similarly well to Eq. (1) as for $I^-_{(aq)}$, suggesting that the dynamics are also broadly similar. The formation time of the electron for $Ph^-_{(aq)}$ is comparable to $I^-_{(aq)}$, while the geminate recombination and dissociation of the contact pair is ~25% faster on average.

Table 2 Lifetimes of electron production (k_p^{-1}), nonadiabatic geminate recombination (k_n^{-1}), and contact pair dissociation (k_d^{-1}) following photo-oxidation of $Ph^-_{(aq)}$ and $I^-_{(aq)}$ at 257 nm, determined from fitting the data to Eq. (1).

	Phenolate			Iodide		
λ_{probe} / nm	k_p^{-1}/ ps	k_n^{-1}/ ps	k_d^{-1}/ ps	k_p^{-1}/ ps	k_n^{-1}/ ps	k_d^{-1}/ ps
560	0.58	26	50	0.65	35	65
720	0.57	28	41	0.53	36	71
920	0.27	28	28	0.12	25	60

3.4.3.2. DISCUSSION

The kinetics following a CTTS transition in $I^-_{(aq)}$ have previously been considered in detail by the Bradforth group following excitation at 255 nm[173] and were adequately captured by the model proposed by Staib and Borgis up to ~100 ps.[168,169] At longer-times, a slow additional decay of the electron signal arises from the diffusional dynamics of the dissociated $I^0_{(aq)}$ and $e^-_{(aq)}$ leading to secondary geminate recombination. The same is observed here for both $I^-_{(aq)}$ and $Ph^-_{(aq)}$, but is not considered because our main interest is in uncovering the photo-oxidation mechanism, and these slow dynamics have been discussed in detail in the literature for other systems.[184]

While the transient absorption spectra measured here for $I^-_{(aq)}$ excited at 257 nm are very similar to those observed by the Bradforth group, the photo-oxidation of $Ph^-_{(aq)}$ by Chen *et al.* has strikingly different dynamics than those observed here. Specifically, they observed a biphasic growth in electron absorption signal which reached a maximum at ~10 ps. Their interpretation was that the initially excited S_1 state undergoes a competition between rapid electron ejection and internal vibrational relaxation in the S_1 state, as some excess vibrational energy was imparted upon excitation (S_1 origin is at λ ~ 290 nm). The ejection from the equilibrated S_1 state would then lead to additional electron emission over a longer timescale. The electron was assumed to be ejected as a close contact pair, $[Ph^0{:}e^-]_{(aq)}$. This latter part is consistent with our observations, while the other aspects of the data are not. Perhaps the main conclusions of the study by Chen *et al*. was the dramatically different photo-oxidation dynamics observed for $Ph^-_{(aq)}$

compared to more commonly studied aqueous inorganic ions such as I^-,[108,173] OH^-,[185] $Fe(CN)_6^{4-}$,[166] NCS^-,[186] and to multiphoton ionisation of water.[102,105] So why are the dynamics observed here for $Ph^-_{(aq)}$ apparently contradictory to this conclusion?

To eliminate the possibility that any differences may be an artefact of the faster repetition rate of our experiment (resulting in possible incomplete relaxation between laser shots), we conducted an experiment at 1 kHz, which showed identical behaviour. Additionally, other control experiments in which we varied pump power and sample concentration had no impact. Therefore, the key difference appears to simply be the slightly different excitation wavelengths used, suggesting that the photo-oxidation mechanism has a non-trivial dependence on the excitation energy.

Despite the apparent discrepancy between our results and those of Chen *et al.*, we attempted to analyse our data using their methodology. Specifically, we focussed on the 650 nm kinetics for which the two probe ranges overlap. We could not replicate the early dynamics in our data using their model. Instead, we essentially only see fast ejection similar to CTTS dynamics suggesting that rapid electron emission from the S_1 state dominates the dynamics and this outcompetes internal vibrational relaxation in S_1. Fast ejection is also seen in the photo-oxidation of the

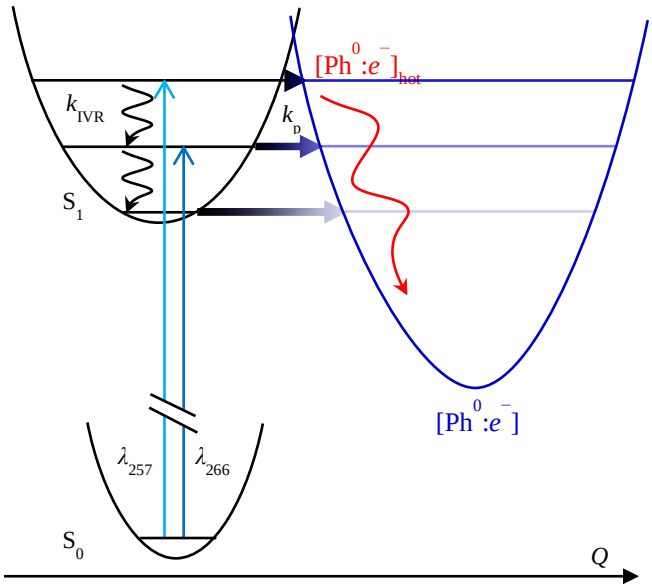

Figure 31 shows the schematic free energy profiles of the phenolate anion along a coordinate, Q. As the excitation energy increases and accesses higher vibrational levels of S_1, the tunnelling rate (k_p) of the electron to form a hot contact pair increases and outcompetes the internal vibrational relaxation rate (k_{IVR}) on S_1. Once the hot contact pair is formed, it cools to form the equilibrated contact pair.

naphtholate anion, indole, tryptophan and aniline derivatives.[183,187–189] The relatively slow signal growth attributed to the formation of the contact pair following electron ejection from the thermalised S_1 state observed by Chen *el al*. is not observed here. The extreme sensitivity of the branching ratio of direct emission and S_1 thermalisation to a small change in vibrational energy content in S_1 (an additional ~1300 cm^{-1}) points to a mechanism that is very sensitive to excess vibrational energy, which points to electron emission involving tunnelling.

In Figure 31, a Marcus-style schematic of free energy curves along a solvent rearrangement coordinate are sketched to aid in the following discussion, which aims to reconcile the differences in the photo-oxidation of $Ph^-_{(aq)}$ observed at 257 and 266 nm. The contact pair free energy is displaced along the solvent coordinate as solvent rearrangement is clearly necessary to achieve this. The final free energy of the contact pair is lower than that of the S_1 state, but much higher than that of S_0 (the reverse electron transfer to reform the S_0 from the contact pair is likely to be in the inverted region). As predicted by Marcus theory, there exists a barrier between the S_1 state and the contact pair along the solvent coordinate. To form $[Ph^0{:}e^-]_{(aq)}$ requires electron tunnelling through this barrier. As tunnelling is very sensitive to the height and width of the barrier ($P_{\text{tunnel}} = \exp(-2\beta Q)$, where $\beta = \sqrt{2m_e(V-E)}/\hbar$), we observe a very sensitive dependence on excitation energy. At 257 nm, we are apparently close to the top of the barrier and tunnelling is sufficiently fast that it outcompetes the vibrational relaxation on the S_1 state. At 266 nm, ~1300 cm^{-1} lower in energy, the barrier is larger (both in height and width) and the rate of tunnelling has slowed sufficiently so that vibrational relaxation can compete. As discussed by Chen *et al*.,[147] at 266 nm a fraction of the hot S_1 forms the contact pair rapidly, while the remainder cools on the S_1 state and this further lowers in energy. As the vibrational energy is dissipated, the tunnelling rate decreases rapidly because the barrier height and width increases (see Figure 31). Electrons are subsequently emitted at a longer timescale from the thermalised S_1 state. This emission from thermalised S_1 leads to the slow growth of absorption attributed to $[Ph^0{:}e^-]_{(aq)}$ formation. The current Marcus picture is fully consistent both with our data and that of Chen *et al*.. So, although the observed dynamics

appear very different at the two different excitation wavelengths, the basic mechanism has the same origin.

The rate of the observed electron appearance is the rate of tunnelling (related to k_p in Figure 31). Given the close agreement between the transient absorption data on $Ph^-_{(aq)}$ and $I^-_{(aq)}$ (Figure 30, Table 1), we conclude that the electron appearance time is similar to that seen for the CTTS state of $I^-_{(aq)}$, which Vilchiz *et al.* determined to be 210 fs.[167] Immediately following tunnelling, the electron is formed as a close contact pair, which, according to Figure 31, is formed in a non-equilibrium solvent geometry. The early time-blue shift observed in Figure 28 represents the thermalisation of this hot contact pair, $[Ph^0{:}e^-]_{hot}$. These dynamics are again consistent with those observed following CTTS of aqueous iodide. Vilchiz *et al.* observed full thermalisation of the contact pair in ~6 ps. Here, we observe similar timescales that converge to a final absorption maximum of 715 nm of the free hydrated electron at 294 K.[165]

The similarity between CTTS dynamics of $I^-_{(aq)}$ and electron emission by tunnelling from S_1 of $Ph^-_{(aq)}$ is remarkable because the basic mechanism for electron emission is different in both cases. The CTTS process involves a specific excited state formed by detachment into the solvent in preformed cavities. For $Ph^-_{(aq)}$, this is not the case and the initial state is the S_1 $^1\pi\pi^*$ excited state of Ph^-. Bradforth and Jungwirth have shown that the orbital associated with the CTTS state is predominantly of s-character.[109] In the case of Ph^- tunnelling, the S_1 state involves π orbitals and, from an isolated gas-phase perspective, we may anticipate that this will lead to emission of electrons with predominantly p-character.[190] Thus, at early times the hydrated electron could be generated in its excited p-state. However, these dynamics are likely not to be captured within our limited temporal resolution; the internal conversion lifetime of the p-state of $e^-_{(aq)}$ is approximately 50 fs.[191,192] The main differences between $Ph^-_{(aq)}$ and $I^-_{(aq)}$ occur at the longest wavelengths (see Figure 30). This spectral region is the most sensitive to the initially formed non-equilibrium contact pair, $[Ph^0{:}e^-]_{hot}$, and therefore electron ejection mechanism. Nevertheless, the rising edge at all wavelengths is very similar (see inset of Figure 30) between $Ph^-_{(aq)}$ and $I^-_{(aq)}$. It is worth noting that Ph^0 has a sufficiently large dipole-moment so that Ph^- can support a dipole-bound state.[193] Such a dipole-

bound state is in principle similar to the CTTS states and has s-character. It is conceivable that the electron emission is mediated by such dipole-bound precursor states,[194–196] in which case the observed dynamics may appear very similar to those involving a CTTS state.

The cooling rate of $[Ph^0:e^-]_{hot}$ is comparable to $[I^0:e^-]_{hot}$ with the largest differences again at longest wavelengths, where the transient absorption is most sensitive to the cooling dynamics. Differences here may be anticipated. As already commented, the Ph^0 radical has a large dipole moment so that the electron will presumably be predominantly localised on the positive end of this dipole (opposite to the oxygen) and so is highly directional, which is not the case for CTTS from $I^-_{(aq)}$ (except at the water/air interface).[172] We also note that $Ph^0_{(aq)}$ may be produced with excess vibrational energy. The vertical detachment of Ph^- in the gas-phase shows that predominantly the ν_{11} mode (a_1 symmetry) of Ph^0 with a frequency of 515 cm^{-1} is excited. This energy must also be dissipated, in contrast to I^0 which is formed in the ground state, and may lead to differences in the cooling dynamics.

Once the equilibrated contact pair is formed, the kinetics of $[Ph^0:e^-]_{(aq)}$ appear to follow those predicted by Staib and Borgis,[168,169] but faster than for $[I^0:e^-]_{(aq)}$, although not dramatically so. It is also noteworthy that the final yield of $e^-_{(aq)}$ is similar for $[Ph^0:e^-]_{(aq)}$ and $[I^0:e^-]_{(aq)}$. The faster geminate recombination dynamics are consistent with the Marcus picture, where we may anticipate that this process is in the inverted region. The larger electron affinity of I^0 compares to Ph^0 suggests that the nonadiabatic geminate recombination to form I^- is further in the inverted region and, hence, has a larger barrier so that k_n for $[Ph^0:e^-]_{(aq)}$ may be expected to be larger than for $[I^0:e^-]_{(aq)}$, consistent with the experimental observations. That k_d is also larger suggests that the free energy well for $[Ph^0:e^-]_{(aq)}$ is shallower than that of $[I^0:e^-]_{(aq)}$.

Finally, we comment that phenolate is a key chromophore in many bioactive chromophores that can undergo photo-oxidation. Examples include the green fluorescent protein and photoactive yellow protein chromophores. The photo-oxidation of the chromophores and proteins have previously been studied following UV excitation.[177–182] As we have shown recently, the excited states

accessible in the UV range involve π* ← π transitions localised on Ph^-,[190] so that the chemical picture developed in the present experiments may be representative of a large class of bio-active molecules. We are currently probing the photo-oxidation of a range of such molecules.

3.4.3.3. CONCLUSION

The photo-oxidation of aqueous phenolate anions following excitation at 257 nm has been measured by transient absorption spectroscopy. In contrast to a previous study from the Bradforth on the same process following excitation at 266 nm, the present data shows a sub-picosecond generation of a contact pair, akin to the dynamics observed for charge-transfer-to-solvent (CTTS) excitations of iodide. We account for this discrepancy using a Marcus model in which electron tunnelling leads to the formation of a contact pair, where the tunnelling is sensitively dependent on excitation energy. The contact pair is formed in a non-equilibrium (hot) solvent geometry and the transient absorption spectra clearly identify the subsequent cooling to form the equilibrium contact pair. At longer times, we observe the well-studied competitive dissociation/recombination kinetics, which again are similar to that seen following CTTS excitation of aqueous iodide, albeit faster. The photo-oxidation model presented here for phenolate can be viewed as a bottom-up picture of the photo-oxidation of many photoactive proteins that have phenolate as a chromophore, in particular for the higher-lying excited states, which are most actively involved in photo-oxidation.

4. SECOND HARMONIC GENERATION

4.1. BASIC THEORY OF NON-LINEAR OPTICAL RESPONSES

When a dielectric material is exposed to an electromagnetic field, the charge distribution is distorted and a polarisation is induced. In linear optics, this induced polarisation, $\mathrm{P}(t)$, is directly proportional to the strength of the applied field, $\mathrm{E}(t)$, and can be described by the relation:[154,156]

$$\mathrm{P}(t) = \varepsilon_0 \chi^{(1)} \mathrm{E}(t), \tag{12}$$

where ε_0 is the vacuum permittivity and $\chi^{(1)}$ is the constant of proportionality known as the linear susceptibility. This relation holds in weak field regimes, but all dielectrics exhibit nonlinear behaviour when the field strength is high enough,[197] and thus the material responds in a manner that is nonlinearly dependent on the intensity of the applied electric field. SHG, for example, is the response that is proportional to the square of the field intensity and results in the coupling of incident electromagnetic waves to generate a wave at twice the incident frequency. In the nonlinear regime, the time dependent dipole moment per unit volume, or polarisation, is best expressed as a power series of the applied field:[154,198]

$$\begin{aligned} \mathrm{P}(t) &= \varepsilon_0 \left[\chi^{(1)} \mathrm{E}(t) + \chi^{(2)} \mathrm{E}^2(t) + \chi^{(3)} \mathrm{E}^3(t) + \cdots \right], \\ &\equiv \mathrm{P}^{(1)}(t) + \mathrm{P}^{(2)}(t) + \mathrm{P}^{(3)}(t) + \cdots, \end{aligned} \tag{13}$$

where the quantities $\chi^{(2)}$ and $\chi^{(3)}$ are known as the second and third order susceptibilities, respectively. Equation (2) assumes an instantaneous response in

$\mathrm{P}(t)$ to $\mathrm{E}(t)$ at any point in time, *t*. It then follows from the Kramers-Kronig relations that the material be both lossless and dispersionless.[154]

Despite nonlinear optical behaviour being noted as early as 1941 in a study of the saturation effects of phosphorescent fluorescein by Lewis *et al.*,[199] the requirement for high field strengths remained a challenge. It is therefore no coincidence that the origin of the study of nonlinear optics is often traced to Franken *et al.*[197] who, in 1961, a year after the first demonstration of stimulated emission in Ruby by Maiman,[200] demonstrated the generation of second harmonic light using intense fields from a pulsed Ruby maser.

4.1.1. SECOND HARMONIC GENERATION (SHG)

The process of SHG can be visualised as two photons of frequency ω being absorbed with the simultaneous emission of a photon of frequency 2ω. SHG is therefore a specialised case of SFG in which the two photons absorbed can be of different frequencies ω_n and ω_m. The process of SHG is shown in Figure 32 where the solid line represents the ground state of the system and the dashed lines represent virtual states.

Consider an electric field, $\mathrm{E}(t)$, with frequency ω,

$$\mathrm{E}(t) = Ee^{-\omega t} + c.c.\ , \tag{14}$$

incident on a nonlinear material with a nonzero second-order susceptibility, then the second order nonlinear polarisation, $\mathrm{P}^{(2)}$, can be extracted from Equation (13),

$$\mathrm{P}^{(2)}(t) = \varepsilon_0 \chi^{(2)} \mathrm{E}^2(t)\ , \tag{15}$$

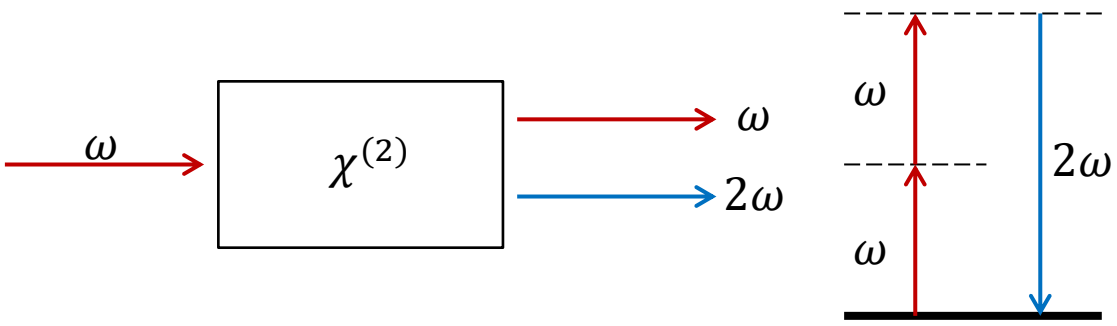

Figure 32 (a) shows that the second harmonic light is geometrically parallel to the transmitted light, (b) shows the energy level relationship.

and can be written as

$$\mathrm{P}^{(2)}(t) = 2\varepsilon_0\chi^{(2)}EE^* + \left(\varepsilon_0\chi^{(2)}E^2e^{-2i\omega t} + c.c.\right). \tag{16}$$

On inspection, it can be seen that the polarisation is composed of two components; one frequency independent term and another term at frequency 2ω. Larmor's theorem of electromagnetic radiation states that electromagnetic radiation is generated from the acceleration of charges. Thus, if a material is considered to be made up from a series of electrons, each with their own dipole moment, then the power, *P*, radiated by that electron, by its acceleration, *a*, can be expressed in terms of its charge, *e*, and the velocity of light, *c*, in the Larmor formula:[201]

$$P = \frac{2}{3}\frac{e^2a^2}{c^3}. \tag{17}$$

As polarisation is the unit charge or dipole moment per volume, the second derivative of the nonlinear polarisation with respect to time, $\partial^2\mathrm{P}^{\mathrm{NL}}/\partial t^2$, is a measure of the charge acceleration. When this is compared to the nonlinear wave equation:

$$\nabla^2\mathrm{E} - \frac{n^2}{c^2}\frac{\partial^2\mathrm{E}}{\partial t^2} = \frac{1}{\varepsilon_0c^2}\frac{\partial^2\mathrm{P}^{\mathrm{NL}}}{\partial t^2}, \tag{18}$$

it can be inspected that the nonlinear polarisation results in electron oscillation and thus drives the emitted electric field. With reference to SHG in Equation (16), it can therefore be seen that the frequency dependent term is responsible for the light generated at double the frequency of the input wave, whilst the first term does not generate any electromagnetic radiation because its second time derivative (and therefore acceleration) is zero. Instead of generating light, this term leads to a process called optical rectification whereby a static electric field is placed across the material.[154] A detailed discussion of the theory underpinning SHG, including the properties of the second order nonlinear susceptibility, can be found in Appendix B. Here, only a brief overview of the most relevant theory will be presented.

4.1.2. INTERFACIAL SHG

Second order nonlinear processes, such as SHG and SFG, gained significant attention as a spectroscopic technique in the 80's due to its surface sensitivity down to sub-monolayer regimes.[202–206] The physical origin of the interfacial nonlinear optical response arises from either the structural or field discontinuities across the interface. Structural discontinuities tend to be more significant when the molecular ordering at the interface differs from that in the bulk, for example, on semi-conductor surfaces where dangling bonds may be present, or the presence of adsorbates (e.g. surfactants) that have a preferential orientation at an interface compared to the bulk. In comparison, field discontinuities tend to be important for liquid surfaces as the interfacial structure is more similar to the bulk.[203,204,206]

The origin of the surface specificity is that second order nonlinear processes are formally forbidden in bulk centrosymmetric materials. Hence, at an interface between two centrosymmetric media, second order nonlinear response must be solely due to the interface, where this symmetry is broken. This can be explained with reference to Equation (15) by changing the sign of the applied field from $\tilde{E}(t)$ to $-\tilde{E}(t)$. If a material possesses an inversion centre, the polarization sign must also change:

$$-\mathrm{P}^{(2)}(t) = \varepsilon_0 \chi^{(2)} \big(-\mathrm{E}(t)\big)^2 = \varepsilon_0 \chi^{(2)} \mathrm{E}^2(t)\,, \tag{19}$$

which can only be satisfied if $\chi^{(2)} = 0$ for all tensor elements.[154] SHG studies that probe the surface are usually limited to centrosymmetric materials as a consequence. This surface sensitivity has been experimentally evidenced through a number of studies in which the SHG from initially clean metals and semiconductor surfaces are affected by orders of magnitude with time by surface oxidation, contamination and adsorbates.[207–211] The focus of this section will be on the interaction of the incident field at the interface generating second harmonic light.

4.1.2.1. BOUNDARY CONDITIONS AND POLARISATION

When an optical field is incident on a material, the wave can either be reflected or transmitted. In 1962, a pioneering study by Bloembergen *et al.*[212] showed that SHG at interfaces similarly obeys the standard laws of reflection and refraction and thus can be described in terms of the incident wave using Fresnel factors (discussed in the next section). This problem was solved completely by Bloembergen *et al.* from first principles.[212] The following discussion, however, will be based on a derivation of boundary conditions across a nonlinearly polarized sheet derived in detail by Heinz[213,214]and Feynman[215].

It is well known that the classical properties of all electromagnetic fields can be described by Maxwell's equations, in terms of a nonlinear source polarisation, $\mathrm{P}^{(2)}$

$$\nabla \cdot \mathrm{E} = -\frac{4\pi}{\varepsilon_0}\nabla \cdot \mathrm{P}^{(2)}\,, \tag{20}$$

$$\nabla \times \mathrm{E} = -\frac{\partial \mathrm{B}}{\partial t}\,, \tag{21}$$

$$\nabla \cdot \mathrm{E} = 0\,, \tag{22}$$

$$c^2\nabla \times \mathrm{E} = \frac{4\pi}{\varepsilon_0}\frac{\partial \mathrm{P}^{(2)}}{\partial t} + \frac{\partial \mathrm{E}}{\partial t}\,, \tag{23}$$

which must be satisfied in both materials either side of the surface, as well as inside the boundary itself. With reference to Figure 33, although a boundary is usually considered to be infinitely thin, in reality the refractive indices change continuously across the interface. A model in which the interface forms its own layer, with dielectric constant, ε', and the same refractive index as the material with ε_2 is therefore often used. Although formally this interfacial layer is of vanishing thickness, it can be imagined that the boundary has been stretched vertically in the z-direction, extending between $z = 0^+$ to $z = 0^-$, whilst maintaining the same dipole moment per unit area.

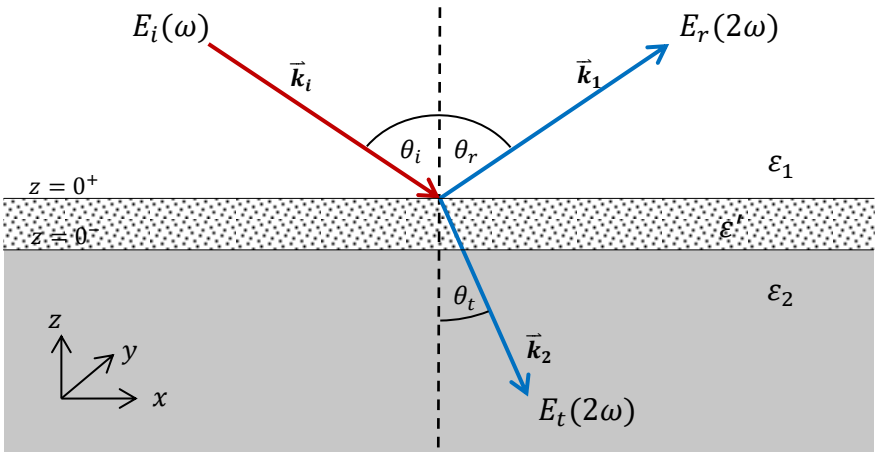

Figure 33 shows the physical relationship between the incident wave and second harmonic wave that is reflected.

The usual conditions of continuity for a polarized sheet of finite thickness (the derivation of which can be found in detail in Feynman[215]) are usually considered to be

$$\left(\varepsilon_0 E_1 + 4\pi P_1^{(2)}\right)_\perp = \left(\varepsilon_0 E_2 + 4\pi P_2^{(2)}\right)_\perp , \tag{24}$$

$$(E_1)_\parallel = (E_2)_\parallel , \tag{25}$$

$$B_1 = B_2 , \tag{26}$$

where the subscripts $\parallel$ and $\perp$ denote electromagnetic components parallel and perpendicular to the interfacial x-y plane. Outside of the polarised sheet, the electromagnetic field is finite. Therefore, as the polarised sheet is reduced in size to a plane of infinite thinness between $z = 0^+$ to $= 0^-$, the above conditions imply that

$$\int_{0^-}^{0^+} \left(\varepsilon_0 E_\perp + 4\pi P_\perp^{(2)}\right) dz = \int_{0^-}^{0^+} E_\parallel \, dz = \int_{0^-}^{0^+} B_\parallel \, dz = \int_{0^-}^{0^+} B_\perp \, dz = 0 , \tag{27}$$

from which it can be deduced that, whilst $E_\parallel$ and B must be finite inside the boundary, $E_\perp$ tends towards a singularity because

$$\varepsilon_0 \int_{0^-}^{0^+} E_\perp \, dz = -4\pi \int_{0^-}^{0^+} P_\perp^{(2)} \, dz = -4\pi P_{\perp,s}^{(2)} , \tag{28}$$

where the subscript s in $P_{\perp,s}^{(2)}$ denotes the surface nonlinear polarisation. Now the magnetic and electric fields have been characterised inside of the boundary, Maxwell's equations can be integrated to determine the relationship between the fields on either side of the interface. This yields the boundary conditions:

$$\Delta E_z = -\frac{4\pi}{\varepsilon_0}\nabla \cdot P^{(2)} ,$$

$$\Delta E_y = -\frac{4\pi}{\varepsilon_0}\frac{\partial P_z^{(2)}}{\partial y} ,$$

$$\Delta E_x = -\frac{4\pi}{\varepsilon_0}\frac{\partial P_z^{(2)}}{\partial x} , \qquad (29)$$

$$\Delta B_x = -i\frac{4\pi\omega}{c}P_y^{(2)} ,$$

$$\Delta B_y = +i\frac{4\pi\omega}{c}P_x^{(2)} ,$$

$$\Delta B_z = 0 .$$

These boundary conditions can be used to determine the SHG field components, at frequency 2ω, propagating away from the interface in either the reflected or refracted geometries, with wave vectors $\vec{k}_1$ and $\vec{k}_2$, respectively. Figure 34 shows schematically that the two components that constitute the SHG wave are either

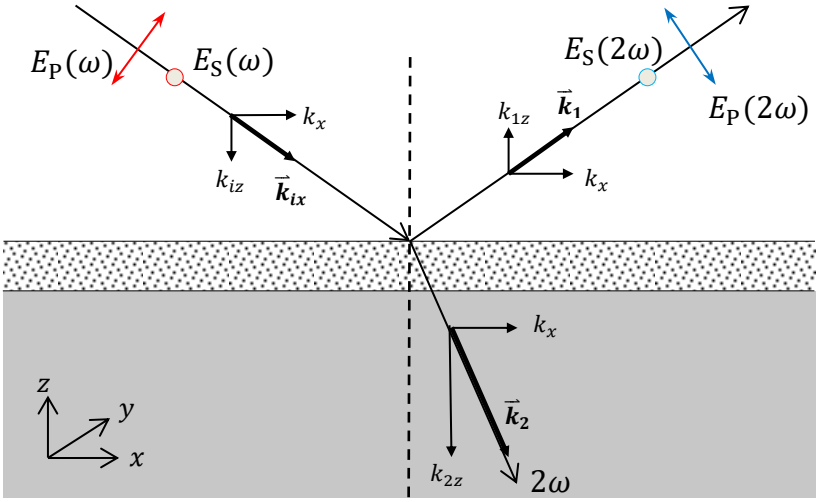

Figure 34 shows the relationship between the different components of the incident wave and the second harmonic waves generated at the surface.

normal to the interface in the *x*-*z* plane, E_S, or parallel to the interface in y direction, E_P. The subscripts P and S therefore represent S- and P-polarised light, respectively. Thus, the polarised electric field amplitudes in material 1 for the reflected SHG wave, as derived by Heinz, can be shown to be[213]

$$E_P = i4\pi k_1 \left(\frac{k_{2z} P_x^{(2)} + \left(\frac{\varepsilon_2}{\varepsilon'}\right) k_x P_z^{(2)}}{\varepsilon_2 k_{1z} + \varepsilon_1 k_{2z}} \right), \tag{30}$$

$$E_S = i4\pi k_1 \left(\frac{k_1 P_y^{(2)}}{\varepsilon_1 (k_{1z} + k_{2z})} \right), \tag{31}$$

where k_{ij} represents the propagation vector component in medium i (which represents either medium 1 or 2 and should not be confused with the imaginary number) and direction j which represents the lab frame axes x, y, and z. Snell's Law can thus be used to relate the individual components to the propagation vector in each material. For example, $k_{1z} = k_1 \cos\theta_r$. For k_x or k_y , no subscript i is required as it is not medium dependent.

Equation (15) with the correct combination of incident waves used, can thus provide expressions for the output nonlinear polarization components $P_z^{(2)}$, $P_x^{(2)}$ and $P_y^{(2)}$. For example, to generate an expression for $P_y^{(2)}$, a susceptibility component of the form $\chi_{ijk}^{(2)}$ is needed where $i = y$. Cross referencing with Equation (114), reveals that the only susceptibility components that satisfy this condition are $\chi_{yzy}^{(2)} = \chi_{yyz}^{(2)}$. Thus, to generate the S-polarised output $P_y^{(2)}$ at the interface, one of the incident fields must be the perpendicular component, E_z', whilst the other must be an incident wave component parallel to the surface either, E_y' or E_x'. This polarisation combination is conventionally described in SFG as SPS or SSP, where the first letter indicates the sum frequency output polarisation, and the second two letters indicate the two input wave polarisations. However, as SHG only has one incident wave, this notation is often abbreviated to SMix which represents S polarised output and mixed polarised input. The allowed SMix polarisation combination is therefore represented by:

SMix: $$P_y^{(2)}(2\omega) = \varepsilon_0 \chi_{yyz}^{(2)} E_y'(\omega) E_z'(\omega)\,, \tag{32}$$

where $E'(\omega)$ indicates the local electric field within the interface. As there are only three independent nonzero susceptibility elements, it follows that there should be only three symmetry allowed polarization combinations. Inspection of the remaining nonlinear susceptibility components and the same rationalisation as above, identifies these combinations as PS and PP, which are given, respectively, by:

PS: $$P_z^{(2)}(2\omega) = \varepsilon_0 \chi_{zyy}^{(2)} E_y'(\omega) E_y'(\omega)\,, \tag{33}$$

PP: $$P_x^{(2)}(2\omega) = \varepsilon_0 \chi_{xxz}^{(2)} E_x'(\omega) E_z'(\omega)\,, \tag{34}$$

PP: $$P_z^{(2)}(2\omega) = \varepsilon_0 \chi_{zzz}^{(2)} E_z'(\omega) E_z'(\omega) + \varepsilon_0 \chi_{zxx}^{(2)} E_x'(\omega) E_x'(\omega)\,. \tag{35}$$

At first the result given in Equations (34) and (35) may seem surprising as it was discussed earlier that the *x* and *y* axes exhibit identical responses at the interface, resulting in $\chi_{xxz}^{(2)} = \chi_{yyz}^{(2)}$ and $\chi_{zyy}^{(2)} = \chi_{zxx}^{(2)}$ and thus $E_x'(\omega) = E_y'(\omega)$. So how can they be used to characterise different polarisation combinations? The answer to this lies in Figure 34, which shows that the P-polarised input/output lies in the *x*-*z* plane and therefore must have components in both $P_x^{(2)}$ and $P_z^{(2)}$, which agrees with Equation (30). So, where as $E_y'(\omega) = E_x'(\omega)$ and $\chi_{xxz}^{(2)} = \chi_{yyz}^{(2)}$, $P_y \neq P_x$ and $E_y \neq E_x$, because the output and input waves are not characterised at the interface.

So now we have expressions for the nonlinear polarization components in terms of the local electric field at the interface. However, in order to be of any consequence, this needs to be related to the incident electric field which can be determined using Fresnel factors.

4.1.2.2. FRESNEL COEFFICIENTS

When light is incident on a surface, the wave can either be transmitted into material 2 via refraction or reflected back into material 1. As previously

mentioned, when second harmonic light is generated at an interface, the resultant light can also be transmitted and reflected in accordance with the laws of reflection and refraction.[204] If, however, we refer back to the three layer model shown in Figure 33 and Figure 34, then the interaction of light with the interface should be considered to be continuous across the interface of vanishing thickness. Thus, in order to generate second harmonic light at the interface, first light must be transmitted into the interface, which is characterised by the same refractive index as material 2. As a consequence of this transmission, the amplitude of the wave will be altered in passing from one material to the other and the amplitude transmission coefficients or Fresnel factors should be considered.[156]

$$t_{\mathrm{P}} = \frac{2sin\theta_{\mathrm{t}}cos\theta_{\mathrm{in}}}{\sin(\theta_{\mathrm{t}} + \theta_{\mathrm{in}})}, \tag{36}$$

$$t_{\mathrm{S}} = \frac{2sin\theta_{\mathrm{t}}cos\theta_{\mathrm{in}}}{\sin(\theta_{\mathrm{t}} + \theta_{\mathrm{in}})\cos(\theta_{\mathrm{in}} - \theta_{\mathrm{t}})}, \tag{37}$$

where the indices in and t refer to incident and transmitted, respectively. These coefficients relate the incident field in material 1 to the transmitted field in material 2. As discussed in the previous section, the electric field is continuous across the interface and thus, the boundary conditions can be used to relate E_{2j} (where j is defined in Figure 34) to the local field in the interface, E'_j:[214]

$$E_{2x} = E'_x \qquad E_{2y} = E'_y \qquad E_{2z} = \frac{\varepsilon_2}{\varepsilon'} E'_z \,. \tag{38}$$

Therefore using Equations (38) and (37) and the geometrical relationships shown in Figure 35, the local fields can be related to the polarised electric field amplitudes. Substituting the relations shown in Equation (39) into Equations (33)-(35) yields the expression for the SHG polarization components in terms of the incident electric fields.

$$E'_x = t_{\mathrm{P}} E_{\mathrm{P}} cos\theta_{\mathrm{t}} \,,$$

$$E'_y = t_{\mathrm{S}} E_{\mathrm{S}} \,, \tag{39}$$

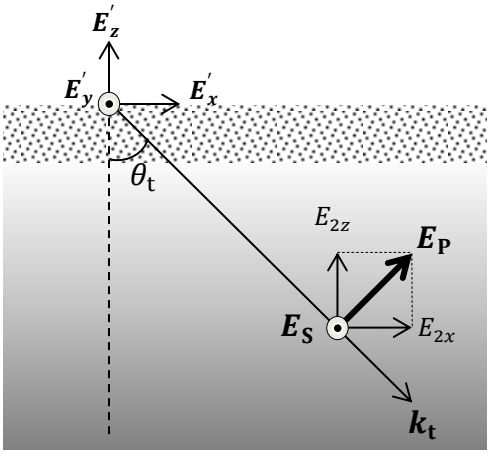

Figure 35 shows the relationship between the transmitted wave and the local electric field components

$$E_z' = \frac{\varepsilon_2}{\varepsilon'} E_P sin\theta_t \ .$$

The Fresnel transmission coefficients can also be used to express the intensity of the SHG light.[216,217]

$$E_\omega(x, z = 0^-) = (E_P^{in} t_P \hat{p}_+ + E_S^{in} t_S \hat{s}) e^{ikx} = e^\omega \left| E^{in} \right| e^{ikx} \ , \tag{40}$$

$$e^\omega = \hat{p}_+ t_P \hat{p}_- + E_S^{in} t_S \hat{s} \ , \tag{41}$$

where $\hat{p}$ and $\hat{s}$ are the unit vectors for P- and S-polarizations of the incident wave propagating into the interface respectively, E_ω is the linear response in the medium, and the Fresnel coefficients are defined as going from medium 1 into medium 2. The +/– sign subscripts on $\hat{p}$ are used to indicate the direction in which the unit vector points, whereby $\hat{p}_+$ represents the unit vector for P-polarization of the fundamental linear wave travelling in the $+z$ direction (i.e. a reflection of the incident wave from the interface back into medium 1). This notation can thus be used to define the intensity of the second harmonic wave in terms of the intensity of the incident wave at frequency ω, and the incident angle relative to the normal, θ_{in}:

$$I(2\omega) = \frac{32\pi^3 \omega^2 sec^2 \theta_{in}}{c^3} \left| e^{2\omega} \cdot \chi^{(2)} : e^\omega e^\omega \right|^2 I^2(\omega). \tag{42}$$

4.1.2.3. CONTRIBUTIONS TO THE SURFACE SHG

Thus far the electric dipole approximation (in which only dipoles are considered to respond to an electric field) has been used to characterise second order nonlinear properties, with contributions from quadrupoles and multipoles ignored. However, in a series of publications between 1986 and 1988 by Guyot-Sionnest *et al.*,[202–204] a

combination of theory and experiment was used to show that SHG always has a contribution from both the surface and the bulk, even in polarization combinations that had previously been considered to be bulk contribution free.[202] This bulk contribution for isotropic materials was shown, by a rigorous mathematical treatment,[204] to originate from symmetry allowed induced electric quadrupoles and magnetic dipoles. These terms are experimentally indistinguishable from the surface contribution. Although contributions arising from induced quadrupoles and magnetic dipoles are inherently weak compared to those from electric dipoles, the number of molecules in the bulk volume is significantly larger than the number of molecules at the surface. The large number of molecules present in the bulk could therefore potentially compensate for the weak response per molecule and thus, the bulk signal could dominate over the surface signal. In such a scenario, interpretation of results with respect to interfacial properties would be extremely difficult and thus the significance with which the bulk contributes to the SHG is of fundamental importance.[205]

Attempts to experimentally determine the extent of the induced quadrupole response in the bulk have been controversial with conflicting results. In 1987 Guyot-Sionnest *et al.*[203] concluded that, although the bulk contribution is significant, it is at most of the same order of magnitude as that originating from the surface. However, it was also reported that the situation is further improved if the material of interest has a high dielectric constant, resulting in the surface contribution dominating over the bulk. This conclusion was further supported in a study by Luca *et al.*[218] who determined that the large bulk contribution for air/liquid interfaces was negligible for a liquid/liquid interface due to the better matching of dielectric constants. In contrast, other studies have reported that only the dipole contribution needs to be considered in order to fully characterise the SHG signal. This has largely been reported to be as a consequence of the absence of significant SHG temperature dependence, which had been previously ascribed to be a source of bulk contributions.[219,220]

When interfaces were studied computationally, neglecting quadrupolar terms, a discrepancy was observed in the sign of the calculated nonlinear susceptibilities when compared to experimental results which are widely reported to be negative

for water and other liquid systems.[221] A recent MD study by Shiratori *et al.*[222] resolved this discrepancy by including quadrupole terms, which showed that the calculated nonlinear susceptibilities in non-resonant regimes agreed with experimental results in both sign and magnitude.[222]

Bulk contributions are not the only obstacle to overcome however. The SHG signal is further complicated by the surface nonlinear susceptibility, having additional terms arising from induced quadrupole and magnetic dipole moments, which have been neglected in the discussion thus far. Some studies in the recent literature conclude that the extent to which the quadrupolar surface contribution dominates under non-resonant conditions increases proportionally with the ratio of refractive indices of the two isotropic materials.[203,221] However, when a degree of order is introduced at the interface, such as an adsorption layer, and one of the input or output frequencies is at or near a resonance, the electric dipole term again dominates due to the enhanced asymmetry.[221]

Although no agreement has yet been made in the field of nonlinear optics as to the extent with which the bulk and surface quadrupole contributions complicate results in non-resonant systems, it has been agreed widely that when present, they are inseparable from the desired surface dipole response. The drive to minimise quadrupole terms and maximise surface specificity has been emphasised by a shifting literature trend in SHG studies towards systems that utilise resonances.[220]

4.2. NON-LINEAR SPECTROSCOPIC TECHNIQUES

Since the first demonstration of SHG in 1961[197], the field of nonlinear optics has experienced a dramatic progression in experimental sophistication and theoretical understanding. As with any developing field, amelioration is necessarily accompanied by nomenclature introduction. However, due to the relatively sudden influx of interest in the 80's (largely related to the development of tuneable infrared laser sources making SFG studies accessible), a large array of different experimental techniques were explored within a short space of time, with varying degrees of success. This resulted in the erratic introduction of new classifications to describe subtly different techniques, inconsistent data analysis, and use of

ambiguous terminology that has evolved in modern literature to have a precise meaning. Although 30 years on, the literature appears to be tending towards an accepted standard, the historical literature makes the task of understanding the development of nonlinear optics both daunting and complex. This chapter therefore is an attempt to discern the significant techniques and highlight the important developments towards the modern methods used today.

Although SHG surface spectroscopy was the predecessor to SFG spectroscopy, the technique was limited to electronic transitions and SHG in the (near) visible region by the restricted availability of suitably sensitive photomultiplier detectors. Vibrational information about the interface using SFG relies on one incident tuneable beam being in the IR and the other at a fixed wavelength in the visible, such that the SFG would be in the visible region where photomultipliers are sensitive. By scanning across the IR region, different vibrational frequencies will resonantly enhance the SFG output resulting in a surface specific vibrational spectrum. This technique is often referred to in the literature as vibrational SFG (VSFG) or SFG vibrational spectroscopy (SFG-VS).[206,223] SFG and SHG are closely intertwined as methods and both will be discussed.

4.2.1. "HOMODYNE"-DETECTED TECHNIQUES

In its most basic form, SHG and SFG experiments simply measure $\left|\chi^{(2)}\right|^2$ through detection of the reflected (or, if the sample is transparent, transmitted) second order nonlinear light intensity. This technique is probably best described in the literature as a direct or simple method. However, the advent of a new 'heterodyning' technique in the 90's, saw the reclassification of direct SHG to 'homodyne' SHG by some authors in an attempt to align with the new nomenclature. Although the two methods are distinct, the validity of the use of the term homodyne and heterodyne is controversial.[224] Indeed, there is an argument that heterodyne techniques should be formally classified as homodyne, discussed in detail in Section 4.2.2.2. In fact, to this author's knowledge, the first appearance of homodyne in the literature to describe an experimental SHG study was in 1995,[225] but was actually an example of a method now considered to be an

interference technique and thus, not comparable with the traditional direct methods. Consequently, referring to techniques as homodyne should be approached with caution, although homodyne will be used henceforth to describe direct SHG measurements in an attempt to conform to the majority of modern literature.

Figure 36 schematically represents a generic experimental set up for homodyne SHG and SFG.[206,225–229] As the intensity of the second order nonlinear light is proportional to $I(\omega_1)I(\omega_2)$ or $I^2(\omega)$ for SFG and SHG, respectively, pulsed lasers are generally used to maximise the weak second order signal, but continuous wave lasers have also been used.[206] Figure 36(b) shows that a SFG set up takes advantage of the highly directional nature of second order light generated at the surface to separate the fundamental waves from the sum frequency wave using spatial filters or beam blocks. In contrast, SHG from only one incident beam, as shown in Figure 36(b), is collinear with the fundamental beam and therefore colour filters are needed to detect only the SHG light.

A key motivation in the development of SHG was the potential to selectively study molecular species present at interfaces. As such, in its homodyne form it was used extensively to probe interfacial characteristics as well as adsorption and desorption from metal surfaces.[207–211] In 1982, Shen and co-workers first demonstrated how SHG spectroscopy could be used to study the $S_2 \leftarrow S_0$ excitation of rhodamine dye molecules in submonolayer concentrations on quartz[230]. Arguably, one of the most significant outcomes of this study was the use of the output SHG polarization dependence to infer molecular orientation at the interface.

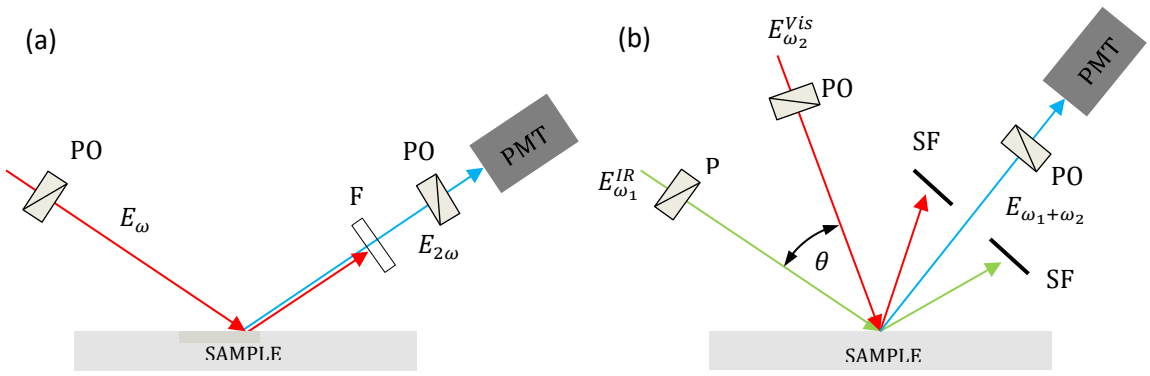

Figure 36 schematically represents typical (a) collinear and (b) nonlinear set ups in the reflection geometry off an interface where PO represents a polarizing optic, F represents a wavelength filter, SF represents a spatial filter and $\boldsymbol{\theta}$ represents the angle between the two incident beams in SFG. It should be noted that both geometries are applicable for both SHG and SFG.

The same group later moved towards studies using VSFG spectroscopy, probing a variety of interfacial systems including the first studies of air/water interfaces with organic monolayers and the utilisation of C-H stretching modes to identify adsorbates.[229,231] In the latter of these two studies, the effects of pressure and concentration on the adopted conformation of pentadecanoic acid at the interface were explored in an attempt to monitor the first order phase transition between an expanded and condensed state. The results clearly showed that the molecules adopted a bent conformation with significant disorder in the expanded phase that transitioned to a linear conformation as concentrations and pressure increased. The study also concluded that in the condensed phase the molecules exhibit a strong orientational preference to be vertical at the surface.[231]

As well as surface specificity, the ability of SHG and SFG to study liquid interfaces is extremely powerful. Indeed, before the development of the technique, pure liquid interfaces had never been reported to have been spectroscopically investigated.[226] However, by 1995 a number of notable studies had been published specifically focusing on pure liquid interfaces using VSFG to begin to address the deficit in understanding about the interfacial properties of liquids, and especially water.[219,232–235] Although these studies are of great interest and nicely explore the evolution of non-linear spectroscopy, the results of VSFG are not strictly relevant to the work herein this thesis. Consequently, key applications of narrowband homodyne VSFG may be found presented in Appendix C.1.

4.2.1.1. BROADBAND NONLINEAR SPECTROSCOPY

By the 90's VSFG as a technique had very limited application. One of the main reasons for this was the requirement for laser systems to be both suitably narrow band in the IR ($\Delta\nu \leq 5\ \mathrm{cm}^{-1}$) and sufficiently intense over the entire IR spectral range.[228] The latter was accounted for in many experimental setups by including a quartz reference from which intensity fluctuations could be normalised, much like a UV-vis spectrometer uses a blank reference. In 1996, however, van der Ham *et al.*[228] published a new experimental arrangement that used a broadband IR laser ($\Delta\nu = 50\ \mathrm{cm}^{-1}$) and a CCD camera instead of a PMT. By setting $\theta > 90°$ (see Figure 36(b)), the intrinsic angular dispersion of the non-linear light was maximised and

the CCD could record all the spectral information within the IR bandwidth at once, thus yielding a self-calibrated spectrum. However, the spectral resolution is highly dependent on the beam divergence. In 1998, with the commercial availability of femtosecond laser systems, Richter *et al.*[236] proposed a solution; by introducing a spectrograph to disperse the SFG light onto the CCD, allowing collinear incident beam geometries, and using broadband femtosecond laser pulses the resulting spectral resolution is dependent only on the input beam characteristics, in particular the visible beams bandwidth. A year later, McGuire *et al.*[227], utilising femtosecond broadband IR pulses, reported an alternative Fourier transform (FT) VSFG set up that purported to have 'virtually unlimited spectral resolution' without the need of a spectrograph or CCD.

Broadband SFG has proven to be an incredibly important development in the field of nonlinear spectroscopy for two principal reasons; firstly, the IR peak intensity of a broadband femtosecond pulse is several orders of magnitude larger than the corresponding narrowband pulses resulting in an improved nonlinear signal intensity that is proportional to the quadratic of the intensity difference between the two pulses. Secondly, the broadband technique required no moving parts unlike the narrowband technique that depends on the wavelength being scanned. This therefore drastically improved the stability of the systems and the reliability of the data collection. Furthermore, the combination of the shot-to-shot data acquisition and ultrafast time resolution afforded by femtosecond spectroscopy reveals the exciting opportunity to extend nonlinear techniques into the study of interfacial molecular dynamics, which will be discussed in detail in section 4.2.3.[237]

In conclusion, by the turn of the century, homodyne nonlinear spectroscopy had demonstrated the potential of SHG and SFG. However, the technique is fundamentally limited to measuring the magnitude of $\chi^{(2)}$, resulting in a complete loss of information held in the complex nature, and sign, of $\chi^{(2)}$. Thus today, homodyne SHG and SFG have largely been replaced by more sophisticated methods that can be used to measure phase information.[224]

4.2.2. PHASE SENSITIVE TECHNIQUES

In section 4.1.2.3, additional contributions to the surface SHG signal were discussed and it was concluded that, although these contributions could be minimised, they are ultimately indistinguishable from the nonlinear signal of interest originating from the interface. Because these nonlinear contributions are always coherent with each other, Snipe describes the nonlinear signal measured as the superposition of the different contributions with the nonlinear response at the interface.[238,239] Thus, the effective nonlinear susceptibility measured in homodyne experiments should be expressed as[240]:

$$\chi^{(2)}_{\mathrm{S,eff}} = \chi^{(2)}_{\mathrm{S}} + \chi^{(2)}_{\mathrm{B}}, \tag{43}$$

where $\chi^{(2)}_{\mathrm{S}}$ and $\chi^{(2)}_{\mathrm{B}}$ are the surface and bulk contributions respectively. As the fundamental basis of VSFG spectroscopy is to deduce a surface specific vibrational spectrum by scanning across the IR and resonantly enhancing the SFG signal at characteristic vibrational transitions, it is logical that Equation (43) can be written to express $\chi^{(2)}_{\mathrm{S,eff}}$ in terms of the nonresonant and discrete frequency dependent resonant contributions:

$$\begin{aligned}\chi^{(2)}_{\mathrm{S,eff}}(\omega_j) &= \chi^{(2)}_{\mathrm{NR}} + \chi^{(2)}_{\mathrm{R}}(\omega_j) \\ &= \chi^{(2)}_{\mathrm{NR}} + \sum_j \frac{A_{\mathrm{j}}(\omega_j)}{\omega - \omega_j + i\gamma_j},\end{aligned} \tag{44}$$

with a nonzero imaginary component of $\chi^{(2)}_{\mathrm{S,eff}}$ characterising a nearby resonance, much like $Im(\varepsilon)$ characterises linear absorption.[156,241]

$$Im\left(\chi^{(2)}_{\mathrm{S,eff}}\right) = \sum_j \frac{\gamma_{\mathrm{j}} A_{\mathrm{j}}(\omega_j)}{(\omega - \omega_j)^2 + {\gamma_j}^2}, \tag{45}$$

where $\chi^{(2)}_{\mathrm{NR}}$ is the nonresonant background, ω_j is the resonant frequency, A_j is the signal amplitude, and γ_j is the damping constant (the origin of this expression can be found in Appendix B).[242] It can therefore be seen how $\chi^{(2)}_{\mathrm{NR}}$, which is real, and

$\chi_{\mathrm{R}}^{(2)}$ which has both real and imaginary parts, can interfere, altering the nonlinear light intensity detected as $I(2\omega) \propto \left|\chi_{\mathrm{S,eff}}^{(2)}\right|^2$.

It was originally thought that the spectra of $I(2\omega)$ as a function of input frequency could be fitted to deduce the resonant and non-resonant contributions, as shown by the many different studies that analysed the VSFG spectra of water in this way.[243–246] Although the VSFG spectra were all remarkably reproduced across the studies, the analysis is different due to the selection of different discrete OH resonances used to fit the data, leading to different interpretations. Shen[242] illustrates this point, as shown in Figure 37, by showing that combinations of different $Im\left(\chi_{\mathrm{S,eff}}^{(2)}\right)$ and $Re\left(\chi_{\mathrm{S,eff}}^{(2)}\right)$ values and signs can produce similarly good fits, and thus the solutions are not unique. This situation is further exacerbated at water interfaces where the hydrogen bonded network possesses smoothly varying geometries and strength of hydrogen bonding and thus, a continuum of resonances, which would not be adequately described by discrete resonances. The only way to interpret the spectral components is to measure the complex nature and sign of the nonlinear susceptibility by measuring its phase.[242]

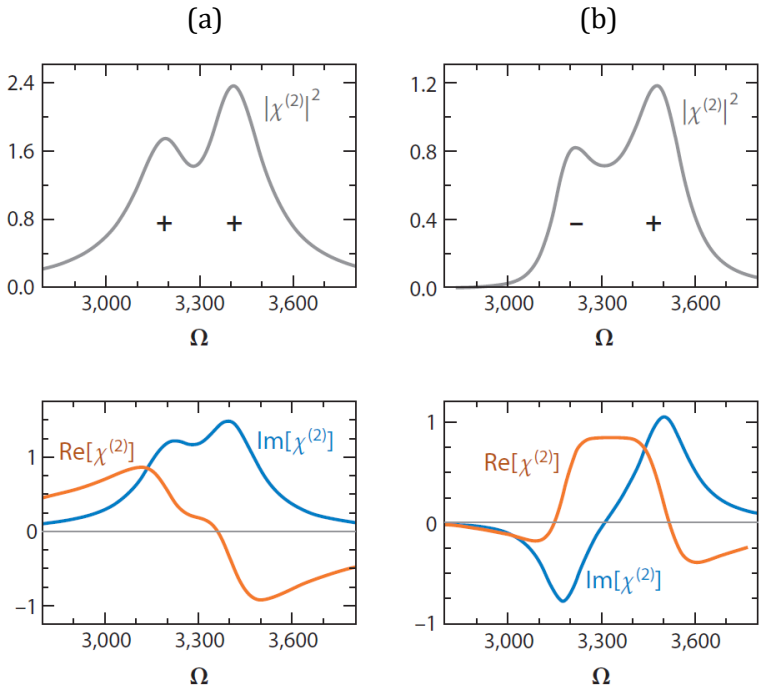

Figure 37 shows that overlapping (a) components of the same sign and (b) constituents of different signs can yield very similar spectra. Reprinted with permission from Shen (2013). Copyright (2018) Annual Reviews.

The phase of the SHG or SFG wave relative to the fundamental input beam can be measured by using an interferometric scheme of which there are two main types; Phase Delay (PD) and Heterodyne (HD). These techniques can largely be discriminated between by the domain in which the interference pattern is detected; frequency or time. Both techniques are underpinned by the same theory but will be discussed separately here for clarity.[224,242]

4.2.2.1. PHASE DELAY INTERFERENCE

Geometrically, there are two common set ups utilised for interference measurements; collinear and non-collinear, as shown in Figure 38(a) and (b), respectively. In both, nonlinear light generated at the sample of interest ($\mathbf{E}_{SHG}$) is interfered with a local oscillator field ($\mathbf{E}_{LO}$) generated at a reference sample (RS) such as GaAs or quartz, which can be positioned either before or after the sample. Between the sample and the RS there is a Phase Modulator (PM) or a Phase Shifting Unit (PSU), which acts to alter the phase of the sample SHG/SFG with respect to the LO. The majority of PD studies report experimental setups based on Figure 38(a) due to better stability.

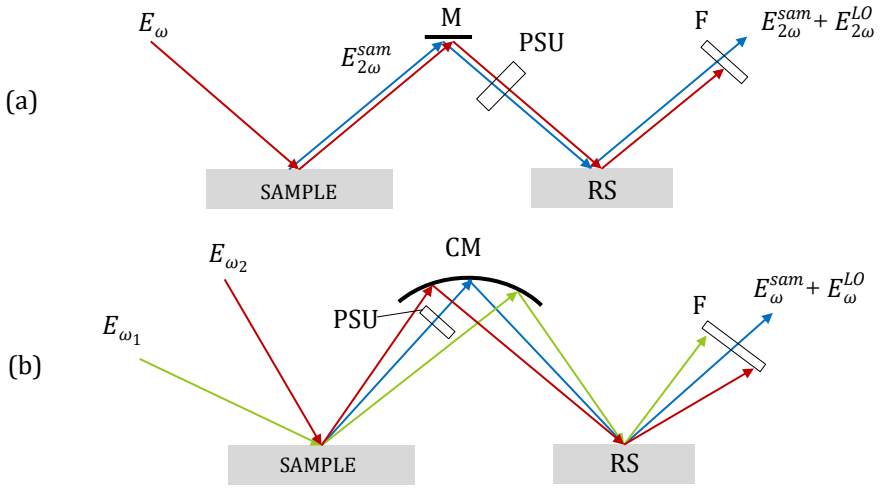

Figure 38 shows the two main experimental set ups (a) collinear and (b) non-collinear, for Phase sensitive measurements in nonlinear spectroscopy, where PSU is the Phase Separating Unit, M is a mirror, CM is a curved mirror used to refocus the divergent input beams onto the RS and F is a filter. It should be noted that both geometries are applicable for SHG and SFG. Although both (a) and (b) utilises reflection geometries, the same principles can be applied to transmission geometries or a combination of transmission and reflection form the LO and sample.

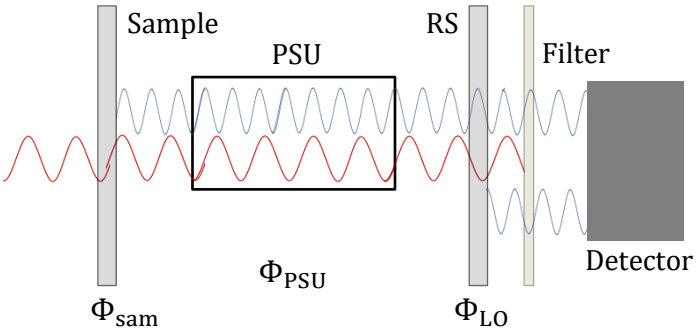

Figure 39 shows a simplified schematic for an interferometric set up with the SHG/SFG in transmission detected.

A simplified schematic of the role of the PSU is shown in Figure 39. The four most common PSU systems have been reviewed by Stolle *et al.*[247] and are summarised in Figure 40. As the nonlinear light is coherent with the fundamental, once it has been generated by the surface, the fundamental and SHG/SFG waves interfere. The waves propagate with a phase velocity, which depends on the refractive index of a medium, n, while the pulse envelope propagates with group velocity, v_g:[156]

$$v_g = \frac{c}{n - \lambda_0 \frac{dn}{d\lambda_0}}, \tag{46}$$

where λ_0 is the wavelength in vacuum. All the methods in Figure 40 work by slowing the shorter wavelength SHG/SFG wave with respect to the fundamental wave yielding a phase velocity that moves in the opposite direction to the propagation vector of the waves. Figure 40(a) uses the introduction of varying gas pressures to change the refractive index through which the beams propagates, Figure 40(b) changes the distance over which the beams propagate between the sample and RS, thus using the refractive index of the air to alter the phase. Figure 40(c) and (d) both use a combination of the methods used in (a) and (b) by introducing a material with a higher refractive index, such as glass, as well as varying the thickness of glass (i.e. the path length) through which the beams must propagate, thus increasing the dispersion. As the phase of the sample, ϕ_{sam}, and reference ϕ_{LO}, will each be constant with respect to the fundamental at the point of generation, the total phase of the superimposed nonlinear wave can be expressed as:[239]

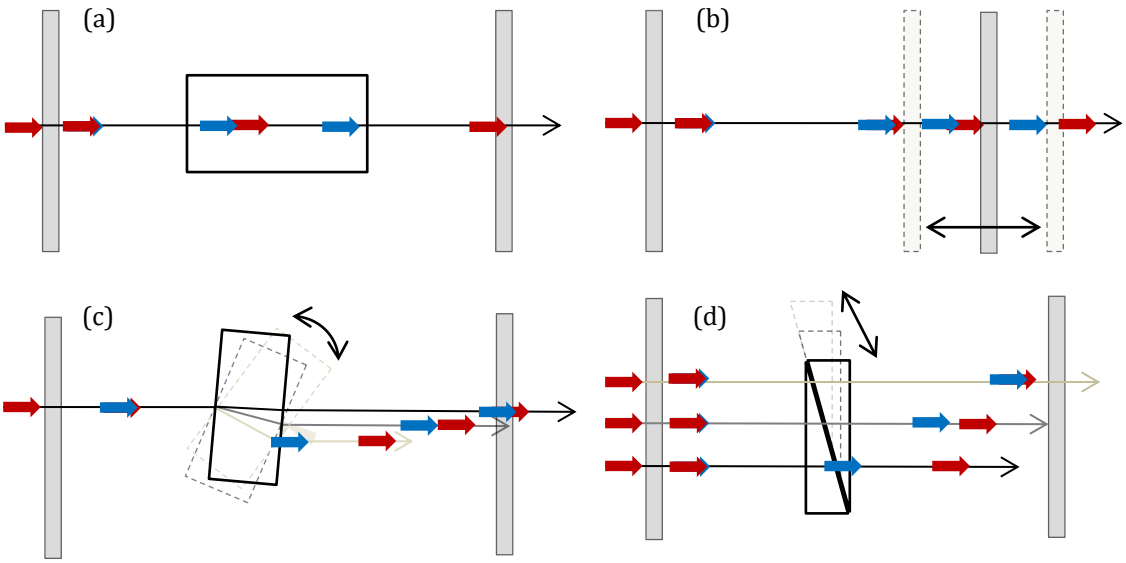

Figure 40 schematically shows the four different PSU systems used to control the phase between the sample and the local oscillator with the red and blue arrows representing the fundamental and surface SHG/SFG respectively; (a) shows a gas cell where the phase difference is altered by varying the pressure, (b) shows that changing the path length between the sample and the LO can control the phase as indicated by the arrows which show increasing dispersion with distance, (c) uses a rotation of a diffraction plate (such as glass or silica), by rotating the plate, the angle of incidence is increased relative to the normal and therefore the refraction angle increases in accordance with Snell's law, and (d) uses the same principle as (c) by varying the amount of glass to propagate through but uses glass wedges to vary the thickness, thus allowing a linear geometry.

$$\Phi = \phi_{\text{sam}} + \phi_{\text{LO}} + \phi_{\text{PSU}}\,, \tag{47}$$

where ϕ_{PSU} represents the phase shift introduced by the PSU. As shown in Equation (42), the intensity of the SHG light from a sample is proportional to $\left|\chi^{(2)}\right|^2$. It therefore follows that the total light intensity measured by the detector can be expressed as:

$$I_{\text{total}} \propto \left|\chi^{(2)}_{\text{S,eff}} + \chi^{(2)}_{\text{LO}}\right|^2 = \left|\chi^{(2)}_{\text{S,eff}}\right|^2 + \left|\chi^{(2)}_{\text{LO}}\right|^2 + 2\chi^{(2)}_{\text{S,eff}}\chi^{(2)}_{\text{LO}}\cos\Phi, \tag{48}$$

with $\chi^{(2)}_{\text{S,eff}}$ defined in Equation (44). The final term contains the phase information. In the PD technique, Φ is varied by changing ϕ_{PSU} resulting in an interference fringe pattern in the time domain. The $\cos\Phi$ term can then be deduced by plotting the interference fringe intensity against the variable of the PSU i.e. distance or rotation angle. Extraction of ϕ_{sam} is then easy if ϕ_{LO} is known and ϕ_{PSU} tends to zero. If this is not the case, substitution of the sample by a reference of known phase gives a second interference pattern, $\Phi^* = \phi_{\text{ref}} + \phi_{\text{LO}} +$

ϕ_{PSU}, where $\Phi - \Phi^* = \phi_{\mathrm{sam}} - \phi_{\mathrm{ref}}$, and thus ϕ_{sam} can be found by calibration against a usually non-resonant material.[242,247] Quartz is a popular reference choice by many groups because: (a) it is bulk non-centrosymmetric so produces a significant SHG signal, (b) it is non-resonant and therefore its $\chi^{(2)}$ is adequately approximated to be real, and (c) the sign of $\chi^{(2)}$ can be measured by piezoelectric measurements such as exerting pressure across the crystal.[248] However, when the reference is a bulk material, the phase of the bulk SHG with respect to that of an optically thin surface must be considered. For quartz, the bulk phase is advanced by $\pi/2$ with respect to the surface, and as such, if the phase of the nonlinear susceptibility of the bulk was determined to be π, the observed phase curve would indicate a surface nonlinear susceptibility of $3\pi/2$.[249] This technique can be used to measure the phase of the SHG/SFG across the spectrum by repeating the phase measurement point-by-point across all frequencies of interest.

The first implementation of the PD technique was, surprisingly, as early as 1965. Bloembergen's group determined the SHG phase of GaAs, InAs and ZnTe samples using a potassium di-hydrogen-phosphate (KDP) crystal reference and a gas cell PSU.[241] However, due to the experimental challenges facing SHG at that time, the technique received little attention. It wasn't until the 80's, when SHG began evolving as a surface specific probe for non-centrosymmetric media, that the phase sensitive interference technique was reintroduced into the literature by the works of Heinz *et al.*[250], Tom *et al.*[251]. and Kemnitz *et al.*[249] with respect to surface SHG, and Superfine *et al.*[240] for surface SFG. In the PhD thesis written by Tom (under the supervision of Shen), the conclusion was made that, when SHG is measured from a non-resonant surface, ϕ_{sam} is always 0 or π depending on the molecular orientation.[242,249,252] In conjunction with this, Berkovic *et al.*[253] discussed the change in SHG phase from a Rhodamine 110 surface, as with the input or output frequency nears a resonance, peaking at $\pi/2$ at the nonlinear absorption maxima characterised by $Im(\chi^{(2)})$, as expected.

Although technically simple, the interference technique described so far is time consuming and requires long time experimental stability which can be challenging. In response to these challenges, Ji *et al.*[254] published a scanning method that could be used to determine the phase by doing just four spectral

scans: two that measure just $\left|\chi^{(2)}_{\mathrm{S,eff}}\right|^2$ and $\left|\chi^{(2)}_{\mathrm{LO}}\right|^2$ by respectively removing the RS and sample from the set up, and another two at two different RS positions corresponding to LO phases of ϕ_{LO} and $\phi_{\mathrm{LO}} + \pi/2$. Repetition of the measurement with the sample replaced by a quartz reference thus provides all the information to measure the phase. However, the gain in experimental efficiency is at the expense of the measurements' accuracy and thus, more scans at different PSU positions will lead to an improved measurement, although the accuracy will always be poorer than when the spectral intensity is weaker i.e. at the edges of the tunable bandwidth.[242,254]

In 1994, Thiansathaporn and Superfine suggested an alternative experimental technique based on the interference geometry.[225] Instead of slowly altering the phase shift between measurements (i.e. by translation of the RS) they argued that a rapid change of the phase through periodic rotations could be used to detect the phase of $\chi^{(2)}$ in real time. To achieve this, they inserted a glass slide between the RS (which was selected for the high intensity SHG) and the sample, to act as a PSU of the type shown Figure 40(c), and rotate it to generate a phase shift between 0 and 2π using a saw-tooth wave form at a frequency of 100 Hz. The lock-in amplifier then detects the SHG interference term varying with a frequency of 100 Hz. Because $I_{\mathrm{LO}}(2\omega) > I_{\mathrm{sam}}(2\omega)$, $\chi^{(2)}_{\mathrm{LO}}$ will dominate the spectrum and therefore the technique is easily normalised to eradicate laser power fluctuations. This set up was then used to demonstrate the improved signal to noise ratio (SNR) of the interference technique compared to that of the direct homodyne technique discussed in section 4.2.2 (by removing the RS). As the SNR is independent of the LO intensity, if the LO output is significantly more intense than that of the sample, the SNR is dramatically improved as the photon count is lifted above the shot noise (such as dark current and read-out noise). However, when the sample has a relatively strong SHG signal such as that generated by metal surfaces, the increase in shot noise, counteracts the increase in photon count generated by interference and thus, the sensitivity of the measurement is not significantly improved compared to the homodyne measurements.[224,225,255]

4.2.2.2. "HETERODYNE"-DETECTED INTERFERENCE

Because PD detects wave interference, typically narrowband nanosecond or picosecond pulses are used to ensure the nonlinear light response of the sample and LO overlap in the time domain. However, as the magnitude of a second order nonlinear response scales with the incident light intensity, the advantages of femtosecond lasers became increasingly desirable to probe weak nonlinear responses. As femtosecond pulses are necessarily broadband in nature, their use in nonlinear spectroscopy allows the acquisition of an entire spectrum simultaneously, as shown by Richter *et al.* who applied this principle in a homodyne set up in 1998.[236]

Just a few months later, Veenstra *et al.*[256] combined femtosecond pulses with SHG interferometry. The set up resembled that of Figure 38(a) except that the metal sample was mounted in an ultrahigh vacuum (UHV) chamber. As a consequence, the sample SHG would necessarily have to propagate through a glass window before being detected and the LO SHG would need to pass through two windows if it was positioned before the UHV. As glass is typically used as a PSU unit in many PD set ups, it might not be immediately obvious that this resulted in a problem, but Veenstra noted that the interference term containing the phase information disappeared when femtosecond pulses were used; the glass dispersion was significant enough that the resultant SHG pulses were not temporally overlapped and consequently could not interfere.

Instead of trying to compensate for the ~1 ps time delay, the group used the broadband nature of the femtosecond pulse to their advantage. By spectrally dispersing the pulses in a spectrograph the interference pattern could be detected in the frequency domain on a CCD camera. Around the same time, Wilson *et al.*[257] published a similar technique in which a constant phase delay was used to temporally delay the SHG pulses with respect to each other. The independent work of these two groups proved to be a somewhat seminal moment in the field of nonlinear optics and in 2005 Shen's group published the first phase sensitive SFG measurement using broadband laser pulses and an internal reference.[258] This was later extended by the groups of Tahara and Benderskii into the more complicated

but more versatile technique using an external reference.[255,259] Thus, just under 20 years after the work of Wilson's and Veenstra's groups, the technique first called frequency-domain SHG has become an extremely powerful tool for studying surfaces and is referred to in recent literature as multiplex or HD spectroscopy.

Figure 41 shows the simplified multiplex scheme for HD SFG based on the interference set up shown in Figure 38(b).[242,259] Femtosecond IR pulses are overlapped on a surface with a visible pulse (typically narrowband) generating a SF nonlinear response that has a pulse width defined by the IR pulse. The SFG and incident beams are refocused by a curved mirror onto a RS (often GaAs) to produce a LO pulse. The two SFG pulses are delayed in time, *T*, with respect to each other by placing a PSU in the path of the SFG beam between the sample and the RS, resulting in a delay between the fundamental pulses and the SFG beam due to their relative group velocity dispersions. The pulses are then spectrally dispersed (illustrated by the prism) and the interference fringes of the frequency components are detected by a CCD camera as shown by the inset on Figure 41. The raw spectrum obtained at this point, before analysis, is shown for both a sample of p-nitroaniline and a quartz reference in panel (a) of Figure 42. This spectrum resembles the $|\chi^{(2)}|^2$ spectrum obtained in a direct homodyne measurement, except now the interference pattern is superimposed on top.[242,259]

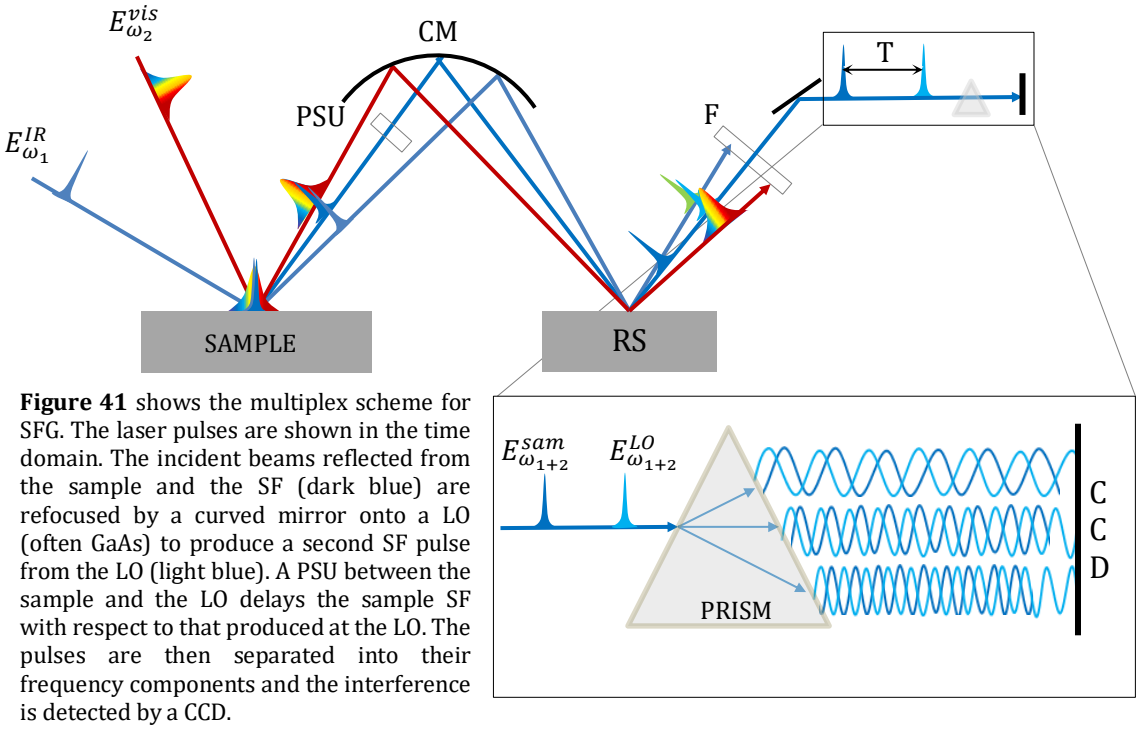

Figure 41 shows the multiplex scheme for SFG. The laser pulses are shown in the time domain. The incident beams reflected from the sample and the SF (dark blue) are refocused by a curved mirror onto a LO (often GaAs) to produce a second SF pulse from the LO (light blue). A PSU between the sample and the LO delays the sample SF with respect to that produced at the LO. The pulses are then separated into their frequency components and the interference is detected by a CCD.

If the measurement was made in the time domain (like in the PD technique) the total electric field would be measured as a sum of the two SFG fields and can therefore, in reference to Figure 41, be expressed as

$$\mathrm{E}_{\mathrm{total}}(t) = \mathrm{E}_{\mathrm{SHG}}(t-T) + \mathrm{E}_{\mathrm{LO}}(t), \tag{49}$$

where $\mathrm{E}_{\mathrm{LO}}(t)$ represents the SFG pulse generated at the RS arriving at some time t, that defines $t = 0$, and $\mathrm{E}_{\mathrm{SHG}}(t-T)$ represents the sample SHG pulse that arrives at some time T after the LO pulse. A Fourier transform of this total field into the frequency domain generates an expression for the total field in the frequency domain,

$$\mathrm{E}_{\mathrm{total}}(\omega) = \mathrm{E}_{\mathrm{SHG}}(\omega)e^{i\omega T} + \mathrm{E}_{\mathrm{LO}}(\omega). \tag{50}$$

In Equation (48) it was shown that the intensity of second order nonlinear light is directly proportional to the product of the incident light intensity. As light intensity can be related to the amplitude of the electric field by the relation[156]

$$I_{\mathrm{total}} = \frac{c\varepsilon_0}{2}|\mathrm{E}|^2, \tag{51}$$

it follows that the spectrum plotted in Figure 42(a) is of the form

$$\begin{aligned} I_{\mathrm{total}}(\omega) &\propto |\mathrm{E}_{\mathrm{total}}(\omega)|^2 \\ &= |\mathrm{E}_{\mathrm{SHG}}|^2 + |\mathrm{E}_{\mathrm{LO}}|^2 + \mathrm{E}_{\mathrm{SHG}}\mathrm{E}_{\mathrm{LO}}^{*}e^{i\omega T} + \mathrm{E}_{\mathrm{LO}}\mathrm{E}_{\mathrm{sam}}^{*}e^{-i\omega T}, \end{aligned} \tag{52}$$

where the first two terms determine the overall peak shape, and the second two terms the interference pattern that holds the phase information. An inverse Fourier transform of Equation (52) generates the interference spectrum in the time domain (of which there are three peaks), as shown in Figure 42(b). The large central peak at $t = 0$ corresponds to the first two terms of Equation (52) and the identical satellite peaks correspond to the two interference terms at $t = \pm T$. Essentially there are two peaks because $e^{+i\omega(-T)}$ and $e^{-i\omega(+T)}$ cannot be distinguished and thus it cannot be deduced by FT analysis whether the LO pulse arrives before $(+T)$ or after $(-T)$ the sample SHG.[259,260] One of the satellite peaks

can then be selectively transformed back into the frequency domain to obtain the spectrum shown in Figure 42(c). The bold lines show the real parts of the sample and quartz reference spectra whilst the dotted lines show the imaginary parts. The phase for both components can then be deduced by normalizing the sample spectrum by the quartz spectrum, thus cancelling any terms in the total nonlinear susceptibility arising from the LO.[259]

Although this technique has very short data acquisition times compared to the scanning method usually used in PD techniques, it is at the expense of the experimental phase stability and spectral resolution. As such, the broadband HD technique has been rather restricted in its application to features with broad vibrational line shapes. This explains the attention water has received from this technique, as the OH stretching bands are sufficiently broad.[261]

It is important to note, however, that SNR and phase determination are not the only advantages to phase sensitive spectroscopy. In the homodyne technique, the signal intensity scales with the square of surface coverage. Therefore, if coverage decreases by a factor of 10, the signal intensity decreases by a factor of 100 times. This makes detecting sub-monolayer species extremely difficult as acquisition time scales with the inverse of the SNR and thus experiments would have to be run for unrealistically long times. In contrast, the interference term scales linearly with

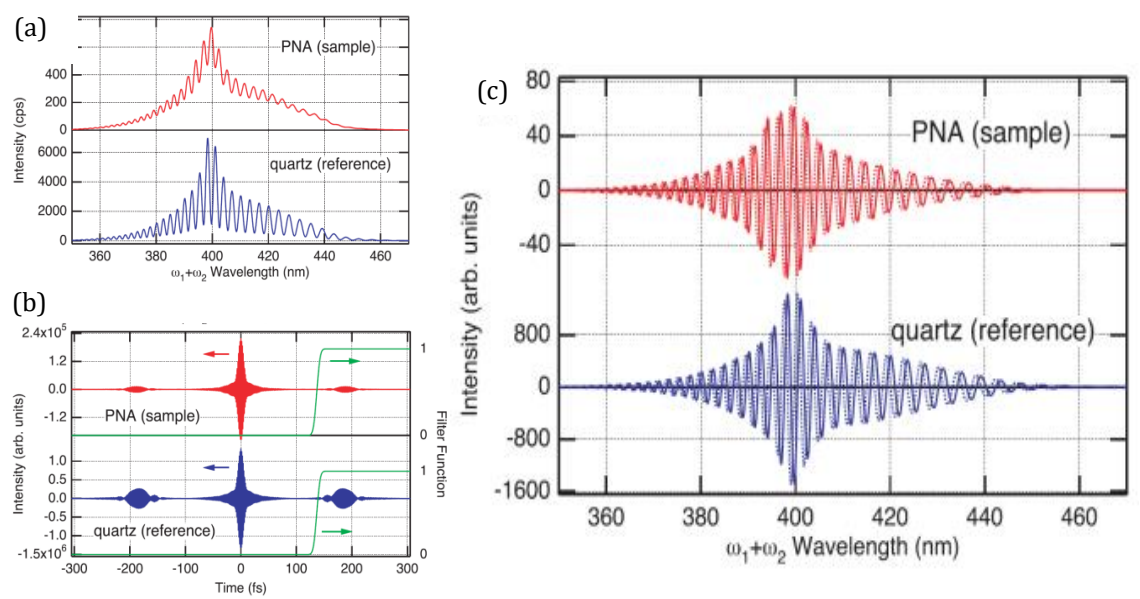

Figure 42 shows the raw HD spectrum obtained by Yamaguchi and Tahara in a study of p-nitroaniline monolayers. (a) shows the raw intensity spectra of both the quartz reference (blue) and the sample (red), (b) shows the time domain interference spectrum and (c) shows the real (bold) and imaginary components of the spectrum which can be normalised to give the imaginary and real spectra. Reprinted with permission from Yamaguchi and Tahara (2008). Copyright (2018) AIP.

surface coverage and thus sub-monolayer detection is viable. [255]

With typical resolutions of broadband HD spectra being reported between 10 and 20 cm^{-1}, the limiting factor in the pursuit of enhanced resolution has been the topic of much investigation. The SFG process can be considered to be the excitation of vibrational resonances by the IR pulse creating linear polarization which is then up-converted in a Raman two photon process by the visible pulse to generate the second order signal. The first order polarization induced by the IR pulse decays exponentially and the detected SFG signal is therefore a convolution of the visible laser pulse with the induced polarization response. Hence, it can be inferred that the visible pulse is a large factor in defining the spectral resolution.[262,263]

Stiopkin *et al.* were one of the groups that used this information to improve the spectral resolution by investigating the effect of changing the visible pulse shape and varying the time of arrival with respect to the IR pulse. By stretching a portion of the fundamental femtosecond pulse, picosecond visible pulses were generated with varying spectral widths. They observed that the broader band pulse (37 cm^{-1}) is more dependent on the delay between the two pulses with a maximum signal and minimal line broadening in the spectra observed for a nonzero delay. Positive delays (IR arrives first) were shown to give more symmetric bands than negative delays which indicates that the positive delay could also reduce the non-resonant background signal interference terms (which may decay more quickly) and enhance the signal intensity. However, in spite of the resolution being improved because of this, the spectral resolution of both pulses was similar. The determination of the optimal delay time is also very challenging and highly dependent on the resonance being probed. As such, in spite of being a remarkably elegant and sophisticated solution, the uniqueness of each delay time with respect to the resonance prevents the technique having universal application.[262]

An alternative solution to this problem appeared in the development of high resolution broadband sum frequency spectroscopy (HR-BB-SFG). In this technique, Verlarde *et al.* showed that spectral resolution was significantly enhanced if the visible pulse had a temporal width that lasted longer than the decay process. Producing such long pulses with good peak intensity is practically impossible by

the traditional method of stretching a portion of the femtosecond fundamental pulse. Thus, the group employed an entirely separate laser, synchronised to the femtosecond laser, to produce visible pulses with widths of ~90 ps and showed that, without the need for a delay, sub wavenumber spectral resolution could be obtained.[263]

A very recent study by Wang's group combined the HR-BB-SFG technique with that of the internal heterodyne phase resolution technique, IHPR, first pioneered by Shen[258], which they called HR-BB-SFG IHPR. In this novel technique, the sample is in physical contact with the quartz reference and is therefore limited to samples that can be deposited on quartz. The measured signal detects the sample SFG signal with interference from the bulk and surface quartz signals which are known to be shifted by $\pi/2$ relative one another. By rotating the quartz around the normal axis, the intensity of the quartz signal, and thus the interference term, is modulated by a function of the rotation angle, ϕ (by either $\cos 3\phi$ or $\sin 3\phi$, depending on the polarization combinations used). Thus a phase cycle is expected within a 60° rotation and the phase of the sample can be extracted by Fourier transform analysis. Using this technique, Fu *et al.*[264] remarkably report SFG spectra with 0.6 cm^{-1} resolution. However, it is worth noting that the adsorption process would reduce the dynamic nature of the same adsorbates on a liquid surface, thus spectral broadening would be expected for liquid interfaces in comparison. IHPR has the obvious advantage that, by eliminating the distance between the RS and the sample, phase fluctuations are also eliminated which are a source of stability issues in the external HD set up. As such, the results demonstrate excellent potential for studying quartz bound samples.

We now turn to the controversy in the literature regarding the name 'heterodyne'. The word heterodyne has its origins in the radio world whereby a signal wave was mixed with a generated LO frequency wave to frequency shift the signal and create interference patterns or 'beats' between the two signals.[265,266] In the technique described here, the interference occurs between two waves of the same frequency (the second order nonlinear response frequency) and therefore no frequency shift occurs and the technique is not traditionally heterodyning in nature. In fact, the technique is more accurately described as a homodyne method as scientific

convention denotes the homo- prefix as being indicative of 'the same' i.e. the same frequency in this instance.[267] However homodyne has already been stated to refer to direct methods in which there is no interference at all, and Tahara argues that HD spectroscopy has previously been used to describe a multitude of other ultrafast techniques such as HD-Raman and 2D-IR, resulting in the name correctly following modern convention.[261] Thus the extent of the confusion within the modern literature is now clearly evident. Even if a new protocol was established for nonlinear optics, in which the definitions of hetero- and homodyne were realigned with the modern conventions, this does not explain the forced distinction between the HD and PD techniques. As the only obvious difference between the two is the domain in which the nonlinear light is collected, it is suggested that the terms heterodyne and homodyne be avoided, and instead the three techniques be referred to as direct spectroscopy and phase sensitive spectroscopy. [224,242,259,260]

Before discussion turns to the applications of these phase sensitive techniques, it is worthwhile discussing the advantages and disadvantages of the two with respect to one another. The first, and most obvious advantage of heterodyne detection is the elimination of the need for any moving parts with the entire spectra recorded at one position by integrating over a number of shots in a relatively short period of time. In contrast, the PD technique requires the delay to be scanned, via a moving component, to build up the spectra point by point, making for a very time consuming measurement. PD also usually requires a lot of material to be propagated through in the PSU which results in GVD issues when short pulses are utilised. However the PD method is less challenging experimentally than the heterodyne technique, with excellent phase stability due to the collinearity of the beams. The long term phase stability of the heterodyne technique is poor due to its extreme sensitivity to mechanical changes (such as mirror temperatures) and the liquid level height. Heterodyne detection also has the added complication of a non-linear geometry which makes obtaining similar path lengths in the two beams challenging experimentally. In conclusion, both techniques have associated issues, but the PD technique is often selected due to its comparatively easier set up. However, the shot-by-shot measurement has obvious consistency advantages.

4.2.2.3. APPLICATIONS

The first experimental study, that reported the absolute phase of a SHG surface nonlinear susceptibility, was published in 1986 by Kemnitz *et al.*[249] who investigated the interface of a phenol solution. By using the PD technique, the sign of each individual tensor element was determined. Once individual tensor elements had been found, known values of the hyperpolarizability, $\beta_{\xi\xi\xi}$, could be used to determine the ratio $\chi^{(2)}_{\mathrm{S,eff}}/\beta_{\xi\xi\xi}$. From the results it can be interpreted that a positive ratio indicates that the dipole mainly points out of the surface. For phenol it was found that the ratio was negative and as such the dipole (defined as a vector from negative charge to positive charge and therefore from the phenyl to the hydroxyl) is pointing away from the surface with the hydroxyl orientated into the liquid.[249] However the published study is full of contradictory conclusions and it is therefore difficult to assert confidence in the interpretations. In 1989 Huang and Lewis published a PD SHG study on the dipole moment of a retinal chromophore bound and unbound to a membrane on excitation. They used an experimental set up of the form shown in Figure 40(c). The extension of the technique developed by Kemnitz and colleagues to real biological systems was exciting, revealing the technique as an interdisciplinary tool.

Phase sensitive interference techniques have been used to study a plethora of different interfacial systems. However, phase sensitive VSFG is extensively favoured over that of SHG, in part due to its ability to resolve molecular orientation. Although interesting, the technique presented in this work is specific only to SHG, and therefore a detailed discussion of phase sensitive SFG studies would not be applicable. Nonetheless, phase sensitive VSFG studies relating to the relevant air/water interface do provide a level of context to the work in this thesis and are therefore presented in Appendix C.2..

4.2.3. TIME-RESOLVED SPECTROSCOPY

Until now, the techniques discussed have been time averaged views of interfacial systems – revealing a snapshot of an orientational equilibrium state – with the analysis assuming a static orientational picture. However, 10 years ago, Xing and

Shen published a new analytical technique which concluded that motional effects can considerably impact the vibrational spectrum such that neglecting the effect has significant consequences on the interpretation of the spectra. This study highlighted the value of obtaining a better understanding of molecular dynamics at the surface in order to correctly analyse results that are not time resolved.[268] The advent of broadband nonlinear techniques made pump-probe spectroscopy an exciting possibility to resolve ultrafast dynamics of physically important interfacial processes, such as adsorption, desorption, bond breaking, and structure deformation.[206,236]

TR spectroscopy uses a short pump pulse that induces a change in either the surface itself or any adsorbates present, such as electronic or vibrational excitation, desorption, or bond cleavage, which is then probed by nonlinear spectroscopy. By altering the delay between the pump and the probe pulse (or pulses in SFG), the transient species or structural changes can be monitored in real time by detecting the time dependent change in $\chi^{(2)}$ spectra.[269] Each $\chi^{(2)}$ element can thus be written as:

$$\chi^{(2)}_{ijk}(t) = \chi^{(2)}_{ijk_{\mathrm{g}}}(t) + \chi^{(2)}_{ijk_{\mathrm{e}}}(t), \tag{53}$$

where the subscripts g and e denote the ground and pump induced excited states, respectively.[270] Experimentally, pump-probe SHG/SFG can be based on heterodyne setups (schematically represented in Figure 36) or phase-sensitive setups (shown in Figure 38 and Figure 41). At negative delays, the probe pulse arrives before the pump and any SHG signal is due to the ground state. At positive delays, the pump arrives first, inducing some physical change in the system and the probe pulse thus monitors the recovery of the ground state of interest.[269]

The pioneering studies of TR-SHG at liquid interfaces utilised picosecond pulses to probe the rotational dynamics and relaxation of dye molecules using the $S_1 \leftarrow S_0$ transition.[271,272] In these studies, a change the rotational relaxation time of the molecules at the surface compared to the same relaxation processes in the bulk was observed. Eosin B (EB) showed a significant decrease in rotational diffusion time from 350 ps in the bulk to 90 ps at the interface. This difference was

attributed to weaker solvating hydrogen bonds at the water surface, with water preferentially hydrogen bonding with itself due to the truncation of the network and surface energy minimisation considerations. This was therefore considered to result in less solvent friction on rotation as the hydrogen bonds are weaker and more easily broken than in the bulk.[272] In contrast, an earlier study by Castro *et al.*[271] showed that, at the air/water interface, Rhodamine 6G (Rh6G) rotational diffusion time is increased to 1 ns from 200 ps in the bulk, with the excited and ground state molecules having different preferential orientations at the interface. This result therefore suggests that rotational friction for Rh6G is larger at the interface suggesting slower motion and stronger hydrogen bonds compared to the bulk.[271] The conflicting results of these two studies suggests that Rh6G possesses an average orientation that fits well with the interfacial hydrogen bond network, resulting in strong intermolecular bonds, whereas EB's average orientation destabilises the hydrogen bonded network and therefore the water molecules preferentially orientate with other interfacial molecules over the dye.[270] In both cases however, the dynamics are markedly different at the interface.

For these studies, picosecond pulses were suitable due to the long relaxation times observed. However, for faster processes and interfacial systems with smaller and arguably more relevant molecules, femtosecond pulses are required.[273] Zimdars *et al.*[270] published a similar study to that on Rh6G, probing coumarin 314 (C314) at the air water interface using femtosecond pulses. Interestingly, very similar behaviour at the interface was observed for C314 as was observed for Rh6G, indicating that frictional forces at the surface are different from the bulk material. The group were also able to resolve, for the first time, the orientational relaxation in the plane of the interface as well as the relaxation out of the plane. Significantly, the published results were able to accurately resolve the interfacial dynamics of different time scale processes, such as; population recovery (<5 ns), orientational relaxation (1-2 ps) and excited state solvation (<1 ps), the latter of which is only resolvable using femtosecond pulses.[270]

In order to fully understand frictional dynamics at interfaces, processes are required in which the kinetics is dominated by solute-solvent interactions or frictional effects. This is the case for barrierless reactions such as the

photoisomerisation of malachite green (MG^+) and was the focus of the study by Shi *et al.*[274]. Previous studies on MG^+ in the bulk concluded that solvent polarity has little effect on its excited state dynamics and, therefore, it was hypothesised that the potential energy surfaces are likely to be similar in the bulk and at the interface. With reference to Figure 43, the mechanism of photoisomerisation in the first excited state involves torsional motion in the bonds between the central carbon and aromatic moieties before internal conversion relaxes MG^+ back to its ground state. As the reaction has no effective activation energy, the decay of the excited state is directly related to the molecule's ability to overcome the frictional forces exerted on the phenyl ring, thus it follows that increasing solvent viscosity results in slower decay timescales.[274]

By using femtosecond pulses Shi *et al.* studied MG^+ at a variety of interfaces using TR-SHG. Using a series of polarisation combinations, it was deduced that the polarisation was independent of the delay between the pump and the pulse, and therefore the ultrafast dynamic changes observed can be attributed to photoisomerisation without contributions of rotational motion. The study ultimately concluded that, at a variety of aqueous interfaces, the ultrafast decay process was always faster than that observed in the bulk. Surprisingly, however, the study reported very similar decays for two alkane/water interfaces where the alkanes had a factor of six difference in their viscosities. This appeared inconsistent with the theory that all three bonds twisted in sync with each other.

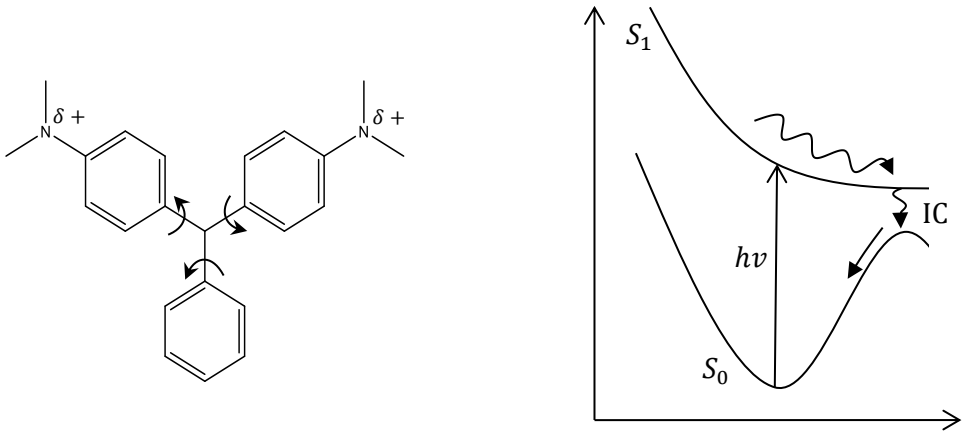

Figure 43 (a) shows the structure of malachite green with the arrows indicating the axis around which photoionization occurs, (b) shows the excitation from the ground state into the excited state which processes along the reaction coordinate resulting in rotation around the carbon-benzene bond, until internal conversion causes the $\boldsymbol{S_0 \leftarrow S_1}$ transition and the molecules returns to its ground state potential. Figure adapted from Shi *et al.,* 1996.

The group proposed a new theory – the orientation of MG^+ was similar at aqueous interfaces but it is only the dimethylaniline moieties (solvated by water) that contribute to the kinetics. However, the alkane/water interfaces compared to the air/water interface have slower decays. At first it might seem that these results contradict each other, however, by considering the conclusions of Eisenthal and Zimdars, this can be physically justified in the following way: if the phenyl group experiences increased solvation in the nonpolar alkane, the result is that the group projects further across the interface into the bulk liquid. As a consequence this pulls the dimethylaniline moieties closer towards the top water interfacial layer. The partial charge of the dimethylaniline moieties causes the water to orient, forming strong hydrogen bonds that stabilise the interface. As the groups get closer to the interface, a larger portion of the partially hydrogen bonded water molecules are re-orientated, resulting in a net increase in hydrogen bonds at the interface and thus stronger resistance to the torsional motion.[270,271,274]

The first TR-VSFG studies on liquid water interfaces were published by McGuire and Shen in 2006. By utilising spectral hole burning of specific IR frequencies by the pump, the hole recovery could be monitored with time by VSFG. The results showed that the dynamics of hydrogen bonded molecules at the interface resemble the dynamics of the bulk remarkably well, whereas the dangling OH exhibited much slower recovery dynamics. This led to the bold conclusion by Shen that structure is ultimately irrelevant on ultrafast timescales, and instead it is the hydrogen bonding that dictates dynamics.[275]

With the important information TR studies afford, it is unsurprising that many groups have been applying pump-probe methods to interferometric experiments for both SFG and SHG, thus combining the combining the enhanced SNR with the ability to record the evolution of the imaginary spectra in time.[276] TR-PS-VSFG was first reported on a prototypical charged aqueous interface (air/cetyltrimethylammonium bromide) by Nihonyanagi *et al.*[277]. Figure 44 shows the change in the imaginary components spectra, $\Delta\mathrm{Im}(\chi^{(2)})$, with time. The spectra show the growth and decay of several peaks over 5 ps, with positive values indicating bleaching of the ground states imaginary signal, and negative values representing the growth of a new imaginary signal i.e. a transient resonant species

appears with time. Arguably, the most significant observation from these spectra is the similarity in spectral shape from 0.2 ps, with the time evolution mainly showing a blue shift. This, combined with the complete signal bleach at 0 ps (indicating that the pump energy spread over the entire OH band) led Tahara's group to the interpretation that the much debated double peaked structure cannot be attributed to two different structural environments, as it would be hypothesised that the more ordered environment would take longer to re-establish. As such, this result to adds gravitas to their previous interpretation that the double peak structure (discussed in Appendix C.1.) can only arise due to an intramolecular coupling or Fermi resonance.[277] The only real limitation of this technique is that a charged system was intentionally chosen that was well known for its large $\chi^{(2)}$ value to maximise signal intensities as TR studies typically generate weaker signals than their static counterparts. This therefore suggests that the technique may not be applicable to all substrates, though TR nonlinear studies are in their infancy compared to the steady state techniques, and therefore there has not yet been time to probe the wealth of interfacial surfaces of interest.

As a concluding remark, it is important to stress the interdisciplinary worth of TR studies. This is encapsulated in a very recent study that used alkane/water interfaces to model biological systems.[278] The study uses the interface to elucidate

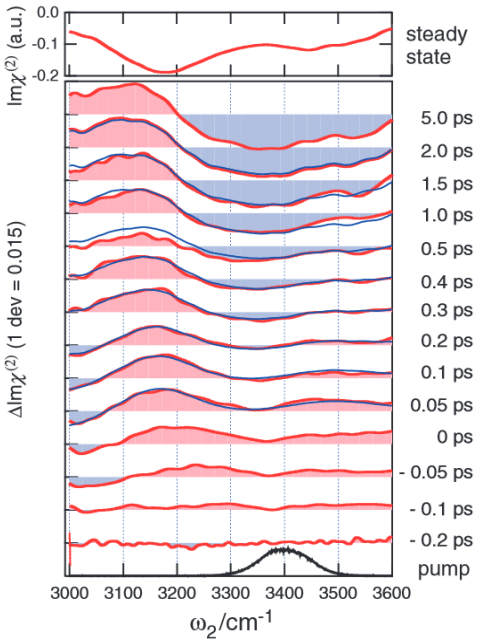

Figure 44 shows the results of the TR-PS-VSFG study. The spectra shown are the $\mathbf{\Delta Im}(\boldsymbol{\chi}^{(2)})$ intensity as a function of wavelength. The red shaded peaks indicate spectral bleaching and the blue shaded peaks indicate resonant transient species. Reprinted with permission from Nihonyanagi *et al.* BCSJ, 85, 2012. Copyright (2018) CSJ.

the potential of several cyanine fluorescent dyes as DNA probes. In order for a dye to be a potential probe, it is important that it be both water soluble and have a high affinity for the non-polar environment of the DNA (i.e. the alkane) as well as remaining fluorescent at the target site. Cyanine dyes are not fluorescent when they aggregate, but in order to be a good probe relatively high concentrations will be needed. This is the power of surface specific studies as it can reveal high concentrations at which aggregation is observed in the bulk but not at the interface. By studying a family of cyanine dyes that mainly differ in substituent chains and charge, fluorescent quenching aggregation behaviour at the interface could be characterised. Thus the comprehensive study not only published surface specific molecular orientation results, but was also able to characterise the excited state decay attributable to fluorescence, of which longer decays are desirable. Although the specific results of this study are not within the scope of this review, the application of the technique to gain insight into biological systems shows the potential of TR spectroscopy and its informative power when combined with surface specific SHG and SFG.

4.2.4. NON-LINEAR SPECTROSCOPY AND THE HYDRATED ELECTRON

The surface specificity of second order nonlinear spectroscopy makes it an ideal technique to interrogate the structure and dynamics of the hydrated electrons at interfaces, the characteristics of which are highly debated, as discussed in section 1.2.3.

In 2010 our group published its first time resolved study on the interfacial hydrated electron with TR-SHG. The first generation of this experiment was homodyne in nature and probed the CTTS from iodide with and without the presence of surfactants that alter the surface environment to which an interfacial electron is extremely sensitive. Two different surfactants were studied; decanol which has a small polar group in the form of OH moieties that do not penetrate the water hydrogen bonding network and therefore induce no observable change in the interfacial electron signal; and $C_{12}E_{6,}$ which has highly polar groups formed from six ethylene glycol units that permeate 1-2 nm into the interface. The high

degree of penetration of $C_{12}E_6$ alters the inversion symmetry to such an extent that the interfacial signal is significantly quenched and the electron's solvation dynamics are more representative of bulk environments.[279] However, the homodyne nature of this technique resulted in very limited information being elucidated from the results without phase information.

Recently, Tahara published a study on the hydrated electron utilising TR-HD-SFG.[280] The decay dynamics of the interfacial hydrated electron at the air/water interface in this study is highly consistent with those of MD simulations, with full solvation into the bulk environment within 100 ps. The results indicate a partial solvation with a significant extension of the electron distribution protruding into the air. This supports the notion that cluster structures could be more representative of the reduced solvent concentration at an interface than originally considered, and the surface bound state may be more distinctive than previous studies have elucidated.[280] However, Tahara's TR-HD-SFG experiment measures the vibrational spectrum of the water OH bonds and therefore the hydrated electron indirectly through interaction with the water molecules. Furthermore, the previous discussion has highlighted that HD techniques are experimentally very challenging. A TR-PD technique in contrast is experimentally easier and when combined with SHG allows direct measurement of the nonlinear response of the hydrated electron at low concentrations.

Thus, a second generation of our SHG experiment with a significantly more sophisticated phase delay design was developed. Using this experimental set up, the solvation dynamics of the CTTS were further interrogated and it was revealed that whilst the initial ultrafast solvation dynamics of all polarisation combinations were different (occurring on timescales less than 700 fs) the final state is representative of a bulk state in all instances with a dissociation lifetime of the $[I^-_0:e^-]$ contact pair of 54 ps. As the analogous lifetime in the bulk phase has been reported to be 70 ps, it is possible that the reduction in solvent density at the interface facilitates more rapid nuclear reorganisation towards a solvated state. This suggests a picture of the hydrated electron which is fully solvated close to the interface with very little extension into the vapour phase.[172] Although this is contradictory to the results of Tahara, this picture is in full support of a recent

theoretical simulation by Uhlig *et al.* who present a picture of the hydrated electron being imbedded into the surface with only ~10 % of the electron charge density extending into the vapour phase.[281] Although this experiment is a vast improvement to the first generation homodyne SHG experiment, there are still multiple aspects in which the experiment is limited.

The remainder of this chapter will therefore first present the details of the second generation TR-PD-SHG experiment of our group and its limitations (section 4.3.1.1) before presenting a new and improved PD design that has been implemented to address these issues.

4.3. EXPERIMENTAL

4.3.1. INTERFERENCE SET UP

4.3.1.1. OLD SPINNING OPTICS SET UP

Full details of the previous set up can be found in Dr Paweł Nowakowski's thesis/instrument paper[282,283]. The required wavelengths for the pump (250 nm) and probe (800 nm and 1320 nm) were generated from part of the output of a commercial Ti:Sapphire chirped pulse amplifier, with the rest of the output dedicated to a different experiment. Wavelength tunability was achieved through an optical parametric amplifier (TOPAS Prime, Light Conversion) and nonlinear frequency conversion. The output from the OPA is then directed onto a separate SHG optical table, the set-up of which is schematically represented in Figure 45. Both the pump and probe enter the table at the same point and are separated by a beam splitter (BS1). The reflected beam 500 nm beam is directed onto a motorised translation stage and then frequency doubled to give the 250 nm pump beam, whilst the 1320 or 800 nm probe beam is transmitted and passes through a continuously variable metallic neutral density (ND) filter before being focused onto the sample. Due to the dependence of the SHG signal intensity on $sec^2\theta_{\mathrm{in}}$, the

shallowest possible angle of incidence is required which is experimentally ~70° with both beams in a collinear geometry to simplify symmetry considerations.

$\mathbf{E}_{SHG}$ generated at the sample surface propagates collinearly with the fundamental probe beam and is directed through a hole of the spinning chopper (CH) before being focused again onto the RS where the $\mathbf{E}_{LO}$ field is generated. In this set up the reference is a (110)-cut gallium arsenide (GaAs) sample as it provides a strong SHG signal on reflectance, the intensity of which can be controlled by rotating the GaAs.

$\mathbf{E}_{LO}$ and $\mathbf{E}_{SHG}$ propagate collinearly resulting in interference. As detailed in section 4.2.2, interference measurements require a PSU of which there are four main types (as discussed by Stolle *et al.*[247]). The old experimental set up uses a PSU of the type shown in Figure 40(b) in which the position of the RS is manually changed using a translation stage that varies the propagation path length between the sample and the reference. The detected interference signal can therefore be expressed as

$$I_{\text{total}} = |\mathrm{E}_{\mathrm{SHG}}|^2 + |\mathrm{E}_{\mathrm{LO}}|^2 + 2f(L)|\mathrm{E}_{\mathrm{SHG}}||\mathrm{E}_{\mathrm{LO}}|\cos\left(\Phi + \frac{2\pi\omega\Delta n}{c}L\right), \tag{54}$$

where Φ represents the phase difference between the sample SHG and LO waves, ω is the angular frequency of the SHG light, and L represents the distance between the sample and the reference.

If L is small, then the pulses remain temporally overlapped with only a small amount of dispersion due to the propagation in air accounted for by the function $f(L)$. However, if L is large enough for dispersion to separate the pulses in time (i.e. the beams propagate through a window of glass), then the interference term in Equation (54) disappears and only the terms quadratic in the SHG signal from both the sample and reference remain:

$$I = |\mathrm{E}_{\mathrm{SHG}}|^2 + |\mathrm{E}_{\mathrm{LO}}|^2. \tag{55}$$

By subtracting Equation (55) from (54), the interference term can be isolated. A 'lock-in' measurement was employing in order to obtain the linear term. This is achieved by a chopper between the sample and the GaAs.

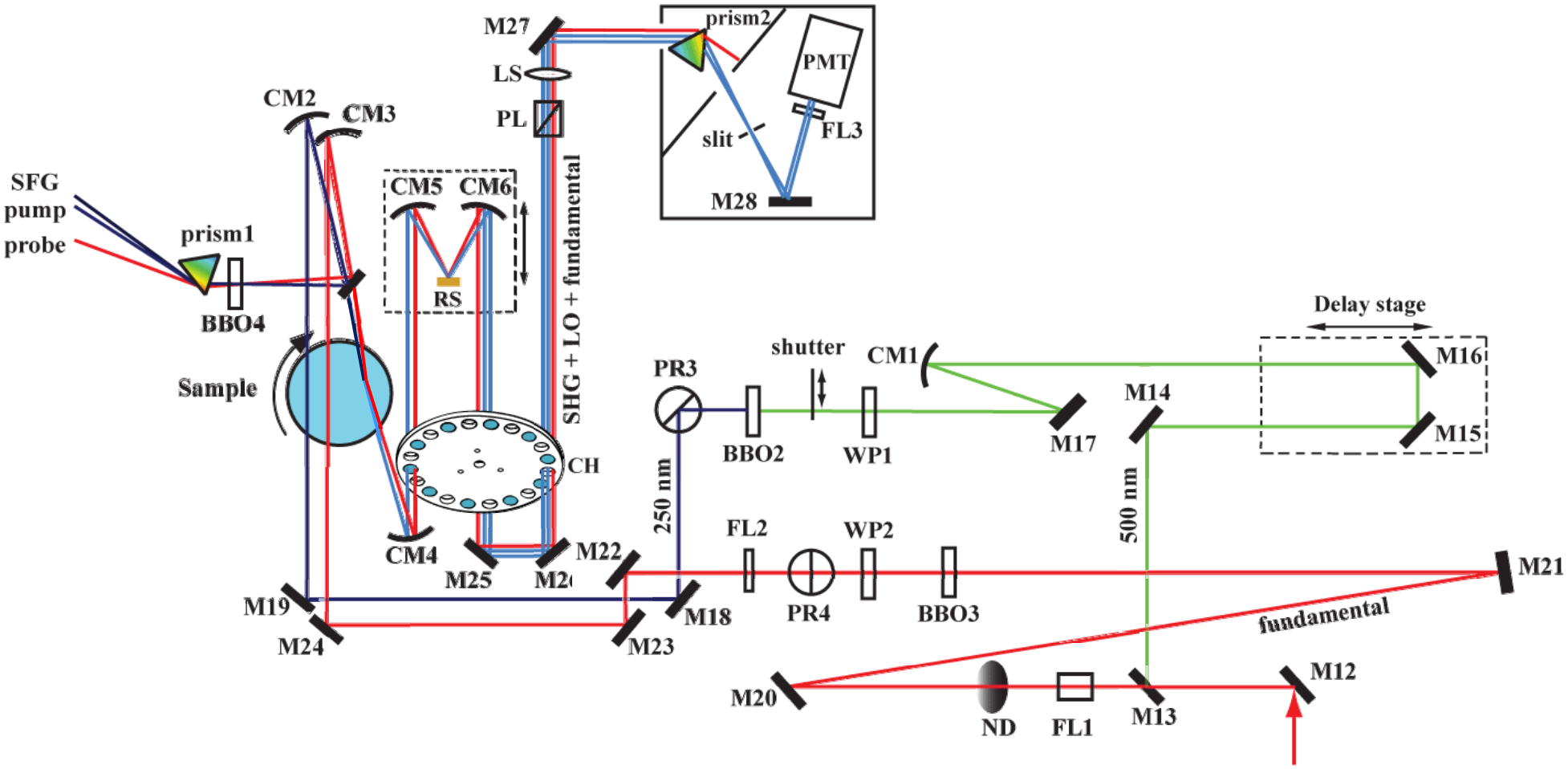

Figure 45 shows a schematic drawing of the previous pump-probe experimental set up. Figure amalgamated from figures 3, 5, and 7 in Chapter 3 of Dr Nowakowski's PhD thesis.

A schematic of the custom made chopper wheel is shown in Figure 46 and consists of 20 holes around the outer edge, with every alternate hole containing a 2 mm window made of SF10 and CaF_2 for 1320 nm and 800 nm probes, respectively.

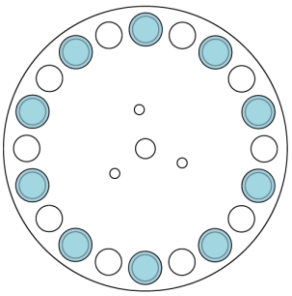

Figure 46 shows a schematic of the spinning chopper used to perform lock-in measurements.

A simple scheme of the lock-in measurement is shown Figure 47. To perform the lock-in, two separate measurements are required, the first in which the fundamental and sample SHG signal propagate through an empty hole site in the chopper (yielding Equation (54)) and a second in which the fundamental and sample SHG beams propagate through a window such that the large GVD means that there is no interference (yielding Equation (55)). This can be done on a shot-by shot basis at 950 Hz using the chopper locked to the laser repetition rate.

When the beams propagate through the glass windows there are losses due to reflections from the window surfaces. Thus, comparison of the signal intensities is not valid unless this offset is considered. Therefore, to account for this, the beams are aligned in such a way that they always propagate through one window either before or after the RS. For example, the signal expressed in Equation (54) propagates through a hole before the reference and therefore must propagate through a glass window after leaving the stage. Consequently both measurements account for approximately the same amount for the transmission and reflection Fresnel factors of the glass windows.

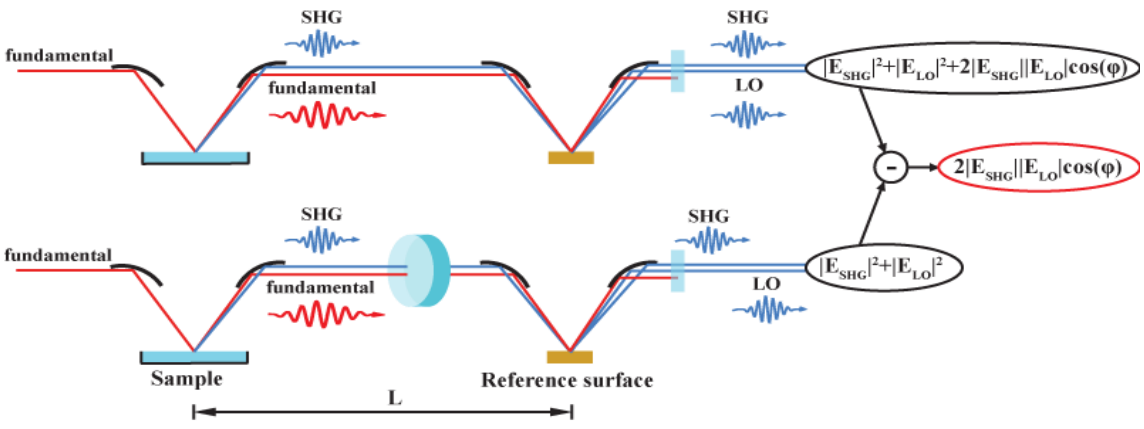

Figure 47 schematically represents the lock in measurement that measures the interference signal. Reprinted with permission from Nowakowski *et al., J Chem Phys,* **142**, 084201, 2015. Copyright (2018) AIP.

After the beams have propagated through the interference set up, they are directed through a polarizer which selects the required output polarization combination. The beams then pass through a focusing lens into the detection blackout box. The fundamental is separated from the LO and SHG frequencies using a dispersive prism and is then blocked by a physical beam block. The LO and SHG then pass through a filter and into a photomultiplier tube (PMT) where the SHG signal's magnitude is recorded. By changing the position of the RS, the interference pattern for each time point can be constructed.

Although this technique has been successfully used to study the hydrated electron at the air/water interface there were many challenges associated with the setup.[172] The tight focus onto the GaAS RS, required to maximise the SH response at the surface, also results in burning of the surface. As such, rotation of the GaAS is required regularly, but this alters the magnitude of the SH nonlinear response at the RS, as well as the alignment due to the surface not being perfectly flat. As such any rotation would change the magnitude phase of the interference terms and data collected after a RS rotation would need to be recalibrated to be compared to previous experiments. The stability of the technique is also compromised by the difficult and unstable alignment through the chopper, twice and off the RS on a manual translation stage. It is this instability that prevents the RS being placed before the sample surface, as the pump-probe overlap could not endure slight alterations in the alignment arising from movement of the manual stage. However, as shown in Dr Nowakowski's thesis, the reflectivity of the fundamental changes with respect to the arrival of the pump. With the RS after the surface, this change in reflectivity will alter the amount of LO generated, which would need to be corrected for in post-processing. Furthermore, the reflection off the RS confuses the polarizations, making clean polarization assignments difficult. Finally, the main limitation of the experiment is the time consuming nature of the measurement. To achieve the phase measurement, the phase has to be manually changed between a time resolved scan – the whole process of which takes several hours, resulting in long-term instabilities. Because of these limitations, we designed and implemented a new experimental method that mitigates some of the challenges and utilises the benefits of the new Carbide laser system.

4.3.1.2. NEW WEDGE SET UP

The new interference set up introduces a phase varying unit (PVU) which is ostensibly based on the PSU system described by Stolle *et al.*[247] shown in Figure 40(d) whereby a pair of glass wedges is placed between the RS and the sample

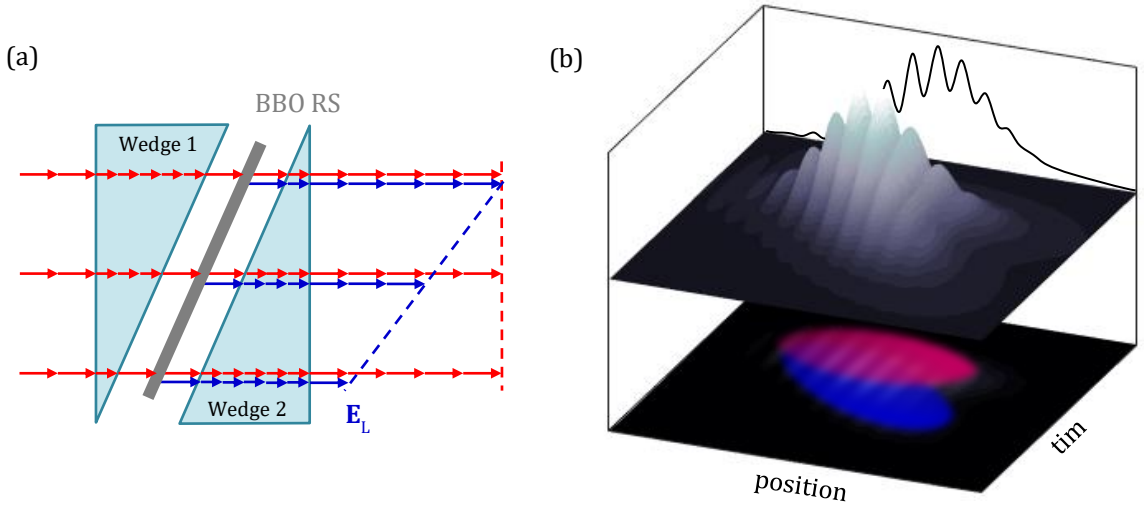

Figure 48. (a) A schematic that represents the phase varying system used to generate a LO with a change in delay agross the beams spatial profile. The arrows represent the position at varying times, with the dashed lines representing the pulse front of the LO and the fundamental. (b) A cartoon where the SHG (pink) and LO (blue) fields are shown as a function of position and time. The interference pattern is superimposed across the beam's spatial profile. This is then projected (black line) onto a CCD sensor.

causing a phase delay between the LO and the SHG waves. By moving one of the wedges, the thickness of glass through which the LO and SHG propagates can be changed, and therefore the phase delay altered. The experimental interference design presented in this thesis modifies this set up by positioning the RS between the two wedges, instead of on the other side.

Figure 48(a) shows an exaggerated and simplified schematic of the underpinning principle of this technique. The red and blue arrows shown represent the fundamental and LO frequencies respectively, with the lengths of the arrows depicting the propagation evolution of one/two wavelengths for the fundamental/LO at characteristic time points. The three sets of arrows are used to represent three different spatial positions along the width of the beam. Each set contains the same number of arrows which depicts resulting propagation position across the same time frame. For simplicity, the slower propagation of the LO due to

the refractive index dependence on wavelength is ignored and the horizontal offset between fundamental and LO beams is purely for clarity.

The fundamental beam, of significant spatial width, propagates into the first wedge and the effective wavelength is reduced compared to outside the wedge due to the larger refractive index as indicated by the reduction in arrow size. The beam propagates through the glass wedge until the edge of the wedge is reached. Due to the width of the beam, the fundamental beam is transmitted through the glass/air interface at different instances in time, thus instigating a change in phase delay across the fundamental beam front. The fundamental beam then propagates through the RS, generating the LO with the same phase delay gradient as the fundamental.

The second wedge acts to counteract the phase delay in the fundamental by ensuring that, on output from the wedge pair, the beam at all points will have propagated through the same amount of glass, and therefore slowed to an identical extent. This is represented in Figure 48(a) by the red dashed line that shows the flat beam front after leaving the wedge set up. It is important that the fundamental has no temporal delay gradient so that the SHG at the sample surface is generated at the same instance in time across the spatial profile of the beam.

In contrast, the LO only passes through the second wedge, meaning different spatial parts of the beam propagate through different amounts of material. Consequently, on leaving the PVU, the LO has a temporal phase gradient with respect to the fundamental beam, and the latter generated sample SHG. The cartoon in Figure 48(b) shows the SHG and LO fields as a function of both position and time with the interference pattern superimposed along the beam profile. The entire interference fringe pattern can therefore be imaged on a position sensitive detector (CCD) with no moving components, as shown by the projected signal. In this manner, the need to scan the phase as per the previous experimental design is eliminated.

In principle this PVU can be placed before or after the sample, however, due to the requirement for the beam to be focused at the sample but expanded at the RS (and

the limitations due to varying reflectivity from a liquid sample as discussed in the previous section), experimentally it is easier to place the PVU before the sample.

REFERENCE SAMPLE

Deciding on a material for the RS required two main considerations: phase matching and resultant LO intensity. The majority of SHG light is produced perpendicular to the fundamental beam polarization and as such, the difference in refractive index in the perpendicular and parallel axes of the crystal must be sufficiently large to allow phase matching for the fundamental and frequency doubled LO. If the difference is small, then the fundamental will continuously generate LO light whilst it propagates through the crystal that is not in phase with the already generated LO light, resulting in destructive interference. In theory there is only one wavelength at which this works perfectly, however, by cutting the crystal at known angles, a large range of wavelengths can be accessed. This is important as the OPA allows the study of systems with a range of wavelengths. Imperfections in phase matching can also be mitigated by reducing the thickness of the crystal; reducing the amount of material through which the beams propagate and the development of the phase delay. As femtosecond pulses are used in this experiment, the bandwidth is necessarily large, so a thin crystal is needed.

The intensity of the LO generated with respect to the sample SHG signal is also important, as a significantly more intense LO will overpower the fringes. As the beam profile is not well characterised and reflections off the surface mean the beam can shift slightly, and thus visible fringes over the course of a measurement are significantly advantageous in ensuring there are no drifts in the interference fringes – as such a well matched LO intensity is needed. A crystal with 5 × or 10 × the SHG signal intensity is desirable. Tuning the LO intensity can be achieved by changing the thickness of the crystal, or choosing a less efficient nonlinear optical crystal. With these factors in mind a 10 μm thick BBO crystal (θ = 25°, ϕ = 90°) supported on a 2 mm thick fused silica substrate (EKSMA Optics) is utilised. Note that the substrate should face the incoming beam to not contribute to the GVD.

WEDGES

As both fundamental and SH frequencies propagate through the second wedge in the pair, it is vital that the two pulses remain temporally overlapped on output otherwise the sample SHG will not interfere with the LO to give the interference pattern. Thus, the thickness of material at which the two femtosecond pulses temporally miss one another, X, needs to be large enough that it corresponds to a useable length of wedge, L. X can be calculated from the wavelength dependent refractive indices[284], $n(\omega)$.

$$v_g(\omega) = \frac{c}{n(\omega) - \lambda_0 \frac{dn}{d\lambda}}, \qquad (56)$$

$$X = \frac{dt}{\frac{1}{v_g(2\omega)} - \frac{1}{v_g(\omega)}}, \qquad (57)$$

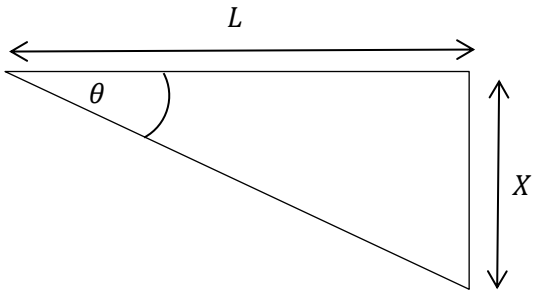

Figure 49 shows the relationship between the amount of material, ***X***, resulting in a temporal mismatch, and the corresponding length of wedge, ***L***, that would be able to produce interference fringes across the beam.

where dt is the temporal width of the femtosecond pulses and v_g is the frequency dependent group velocity. As X and L are related by trigonometry (as shown in Figure 49),

$$L = \frac{X}{\tan(\theta)}, \qquad (58)$$

where θ represents the wedge angle. L needs to be at least as large as the beam diameter in order to ensure that interference fringes occur across the entire beam front. If X is too small, θ will need to be small to compensate. Small wedge angles are available from around $\theta > 3^{\circ}$, but as θ decreases the thickness at the pointed edge increases as it is impossible to have the wedge terminating at a point due to the fragility. Very small wedges therefore tend to be truncated by a flat edge rather than a point (typically of 200 μm thickness). Although the technique works without a pointed wedge end, the amplitude of the interference is at is greatest when the temporal overlap is maximised, i.e. when going through the least amount of material. Having large fringes is advantageous during a pump probe

measurement because it is the change in the fringe amplitude that constitutes the signal, therefore the bigger the contrast in the interference pattern, the more easily the signal will be resolved. Consequently, values of X are required such that commercially available wedge angles can be accessed with a point as thin as possible.

As well as maintaining temporal overlap between the fundamental and the LO, the material must also generate enough interference fringes across the beam that the frequency can be well characterised against the signal noise in a Fourier transform, whilst also not exceeding the camera's resolution. The number of interference fringes across a wedge can be calculated from the difference in the spatial frequencies between the fundamental and LO per mm of wedge, Δk,

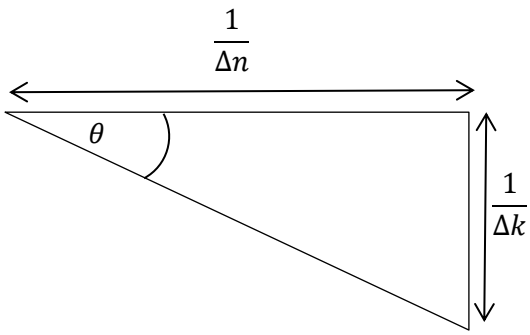

Figure 50 shows the relationship between the differences in the spatial frequencies per unit distance across, vs the difference in the spatial frequencies per unit distance of thickness between two different propagating frequencies.

$$\Delta k = \frac{n(2\omega)}{\lambda(2\omega)} - \frac{2n(\omega)}{\lambda(\omega)}, \tag{59}$$

where $1/\Delta k$ represents the extra thickness of material the beams would need to propagate through to shift a fringe phase by 2π. Using trigonometry Δk can be related to the difference in spatial frequencies per unit thickness of the wedge, Δn, as shown in Figure 50, by

$$\Delta n = \Delta k \tan(\theta), \tag{60}$$

where Δn is the number of interference fringes per mm of wedge across (i.e. L) and $1/\Delta n$ represents the distance a wedge would need to be translated perpendicularly to the direction of beam propagation in order to shift a fringe phase by 2π. The tangential dependence on θ shows that the number of interference fringes will increase as the wedge angle is increased. This is desirable as the more fringes there are, the more easily the frequency will be detected above the signal noise.

Therefore a feasible material will have wedge angle that compromises between maximising Δn whilst still maintaining a value of L that exceeds the beam diameter.

With these considerations in mind, several materials were tested for their suitability including SF10, SF11, CaF_2, N-BK7 and fused Silica. Figure 51 shows the calculated values of X between the fundamental and SHG 250 fs pulse pairs across all wavelengths of interest output by the OPA. SF10 and SF11 however have such small values of X that θ values are unfeasibly small across the entire range. Compared to SF10 and SF11, CaF_2, fused Silica and BK7 have much larger values of X and are therefore more viable as wedge materials. The positive correlation between X and fundamental wavelength in all materials means θ would need to be smallest at the shortest wavelengths.

Before entering the sample, the fundamental beam measures 9 mm in diameter. As the intensity of the second harmonic is proportional to the square of the intensity of the fundamental, the beam size of the second harmonic will be a factor of $\sqrt{2}$ smaller than the fundamental.[285] Therefore a 9 mm fundamental beam diameter corresponds to a SHG beam diameter of approximately 6.5 mm. Setting this as the absolute minimum value of L, and using the value of X for the 620 nm system, the maximum values of θ, θ_{max}, that generates interference fringes across the entire

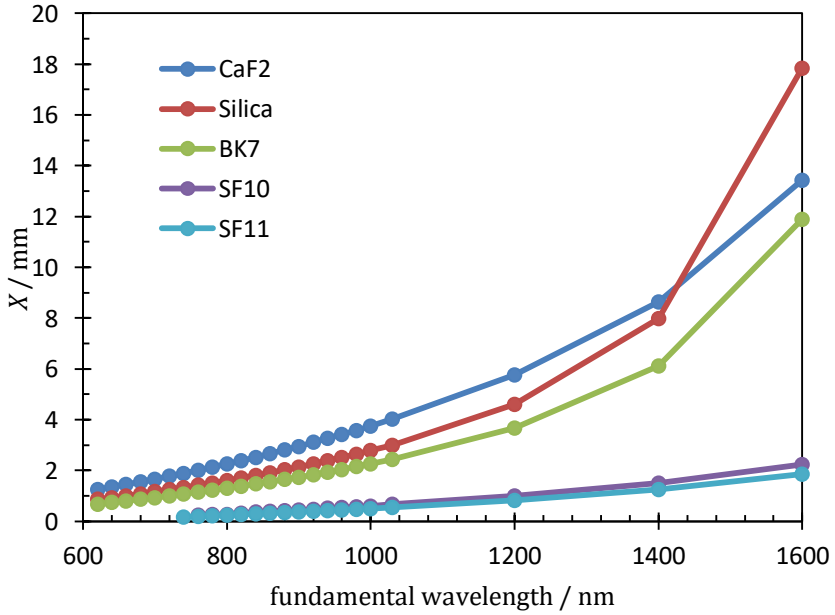

Figure 51 shows the relationship between the wavelength of the fundamental and the amount of material, X, needed to separate it temporally from its second harmonic assuming pulse widths of 250 fs.

beam front, and across all wavelengths of interest, can be calculated. The values of θ_{max} for CaF_2. Fused Silica, and N-BK7 are given in Table 3.

Table 3 shows the calculated maximum wedge angle required to generate interference fringes across the entire beam front at all wavelengths of interest.

Material	Value of *X* for 620 system / mm	Corresponding θ_{max} / °
CaF_2	1.25	10.9
Fused Silica	0.86	7.6
N-BK7	0.68	6.0

Thus these three materials yield values of θ_{max} that are large enough to be commercially viable whilst maintaining temporal overlap of the pulses, although 6° for N-BK7 is very close to the boundary of acceptability. θ values bigger than θ_{max} could be used but this would then increase the fundamental wavelength at which the wedges could start to be used whilst maintaining temporal overlap. The values of Δn were then calculated for these materials across the range of fundamental wavelengths in order to ensure that enough fringes are present per mm of wedge across. Figure 52 shows the results of these calculations when θ = 1°.

The Nyquist Theorem states that a resolvable unit needs a minimum of two pixels to be characterised. As such, one fringe oscillation must occur over a minimum of 4

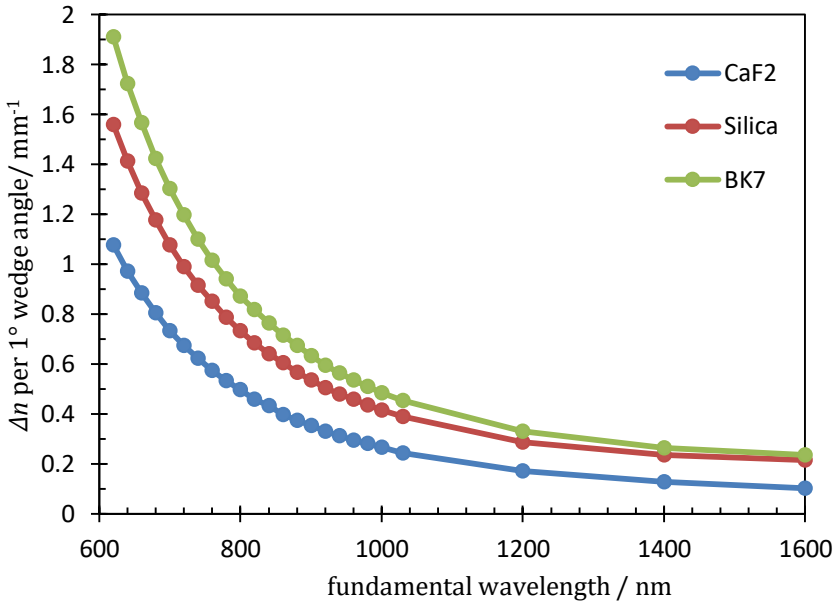

Figure 52 shows the relationship between Δn per 1° wedge angle and the fundamental wavelength of the system of interest.

fringes (2 pixels peak and trough).[286] As the pixel size on the camera is 13.5 µm x 13.5 µm, this yields a resolution limit of 18.5 fringes per mm of beam. At θ_{max}, all three materials would produce a Δn below this limit and are therefore suitable.

Taking into account Figure 51 and Figure 52, CaF_2 is considered to provide the best compromise across all wavelengths between maximising θ and therefore Δn, whilst minimising the thickness at the pointed end to give the optimised temporal overlap. As such two 10° CaF_2 wedges (Crystran) with a pointed end <0.2 mm were purchased, which have a calculated Δn of 5.03 fringes per mm of wedge length at 800 nm. Experimental validation of this value is shown in section 4.3.6.

4.3.2. SHG SAMPLE

Both the SHG and Reflectance experiments study the dynamics at the air/liquid interface. The liquid sample is held in a glass dish which is rotated in order to supply a constantly refreshed sample surface. Slight changes in the liquid height (because of evaporation, for example) alter the laser intensity at the surface, the spatial overlap of the pump and probe and therefore the pump-probe signal intensity of both the reflectance and the SHG signal. To minimise the height variation's effect on the signal intensity, a liquid height monitor (LHM) was designed that uses a feedback loop to refill the dish when the height changes by a significant amount resulting in height stabilisation.

The basic premise of the LHM is shown in Figure 53; a laser pointer is reflected off of the sample surface and directed onto a quadrant photodiode that measures the difference between the top and bottom vertical halves and outputs a voltage

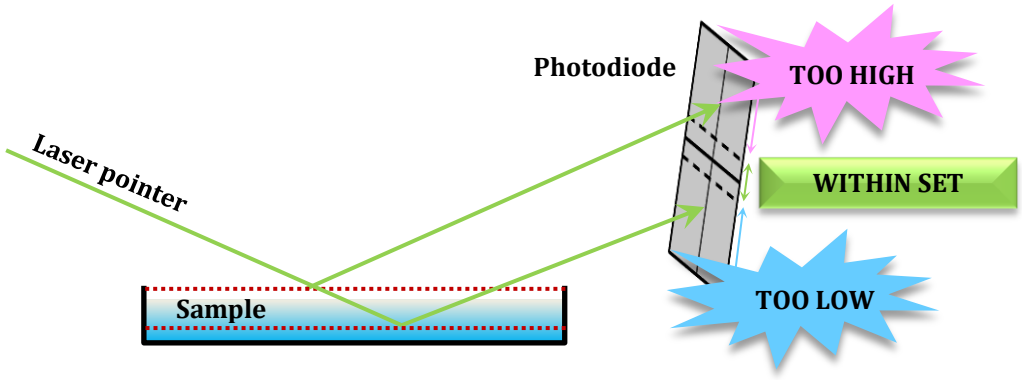

Figure 53; shows the basic premise of the liquid height monitor using a quadrant photodiode and laser pointer.

between −5 V and +5 V, with an output of 0 V corresponding to a vertical central alignment of the laser on the photodiode. A programmable interface controller (PIC) converts this voltage output into a RS232 signal that communicates with a programmable syringe pump, filling the reservoir in an automated feedback loop. Only the key results are presented here with a full discussion of the LHM program, including the motivation for its development and parameter optimisation can be found in Appendix A.

Figure 54 shows the LHM signal position as a function of time for several different data sets (encompassing a range of different liquid infusion rates and time averaging combinations). To demonstrate the effectiveness of the liquid monitor data taken with the liquid monitor inactive (grey) has also been plotted against each data set to show that over the same period of time the level height does not exhibit the same decrease in position (corresponding to a reduction in liquid height). Although this plot only shows the monitor working over 14 minutes, it can clearly be seen that evaporation has a marked effect in that time and considering each measurement in the previous experiment took ~30 minutes, this evaporation is not negligible over the time scale of the experiment.

Statistical analysis of the data shows no trend between the standard deviation of the data sets and the infusion rate or averaging constant; although for almost all infusion rates averaging the signal over 2 s yields the largest variation in height. By

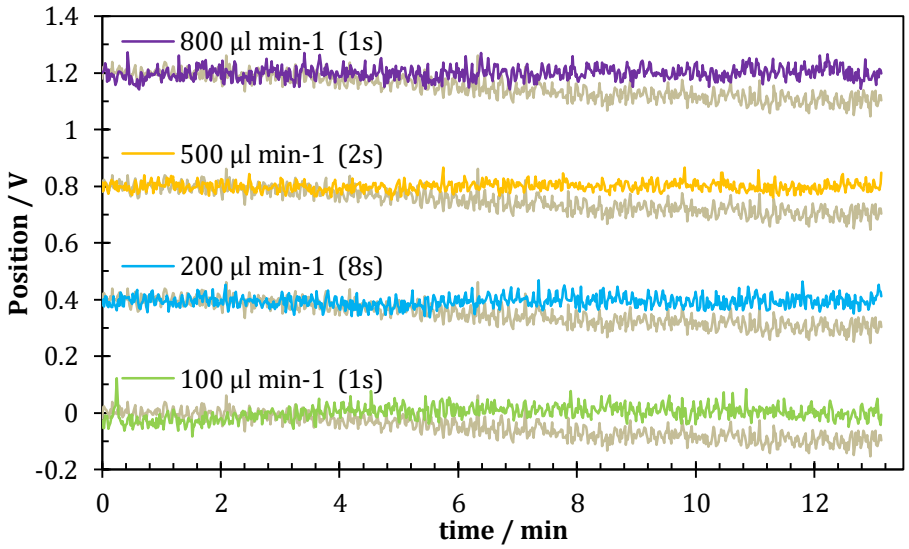

Figure 54 plots the photodiode output with a variety of program parameters. The grey lines show the change in voltage when the program is deactivated. All data sets are offset by multiples of 0.4V.

correlating position on the photodiode to height (as shown in Appendix A) the liquid height can be calculated to be stable down to ±13.5 µm on average across all parameter combinations, and ±12.9 when the 2 s data set is removed. As the camera used in the SHG experiment has a pixel size of 13.5 µm × 13.5 µm, this corresponds to long term maintenance of the detected signal to within 2 rows of pixels.

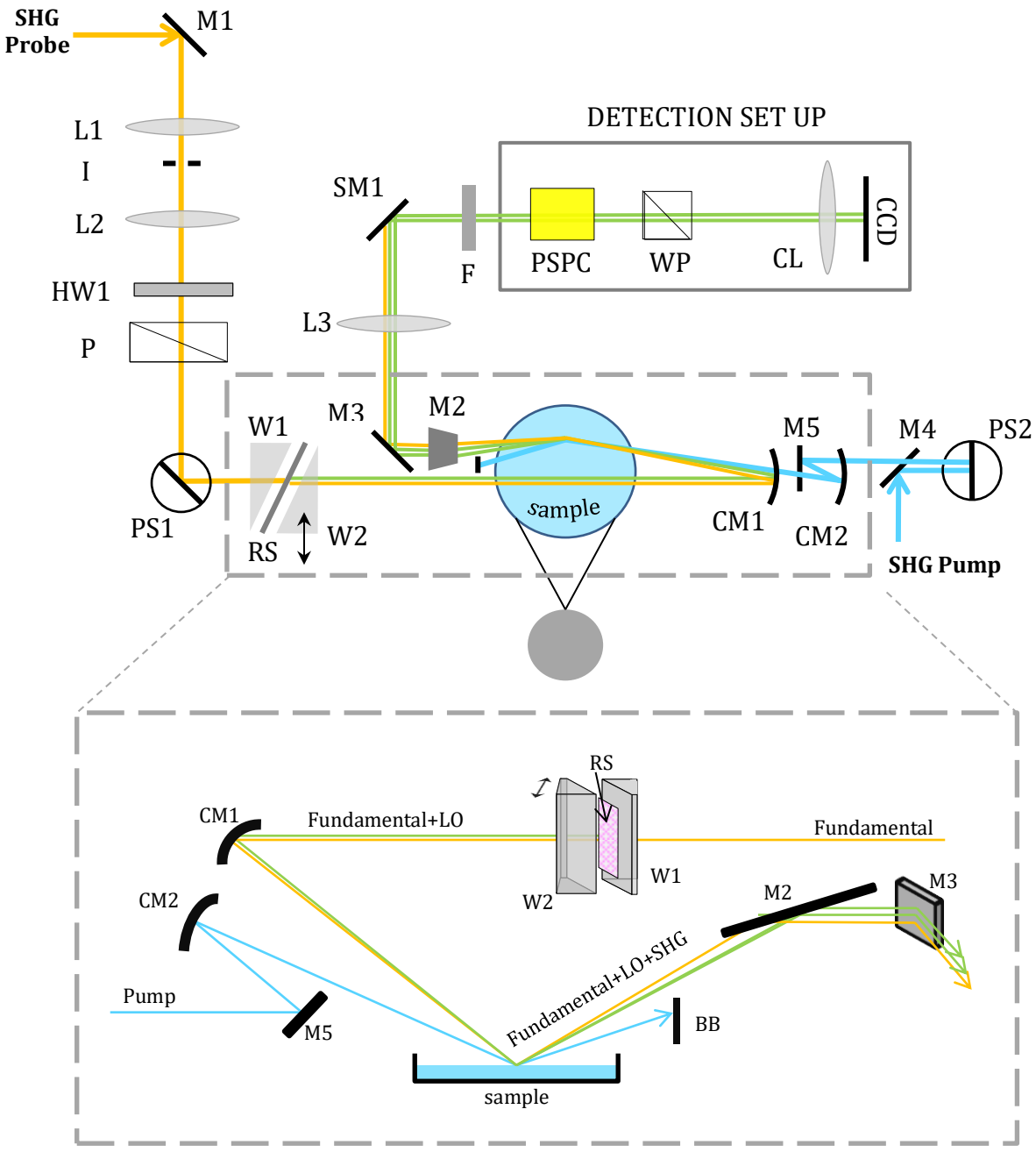

Figure 55 shows a schematic representation of the pump-probe experimental set up of the SHG experiment where L = lens, PS = periscope, P = polariser, M = cold mirror, F = filter, HW = half waveplate, W = wedge, RS = reference sample, CM = curved mirror, SM = selective mirror, CL = cylindrical lens, PSPC = polarisation switching pockels cell, I = iris and WP = wollaston prism. The orange and green beam paths represent the fundamental and second harmonic (SH) frequencies. The boxed insert shows the out of plane part of the experiment as a side on representation. The origin of the pump and probe inputs before M1 and M4 respectively are shown in Figure 10.

4.3.3. PUMP-PROBE

Figure 55 shows the SHG pump-probe experimental set up as viewed from above the optical table, and from a side-on perspective in the boxed insert. The pump (light blue) and probe (orange) inputs are a continuation from the paths shown in Figure 10.

4.3.3.1. PUMP SET UP

Figure 10 and section 2.1.2, shows the generation of the pump beam and the path into the SH experimental set up. The beam is then directed onto a periscope (PS2) by a cold mirror (M4) which raises the beam height before M5 directs the beam out of the plane onto a curved mirror (CM2, f=200 mm) which focuses the pump beam onto the surface. After the surface the beam is blocked by a physical beam block (BB). It should be noted that the horizontal offset shown from M4 to PS2, PS2 to M5, and then M5 to CM2 is just for clarity with the beam propagating collinearly in the same horizontal plane in reality.

4.3.3.2. PROBE SET UP

As described in section 2.1.1 the SHG probe is generated via an OPA. Due to the collinear nature of the amplification processes, the signal and idler wavelengths both exit the OPA housing from the same place, in the same direction but with perpendicular polarizations. To separate the signal from the idler, wavelength separators (provided by Light Conversion), are used alongside a wavelength selective filter. As the OPA output is divergent the beam is collimated by propagation through a telescope, L1 (f = 50 mm) and L2 (f = 300), that expands the beam diameter by 6 times. At the focus of L1, an iris is used to spatially filter and clean the OPA output. The polarisation of the beam is changed using a half wave plate (HW) and polariser (P) before entering a periscope (PS1). The raised beam is directed through the wedge pair PVU where the LO is generated in transmission through the BBO RS (the green beam). The BBO crystal is located in a rotation mount that allows fine modulation of the LO signal intensity. The collinear LO and fundamental then propagates through the second wedge (W2) and is focused onto

the sample by a curved mirror (CM1, f=200 mm) to overlap with the pump spot. W2 is located on a 1 inch translation stage to allow fine control of the interference fringes.

At the surface the sample SH is generated in the reflection geometry. As with the pump line, the horizontal offset shown in Figure 55 is just for clarity, with the beam paths from PS1 to CM1, and then CM1 to the surface to M2 all propagating collinearly in the same horizontal place. Due to the dependence of the SHG signal intensity on $sec^2\theta_{\text{in}}$, as shown in Equation (42), an angle of incidence as close to 90° to the surface normal as possible is required for maximal SH response. However, the shallower the angle, the larger the focus appears at the surface, thus reducing the signal intensity. As such, the best compromise was found to be an angle of incidence close to 70° with both the pump and probe beams impinging on the interface in a geometry whereby both beams are in the same plane normal to the surface to simplify symmetry considerations.

After the surface, the collinearly propagating fundamental, LO and sample SHG are redirected into the horizontal plane by M2, and then directed through a collimating lens L3 by M3. Both M2 and M3 are used to only change the direction of propagation in one axis each to ensure polarisation preservation. A selective mirror (SM1) paired with a filter (F2) selectively removes the fundamental before the interfering LO and sample SHG propagate into the detection setup which will be described in detail in section 4.3.4.

4.3.3.3. FINDING TEMPORAL AND SPATIAL OVERLAP

As described in section 2.1.2, the pump set up includes a motorised delay stage that is used to change the temporal delay between the pump and probe pulses. For a pump-probe time-resolved experiment, the position on the delay stage that results in both the pump and probe pulses arriving at the stage at the same instance in time is denoted as t_0, with positive time being any position on the stage at which the pump arrives after the probe and thus the excited state dynamics are being detected.

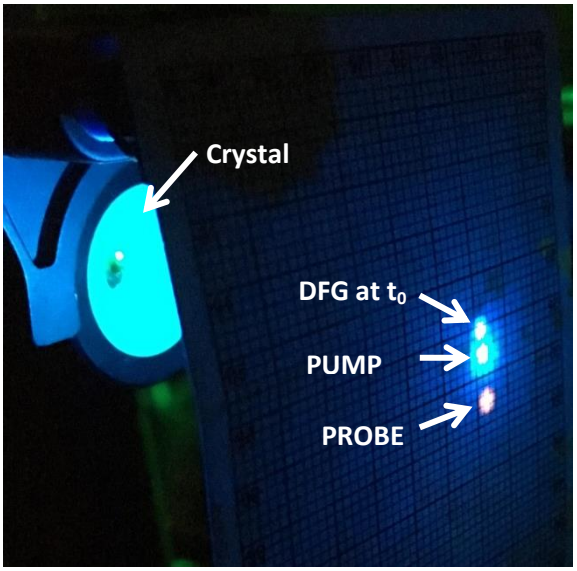

Figure 56 is a photograph of the transmission output from the crystal used to find t_0. When there is temporal and spatial overlap the DFG spot appears as shown.

As all time is relative to t_0, it is important to find this position on the stage. To do this, the sample dish is replaced with a BBO crystal at the approximate position at which the spatial overlap occurs at the surface. Difference frequency generation processes within the crystal will only occur when the pulses are both temporally and spatially overlapped in the crystal. By scanning through the translation stage this DFG signal at t_0 can be observed by eye on output from the crystal with the DFG spot appearing above the two fundamental and pump spots, as shown in Figure 56. Spatial overlap is found by substituting the liquid water sample with a more viscous liquid sample, such as glycol. Using the LHM, the height of the liquid can be perfectly matched to that of the sample.

4.3.4. DETECTION SET UP

As described in section 2.1.2, a rubidium titanyl phosphate (RTP) crystal Pockels cell is used to chop the pump beam at 30 kHz, thus allowing a shot-to-shot time-resolved measurement. However, the probe path to the detection setup is identical irrespective of whether the sample has been pumped or not. The detection setup shown in Figure 55 therefore has two functions: it differentiates and separates the 'pump on' interference signal from the 'pump off' background using a polarisation switching pockels cell (PSPC) and a Wollaston Prism (WP); and then focuses the SH and LO to a line across which the interference fringes are superimposed using a

cylindrical lens (CL). The result is the generation of two lines on the Newton 940 CCD sensor (Andor).

The functionality of the PSPC is identical to that of the RTP cell used to chop the pump beam; the polarisation of the input beam is switched to its orthogonal counterpart on application of an electric field across the crystal which is triggered by the laser. ATP was used as the crystal instead of RTP due to RTP absorbing wavelengths bellow 400 nm and thus the wavelength range of interest. As the PSPC and RTP cell are triggered by the same digital output from the laser, one polarisation will correspond to the 'pump on' and the other to 'pump off'. These orthogonal polarisations can then be separated by a Wollaston Prism (WPM10, ThorLabs) with a deviation angle of 1° 20' between the two polarisation beam paths. When combined with CL, the result is two lines focused onto the CCD sensor with interference fringes running horizontally across them that before t_0 should be identical in both phase and amplitude. Once an image has been collected, the 2048 x 512 image array is sent via a USB connection to the computer.

4.3.5. EXPERIMENTAL CONTROL

The timings and parameters of the experimental hardware, such as the camera and translation stage, are interfaced through a program written in the National Instruments LabVIEW 2011 software package. Figure 57 schematically represents the LabVIEW program used to control the operation of the SHG experimental set up. In essence, the program is a series of embedded while loops, with operations within the same loop colour coded and surrounded by arrowed boxes.

Before entering the first loop, the camera parameters that remain constant throughout the experiment are set, the delay stage is configured and the time file is read, into which all the time points to be interrogated in the experiment are written. Once inside the first loop the delay stage position is moved to the first time position before capturing an image from the camera at that time point in the third loop. Once acquired, the 2048 x 512 array is integrated across all the rows to yield the total intensity for each row index. The two indices with the biggest intensity values can then be identified as the two signal lines and are used to

extract the interference data from the original array. This loop is repeated N_3 times where N_3 is the pre-set number of spectra to average over per time point. After all of the spectra have been recorded, the data is averaged and analysed in a signal processing step that is discussed in the next section. If the end of the time file has not been reached, the delay stage is moved to the next position and loop 2 and 3 are repeated N_2 times until spectra for all time positions have been recorded. This

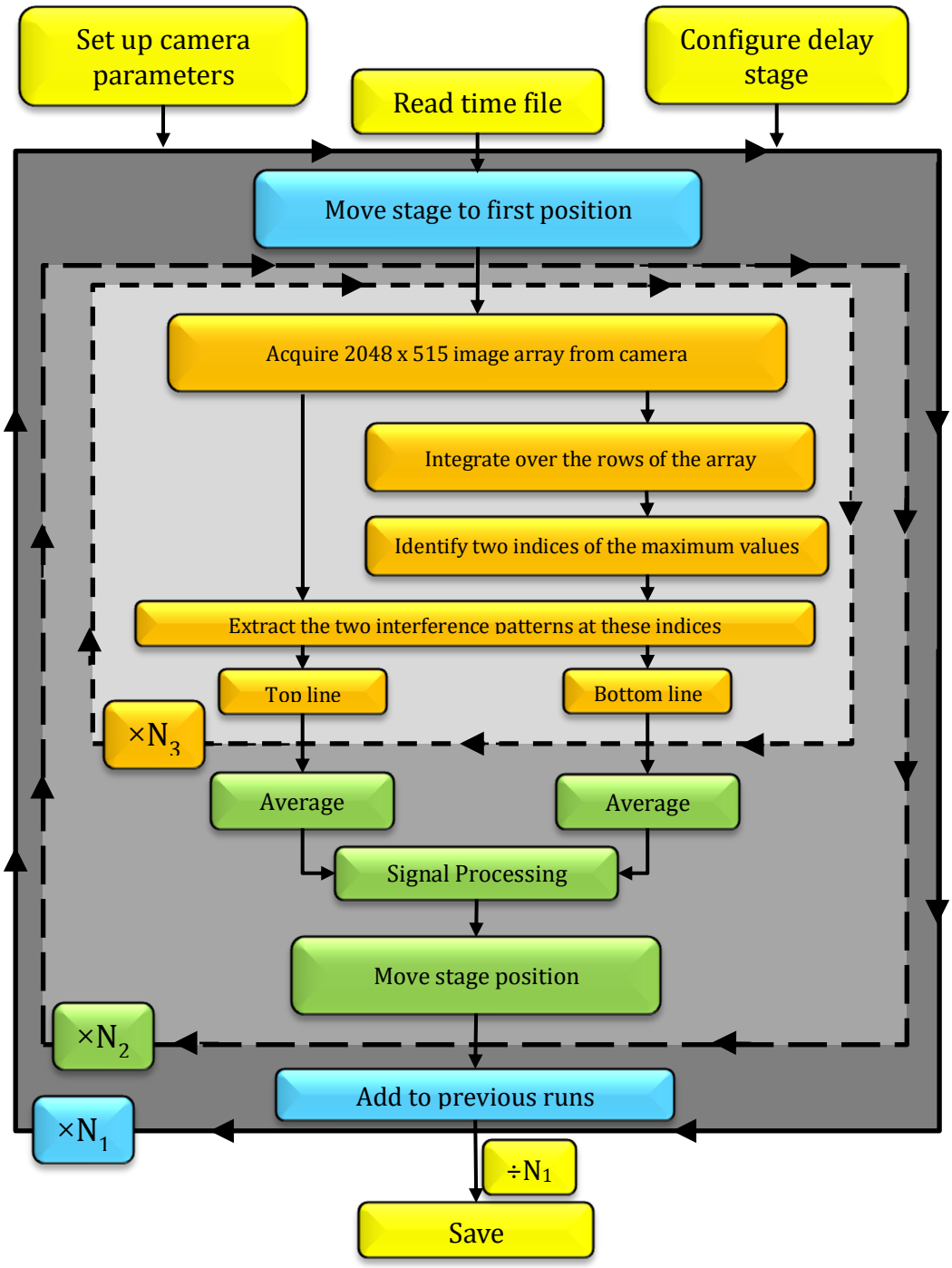

Figure 57 shows a flow diagram schematic representation of the LabVIEW program that controls the SHG experiment where n_3 is the number of spectra to average per time point, n_2 is the number of time points per scan, and n_1 is the number of delay stage scans per experiment.

process is then repeated N_1 times (where N_1 is the required number of times the delay stage runs through the time file) and the spectra from different runs are added together. Once finished, the data is averaged by N_1 and saved.

4.3.6. SIGNAL PROCESSING

From Equation (54) the intensity of the interference signal as a function of the LO and sample SHG electric fields can be simplified to

$$I_{\text{total}} = g(x)\left[\left|\tilde{E}_{\text{S}}\right|^2 + \left|\tilde{E}_{\text{LO}}\right|^2 + 2f(x)\left|\tilde{E}_{\text{S}}\right|\left|\tilde{E}_{\text{LO}}\right|\sin(\Phi + \nu x)\right], \tag{61}$$

where ν is the frequency of the interference fringes, and $f(x)$ represents the change in temporal overlap across the beam and $g(x)$ is the Gaussian profile of the line, both as a function of pixel position, x. Figure 58 shows an experimentally measured interference pattern for an 800 nm fundamental, shown in blue, and the fit of the form in equation (61), shown in red. The function $g(x)$ is largely formed from a single Gaussian profile to which satellite Gaussians have been added either side to fit the imperfect beam profile.

From equation (61), expressions for the signal, $I_{\text{SIG}}(x,t)$, and background, $I_{\text{BKG}}(x)$, lines at any time point, t, can be shown to be

$$I_{\text{SIG}}(x,t) = g(x)\left[{A_t}^2\left|\tilde{E}_{\text{S}}\right|^2 + \left|\tilde{E}_{\text{LO}}\right|^2 + 2A_t f(x)\left|\tilde{E}_{\text{S}}\right|\left|\tilde{E}_{\text{LO}}\right|\sin(\Phi_t + \nu x)\right], \tag{62}$$

$$I_{\text{BKG}}(x, t \leq 0) = g(x)\left[{A_0}^2\left|\tilde{E}_{\text{S}}\right|^2 + \left|\tilde{E}_{\text{LO}}\right|^2 + 2A_0 f(x)\left|\tilde{E}_{\text{S}}\right|\left|\tilde{E}_{\text{LO}}\right|\sin(\Phi_0 + \nu x)\right], \tag{63}$$

where A is the amplitude of the sample SHG response, and the subscripts 0 and t denote whether the term is time dependent or independent respectively. The time dependent phase, Φ_t and amplitude, A_t, can be written as a function of the time independent terms,

$$A_t = A_0 + \Delta_t A\,, \tag{64}$$

$$\text{and } \Phi_t = \Phi_0 + \Delta_t \Phi\,, \tag{65}$$

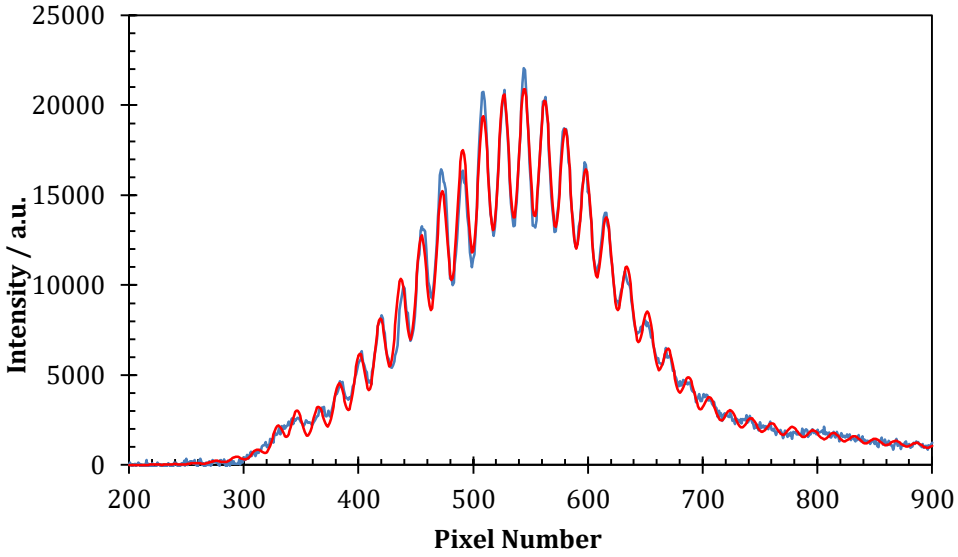

Figure 58 shows the experimentally recorded interference pattern (blue line) and the theoretical fit (red line).

with $\Delta_t A$ and $\Delta_t \Phi$ denoting the time dependent change in amplitude and phase shift respectively, which both equal zero when $t \leq 0$. In a time resolved experiment $I_{\mathrm{SIG}}(x,t)$ would equal the pump-probe signal, and $I_{\mathrm{BKG}}(x,t)$ would be the pump off line. By subtracting equation (62) from (63) the time resolved signal, $\Delta I(x,t)$, can then be shown to have the functional form,

$$\Delta I(x,t) = g(x)\left[\begin{matrix}\left({A_t}^2 - {A_0}^2\right)\left|\tilde{E}_S\right|^2 + 2f(x)\left|\tilde{E}_{\mathrm{S}}\right|\left|\tilde{E}_{\mathrm{LO}}\right|(A_t \sin(\Phi_t + \nu x) \\ -A_0 \sin(\Phi_0 + \nu x))\end{matrix}\right]. \tag{66}$$

However, although equations (61)-(66) characterise experimental data well, as shown in Figure 58, the fit cannot distinguish between a reduction in fringe amplitude (experimentally caused by a reduction in surface concentration) and a phase shift with a constant amplitude (experimentally due to a change in surface species identity) both of which result in a reduction in fringe amplitude[283]. The fit is therefore only able to characterise the frequency of the fringes.

To accurately extract phase shifts and amplitude changes, Fourier transforms are required. The Fourier transform of a data set outputs a complex number for each input value of the form,

$$z = x + iy, \tag{67}$$

where both x and y are real numbers. The corresponding frequency for each output point is calculated from the sampling frequency, *fs*, and the number of input data points, *sa*, where the frequency step size is defined as[287]

$$\text{step size} = \frac{fs}{sa}. \tag{68}$$

The first output value always corresponds to a frequency of 0, and the last value corresponds to *fs*, which for this data would hold a value of 1 as there is one Fourier input per pixel number. The frequency output therefore has units of pixel^{-1} but will be stated without units from this point onwards for simplicity.

The amplitude, A_m, and phase, Φ, at each frequency value can then be calculated from the complex Fourier output using the following

$$A = \sqrt{x^2 + y^2}, \tag{69}$$

$$\text{and } \Phi = tan^{-1}\left(\frac{y}{x}\right). \tag{70}$$

As it is the change in both the amplitude and phase between the signal and the background, from a signal processing perspective there are two possibilities: Fourier transforming the individual terms $I_{\text{ON}}(x,t)$ and $I_{\text{OFF}}(x,t)$ and then taking the difference, $\Delta\mathcal{F}[I]$; or Fourier transforming $\Delta I(x,t)$, $\mathcal{F}[\Delta I]$. The following sections will discuss which processing method accurately extracts the phase and amplitude changes by analysing experimental data.

4.3.6.1. PHASE

To deduce the best method to resolve the phase of an interference pattern, a time dependent phase shift was experimentally generated by varying the position of the second wedge. The furthest most wedge position, and as such the position whereby the beam propagates through the most glass, and is therefore the most temporally shifted, is set to $I_{\text{BKG}}(x)$. The wedge position is then translated so that the beam propagates through increasingly less glass relative to the background. As mentioned above, the approximation can be made that $f(x) = f'(x)$ and

$g(x) = g'(x)$ as the wedge position is constant. In this pseudo-time-resolved data, the approximation is not valid as the wedge position is moved. Furthermore the subscript, *t*, denoting time-dependence in equations (62) and (63) should correctly be replaced by a dependence on the wedge position, *L*.

Table 4 shows the Fourier transform phase output for each of the three data sets shown in Figure 59

	$\Phi(\mathcal{F}[I_{SIG}])$	$\Phi(\mathcal{F}[I_{BKGD}])$	$\Phi(\mathcal{F}[\Delta I])$
Phase Output / rad	-0.22	2.70	2.81

To explore the difference between $\Delta\mathcal{F}$ and $\Delta\mathcal{F}[\Delta I]$, a wedge position that to the eye generated an $I_{SIG}(x, L)$ interference pattern π out of phase with $I_{BKGD}(x)$ was chosen, with the data used shown in Figure 59. Both $\Delta\mathcal{F}$ and $\mathcal{F}[\Delta I]$ output a maximum amplitude at 0.3497 for all three data sets, with the fits based on equations (62), (63) and (66) outputting a frequency of 0.3501 for $I_{BKGD}(x)$ and 0.34904 for $I_{SIG}(x, L)$ which falls in the same frequency bin as the Fourier output. At this frequency the phase output by Fourier transforming each data set, $\Phi(\mathcal{F}[I])$, is shown in Table 4. $\Phi(\Delta\mathcal{F})$ can then be calculated to be 0.928 π whilst $\Phi(\mathcal{F}[\Delta I])$ is 0.894 π. Initially, these phase shifts both appear plausible and close to the expected π shift. However, when the experiment was repeated on a data set where $I_{SIG}(x, L)$

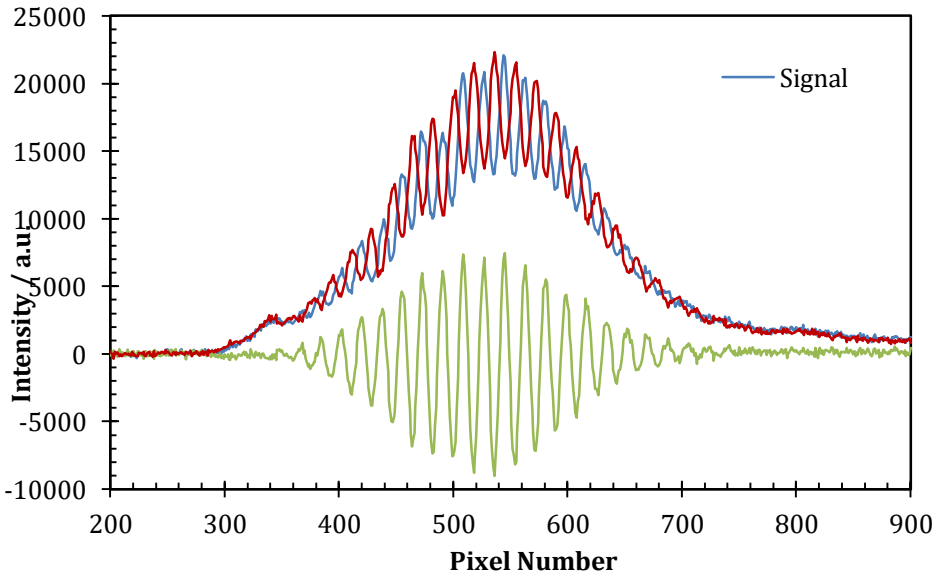

Figure 59 shows the assigned background interference pattern, $\boldsymbol{I_{BKGD}(x)}$ (blue line), with an approximate π out of phase interference pattern as $\boldsymbol{I_{SIG}(x, L)}$ (red line), and the difference between them $\boldsymbol{\Delta I(x, t)}$ shown (green line).

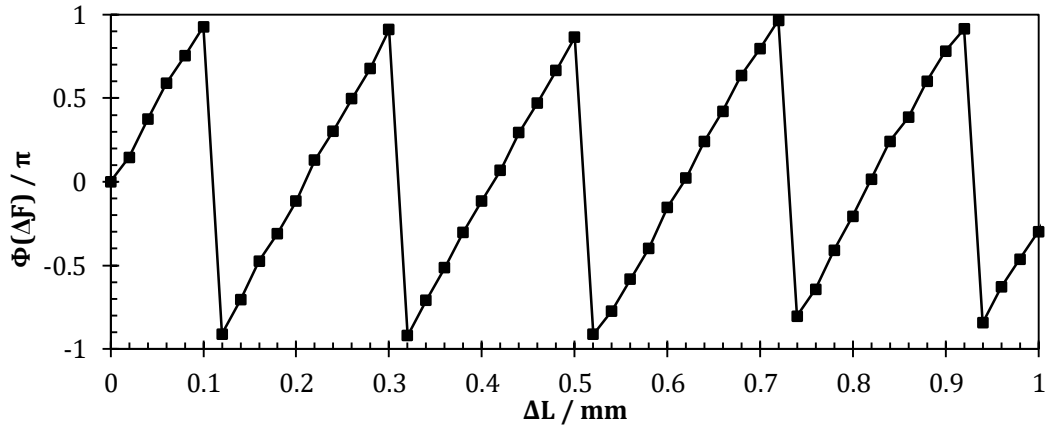

Figure 60 shows the phase shifts observed every 20 μm across 1 mm of wedge translation. The sawtooth pattern arises from the fact that a shift of +π is the same as a shift of –π.

was approximately in phase, $\Phi(\mathcal{F}[\Delta I])$ was 0.953 π whilst $\Phi(\Delta\mathcal{F})$ was the expected -0.009 π. Indeed, when compared across a range of wedge positions, the phase outputs of $\mathcal{F}[\Delta I]$ reveal an approximately constant phase shift, whilst $\Delta\mathcal{F}$ shows a linear phase shift trend from 0 to +π with increasing wedge position. Thus, to extract meaningful values for $\Delta_L\Phi$, the difference of the Fourier transforms, $\Delta\mathcal{F}[I]$, is required.

To further explore this, the increasing $\Delta_L\Phi$ across 1 mm of wedge translation was extracted, with all phases referenced to the same background and shown in Figure 60. It can be seen that the observed pattern is saw tooth which arises from the fact that a phase shift of +π could also be conceived as a shift of –π. From Figure 60 it can be seen that a wedge translation of 1 mm cycles through nearly 5 fringes and therefore a shift of nearly 10 π in total. Figure 61 shows the data from Figure 60 after adding 2πc to each new cycle (where c equals the cycle number) which then shows the linear change in phase across the wedge. The gradient of the change in wedge position as a function of the phase shift is equal to $1/(2\Delta n)$ which is calculated by linear regression to equal 0.10085 mm rad^{-1}. This yields an experimental value for Δn of 4.96 mm^{-1}, with the theoretically calculated value for the 10° CaF_2 wedges being 5.0253 mm^{-1}, thus validating the calculations in section 4.3.1.2.

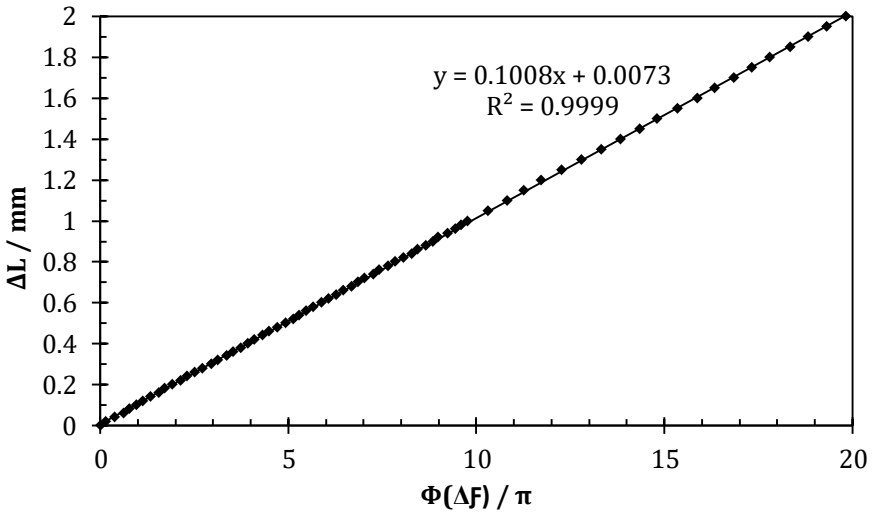

Figure 61 the linear phase shift across 2 mm of wedge translation where the gradient represents 1/Δn of the material.

4.3.6.2. AMPLITUDE

The same analysis was then applied to identify the best method by which the time-dependent amplitude change can be extracted. Inspection of the $\Delta Ƒ[\Delta I]$ amplitude analysis reveals an oscillating change in amplitude as the wedge position is changed, rising to a maximum value when the signal and background fringes approach being π out of phase. However, unlike the phase, changing the wedge position should not significantly alter the amplitude. A small reduction in amplitude could be reasonably anticipated due to the increased group velocity mismatch but over the 2 mm range this should be very slight.

This result is indicative of $\Delta Ƒ[\Delta I]$ being insensitive to changes due to decreasing amplitude of the interference pattern or alternatively a phase shift with constant amplitude. Additionally, the amplitude change from $\Delta Ƒ[\Delta I]$ is always positive as the analysis takes the magnitude of the Fourier transform thus losing sign information. In comparison, ΔƑ analysis yields small amplitude changes randomly varying around zero (and thus is insensitive to any phase shifts), with retention of sign. As a result, amplitude, like phase, is extracted most effectively by ΔƑ analysis.

4.3.7. PHASE CALIBRATION

Being able to extract the phase of the species of interest is one of the main advantages of interference SHG techniques. However, the phase shift output by the difference of the signal and background Fourier transforms is defined relative to the LO phase, and if this is not well characterised, the deduced phase is not very informative. To obtain an absolute phase, the RS needs to be extracted by calibrating against a sample surface of known phase.

To generate the calibration shift, the experiment is repeated on a sample, such as quartz, with a known phase, to generate $\Phi_R(\Delta f)$ for the calibration surface. This can be compared to the known phase, Φ_K by

$$\Phi_K = \Phi_R + \Delta\Phi_{CALI}, \tag{71}$$

where $\Delta\Phi_{CALI}$ is the calibration shift required to generate the known phase. The absolute phase of an unknown sample, $\Phi_S(\Delta f)$, can then be

$$\Phi_{ABS} = \Phi_S(\Delta f) + \Delta\Phi_{CALI} \tag{72}$$

The absolute phase of the known sample, such as quartz, consequently allows the phase of the time independent sample to be determined. Although quartz is a well utilised surface, experimentally obtaining an identical surface flatness to that of a liquid surface is non-trivial. As such, a non-resonant liquid surface, such as water, with a known phase of $\pi/2$ relative to quartz, would be more suitable.

4.4. RESULTS

4.4.1. MALACHITE GREEN

MG has been the subject of a number of previous investigations, including at the water/air interface using time-resolved SHG.[274,283,288] Here it is used as a proof of concept for the new experimental methodology. Figure 62 shows the relevant electronic states of MG. The excitation pulse at 257 nm is resonant with S_3 or S_4 excited states. These subsequently decay to recover the ground states. The dynamics can be tracked by probing the $S_2 \leftarrow S_0$ transition, for which the second harmonic of the 800 nm probe is resonant, resulting in resonant enhancement of the SHG field at the sample surface. Most previous experiments have used the $S_1 \leftarrow S_0$ transition, which produces a much stronger SHG response.[274,288]

All the experimental results presented here use a 50 μM sample solution of Malachite Green (Malachite Green Carbinol Hydrochloride, Sigma-Aldrich) made in high purity water. The fundamental probe beam generated by the OPA was set to 800 nm (1.7 μJ pulse^{-1}), thus matching the $S_2 \leftarrow S_0$ transition. The fourth harmonic of the Carbide fundamental, 257 nm (1.3 μJ pulse^{-1}) was used as the pump beam. The P output polarization was selected by the Glan-Taylor polarizer so that only the dipole allowed PP polarization combination was probed.

Figure 63 shows the results of the experiment on MG at the water/air interface. The raw signal is shown in Figure 63(a), which shows the direct read-out from the CCD camera with a 1 s integration time. The two lines correspond to the pump-

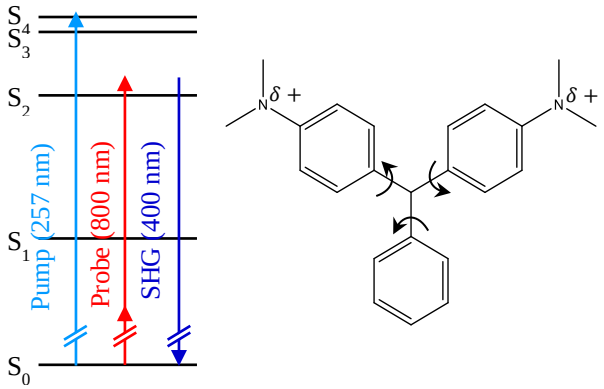

Figure 62 shows the energy levels of MG (left) and its structure (right). Pump, probe and SHG energies are indicated.

probe and probe-only signals separated by the Pockels cell and Wollaston prism combination. Superimposed on these signals are clear oscillations that correspond to the interference fringes generated by the non-parallel SHG and LO pulse profiles. The individual lines were then integrated to provide a 1D spectrum of the profile across the pulse. This is shown in Figure 63(b) and clearly highlights the interference fringes. We note the decreasing fringe amplitude across the beam profile. This is a consequence of the reduced temporal overlap between the SHG and LO pulses as the LO travels through a larger portion of the wedge and thus incurs a larger group velocity delay. The current wedges have been chosen as a compromise between number of fringes and group velocity mismatch.

Figure 63(c) shows the amplitude of the Fourier transform of both traces in (b). A peak at frequency $\nu \sim 0.38$ rad can readily be identified in both spectra and this region is expanded in Figure 63(c). At low frequency, there is a large peak (not shown here) that originates from the noise in the CCD camera and effectively has the typical $1/\nu$ shape of pink noise. The key benefit of measuring the interferogram is that the frequency of the interference pattern can be readily moved outside that of the noise (*i.e.* towards higher ν). Hence, the Fourier transform amplitude is essentially insensitive to offsets (as exist in Figure 63b)) and small variations in the pulse profile between the two spectra.

The spatial ν of the fringes is defined by the wavelength and choice of wedge angles. The wedge angle scales with ν and, hence, a higher angle leads to lower noise (up to a point where $1/\nu$ approaches the pixel dimensions of the CCD). However, as the angle increases, so does the group velocity mismatch between the SHG and LO fields, reducing the amplitude of the Fourier transform. The compromise is one in which the signal to noise of the Fourier transform remains excellent and fringes can be seen across the profile.

The peak of the amplitude in Figure 63(c) has a shape that is determined by the amplitude variation across the pulse profile and the pulse profile itself. In principle, this allows the entire peak to be used as a measure of the amplitude. However, the phase across the peak varies significantly. In Figure 63(d), the phase is shown. Note that this is a relative phase; however, it can easily be referenced to

an absolute scale using a RS such a *z*-cut quartz as we have done previously.[283] The phase varies quite erratically across the range of ν where the peak in the amplitude exists. These variations arise simply because a relative phase is measured; each ν would need to be calibrated to exploit the entire peak. Outside the ν-range of the amplitude peak, the phases clearly do not match between the two spectra, because both real and imaginary parts are close to zero (*i.e.* there is no signal).

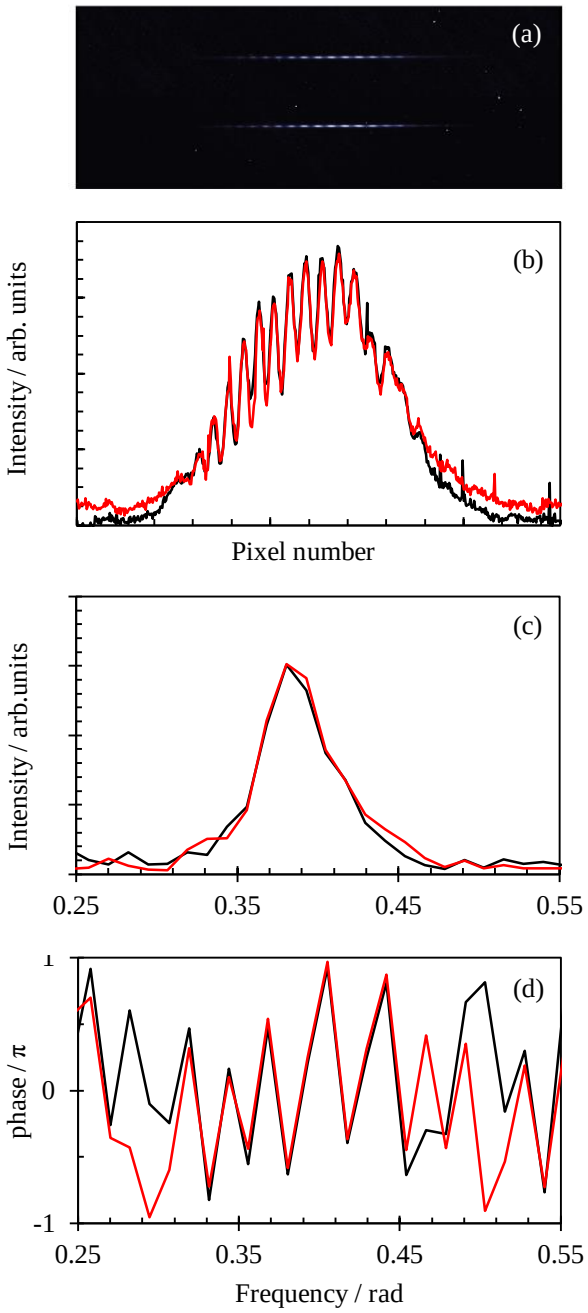

Figure 63. Phase sensitive SHG collected from MG at the water/air interface, with the pump pulse blocked. (a) The direct image output from the CCD camera with a 1 s integration time. (b) Interference pattern following the selection of a region of interest and vertical integration. (c) and (d) The amplitude and phase, respectively, recovered from Fourier transforms of each line in (b).

Finally, we demonstrate the methodology by probing the dynamics of MG following excitation at 257 nm. Specifically, the S_0 state recovery was probed by delaying the 800 nm probe relative to the pump. In Figure 64(a), the difference in the Fourier transform amplitude is shown for pump-probe and probe-only interferograms (see Figure 63(c)) at ν = 0.38 rad. For $t < 0$, the signal is very close to zero. In principle, of course, it should be exactly 0, but small variations in the fringes result in a small offset. These probably arise from variations across the CCD array or imperfections in the polarisation change introduced by an ammonium dihydrogen phosphate (ADP) crystal Pockels cell, leading to small variations between the two lines in Figure 63(a). As it is an experimental artefact, this simple offset can be subtracted off, but we have not done so here for transparency. At t = 0, the signal rapidly becomes very negative – that is, the pump-probe amplitude (Figure 63(c)) becomes smaller than the pump-only amplitude. As the SHG at 400 nm is resonant with the $S_2 \leftarrow S_0$ transition, excitation to the S_3/S_4 results in a ground-state bleaching of the interference amplitude as fewer molecules are in S_0. Note that, because the signal is an interference term, the change in signal is linearly proportional to $\mathbf{E}_{SHG}$ and therefore also N_S (the number of MG molecules in S_0 per unit area).[283]

After ~10 ps, the signal recovers and then decays further on a much longer time-scale. The initial decay can be fit to a single exponential with a lifetime of 6.7 ps, with a much more slowly decaying offset at longer times. The measured lifetime is in reasonable agreement with previous work[274,288] although these experiments followed the MG dynamics by probing the $S_2 \leftarrow S_0$ transition of MG at ~620 nm. In

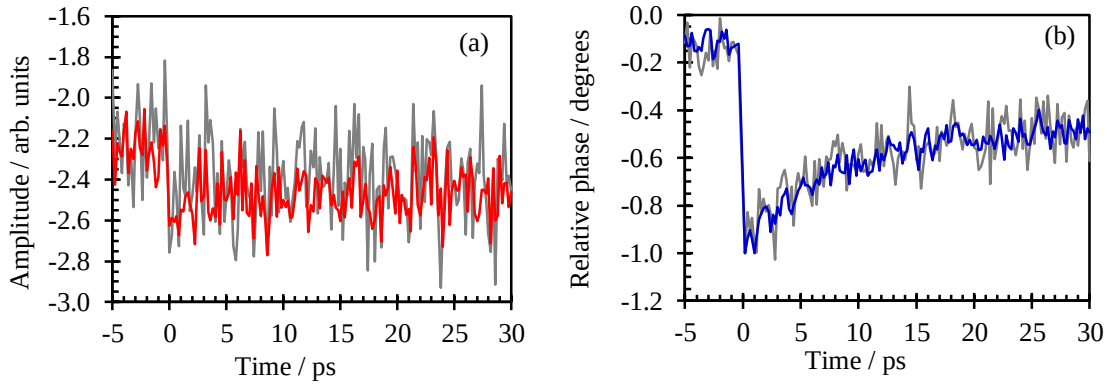

Figure 64 shows time resolved amplitude (a) and relative phase (b) of the ground state recovery of MG at the water/air inteface. The coloured lines show an average of 10 measurements and the grey lines show a single measurement based on 1 s exposure times of the CCD at each time point.

Figure 64(b), the change in phase at ν = 0.38 rad is shown. This is shown in degrees for clarity and corresponds to the relative phase of pump-probe to probe-only signals. At t = 0, there is a clear change in phase. The phase shift amounts to 0.7 ± 0.3°, which, while very small, is perfectly reproducible. At present, we do not quite understand the origin of the phase change. It may be that the relative contributions of resonant and non-resonant second order nonlinear susceptibility are changing, but this would then also show in the decay dynamics. Alternatively, the phase may reflect the phase change of only the long-term decay component.

The grey data in both Figure 64(a) and (b) represents a single scan, where each data point (175 in total) is acquired over a 1 s integration time of the CCD camera (*i.e.* 3×10^4 pump-probe minus probe-only cycles). Hence, the entire dynamics trace shown for a single scan was acquired in ~3 minutes. The blue and red lines in Figure 64(a) and (b), respectively, are the average of 10 successive measurements (~30 minutes). During this acquisition time, the phase change is better than $1{:}10^3$ and the signal to noise ratio of the amplitude is excellent.

In the previous version of the experiment, we reported acquisition times for a pump-probe kinetic trace of similar quality as taking approximately 1 hr.[283] Crucially, however, that data only presented the dynamics in signal intensity (*i.e.* amplitude) at one phase delay and therefore did not distinguish between a change in SHG intensity due to a decreasing amplitude of the interference pattern or alternatively a small phase shift with a constant amplitude. In order to obtain data that is comparable with present data, an interferogram would need to be constructed by repeating the kinetic experiment and multiple phase differences between 0 and π. With 8 phase points, this would have taken ~ 8 hrs. Additionally, because of the inaccuracies in defining the phase delay and long-term drifts, the phase-change observed here for MG was not observable. The improvement of the new method is thus clear as a full interference pattern is characterised at all time points in less time than it previously took to record one data point along the phase curve. Moreover, the sensitivity in phase changes is surprisingly good. Note, however, that the error in the absolute phase is relatively large, because this needs to be calibrated to a reference. Nevertheless, as one is mostly interested in changes

in signals in time-resolved measurements, we anticipate that the presented relative phase stability will be very informative.

As a final point, the technique will be compared to other techniques for measuring surface sensitive dynamics using second order non-linear spectroscopy.[216,242,247,289–292] A simple pump-probe scheme in which the total SHG signal, $\mathbf{E}_{SHG}^2$, is simpler and faster, but of course suffers from the fact that it depends on the number of adsorbates, N_S^2 (and that it does not provide phase information). In the present experiment, the Fourier transform effectively recovers the term proportional to $\mathbf{E}_{SHG}\mathbf{E}_{LO}$. Hence, for a weak SHG response, the measured signal amplitude can be increased by increasing the amplitude of the LO field. In reality of course, there is a limit to which point $\mathbf{E}_{LO}$ can be increased. Specifically, if $\mathbf{E}_{LO} >> \mathbf{E}_{SHG}$, then $S_{fringe} \sim \mathbf{E}_{LO}^2$ and the oscillation of amplitude $2\mathbf{E}_{SHG}\mathbf{E}_{LO}\sin(\phi)$ may not be distinguishable from the pulse profile. Therefore, the choice of reference material can become important.

As discussed in section 4.2.2.2, heterodyne-detected techniques have been actively developed.[255,261,280,293–296] A key advantage of these is that they also acquire spectral information which has been very informative in vibrational SFG spectroscopy.[260,261,295,296] The main difficulty with such experiments is the phase stability: micrometer accuracy is essential in the beams' propagation distances between the sample and RS.[261,283] While some key advancements have been made to improve this,[297] our method is effectively indefinitely phase-stable as all beams are collinear and the sensitivity to phase changes is outstanding. Additionally, the shortened acquisition time for our new time-resolved measurements compares extremely favourably with the ~50 min/delay for a heterodyne-detected measurement,[261] but of course we note that this is at the expense of obtaining the full spectral information. The simplest way to gain the spectral information in the present experiment is to scan the probe photon energy. This would in fact be quite feasible over limited ranges of ~1000 cm^{-1} in the fundamental. Beyond this, changes in alignment may be required. We note however, that most heterodyne-detected experiments are limited to smaller bandwidths.[261,262]

5. OUTLOOK

This thesis presents the first completed experiments of the multi-experiment spectroscopy suite, or MESS, that can be used to build a picture of molecular dynamics in different solvation environments, with minimal alignment or stability consequences. The second chapter of this thesis thus describes the interchangeable components of the MESS which have been designed to allow expansion to include more experiments. Chapters three and four focus on the transient absorption (TA) and second harmonic generation (SHG) techniques in detail and present key results used to characterise and illustrate the capacity of the techniques.

TA as a technique is well known for studying bulk species and has been implemented widely within the literature. Here we demonstrate a broadband shot-to-shot technique run at 30 kHz which effectively compromises data acquisition times with noise. Compared to other broadband techniques that exceed the few kHz regime, our chopping mechanism is comparatively simple to implement with no moving components, yielding high phase stability.

The SHG technique provides a method for specifically studying adsorbates present at interfaces. Chapter four presents a new-time resolved technique which is an improvement to a previous phase-sensitive measurement designed by our group which measures the interference term between SHG from a sample surface and

that from a reference sample, termed the local oscillator, LO. Our new method retains this interference but places the RS between two glass wedges, yielding a spatially varying phase delay across the LO and thus the interference pattern. Combining this with a 30 kHz pumping regime, extraordinary phase sensitivity can be obtained from pump-probe measurements in significantly shorter acquisition times.

The power of the SHG technique is demonstrated on malachite green at the air/water interface, for which excellent time-resolved data is presented. However, malachite green has a large $\chi^{(2)}$and therefore a huge nonlinear optical response compared to water or the hydrated electron. Thus, at present the experiment suffers from being limited by the intensity of the LO which, to obtain well resolved interference fringes, must be well matched to the sample SHG. For malachite green this was easily obtained with BBO which could be tuned by rotating the crystal in the axis perpendicular to the propagation of the beam. For samples with weaker nonlinear responses however, the LO term dominates the interference term (even when at its minimum) and interference fringes are virtually impossible to distinguish. Currently we estimate that the LO needs to be reduced by up to 120 times to study species such as the hydrated electron. Mechanisms by which the LO can be selectively reduced without adding material such that the fundamental and LO pulses become temporarily mismatched are thus required. At present a technique for dying 5 μm polyethylene sheets to make filters is being explored and has shown initial promise, with LO reduction of up to 20 times, but needs time investment beyond the scope of this work. Another potential solution for the LO intensity is to place the spatially varying phase unit after the sample rather than before, although this adds additional problems in the reflectivity of the sample also having a time resolved component and therefore making the LO a non-constant contributing term.

Beyond improvements to the SHG technique, the MESS can be expanded to include more techniques that add depth to the information provided by TA and SHG. One such experiment would be time-resolved reflectance spectroscopy on liquid interfaces which would allow the characterisation of the reflectivity changes as a function of wavelength and therefore making placing the RS after the sample more viable.

APPENDICES

A – LIQUID HEIGHT MONITOR PROGRAM

The procedure of the liquid height monitor (LHM) can be summarised to be:

1. The photodiode output is converted into an 8-bit number.
2. The 8-bit number is mathematically tested by the PIC to determine the beam's vertical position on the quadrant photodiode.
3. The position is used to determine whether the height is within an appropriate range or if action is required.
4. The required command is sent to the pump i.e. if the height is too low, the decided pump action will be to 'infuse'.

The central component to the designed liquid level monitor is the 8-bit PIC microcontroller, PIC16(L)F721. Using assembler language and the software package MPLABX IDE 3.20, the PIC was programmed to compute an averaged voltage value, test its position on the photodiode, use the position to determine what action is required (i.e. infuse or withdraw) and then send that action using ASCII coded commands, via an RS232 interface, to the pump which implements the action. The full assembler program constitutes a feedback loop through four main sub-programs called routines:

1. NUMBER AVERAGE: averages n photodiode voltages over 1 s.
2. TIME AVERAGE: averages $t \times 1$ s averages outputting an average voltage over t s.
3. DECISION: calculates the voltage's corresponding position on the photodiode and determines the necessary action required.
4. RS232: communicates with the pump to enact the desired response.

Figure 66 represents a single pass through these four routines as a flow diagram. The chart has been crudely segmented into the different routines with the numbers above used as identifiers. The box colours are used to signify different types of coding according to the following key:

- GREEN boxes represent code relating to setting or altering the variables that define the parameters of the average voltage output i.e. n and t,
- BLUE boxes correspond to code that performs mathematical operations,
- ORANGE boxes represent code that tests the validity of a mathematical expression on a variable, and
- YELLOW boxes represent contextualising information or overviews of large segments of code that are condensed for simplification of the process.

Throughout the program represented in Figure 66 a number of 8-bit variables are used of which there are three types; 'constant' or 'programmable', 'dummy' and 'temporary'. Constant variables are set before the program loop and represent the programmable parameters of the program and thus the numbers held in these variables are not changed during the program whilst it is running. Dummy variables are reset at the beginning of every loop to equal the value of the constant variable. Throughout the program the value held within the dummy variable is changed and tested to indicate the point at which to move on to the next routine, thus preserving the constant variable value. Temporary variables are cleared (i.e. set equal to zero) at the beginning of the program loop and are used to hold the voltage data being worked on by the program. Table 6 defines and categorises the variables used in the flow diagram.

Figure 66 shows that the final averaged digital voltage over t s is output from routine 2 and held as an 8-bit number in RESULT_L. This number is then related to the position on the photodiode by a series of mathematical calculations. The

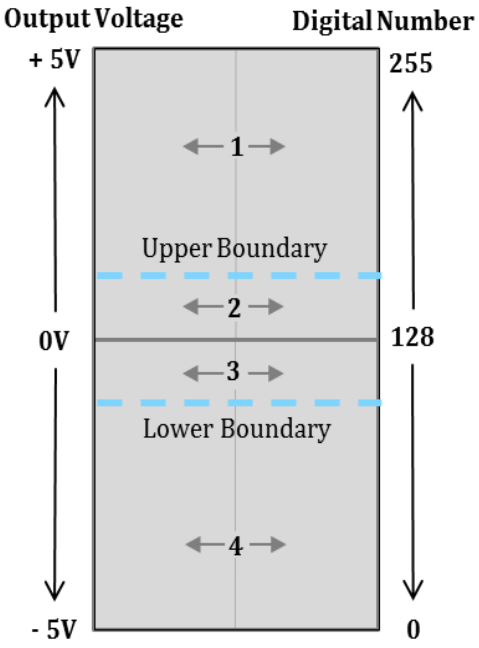

Figure 65 shows a schematic representation of the four possible position averages.

relation between the difference voltage output from the photodiode and its corresponding 8-bit digital value is shown in Figure 65. A 10 V swing factored into 2^8 provides a minimum increment of ~40 mV.

If the optimum height is set to equal 0 V (digital=127 or 128) and the boundary is set to equal ±0.2 V (digital = ±5) there are four possible scenarios (numbered in Figure 65):

1. Too high e.g. +3 V indicating that the level needs to be decreased
2. High but within set limits e.g. +0.1 V
3. Low but within set limits e.g. –0.1 V
4. Too low e.g. –2.1 V indicating that the level needs to be increased.

Table 5 shows how routine 3 in the program mathematically manipulates the digital output values to determine the position on the photodiode in relation to the boundaries. This process is shown schematically in the flow chart in Figure 66.

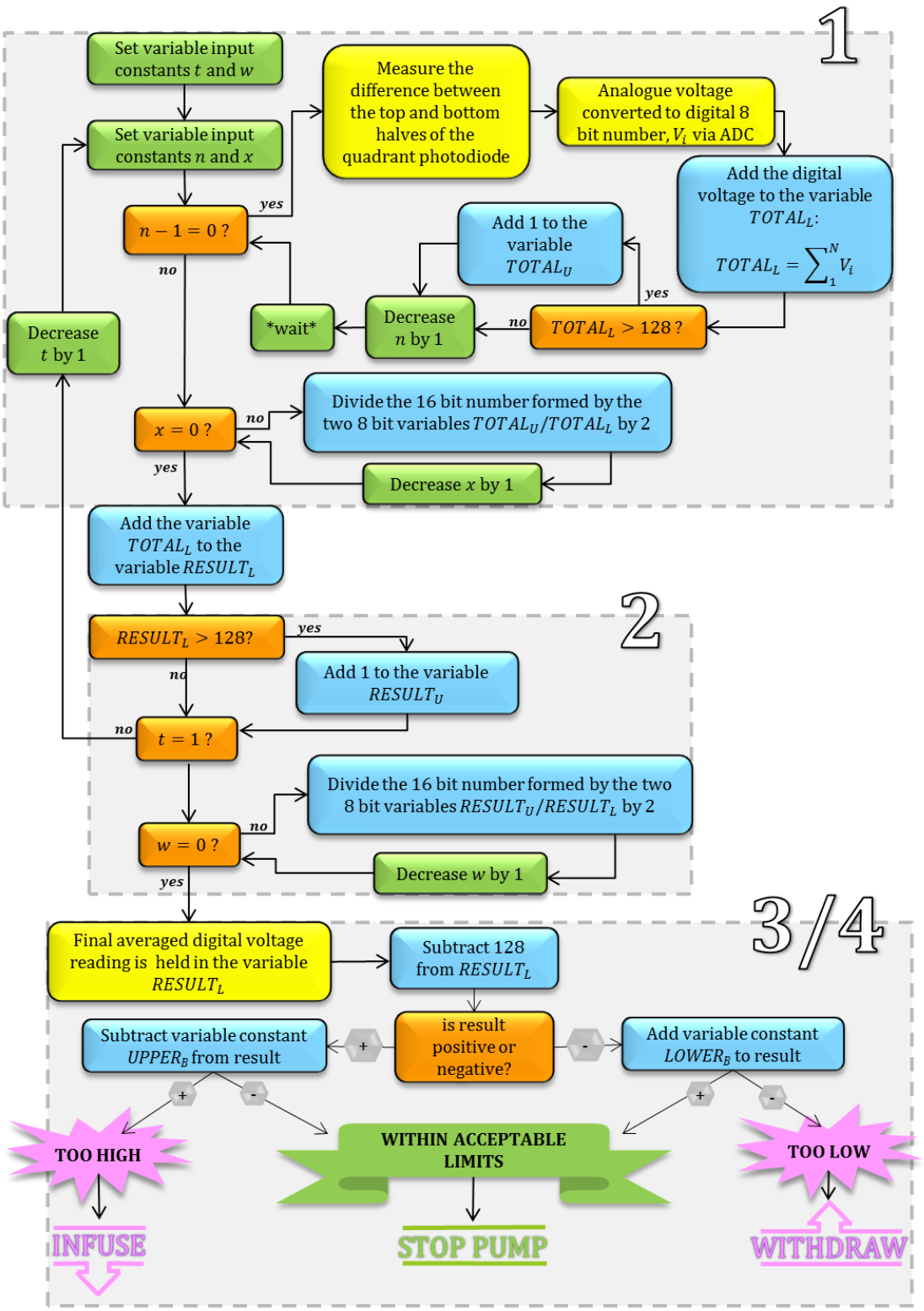

Figure 66 a flow diagram representation of the assembler program used to monitor the liquid level height.

Table 5 shows how routine 3 in the program mathematically manipulates the digital output values

Photodiode average output	+3 V	+0.1 V	-0.1 V	-2.1 V
1. Convert to digital number	+200	+130	+125	+75
2. Subtract 128	+72	+2	-3	-53
3. (a) +ve: add $UPPER_B = 5$	+67	-3	-	-
(b) –ve: subtract $LOWER_B = 5$	-	-	+2	-48
4. Sign change between step 2 and 3?	No	Yes	Yes	No
5. Position?	Too High	Within Limits		Too Low
6. Pump action required?	Infuse	Do Nothing		Withdraw

The calculated position is used to determine the required action in the syringe pump to return to liquid height to within the boundary. To communicate with the pump, the required ASCII coded RS232 command is written to a temporary variable, one character at a time, and transmitted serially as a bit stream. Once received by the pump the RS232 command changes the pumping program function for a desired response. The monitor therefore works as a negative feedback loop.

The pump attached to the microcontroller is the commercially available Aladdin programmable syringe pump from World Precision Instruments. The pump has a number of functions that can be programmed, the most relevant of which are the rate of pumping, the syringe diameter, starting or stopping the pumping program, and the direction of pumping e.g. infuse or withdraw. These functions can either be programmed manually or can be set using RS232 communication.

- Functions that depend on the outcome of the programs decision are programmed using RS232 and communicated using ASCII code as described in the previous section. These functions include starting and pausing/stopping the pumping action and the direction of pumping.

- Manually input functions remain set after the LHM has been turned off. Manual programming is therefore preferred for functions that remain unchanged over time, i.e. pumping rate and syringe diameter, simplifying the assembler program. The pump can accommodate syringe diameters ranging from 0.1 mm to 50.0 mm. For this application a 20 ml syringe with a 19 mm diameter was chosen to allow a sufficiently large reservoir for refilling over <12 hours.

Table 6 shows a selection of variables, their variable type and their definitions used in the assembler program.

NAME	CATEGORY	Definition
n	Dummy	The remaining number of photodiode measurements needed before a sum over N is obtained - where N represents the corresponding constant variable. n is decremented by 1 every time a voltage is added to the running total held in $TOTAL_L$.
x	Dummy	The number of divisions by 2 required to output the final 1 s $\therefore x = log_2(n)$. Each rotation is an effective division by 2.
t	Dummy	The remaining number of 1 s photodiode averages needed before a sum over T seconds is obtained - where T represents the corresponding constant variable. t is decremented by 1 every time a 1 s average is added to the running total held in $RESULT_L$.
w	Dummy	The number of rotations required to output the final average over t s $\therefore\ w = log_2(t)$. A rotation is an effective division by 2.
$TOTAL_L$	Temporary	Before the division step, $TOTAL_L$ holds the lower half of the 16 bit running sum of the photodiode output: $$TOTAL_U\text{«»}TOTAL_L = \sum_1^N V_i$$ where V_i represents the digital photodiode voltage and «» indicates the two 8 bit numbers held in the variables $TOTAL_L$ and $TOTAL_U$ being put together to give one 16 bit number. After the division, the final 1 s 8 bit average is held in $TOTAL_L$.
$TOTAL_U$	Temporary	When the running summation of the photodiode reading over N exceeds 8 bits, 1 is added to $TOTAL_U$ whereby the 8 bits of $TOTAL_U$ form the upper half of the total summation value.
$RESULT_L$	Temporary	Before the division step, $RESULT_L$ represents the running sum of the 1 s average output from the NUMBER AVERAGE routine: $$RESULT_U\text{«»}RESULT_L = \sum_1^T TOTAL_{L_i}.$$ After the division step, the final t s average to be tested in the DECISION routine is held in $RESULT_L$.
$RESULT_U$	Temporary	When the running summation of the 1 s averages over T exceeds 8 bits, 1 is added to $RESULT_U$ whereby the 8 bits of $RESULT_U$ form the upper half of the total summation value.
$UPPER_B$	Constant	The upper boundary limit that represents the largest voltage reading indicating an acceptable height above optimum.
$LOWER_B$	Constant	The lower boundary limit that represents the smallest voltage reading indicating an acceptable height below optimum.

A.1. WATER EVAPORATION

The evaporation rate of water is a complex function depending on a number of variables: temperature of the water and the air; air humidity and pressure; velocity of the air at the interface, and the surface area of the interface. Assuming the environmental conditions within the lab are approximately constant, the rate of evaporation can be considered to be a pseudo linear function with respect to time. Figure 67 validates this approximation by plotting the photodiode output voltage as a function of time without the liquid monitor program activated. Therefore, to a first approximation, the evaporation rate is proportional to the photodiode voltage and the liquid height (or volume).

To characterise the relationship between the liquid level height and the photodiode voltage, a technique resembling a knife edge measurement was used. The sample dish was filled using a micropipette with various volumes of water, ranging from 15 ml to 25 ml and the photodiode output voltage recorded and averaged over the first 3 minutes. Figure 68 shows the mean voltage as a function of the liquid level height. The vertical error bars show the standard deviation of each mean. The horizontal error bars (too small to be seen) are propagated assuming an error of 1 µl in every 1000 µl pipetted

The line shown in Figure 68 is the cumulative integral of a Gaussian function (generated using the NORM.DIST function in Excel), and is fit to the data by optimising 4 fitting parameters (centre, height, offset and radius) to minimise the chi-squared, χ^2 value (not to be confused with the optical nonlinear response

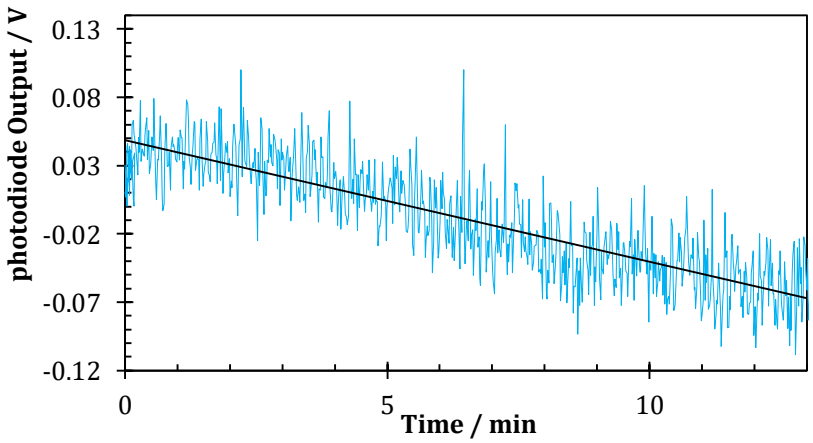

Figure 67 shows the photodiode voltage output plotted as a function of time with the liquid monitor program disabled.

parameter, $\chi^{(2)}$). The goodness of fit is characterised by the reduced chi-squared, χ_R^2, with a value of 1 indicating a perfect characterisation of the data. χ_R^2 for the data shown in Figure 68 is calculated to be 1.2 indicating good confidence in the fit. However, this fit generates the voltage as a function of height, when the height as a function of voltage as is required.

To map voltage to height, the inverse of the cumulative integral is needed as a function of the optimised fitting parameters (generated using the NORM.INV function in Excel). The result is shown in Figure 69 The error in the overall fit can be calculated using the errors in the errors in the cumulative integral fitting parameters as shown by[298]

$$-\delta_{\text{fit}}^{C} = f(C - \delta_C, H, R, O) - f(C, H, R, O), \tag{73}$$

where C, H, R and O represent the fitting parameters centre, height, radius and offset respectively, and δ_{fit}^{C} indicates the error in the fit being calculated is the error associated with the centre fitting parameter. The overall error associated with the fit can therefore be expressed as

$$\delta_{\text{fit}} = \delta_{\text{fit}}^{C\,2} + \delta_{\text{fit}}^{H\,2} + \delta_{\text{fit}}^{R\,2} + \delta_{\text{fit}}^{O\,2} + \left(-\delta_{\text{fit}}^{C}\right)^2 + \left(-\delta_{\text{fit}}^{H}\right)^2 + \left(-\delta_{\text{fit}}^{R}\right)^2 + \left(-\delta_{\text{fit}}^{O}\right)^2, \tag{74}$$

where, due to the asymmetry, $+\delta_{\text{fit}}^{C}$ and $-\delta_{\text{fit}}^{C}$ should not be assumed to be equal. Figure 69 shows the data from Figure 68 with the fitting function ± its error

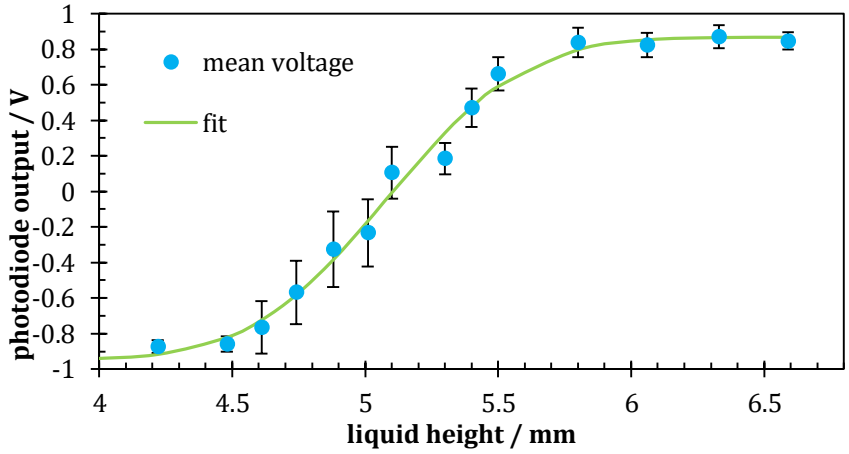

Figure 68 plots the average photodiode voltage as a function of the liquid height.

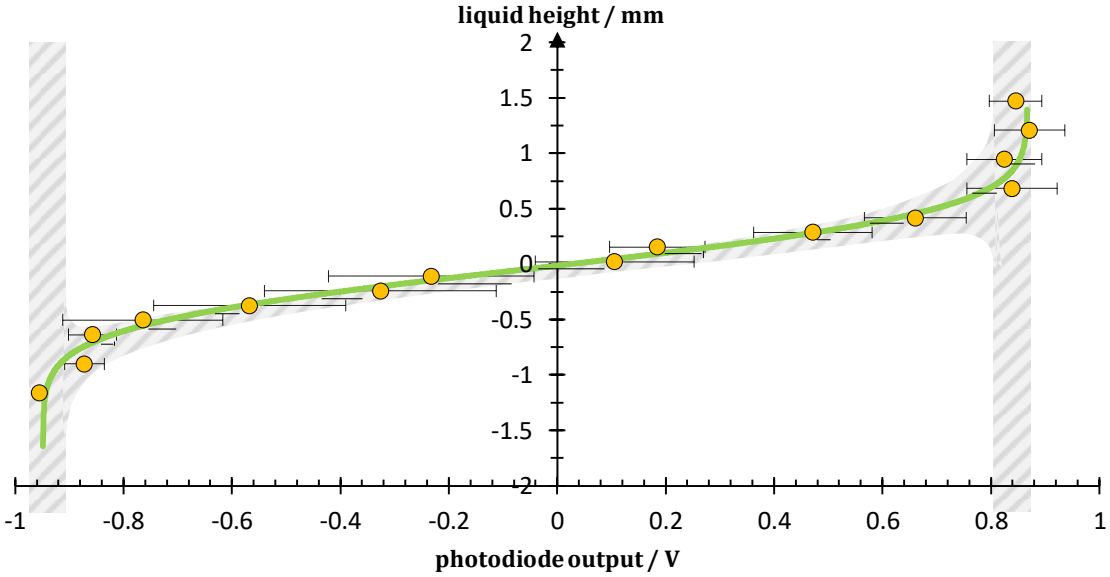

Figure 69 plots the liquid height as a function of the average photodiode output.

(shown in grey) for the photodiode voltage as a function of height. The height has been rescaled with 0 mm indicating the optimum height at 0 V. Thus, Figure 67 can now be re-plotted with height as a function of time, and the rate of change of the liquid height can be deduced from the gradient to be 0.0048±0.0002 mm min^{-1}. This corresponds to a rate of evaporation of 20±1 µl min^{-1} and represents the minimum rate required by the pump to counteract evaporation.

A.2. PARAMETER OPTIMISATION

Initially, a rate of 1 ml min^{-1} was tested as it seemed logical that the faster the rate, the more responsive the pump would be in counteracting changes in the height. However, at this rate sinusoidal oscillations were observed in which the position fluctuates between being too high, and above the uppermost acceptable position, and too low. Similar oscillations were observed when the time constant variable was increased (resulting in averaging over more seconds). This can be attributed to Poiseuille's Law which states that the flow rate is directly proportional to the pressure difference at both ends of a tube and the radius of that tube raised to the power of 4.[299] As the tube used as in the liquid monitor set up requires a long length to reach the sample, and a small radius, the flow rate is expected to be slow. Thus, when a fast rate such as 1 ml min^{-1} is applied which exerts a large force on the syringe; the pressure on the end attached to the syringe is expected to be large compared to the end at the sample. The flow of liquid is therefore relatively unresponsive to the pump movement, and even after

the pump stops pumping, the pressure from when the pump was in motion is still exerting a force on the liquid at some point in the tube causing the liquid to continue to flow. Thus, a rate is needed that is fast enough to combat evaporation but slow enough that the pressure difference between the two ends of the tube is small enough that the flow rate is responsive to the pump action.

It was found that setting the rate to less than 1 ml min^{-1} eliminated the regular oscillations. By independently investigating the effect of varying the rate and averaging time constant, it was hoped that it would be possible to calibrate the optimum combination of program parameters. The results showed that the mean pumping values were not statistically different across the range of parameters investigated, as shown in Figure 70. However, there were several trends that, although not statistically significant, are worth noting: Firstly, it can be seen that, as the rate increases, the mean value also increases. This is not unsurprising as a faster rate will result in a larger volume of water being infused per second and, thus, a larger change in liquid height between photodiode voltage inputs into the program. Thus, overshooting the upper boundary is more likely with a faster rate resulting in a higher mean position. Secondly, it can be noted that the 1 s time average gives the lowest mean position across all the rates investigated. This implies that a quicker sampling time results in a more responsive liquid monitor.

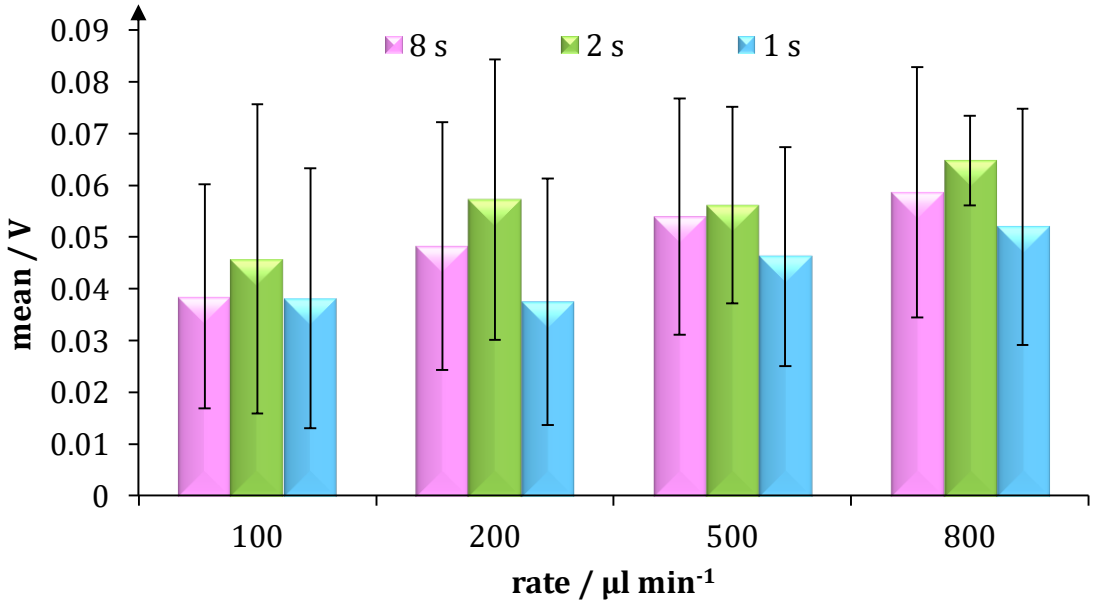

Figure 70 shows the average photodiode voltage at various averaging time constants and pumping rates.

Finally, the necessity of the withdraw function was investigated. Figure 71 shows that when the withdraw function was deactivated (and evaporation was utilised to return the liquid height to within acceptable limits), the average values increase across all pumping rates (although it should be noted that these are not statistically significant differences). This can be justified by the evaporation rate being so much slower that, on average, the liquid height spends more time above optimum levels than below where the pump is active. As the pumping rate increases this effect is exacerbated as comparatively more liquid volume is infused, thus resulting in higher liquid levels that can only be counteracted by evaporation.

Ultimately, the ideal parameters are reached when the means lie between the upper and lower boundary limits. The data shown in this section demonstrates that all programmable variables are statistically equally good at maintaining the liquid height. However, general trends across all data sets show that by minimising the rate and time constants, the mean value of the data is lowered and thus more likely to exist within the defined limits of the program. Thus in conclusion, the programmable parameters can be confidently varied depending on experimental requirements with little change in the effectiveness of the liquid monitor's functionality. However, the recommended starting point for the program is a 1 s time average with a pump rate of 100 µl min^{-1} and then the parameters can be increased from that point with confidence.

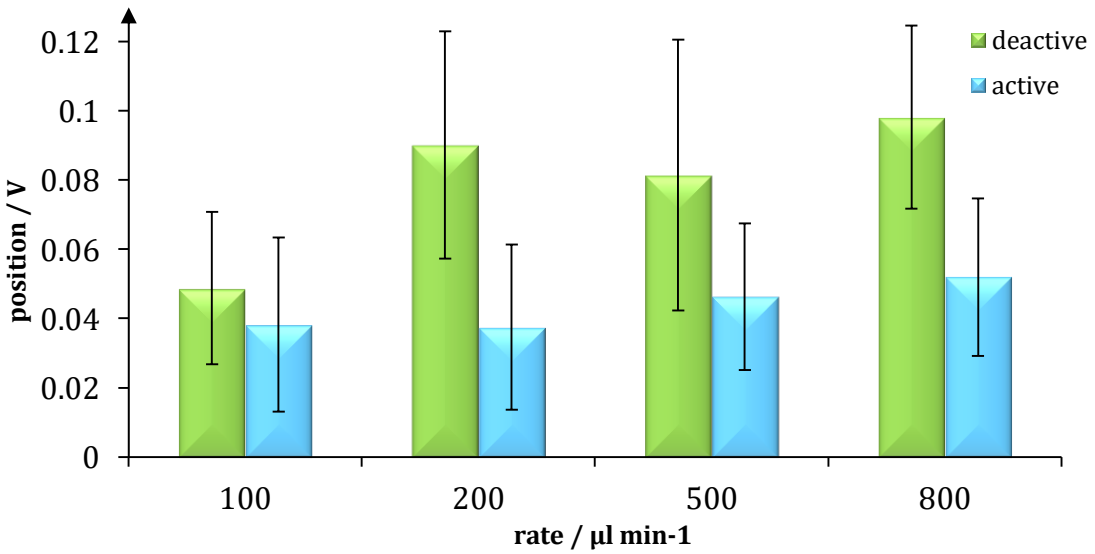

Figure 71 shows the average photodiode output with the withdraw function activated and deactivated.

B – THEORY OF NON-LINEAR SPECTROSCOPY

B.1. LORENTZ OSCILLATOR MODEL

When electromagnetic radiation is incident on a dielectric material, the charge distribution is altered to generate dipoles that contribute to the field. If the material has polar constituents, then the dipoles align with the field resulting in orientational polarisation. If the material is composed of non-polar constituents, then the field distorts the electron cloud, inducing dipoles to align with the field. In the case of a harmonic incident wave, the field will oscillate, forcing the permanent and induced dipoles to follow the oscillation in order to stay aligned with the field. However, as molecules are large with significant moments of inertia, at sufficiently high driving frequencies, ω, the molecules will be unable to follow the driving field oscillation. In contrast, electrons are light and can maintain the oscillation at large frequencies and, therefore, the electron motion can be used to describe the optical properties of a material.[154,156,300] The following discussion can be found in many standard textbooks, with that presented in this section based on the works of Boyd[154], Hecht[156], Wooten[300] and Brevet[301].

The Lorentz oscillator model considers the positive electrostatic force from the nucleus acting on the electrons, keeping them in some equilibrium position, as analogous to a harmonic oscillator with the electrons attached to the infinitely heavy nucleus by a harmonic spring. In the absence of a force to drive the displacement, the electron oscillates around the equilibrium position called its natural frequency, ω_0, which is defined as:

$$\omega_0 = \sqrt{\frac{k_{\mathrm{E}}}{m_e}}\,, \tag{75}$$

where m_e is the electron mass and k_{E} is the elastic force constant. When a force acts on the electron, a restoring force acts in opposition to return it to its equilibrium state. At small displacements, this force is considered to be linearly proportional to position, x, and can thus be described by Hooke's Law as:

$$F_{\mathrm{R}} = -k_{\mathrm{E}}x = -m_e\omega_0^2 x\,. \tag{76}$$

When an electromagnetic field is incident on the medium, the electron oscillation is driven by the field $\tilde{E}(t)$. The time dependent force, $F_{\mathrm{E}}(t)$, exerted on the electron, with charge $-e$, by the field is expressed as:

$$F_{\mathrm{E}}(t) = -e\tilde{E}(t)\,. \tag{77}$$

The total field can now be expressed as the sum of F_{R} and $F_{\mathrm{E}}(t)$. However, this total force neglects to account for the behaviour of the oscillator at resonant frequencies, where the imaginary component of the refractive index is responsible for the absorption of the incident light and dampening of the oscillator motion.[302] To ensure continuity across resonant frequencies, the damping force must be introduced to the total force with a damping constant, γ:

$$F_{\mathrm{damp}} = m_e\gamma\frac{dx}{dt}\,. \tag{78}$$

Using Newton's second law of motion ($F = ma = m\ddot{x}$) the equation of motion can be written as follows in the harmonic model:

$$\frac{d^2x}{dt^2} + 2\gamma\frac{dx}{dt} + \omega_0^2 x = -\frac{e}{m_e}\tilde{E}(t). \tag{79}$$

It should be noted that the factor of 2 has been included here for convenience.[301] This equation can be solved for displacement $x(t)$ to give the solution

$$x(t) = \frac{-e}{m_e}\frac{1}{(\omega_0^2 - \omega_j^2 - 2i\omega_j\gamma)}\left(\frac{1}{2}\left\{E_0 e^{-i\omega_j t} + c.c.\right\}\right), \tag{80}$$

where j refers to the incident field. This result can now be used to define the linear susceptibility, $\chi^{(1)}(\omega_j)$, using Equation (12) and the relation $P = -Nex(\omega, t)$ where N is the number density of atoms.

$$P^{(1)}(\omega_j, t) = \varepsilon_0\chi^{(1)}(\omega_j)E(\omega_j, t) = -Nex(\omega_j, t)\,, \tag{81}$$

$$\therefore\ \chi^{(1)}(\omega_j) = \frac{Ne^2}{\varepsilon_0 m_e}\frac{1}{(\omega_0^2 - \omega_j^2 - 2i\omega_j\gamma)}\,. \tag{82}$$

This Lorentz model works well at small displacements, within the linear optical response, but accounting for nonlinear optical behaviour requires extension an anharmonic oscillator model. The following analysis is only applicable to noncentrosymmetric materials with a different analysis required for media containing a centre of inversion symmetry. The analysis for centrosymmetric media will not be touched upon here due to second order optical nonlinearity being forbidden in such materials.

B.2. ANHARMONIC OSCILLATOR MODEL

The anharmonicity in noncentrosymmetric materials can be accounted for by including nonlinearity in the restoring force:

$$F_{\mathrm{R}'} = -m_e(\omega_0^2 x - ax^2)\,, \tag{83}$$

where a is a parameter that describes the strength of the nonlinearity. The corresponding anharmonic potential energy becomes

$$U(x) = -\int F_{\mathrm{R}'}\,dx = -m_e \int \omega_0^2 x + ax^2\,dx \tag{84}$$

$$U(x) = -\frac{1}{2}m_e\omega_0^2 x^2 + \frac{1}{3}m_e a x^3\,, \tag{85}$$

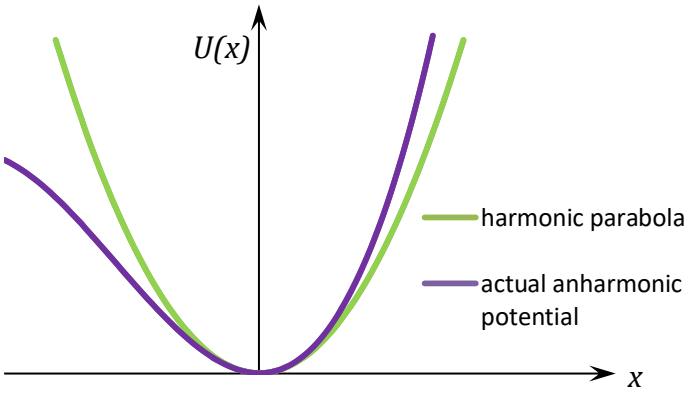

Figure 72 shows the potential energy function for a noncentrosymmetric material. Figure adapted from Boyd.

and contains a harmonic component and an anharmonic correction term, which is illustrated in Figure 72.

By substituting F_{R} for F_{R}, in Equation (79), we obtain the anharmonic equation of motion

$$\frac{d^2x}{dt^2} + 2\gamma\frac{dx}{dt} + \omega_0^2 x + ax^2 = -\frac{e}{m_e}\tilde{E}(t). \tag{86}$$

If the field is assumed to be a monochromatic wave of the form

$$\tilde{E}(t) = E_0\cos(\omega t) = \frac{1}{2}\left\{E_0 e^{-i\omega t} + E_0^* e^{+i\omega t}\right\}, \tag{87}$$

the wave equation can be solved for the displacement. However, there is no known solution for a generic optical field of the form given in Equation (87). As such, perturbation theory is employed in which $\tilde{E}(t)$ in Equation (86) is replaced by $\lambda\tilde{E}(t)$

$$\frac{d^2x}{dt^2} + 2\gamma\frac{dx}{dt} + \omega_0^2 x + ax^2 = -\frac{e}{m_e}\lambda\tilde{E}(t), \tag{88}$$

where λ is the expansion parameter that characterises the strength of the perturbation and varies continuously between 0 and 1. A solution of the form

$$x(t) = \sum_{i=1}^{\infty}\lambda^i x^{(i)}(t) = \lambda x^{(1)}(t) + \lambda^2 x^{(2)}(t) + \lambda^3 x^{(3)}(t) + \cdots, \tag{89}$$

is required. In order to find a solution for any value of λ, every component proportional to λ^i needs to be considered separately to satisfy Equation (88). This yields the following set of equations

$$\frac{d^2x^{(1)}}{dt^2} + 2\gamma\frac{dx^{(1)}}{dt} + \omega_0^2 x^{(1)} = -\frac{e}{m_e}\tilde{E}(t), \tag{90}$$

$$\frac{d^2x^{(2)}}{dt^2} + 2\gamma\frac{dx^{(2)}}{dt} + \omega_0^2 x^{(2)} + a\left(x^{(1)}\right)^2 = 0, \tag{91}$$

$$\frac{d^2x^{(3)}}{dt^2} + 2\gamma\frac{dx^{(3)}}{dt} + \omega_0^2 x^{(3)} + ax^{(1)}x^{(2)} = 0, \tag{92}$$

to be solved. It should be noted that Equation (90) does not contain the anharmonic correction term because $x^{(1)}(t)$ is the linear displacement. As $x^{(2)}(t)$ represents the second order nonlinear displacement, this is the lowest order term in which anharmonicity is present.

It can be seen that substitution of the linear displacement, $x^{(1)}(t)$, into the wave equation yields the same equation as the harmonic oscillator Lorentz model wave equation given in Equation (79). This equation can again be solved for displacement $x^{(1)}(t)$ as shown in the previous section with the result given in Equation (80). Squaring this term and substituting it into Equation (91) allows the derivation of the lowest order correction term solution, $x^{(2)}(t)$. By using the steady state approximation, $x^{(2)}(t) = x^{(2)}(2\omega_j)\left(e^{-2i\omega_j t} + c.c.\right)$, a solution for the amplitude of the motion of the electron displacement, $x^{(2)}(2\omega_j)$, can be derived:

$$x^{(2)}(2\omega_j) = -\frac{ae}{m_e^2}^2 \frac{E_0^2}{\left(\omega_0^2 - \omega_j^2 - 2i\omega_j\gamma\right)^2\left(\omega_0^2 - \left(2\omega_j\right)^2 - 4i\omega_j\gamma\right)}. \qquad (93)$$

Just as with the linear susceptibility, this result can be used to define the nonlinear susceptibility, $\chi^{(2)}(2\omega_j, \omega_j, \omega_j)$ where

$$P^{(2)}(2\omega_j, t) = \varepsilon_0\chi^{(2)}(2\omega_j, \omega_j, \omega_j)E^2(\omega_j, t) = -Nex^{(2)}(2\omega_j, t), \qquad (94)$$

$$\therefore \chi^{(2)}(2\omega_j, \omega_j, \omega_j) = \frac{Nae^3}{\varepsilon_o m_e^2}\frac{1}{\left(\omega_0^2 - \omega_j^2 - 2i\omega_j\gamma\right)^2(\omega_0^2 - (2\omega_j)^2 - 4i\omega_j\gamma)}. \qquad (95)$$

Equation (95) therefore shows that $\chi^{(2)}$ is resonantly enhanced when ω_j or $2\omega_j$ are close to a natural frequency, ω_0, which would correspond to a resonant transition in a material or molecule.[206]

B.3. SECOND ORDER NONLINEAR SUSCEPTIBILITY

As can be seen in Equation (15) the second order nonlinear susceptibility, $\chi^{(2)}$, is a proportionality constant that relates the macroscopic polarization to the externally applied electric field in a lossless and dispersionless material.

However, as only vacua are non-dispersive in nature, a more general case is required for materials that exhibit dispersion and/or loss. In this instance $\chi^{(2)}$ becomes a complex quantity with both real and imaginary components that relate the complex amplitudes of the applied electric field and polarization.[154]

Thus far we have used the macroscopic Lorentz model to describe the response of the electrons to the applied electric field, assuming that the response of each electron to the applied electric field is unaffected by the response of the oscillators around it.[154,301] This assumption thus fails to account for the local electric field felt by each oscillator. The optical properties therefore need to be explored at the molecular level in order to define the susceptibilities observed at the macroscopic level.

B.3.1. POLARIZABILITY AND HYPERPOLARIZABILITY

The detailed information on which the following discussion is based can be found in any standard quantum mechanics textbook though the working here is largely founded on the work in Atkins.[303] It will be assumed henceforth that the electric field is constant across the whole material, and therefore multipole interactions can be neglected. As any wave can be formed by the superposition of simple harmonic waves at different frequencies, the optical electric field can be written in terms of the field strength or varying field amplitude, $A(\omega_n)$, unit vector, k, and frequency, ω_n:[154]

$$\tilde{E}(r,t) = \sum_n A(\omega_n) e^{i(k_n \cdot r - \omega_n t)}. \tag{96}$$

In the pursuit of keeping the notation as simple as possible, it will be assumed that the field is only applied in the z direction and therefore will be expressed as

$$E = A_n k\,, \tag{97}$$

where A_n represents the field strength and k the unit vector in the z-axis.

In the absence of an applied electric field, the only dipole present in the z-axis must be a permanent dipole. Thus, it is reasonable that the averaged dipole value

over all orientations, $\langle\mu_z\rangle$, be defined as the change in energy y, E, with respect to the field strength,[303]

$$\left(\frac{dE}{dA_n}\right) = -\langle\mu_z\rangle\,. \tag{98}$$

When an electric field is applied, the molecular energy can be expressed as a Taylor series expansion:

$$E = E(0) + \left(\frac{dE}{dA_n}\right)A_n + \frac{1}{2!}\left(\frac{d^2E}{dA_n^2}\right)A_n^2 + \frac{1}{3!}\left(\frac{d^3E}{dA_n^3}\right)A_n^3 + \cdots, \tag{99}$$

where $E(0)$ indicates the molecular energy in the absence of an applied field. Taking the first derivative with respect to the field strength and substituting the result into Equation (99) we obtain:

$$\langle\mu_z\rangle = -\left(\frac{dE}{dA_n}\right) - \left(\frac{d^2E}{dA_n^2}\right)A_n - \frac{1}{2}\left(\frac{d^3E}{dA_n^3}\right)A_n^2 + \cdots, \tag{100}$$

$$\therefore \langle\mu_z\rangle = \mu_{0z} + \alpha_{zz}A_n + \beta_{zzz}A_n^2 + \cdots\,. \tag{101}$$

Equation (101) shows that, in the presence of an electric field the dipole expectation value in the z-direction is equal to the permanent dipole moment, μ_{0z}, plus the dipole moment induced by the field with the polarizability, α, indicating the strength of the linear response, and the first hyperpolarizability, β, defining the second-order nonlinear response.

The polarizability is described as a second rank tensor and the notation used in Equation (101) characterises this. At the beginning of this discussion, it was stated that the applied field was only in the z-direction. The induced dipole can, however, have character in the x-, y- and z-directions, represented as μ_x, μ_y, and μ_z, respectively, where

$$\mu_x = \alpha_{xz}E_z\,. \tag{102}$$

Therefore, when the field is applied in the z-direction, there are three contributions to the polarizability; α_{xz}, α_{yz} and α_{zz}. This then gives a 3×3 matrix

when the contributions from the applied field in the *x*- and *y*- directions are included.

A similar rationalisation applies to the hyperpolarizability, except now there are three subscripts included in β due to the hyperpolarizability being a third rank tensor. The hyperpolarizability can be thought of as a measure of strength of the induced dipole response after interacting with two fields:

$$\mu_x = \beta_{xyz} E_y E_z \,. \tag{103}$$

Equation (103) therefore indicates that β_{xyz} measure the strength of the induced dipole in the *x*-direction when it interacts with the electric field applied in the *y*-direction, after the molecule has already interacted with a field applied in the *z*-direction. Thus β_{xyz}, β_{xxz}, β_{xzx}, β_{xxx}, β_{xzy}, β_{xyy}, and β_{xzz} all measure the induced dipole in the *x*-direction.

In order to relate the molecular properties of polarizability and hyperpolarizability to the macroscopic property of polarization, the local electric field needs to be considered. If we consider that $\tilde{P}(t)$ is equal to the dipole moment density, then it follows that the polarization will be equal to the average dipole moment multiplied by the number density of molecules, $\mathcal{N} = N/V$. If it is assumed that the molecules are non-polar, the lowest order contribution to the average dipole will be the linearly induced dipole moment. Therefore, using the relation between the linearly induced dipole and polarizability tensor given in Equation (102), the polarization can be defined as

$$\tilde{P}(t) = \alpha \mathcal{N} \tilde{E}_{\text{local}}(t) \,, \tag{104}$$

where $\tilde{E}_{\text{local}}(t)$ is the local electric field felt by each oscillating electron in the material. The Lorentz local field can thus be used to approximate the relationship between $\tilde{E}_{\text{local}}(t)$ and the externally applied field, $\tilde{E}(t)$

$$\tilde{E}_{\text{local}}(t) = \tilde{E}(t) + \frac{\tilde{P}(t)}{3\varepsilon_0}. \tag{105}$$

Substitution of Equation (105) into Equation (104) yields an expression for the macroscopic polarization that accounts for the local field and can then be cross referenced with Equation (12) to give the relationship between the polarizability and the linear susceptibility constant

$$\chi^{(1)} = \frac{\alpha\mathcal{N}}{\varepsilon_0\left(1 - \frac{\alpha\mathcal{N}}{3\varepsilon_0}\right)}. \tag{106}$$

In the nonlinear optical case, the Lorentz local field still applies, but now the polarization has both linear and nonlinear contributions:

$$\tilde{E}_{\text{local}}(t) = \tilde{E}(t) + \frac{\tilde{P}_{\text{L}}(t) + \tilde{P}_{\text{NL}}(t)}{3\varepsilon_0}. \tag{107}$$

After a similar analysis as shown above, and given in detail in Boyd,[154] the second-order nonlinear susceptibility for SHG can be shown to be the statistical average of the molecular hyperpolarizabilities, where the indices i, j and k can each be x, y or z.[304]

$$\chi^{(2)}_{ijk}(2\omega, \omega, \omega) = \mathcal{L}^{(2)}(2\omega, \omega, \omega)\mathcal{N}\langle\beta_{ijk}(2\omega, \omega, \omega)\rangle_{ijk}\,, \tag{108}$$

where $\varepsilon^{(1)}$ represents the linear dielectric permittivity and with

$$\mathcal{L}^{(2)}(2\omega, \omega, \omega) = \left(\frac{\varepsilon^{(1)}(2\omega) + 2}{3}\right)\left(\frac{\varepsilon^{(1)}(\omega) + 2}{3}\right)^2. \tag{109}$$

The important point here is that $\chi^{(2)}$ is proportional to the number density of molecules and, therefore, measurement of $\chi^{(2)}$ can be used as a direct measure of solution concentration.[13, 14]

B.3.2. PROPERTIES OF $\chi^{(2)}$

Using notation similar to Equation (96), the nonlinear polarization can be expressed as

$$\tilde{P}^{(2)}(r, t) = \sum_n P^{(2)}(\omega_n)e^{-i\omega_n t}\,. \tag{110}$$

Cross referencing this with Equation (15) yields a general expression for the SFG polarization amplitude of the nonlinear signal at frequency ω_{n+m} in terms of the two externally applied field amplitudes at frequency ω_n and ω_m,

$$P_i^{(2)}(\omega_3) = \sum_{jk} \chi_{ijk}^{(2)}(\omega_{n+m}, \omega_n, \omega_m)\, E_j(\omega_n) E_k(\omega_m)\,. \tag{111}$$

In order to fully characterise the interaction of the three waves (the two incident waves and the frequency mixed wave), there are 12 tensors that need to be identified, the six shown below plus the six produced when each frequency is substituted by its negative.

$$\chi_{ijk}^{(2)}(\omega_{n+m}, \omega_n, \omega_m) \qquad \chi_{ijk}^{(2)}(\omega_m, \omega_{n+m}, -\omega_n) \qquad \chi_{ijk}^{(2)}(\omega_n, \omega_{n+m}, -\omega_m)$$

$$\chi_{ijk}^{(2)}(\omega_{n+m}, \omega_m, \omega_n) \qquad \chi_{ijk}^{(2)}(\omega_m, -\omega_n, \omega_{n+m}) \qquad \chi_{ijk}^{(2)}(\omega_n, -\omega_m, \omega_{n+m})$$

As each of these 12 tensors has 27 different components, there are a 324 complex numbers needed to fully characterise the second order interaction.[154] However, using a series of symmetry arguments, this number can be dramatically reduced and it is the intention to show, by the end of this section, that to characterise SHG interactions, there are only three independent tensor elements to consider.

B.3.3. SYMMETRY

The first symmetry restriction that can be applied arises from intrinsic permutation theory. The indices i, j, k, m and n used in Equation (111) are known as dummy indices and, therefore, Equation (111) could be equally be written with n and m, and j and k interchanged.[154] This leads to the symmetry condition that

$$\chi_{ijk}^{(2)}(\omega_{n+m}, \omega_n, \omega_m) = \chi_{ikj}^{(2)}(\omega_{m+n}, \omega_m, \omega_n)\,, \tag{112}$$

which reduced the 27 elements of each third rank tensor to 18 independent components. To further reduce the number of nonvanishing independent elements in the $\chi_{ijk}^{(2)}$ tensor, the symmetry of the material itself needs to be considered. This follows from Neumann's principle in which it is stated that the symmetry properties of any physically observable property must fundamentally

match the symmetry point group of the material itself.[306] The optical media studied using SHG in the experiment presented in this work differ, however, in all instances it is only the liquid surface that is probed due to SHG being formally forbidden in the centrosymmetric bulk material. As such, the symmetry of a generic surface can be applied. There are a number of different surface symmetry classes possible, discussed in detail by Guyot-Sinnest *et al.*.[204] If we consider the isotropic surface to lie in the *x*-*y* plane, with the *z*-axis normal to the surface, its point group can be identified as a $C_{\infty v}$ surface with two mirror planes normal to the surface in the *y*-*z* and *x*-*z* planes, as well as infinite possible rotations around the *z*-axis. This symmetry behaviour is therefore the same as the point groups C_{4v}, C_{6v}, $4mm$, and $6mm$ and can be found through any of these point group tables. Thus, only 7 nonzero elements of $\chi_{ijk}^{(2)}$ are present and can be identified to be

$$\chi_{xxz}^{(2)}, \chi_{xzx}^{(2)}, \chi_{yzy}^{(2)}, \chi_{yyz}^{(2)}, \chi_{zxx}^{(2)}, \chi_{zyy}^{(2)}, \chi_{zzz}^{(2)}, \tag{113}$$

However, these elements are not all independent. It should be fairly clear that the elements $\chi_{xxz}^{(2)}$ and $\chi_{xzx}^{(2)}$ are equal due to the intrinsic permutation symmetry. Additionally, the symmetry of the surface has the consequence that the *x*- and *y*-axes are considered to be identical. As such the optical response should be identical for any of the incident waves or the output SHG signal polarized in either of these directions.[154,204] Using these symmetry restrictions, it can be shown that the 7 elements in Equation (113) yield only 3 independent susceptibility tensor elements present:

$$\begin{gathered} \chi_{xxz}^{(2)} = \chi_{xzx}^{(2)} = \chi_{yzy}^{(2)} = \chi_{yyz}^{(2)}, \\ \chi_{zxx}^{(2)} = \chi_{zyy}^{(2)}, \\ \chi_{zzz}^{(2)}. \end{gathered} \tag{114}$$

Kleinman's symmetry, based on the assumption that the incident wave frequencies lie far below the lowest resonance frequency, ω_0, is often discussed in relation to the susceptibility. However, as the basis of the experiment

presented in this work uses resonances to enhance the SHG signal, Kleinman's symmetry does not apply here.

B.3.2. MAGNITUDE

As a final remark on susceptibilities, it should be noted that the anharmonic oscillator fails to correctly predict the linear and nonlinear response magnitude, due to the assumption that only internal vibrations of a given material contribute. In practice, the majority of SHG and SFG experiments use frequencies in or near the visible region, far above vibrational resonances. Thus it is the electronic, not the vibrational, degrees of freedom, from which nonlinear behaviour originates.[307] By considering this, $\chi^{(1)}$ can be deduced to be of the order of unity and $\chi^{(2)}$ of the magnitude of 10^{-12} m V^{-1}.[154]

C – INTERESTING APPLICATIONS OF NON-LINEAR SPECTROSCOPY

C.1. HOMODYNE VSFG

In 1993 Du *et al.* published an important study showing that 20% of the surface water molecules in a pure water sample had one free OH. Analysis of the orientation, using symmetry arguments and different polarization combinations, concluded that this free OH points out of the liquid, with the other hydrogen bonded with the bulk. This structure was confirmed by terminating the free OH bond using hydrogen terminated quartz,[232] or alcohol monolayers,[219] which in both cases resulted in a VSFG spectrum comparable to the IR spectra of ice. These spectra are shown in Figure 73.[219] Comparison of this result with that of hydrophobic surfaces and water, including the hexane/water interface, revealed similarities between the spectra that resulted in the conclusion that hydrophobic interactions can be characterised by the presence of free OH bonds across an interface. Furthermore, if the hydrophobic surface is rigid i.e. a solid, a larger degree of ordering in the water is observed when compared to liquid/liquid and liquid/air interfaces. This result provided a physical model for wetting at a surface on a molecular level for the first time and is impactful in multiple areas of scientific understanding.[233]

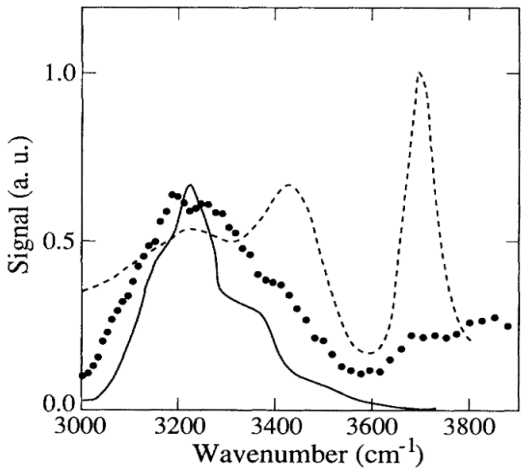

Figure 73 shows the SFG spectrum of pure water (dashed line) with SSP polarization combination, the SFG spectrum of water with a monolayer of alcohol (dots) and the IR absorption spectrum of ice (solid line)/ Reprinted with permission from Du *et al.,* Phys. Rev. Lett., **70**, 2313, 1993. Copyright (2018) by the American Physical Society.

Although the theory of dangling OH bonds at the interface has received little criticism, in contrast the assignment of the double peak structure between 3200 and 3600 cm^{-1} has been much debated. The initial interpretation by Shen's group was that the two peaks arise from two interfacial resonances of varying hydrogen bond strength i.e. 'ice-like' with tetrahedrally hydrogen bonded molecules and 'liquid-like' distorted structures.[232] However many theories have been proposed to explain the existence of the two band structure including (but not limited) to intramolecular vibrational coupling of the two OH oscillators in one molecule to generate symmetric and asymmetric stretching bands. In 2008, Sovago *et al.*[245] proposed a new theory in which the symmetric stretching vibration is quantum mechanically mixed with the bending overtone to result in a splitting, otherwise known as a Fermi resonance. By using a series of isotopic dilution studies, the simplification of the water spectra could be observed (due to the decoupling of the two OH/D bonds in HDO) and it was revealed that the double peak structure vanishes with increasing HDO concentration. If the double peak structure was a consequence of different structural environments (i.e. ice-like/water-like), it would be expected that on isotopic dilution the double band would remain, therefore, the merging of the band to one peak implies that there is splitting of the normal symmetric mode or intramolecular coupling. This conclusion supported the prior work of Raymond *et al.*[308] that stated the water interfacial structure was more liquid-like than initially expected. However, the findings from all of these studies are far from definitive as the resonance spectrum (i.e. the imaginary component) has not been directly measured and is instead inferred from fitting procedures. Therefore, in order to come to any physically meaningful conclusion, it became evident that phase resolved studies would be necessary to act as a standard for computational studies to compare to.

C.2. PHASE SENSITIVE VSFG

The following discussion will therefore focus on the two most relevant phase sensitive VSFG studies to the work in the main body of the thesis; experiments

that utilise the phase sensitivity to determine molecular orientation; and experiments that probe the air/water interface.

C.2.1. AIR/WATER INTERFACES

Attempts to fit OH resonances to the $\left|\chi^{(2)}_{\mathrm{S,eff}}\right|^2$ spectrum, both computationally and experimentally resulted in a variety of conclusions and academic debate, especially regarding the double peak nature (for the reasons already discussed). However, the majority of researchers agreed that they expected $Im\left(\chi^{(2)}_{\mathrm{S,eff}}\right)$ to be negative for all vibrations excluding the dangling, partially unbounded OH groups. As such, it was believed that all other OH bond dipoles would point into the liquid.[242,309–311] This paradigm was shifted in 2007 with the publication of the first $Im\left(\chi^{(2)}_{\mathrm{S,eff}}\right)$ spectrum by Ji *et al.*[312]. In a phase resolved study, the group showed that the imaginary $\chi^{(2)}$ spectra exhibited a change of phase from negative to positive at low frequencies. This observation had never before been hypothesised via fitting methods or shown through computational calculations and thus affirmed the importance of phase sensitivity measurements. The group's physical interpretation of their result manifested as an extension of their earlier proposed ice-like/liquid-like structure with a dynamic hydrogen bond

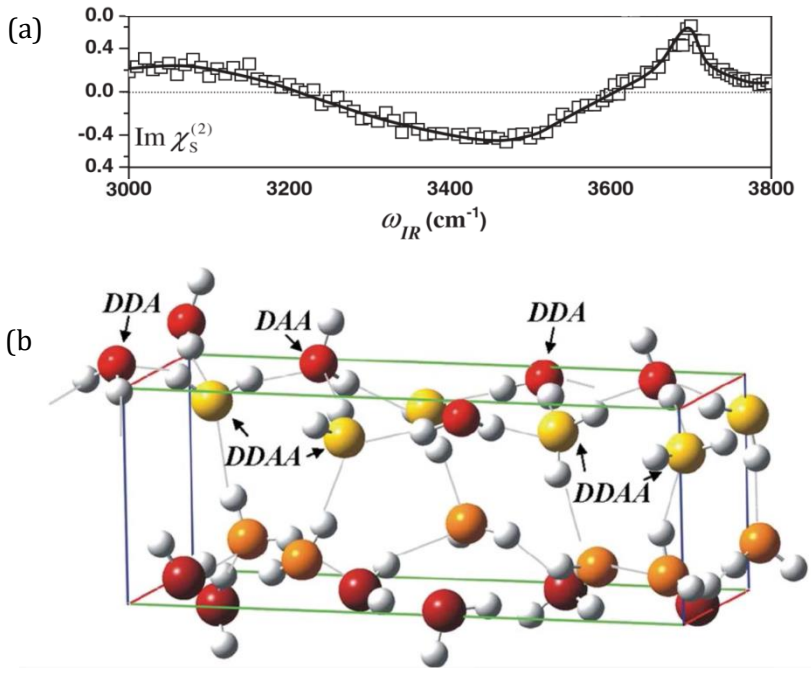

Figure 74 (a) shows the imaginary spectra measured for the air/water interface, (b) schematically shows a cartoon molecular model of the interpreted results for the water/vapour interface. Reprinted with permission from Ji *et al.,* Phys. Rev. Lett., **100**, 096102, 2008. Copyright (2018) by the American Physical Society.

structure varying in strength from the hydrogen donors (D) to the oxygen atom acceptors (A). The model proposed is schematically characterised in Figure 74(b) and shows three different water molecule structures; DDA, DAA and DDAA. The first two environments characterise molecules at the interface with incomplete hydrogen bonding (due to truncation), and the latter case indicates molecules with a complete hydrogen bond network just below the interfacial layer. Cross-reference of this to the imaginary spectra shown in Figure 74(a) reveals that the sharp peak at 3700 cm^{-1} is attributed to the stretch of the dangling OH bond of the DAA molecules, whilst the other OH bond in the DDA molecules would have a dipole moment pointing towards the bulk liquid and therefore contribute to the negative band bellow 3600 cm^{-1}. This however is only the case if the bonds are decoupled due to strong hydrogen bonds between the donor on the DDA and the acceptor on another molecule. If this bond is weak, this approximation is no longer valid and the DDA molecule instead possesses asymmetric and symmetric stretches, both with transition dipoles pointing towards the interface. This is argued to be the origin of the broadening of the base of the positive peak at ~3700 cm^{-1}. The broad negative peak is considered to resemble the interfacial molecules that are bulk liquid-like and therefore is mainly attributed to the hydrogen bonded OH stretching modes of the DDA and DAA molecules and DDAA molecules with asymmetric hydrogen bond strengths. At first it may appear surprising that there is any orientational preference for the DDAA molecules as one might expect the transition dipoles to exactly cancel out due to the isotropic liquid nature. However, at the interface the DDAA molecules necessarily act as acceptors for the donors in the DA and DDA interfacial molecules and therefore, at the interface, there is a net preference for the OH bonds of DDAA molecules to point towards the bulk liquid, contributing to the negative band. [312]

The only band now left unassigned is the positive peak below ~3700 cm^{-1}. Shen's group interpret this peak as being the symmetric stretch of ice-like structure of strongly and symmetrically hydrogen bonded DDAA groups, of which the main contribution arises at the interface by straddling DDA and DAA molecules. This ice-like interpretation was supported by the phase sensitive measurement of ice, which showed a positive peak that switched sign at higher frequencies. This

indicates that ice has a maintained symmetric bonded structure and at the interface ordering of the hydrogen bonded network is necessarily more rigid than the bulk due to restricted degrees of freedom.

In an attempt to give credit to their increasingly controversial ice-like/liquid-like structure, Shen and Tian quickly published a parallel study to the isotopic dilution study by Raymond *et al.*[308] that used phase sensitive techniques to derive the HOD/air interface spectra from several isotopic mixtures.[313] The advantage of the imaginary HOD spectrum is that the OH/OD bonds are decoupled and therefore the spectrum is a direct measure of orientation, without non-resonant contributions, and thus a good starting point for computational modelling. By approximating an isotropic mixture as a linear combination of the two pure isotropic components, the HOD/air spectrum was produced by subtraction of the pure component contributions in a $H_2O/HDO/D_2O$ spectrum. It was observed that the HOD spectra exhibited the same positive peak at low frequencies as H_2O, but the cross over point between positive and negative phases is blue shifted due to the decoupling. These positive and negative peaks are exhibited at the characteristic IR resonances of HOD ice, supporting the interpretation of the positive band is largely due to the symmetrically hydrogen bonded ice-like DDAA molecules just below the interface. However, it is only in combination with theoretical models that this can be verified.

Producing computational spectra of the air/water interface has been a long standing challenge for theoreticians. Before Shen's seminal publication of the $Im(\chi^{(2)})$ spectrum, all theoretical calculations had failed to predict the positive peak exhibited at low frequencies.[309,311] The first theoretical study that produced this peak was generated by Ishiyama and Morita by accounting for intermolecular correlations that generate local anisotropic fields in the interface. This can be physically interpreted as there being strong lateral orientational preferences of the hydrogen bonded pairs to the DAA molecules, which is induced by the limited number of orientations possible for the dangling OH, and therefore not related to a tetrahedrally ice-like structure at all.[314] This model was further supported by the work of Tahara who used the same molecular dynamics

model to generate the HOD/vapour spectrum, yielding the same conclusions.[315] Another physical interpretation arose from MD calculations using a water simulation method designed by Pieniazek *et al.*[316] called E3B. This method included three body interactions important in liquid systems and successfully reproduced the positive peak in $Im(\chi^{(2)})$ at low frequencies. This was interpreted by Pieniazek *et al.* to be a direct indication that three body interactions enhance tetrahedral structure at the interface.[317]

Even more uncertainty was introduced to this already complex situation with the recent publication of several experimental measurements that did not observe the positive phase at low frequencies. In a comprehensive study by Nihonyanagi *et al.*[248], it was concluded that the positive peak is an experimental artefact. It was hypothesised that the reason so many groups have observed the same result, though magnitude often differs, is because quartz is the reference of choice in the large majority of studies. By using a non-resonant liquid reference, such as D_2O, to normalise the spectra instead of quartz, the phase measurement error is significantly reduced and the positive feature is almost completely cancelled. This theory was thoroughly investigated with a variety of different experimental set ups, including reversing the positions of the LO and the sample, as well as other non-resonant liquid references; the same result was always observed. Yamaguchi also reported the same findings in an independent paper published around the same time.[318] The observation that the positive peak intensity is reduced after cleaning of the quartz sample suggests that the quartz may, with time, accumulate contaminants on its surface which could then explain the change in magnitude of the signal across groups. The experimental spectra published were quickly reproduced computationally by Medders and Paesani using a sophisticated level of theory in many body MD simulations.[317] However, the significance of this is rather diluted by the fact that, before Shen's positive results, spectra were already being calculated that showed this behaviour, and it was only after the work of Ji *et al.*[312] that these calculations were deemed not to correctly represent the air/water interface.

The evidence presented by Tahara's group is extremely compelling and implies that liquid references could provide a more appropriate RS akin to the sample,

resulting in a more accurate phase measurement, especially in the non-collinear geometries where the flatness of the surface can dramatically affect the measurements. This however only appears to be significant if a high level of phase accuracy is required as it is noted that the quartz reference produces the same spectra as the D_2O spectra within experimental error.[248]

C.2.2. MOLECULAR ORIENTATION

Linear optical spectroscopy can be used to measure molecular dipole alignment, but to measure the orientation (i.e. up vs. down) requires the use of nonlinear and phase sensitive techniques.[319] The determination of the dipole sign affords great insight into the understanding of molecular structure. The same can be said of the molecular polarizability and hyperpolarizability, which are shown by Equations (100) and (101) to be the second and third derivative of the molecular energy with respect to the applied field.[320] In fact, polarizability has been shown to be one of the most important factors for anions when considering their propensity for existing at an interface.[321]

Resonant excitation is necessarily accompanied by a transition dipole or polarizability moment, defined as the derivatives of the dipole and linear polarizability with respect to the normal mode, respectively. The magnitudes of these derivatives are easily measured by absorption and Raman techniques, but the sign of the derivative is lost. However, for an isotropic distribution in the surface, the following relation can be shown to be true[320]:

$$\chi^{(2)}_{\mathrm{S,eff}} \propto \frac{\partial \mu_\xi}{\partial r}\frac{\partial \alpha_{\xi\xi}}{\partial r}, \tag{115}$$

where ξ is a specific bond axis with bond length r. Thus, the sign of $\chi^{(2)}_{\mathrm{S,eff}}$ can be determined if the sign of one derivative is known. Superfine *et al.* use the theoretical studies of Gough and co-workers to justify that for C-H bonds of any degree of hybridization, the sign of $\partial\alpha_{\xi\xi}/\partial r$ is always positive. This means that for hydrocarbon systems, the sign of $\chi^{(2)}_{\mathrm{S,eff}}$ is a direct indication of the dipole orientation.

The sign of $Im\left(\chi^{(2)}_{\mathrm{S,eff}}\right)$ at resonances and its relation to the molecular orientation was elegantly demonstrated by Ji *et al.*[254]. The phase sensitive VSFG study focused on an octadecyltrichlorosilane, OTS, monolayer on a silica substrate. The results are given in Figure 75, and show that the peaks at 2873 and 2935 cm^{-1} (corresponding to the symmetric stretch and bending mode of the terminal methyl, respectively), have a positive sign and thus indicate that the average orientation of the methyl groups is pointing out of the surface, away from the bulk substrate. In contrast the weak negative peak in the $Im\left(\chi^{(2)}_{\mathrm{S,eff}}\right)$ spectrum at 2847 cm^{-1} is related to the methylene chain symmetric stretch. The weakness is interpreted to be an indication that the methylene chains lie flat on the surface, and the negative amplitude an indication that the net dipole moment points towards the substrate, possibly due to gauche effects along the chain.[254]

The work of Gan *et al.*[244] showed that the phases of the individual elements of the nonlinear susceptibility tensor can be used to determine the absolute molecular orientation of the molecules at an isotropic surface using the relation

$$\chi^{(2)}_{ijk} = N_s \sum_{i'j'k'} \langle R_{ii'} R_{jj'} R_{kk'} \rangle \beta^{(2)}_{i'j'k'} , \tag{116}$$

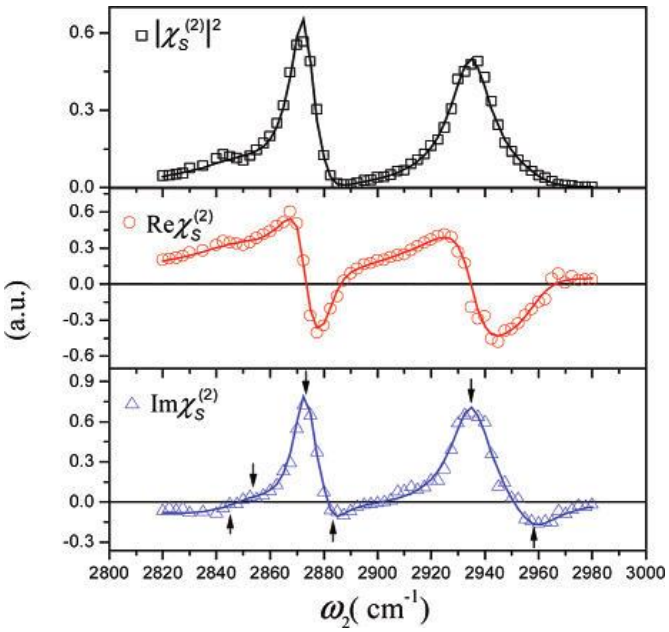

Figure 75 shows the phase sensitive VSFG spectrum of an OTS monolayer on silica. The top panel shows the magnitude spectra of the nonlinear susceptibility. The middle panel the real component, and the bottom panel the imaginary component that corresponds directly to resonances. Reprinted with permission from Ji *et al.*, **129**, 10056, 2007. Copyright (2018) ACS.

where, with reference to Figure 76, i, j and k are dummy indicies that can each represent the laboratory frame axes x, y or z; i', j' and k' are dummy indices representing the axes in the molecular frame a, b or c, where c defines the molecular axis; $R_{\lambda\lambda'}(\theta, \phi, \psi)$ is the Euler matrix element that relates the molecular axes (a, b, c) to the laboratory axis frame (x, y, z); and N_s is the number density at the surface. Tahara's group used this theory to determine the molecular orientation of water molecules at the interface in the presence of different surface charges introduced by surfactants.[260] Using Equation (116), the nonlinear susceptibility element for the OH symmetric stretch under SSP polarization experimental conditions can be expressed as

$$\chi^{(2)}_{yyz} = \frac{1}{2}N_s\Big(\Big(\langle\cos^2\psi\rangle\beta^{(2)}_{aac} + \langle\sin^2\psi\rangle\beta^{(2)}_{bbc} + \beta^{(2)}_{ccc}\Big)\langle\cos\theta\rangle + \Big(\langle\sin^2\psi\rangle\beta^{(2)}_{aac} + \langle\cos^2\psi\rangle\beta^{(2)}_{bbc} - \beta^{(2)}_{ccc}\Big)\langle\cos^3\theta\rangle\Big), \quad (117)$$

where θ defines the molecular orientation with respect to the normal of the interface. It is assumed that the distribution is random in the angle ϕ. Utilising computationally calculated hyperpolarizability elements, Nihonyanagi *et al.*[260] experimentally showed the molecular 'flip-flop' of water molecules at the surface, a model which had long been accepted but never conclusively proven. Figure 76 shows the physical interpretation of the experimental results with the conclusion that when the surface electric field is negative, $Im\left(\chi^{(2)}_{yyz}\right)$ is positive and the water

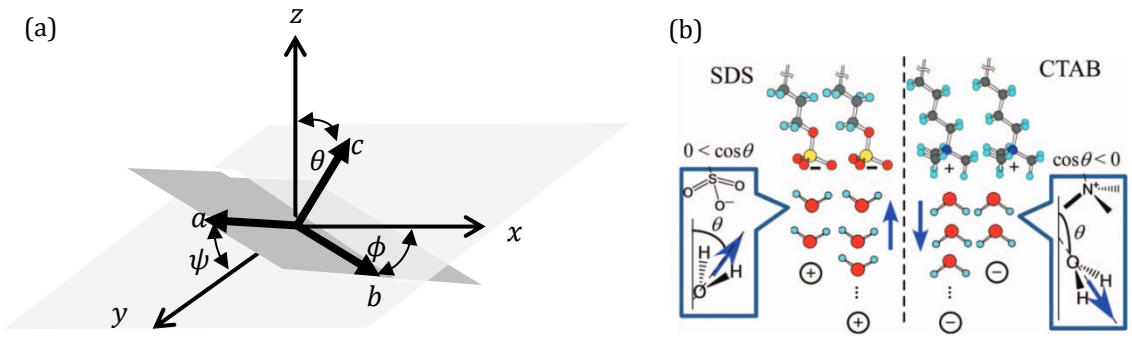

Figure 76 (a) shows the schematic representation of the relationship between the molecular frame and the laboratory frame, (b), taken from Nihonyanagi *et al.*,2009, diagrammatically shows the flip flop model of water in the presence of surface charge reprinted with permission from Nihonyanagi *t al., J chem phys.***130**, 204704, 2009. Copyright (2018) AIP.

orientates with the hydrogen atoms directed towards the surface, and when the surface is positively charged, $Im\left(\chi_{yyz}^{(2)}\right)$ is negative and the hydrogens point towards the bulk liquid. The same result was observed by Chen *et al.*[322] who observed the induced water orientation by phospholipids with various head group charges. This result therefore indicates that molecular identity is less impactful on the interfacial structure of water than electrostatic potential.

As water is the fundamental basis for life on earth, it is unsurprising that water/air interfaces have been studied extensively by phase sensitive techniques. However, arguably, the most important information to be gained is in the interaction between water and biological molecules. For example, it is famously known that the interactions between water and DNA phosphoric acid backbones cause the formation of the double helix. A recent study, Strazdaite *et al.*[323] investigated the mechanism of protein denaturation by urea molecules. In modern literature there are two proposed mechanisms for denaturisation; direct and indirect. The direct mechanism is suggested to due to the displacement of water by urea due to direct binding at the protein surface. The indirect mechanism suggests that urea molecules induce a change in the water structure which instigates protein denaturation. Experimental results show that as the pH changes, the surface charge of the protein is altered and this electrostatic field induces an orientation in the urea amide, just like it has been shown to do with water, resulting in a sign change of $Im\left(\chi^{(2)}\right)$. Thus, it can be inferred that denaturation arises through the indirect mechanism as the orientation of the urea molecule would remain the same if it was directly bound to the surface. This result, once again, reveals the power of the surface specificity of even order nonlinear spectroscopy as a versatile tool across disciplines.

REFERENCES

1 history of photography | Inventions & Events, https://www.britannica.com/technology/photography, (accessed June 12, 2018).
2 Jan Ingenhousz | Biography, Experiments, & Facts | Britannica.com, https://www.britannica.com/biography/Jan-Ingenhousz, (accessed June 12, 2018).
3 J. Van Houten, A Century of Chemical Dynamics Traced through the Nobel Prizes. 1967: Eigen, Norrish, and Porter, *J. Chem. Educ.*, 2002, **79**, 548.
4 J. Van Houten, A Century of Chemical Dynamics Traced through the Nobel Prizes. 1999: Ahmed H. Zewail, *J. Chem. Educ.*, 2002, **79**, 1396.
5 A. Stolow, A. E. Bragg and D. M. Neumark, Femtosecond Time-Resolved Photoelectron Spectroscopy, *Chem. Rev.*, 2004, **104**, 1719–1758.
6 A. H. Zewail, Femtochemistry: Atomic-Scale Dynamics of the Chemical Bond Using Ultrafast Lasers (Nobel Lecture), *Angew. Chem. Int. Ed.*, 2000, **39**, 2586–2631.
7 F. Kanal, Ph.D. Thesis, Julius Maximilians Universtitat Wurzburg, 2015.
8 J. M. Hollas, *Modern Spectroscopy*, John Wiley & Sons, 2004.
9 C. E. Wayne, *Photochemistry*, Oxford University Press, U.S.A., Oxford, 1996.
10 A. Gilbert and J. Baggott, *Essentials of molecular photochemistry*, Oxford : Blackwell Scientific, 1991.
11 V. Brückner, *Applications of Time-resolved Optical Spectroscopy*, Elsevier, 1990.
12 S. J. M. Thomas, P. P. Edwards and V. L. Kuznetsov, Sir Humphry Davy: Boundless Chemist, Physicist, Poet and Man of Action, *ChemPhysChem*, 2008, **9**, 59–66.
13 C. A. Kraus, Solutions of metals in non-metallic solvents; IV.1 Material effects accompanying the passage of an electrical current through solutions of metals in liquid ammonia. Migration experiments., *J. Am. Chem. Soc.*, 1908, **30**, 1323–1344.
14 C. A. Kraus, Solution of metals in non-metalic solvents; II.1 On the formation of compounds between metals and ammonia., *J. Am. Chem. Soc.*, 1908, **30**, 653–668.
15 G. E. Gibson and W. L. Argo, The absorption spectra of the blue solutions of certain alkali and alkaline earth metals in liquid ammonia and in methylamine., *J. Am. Chem. Soc.*, 1918, **40**, 1327–1361.
16 G. E. Gibson and W. L. Argo, The Absorption Spectra of the Blue Solutions of Sodium and Magnesium in Liquid Ammonia, *Phys. Rev.*, 1916, **7**, 33–48.
17 J. M. Herbert and M. P. Coons, The Hydrated Electron, *Annu. Rev. Phys. Chem.*, 2017, **68**, 447–472.
18 G. Stein, Some aspects of the radiation chemistry of organic solutes, *Discuss. Faraday Soc.*, 1952, **12**, 227–234.
19 D. C. Walker, The hydrated electron, *Q. Rev. Chem. Soc.*, 1967, **21**, 79–108.
20 J. P. Keene, Absorption Spectra in Irradiated Water and Some Solutions: Optical Absorptions in Irradiated Water, *Nature*, 1963, **197**, 47–48.
21 E. J. Hart and J. W. Boag, Absorption Spectrum of the Hydrated Electron in Water and in Aqueous Solutions, *J. Am. Chem. Soc.*, 1962, **84**, 4090–4095.
22 B. C. Garrett, D. A. Dixon, D. M. Camaioni, D. M. Chipman, M. A. Johnson, C. D. Jonah, G. A. Kimmel, J. H. Miller, T. N. Rescigno, P. J. Rossky, S. S. Xantheas, S. D. Colson, A. H. Laufer, D. Ray, P. F. Barbara, D. M. Bartels, K. H. Becker, Bowen Kit H., S. E. Bradforth, I. Carmichael, J. V. Coe, L. R. Corrales, J. P. Cowin, M. Dupuis, K. B. Eisenthal, J. A. Franz, M. S. Gutowski, K. D. Jordan, B. D. Kay, J. A. LaVerne, S. V. Lymar, T. E. Madey, C. W. McCurdy, D. Meisel, S. Mukamel, A. R. Nilsson, T. M. Orlando, N. G. Petrik, S. M. Pimblott, J. R. Rustad, G. K. Schenter, S. J. Singer, A. Tokmakoff, L.-S. Wang and T. S. Zwier, Role of Water in Electron-Initiated Processes and Radical Chemistry: Issues and Scientific Advances, *Chem. Rev.*, 2005, **105**, 355–390.
23 E. Alizadeh and L. Sanche, Precursors of Solvated Electrons in Radiobiological Physics and Chemistry, *Chem. Rev.*, 2012, **112**, 5578–5602.
24 B. Boudaïffa, P. Cloutier, D. Hunting, M. A. Huels and L. Sanche, Resonant Formation of DNA Strand Breaks by Low-Energy (3 to 20 eV) Electrons, *Science*, 2000, **287**, 1658–1660.

25 M. A. Huels, B. Boudaïffa, P. Cloutier, D. Hunting and L. Sanche, Single, Double, and Multiple Double Strand Breaks Induced in DNA by 3−100 eV Electrons, *J. Am. Chem. Soc.*, 2003, **125**, 4467–4477.
26 C.-R. Wang, J. Nguyen and Q.-B. Lu, Bond Breaks of Nucleotides by Dissociative Electron Transfer of Nonequilibrium Prehydrated Electrons: A New Molecular Mechanism for Reductive DNA Damage, *J. Am. Chem. Soc.*, 2009, **131**, 11320–11322.
27 Q.-B. Lu and L. Sanche, Effects of Cosmic Rays on Atmospheric Chlorofluorocarbon Dissociation and Ozone Depletion, *Phys. Rev. Lett.*, 2001, **87**, 078501.
28 Q.-B. Lu and L. Sanche, Enhanced dissociative electron attachment to CF2Cl2 by transfer of electrons in precursors to the solvated state in water and ammonia ice, *Phys. Rev. B*, 2001, **63**, 153403.
29 Q.-B. Lu and T. E. Madey, Giant enhancement of electron-induced dissociation of chlorofluorocarbons coadsorbed with water or ammonia ices: Implications for atmospheric ozone depletion, *J. Chem. Phys.*, 1999, **111**, 2861–2864.
30 B. Behmand, P. Cloutier, S. Girouard, J. R. Wagner, L. Sanche and D. J. Hunting, Hydrated Electrons React with High Specificity with Cisplatin Bound to Single-Stranded DNA, *J. Phys. Chem. B*, 2013, **117**, 15994–15999.
31 Q.-B. Lu, S. Kalantari and C.-R. Wang, Electron Transfer Reaction Mechanism of Cisplatin with DNA at the Molecular Level, *Mol. Pharm.*, 2007, **4**, 624–628.
32 Q.-B. Lu, Molecular Reaction Mechanisms of Combination Treatments of Low-Dose Cisplatin with Radiotherapy and Photodynamic Therapy, *J. Med. Chem.*, 2007, **50**, 2601–2604.
33 C.-R. Wang, A. Hu and Q.-B. Lu, Direct observation of the transition state of ultrafast electron transfer reaction of a radiosensitizing drug bromodeoxyuridine, *J. Chem. Phys.*, 2006, **124**, 241102.
34 P. Kambhampati, D. H. Son, T. W. Kee and P. F. Barbara, Solvation Dynamics of the Hydrated Electron Depends on Its Initial Degree of Electron Delocalization, *J. Phys. Chem. A*, 2002, **106**, 2374–2378.
35 J. Savolainen, F. Uhlig, S. Ahmed, P. Hamm and P. Jungwirth, Direct observation of the collapse of the delocalized excess electron in water, *Nat. Chem.*, 2014, **6**, 697–701.
36 E. Alizadeh, T. M. Orlando and L. Sanche, Biomolecular Damage Induced by Ionizing Radiation: The Direct and Indirect Effects of Low-Energy Electrons on DNA, *Annu. Rev. Phys. Chem.*, 2015, **66**, 379–398.
37 J. M. Falcone, D. Becker, M. D. Sevilla and S. G. Swarts, Products of the reactions of the dry and aqueous electron with hydrated DNA: hydrogen and 5,6-dihydropyrimidines, *Radiat. Phys. Chem.*, 2005, **72**, 257–264.
38 E. Alizadeh, A. G. Sanz, G. García and L. Sanche, Radiation Damage to DNA: The Indirect Effect of Low-Energy Electrons, *J. Phys. Chem. Lett.*, 2013, **4**, 820–825.
39 J. Simons, How Do Low-Energy (0.1−2 eV) Electrons Cause DNA-Strand Breaks?, *Acc. Chem. Res.*, 2006, **39**, 772–779.
40 F. Martin, P. D. Burrow, Z. Cai, P. Cloutier, D. Hunting and L. Sanche, DNA Strand Breaks Induced by 0--4 eV Electrons: The Role of Shape Resonances, *Phys. Rev. Lett.*, 2004, **93**, 068101.
41 J. Gu, Y. Xie and H. F. Schaefer, Electron Attachment to Nucleotides in Aqueous Solution, *ChemPhysChem*, 2006, **7**, 1885–1887.
42 M. Smyth and J. Kohanoff, Excess Electron Localization in Solvated DNA Bases, *Phys. Rev. Lett.*, 2011, **106**, 238108.
43 L. Sanche, Low energy electron-driven damage in biomolecules, *Eur. Phys. J. D*, 2005, **35**, 367–390.
44 L. D. Jacobson and J. M. Herbert, Polarization-Bound Quasi-Continuum States Are Responsible for the “Blue Tail” in the Optical Absorption Spectrum of the Aqueous Electron, *J. Am. Chem. Soc.*, 2010, **132**, 10000–10002.

45 J. V. Coe, Fundamental properties of bulk water from cluster ion data, *Int. Rev. Phys. Chem.*, 2001, **20**, 33–58.

46 F. Uhlig, J. M. Herbert, M. P. Coons and P. Jungwirth, Optical Spectroscopy of the Bulk and Interfacial Hydrated Electron from Ab Initio Calculations, *J. Phys. Chem. A*, 2014, **118**, 7507–7515.

47 L. D. Jacobson and J. M. Herbert, A one-electron model for the aqueous electron that includes many-body electron-water polarization: Bulk equilibrium structure, vertical electron binding energy, and optical absorption spectrum, *J. Chem. Phys.*, 2010, **133**, 154506.

48 S. Golden and T. R. Tuttle, Shape stability of solvated-electron optical absorption bands. Part 2.—Theoretical implication, *J. Chem. Soc. Faraday Trans. 2 Mol. Chem. Phys.*, 1981, **77**, 889–897.

49 S. Golden and T. R. Tuttle, Nature of solvated electron absorption spectra, *J. Chem. Soc. Faraday Trans. 2 Mol. Chem. Phys.*, 1979, **75**, 474–484.

50 N. R. Kestner and J. Jortner, Radiative processes of the solvated electron in polar fluids, *J. Phys. Chem.*, 1973, **77**, 1040–1050.

51 L. Turi, G. Hantal, P. J. Rossky and D. Borgis, Nuclear quantum effects in electronically adiabatic quantum time correlation functions: Application to the absorption spectrum of a hydrated electron, *J. Chem. Phys.*, 2009, **131**, 024119.

52 P. M. Hare, E. A. Price, C. M. Stanisky, I. Janik and D. M. Bartels, Solvated Electron Extinction Coefficient and Oscillator Strength in High Temperature Water, *J. Phys. Chem. A*, 2010, **114**, 1766–1775.

53 J. R. R. Verlet, A. E. Bragg, A. Kammrath, O. Cheshnovsky and D. M. Neumark, Observation of Large Water-Cluster Anions with Surface-Bound Excess Electrons, *Science*, 2005, **307**, 93–96.

54 J. V. Coe, G. H. Lee, J. G. Eaton, S. T. Arnold, H. W. Sarkas, K. H. Bowen, C. Ludewigt, H. Haberland and D. R. Worsnop, Photoelectron spectroscopy of hydrated electron cluster anions, (H2O)−n=2–69, *J. Chem. Phys.*, 1990, **92**, 3980–3982.

55 L. Ma, K. Majer, F. Chirot and B. von Issendorff, Low temperature photoelectron spectra of water cluster anions, *J. Chem. Phys.*, 2009, **131**, 144303.

56 Y. Tang, H. Shen, K. Sekiguchi, N. Kurahashi, T. Mizuno, Y.-I. Suzuki and T. Suzuki, Direct measurement of vertical binding energy of a hydrated electron, *Phys. Chem. Chem. Phys.*, 2010, **12**, 3653–3655.

57 T. Sommerfeld, S. D. Gardner, A. DeFusco and K. D. Jordan, Low-lying isomers and finite temperature behavior of (H2O)6−, *J. Chem. Phys.*, 2006, **125**, 174301.

58 G. Makov and A. Nitzan, Solvation and Ionization near a Dielectric Surface, *J. Phys. Chem.*, 1994, **98**, 3459–3466.

59 B. Abel, U. Buck, A. L. Sobolewski and W. Domcke, On the nature and signatures of the solvated electron in water, *Phys. Chem. Chem. Phys.*, 2012, **14**, 22–34.

60 R. N. Barnett, U. Landman, C. L. Cleveland and J. Jortner, Electron localization in water clusters. II. Surface and internal states, *J. Chem. Phys.*, 1988, **88**, 4429–4447.

61 L. Turi, W.-S. Sheu and P. J. Rossky, Characterization of Excess Electrons in Water-Cluster Anions by Quantum Simulations, *Science*, 2005, **309**, 914–917.

62 L. D. Jacobson and J. M. Herbert, Theoretical Characterization of Four Distinct Isomer Types in Hydrated-Electron Clusters, and Proposed Assignments for Photoelectron Spectra of Water Cluster Anions, *J. Am. Chem. Soc.*, 2011, **133**, 19889–19899.

63 A. Lübcke, F. Buchner, N. Heine, I. V. Hertel and T. Schultz, Time-resolved photoelectron spectroscopy of solvated electrons in aqueous NaI solution, *Phys. Chem. Chem. Phys.*, 2010, **12**, 14629–14634.

64 K. R. Siefermann, Y. Liu, E. Lugovoy, O. Link, M. Faubel, U. Buck, B. Winter and B. Abel, Binding energies, lifetimes and implications of bulk and interface solvated electrons in water, *Nat. Chem.*, 2010, **2**, 274–279.

65 A. T. Shreve, T. A. Yen and D. M. Neumark, Photoelectron spectroscopy of hydrated electrons, *Chem. Phys. Lett.*, 2010, **493**, 216–219.

66 Y. Yamamoto, S. Karashima, S. Adachi and T. Suzuki, Wavelength Dependence of UV Photoemission from Solvated Electrons in Bulk Water, Methanol, and Ethanol, *J. Phys. Chem. A*, 2016, **120**, 1153–1159.

67 M. P. Coons, Z.-Q. You and J. M. Herbert, The Hydrated Electron at the Surface of Neat Liquid Water Appears To Be Indistinguishable from the Bulk Species, *J. Am. Chem. Soc.*, 2016, **138**, 10879–10886.

68 L. Turi and P. J. Rossky, Theoretical Studies of Spectroscopy and Dynamics of Hydrated Electrons, *Chem. Rev.*, 2012, **112**, 5641–5674.

69 J. M. Herbert and L. D. Jacobson, Structure of the Aqueous Electron: Assessment of One-Electron Pseudopotential Models in Comparison to Experimental Data and Time-Dependent Density Functional Theory, *J. Phys. Chem. A*, 2011, **115**, 14470–14483.

70 J. Jortner, Energy Levels of Bound Electrons in Liquid Ammonia, *J. Chem. Phys.*, 1959, **30**, 839–846.

71 M. Natori and T. Watanabe, Structural Model of the Hydrated Electron, *J. Phys. Soc. Jpn.*, 1966, **21**, 1573–1578.

72 S. Schlick, P. A. Narayana and L. Kevan, ESR line shape studies of trapped electrons in γ-irradiated 17O enriched 10M NaOH alkaline ice glass: Model for the geometrical structure of the trapped electron, *J. Chem. Phys.*, 1976, **64**, 3153–3160.

73 L. Kevan, Solvated electron structure in glassy matrixes, *Acc. Chem. Res.*, 1981, **14**, 138–145.

74 D.-F. Feng and L. Kevan, Theoretical models for solvated electrons, *Chem. Rev.*, 1980, **80**, 1–20.

75 P. J. Rossky and J. Schnitker, The hydrated electron: quantum simulation of structure, spectroscopy, and dynamics, *J. Phys. Chem.*, 1988, **92**, 4277–4285.

76 A. Staib and D. Borgis, Molecular dynamics simulation of an excess charge in water using mobile Gaussian orbitals, *J. Chem. Phys.*, 1995, **103**, 2642–2655.

77 B. J. Schwartz and P. J. Rossky, Aqueous solvation dynamics with a quantum mechanical Solute: Computer simulation studies of the photoexcited hydrated electron, *J. Chem. Phys.*, 1994, **101**, 6902–6916.

78 K. A. Tay and A. Boutin, Hydrated Electron Diffusion: The Importance of Hydrogen-Bond Dynamics, *J. Phys. Chem. B*, 2009, **113**, 11943–11949.

79 M. Boero, Excess Electron in Water at Different Thermodynamic Conditions, *J. Phys. Chem. A*, 2007, **111**, 12248–12256.

80 M. Boero, M. Parrinello, K. Terakura, T. Ikeshoji and C. C. Liew, First-Principles Molecular-Dynamics Simulations of a Hydrated Electron in Normal and Supercritical Water, *Phys. Rev. Lett.*, 2003, **90**, 226403.

81 A. Kumar, J. A. Walker, D. M. Bartels and M. D. Sevilla, A Simple ab Initio Model for the Hydrated Electron That Matches Experiment, *J. Phys. Chem. A*, 2015, **119**, 9148–9159.

82 C.-C. Zho, E. P. Farr, W. J. Glover and B. J. Schwartz, Temperature dependence of the hydrated electron's excited-state relaxation. I. Simulation predictions of resonance Raman and pump-probe transient absorption spectra of cavity and non-cavity models, *J. Chem. Phys.*, 2017, **147**, 074503.

83 R. E. Larsen, W. J. Glover and B. J. Schwartz, Does the Hydrated Electron Occupy a Cavity?, *Science*, 2010, **329**, 65–69.

84 L. D. Jacobson and J. M. Herbert, Comment on "Does the Hydrated Electron Occupy a Cavity?," *Science*, 2011, **331**, 1387–1387.

85 R. E. Larsen, W. J. Glover and B. J. Schwartz, Response to Comments on "Does the Hydrated Electron Occupy a Cavity?," *Science*, 2011, **331**, 1387–1387.

86 L. Turi and Á. Madarász, Comment on "Does the Hydrated Electron Occupy a Cavity?," *Science*, 2011, **331**, 1387–1387.

87 R. R. Hentz and D. W. Brazier, γ Radiolysis of Liquids at High Pressures. X. The Reaction H+OH− and the Partial Molal Volume of the Hydrated Electron, *J. Chem. Phys.*, 1971, **54**, 2777–2780.
88 E. P. Farr, C.-C. Zho, J. R. Challa and B. J. Schwartz, Temperature dependence of the hydrated electron's excited-state relaxation. II. Elucidating the relaxation mechanism through ultrafast transient absorption and stimulated emission spectroscopy, *J. Chem. Phys.*, 2017, **147**, 074504.
89 F. Uhlig, O. Marsalek and P. Jungwirth, Unraveling the Complex Nature of the Hydrated Electron, *J. Phys. Chem. Lett.*, 2012, **3**, 3071–3075.
90 E. J. Hart and M. Anbar, *Hydrated Electron*, John Wiley & Sons Inc, New York, 1970.
91 L. Dharmarathne, M. Ashokkumar and F. Grieser, On the Generation of the Hydrated Electron during the Sonolysis of Aqueous Solutions, *J. Phys. Chem. A*, 2013, **117**, 2409–2414.
92 Y. Tabata, *Pulse Radiolysis of Irradiated Systems*, CRC Press, 1991.
93 S. M. Pimblott, Independent pairs modeling of the kinetics following the photoionization of liquid water, *J. Phys. Chem.*, 1991, **95**, 6946–6951.
94 Q.-B. Lu, J. S. Baskin and A. H. Zewail, The Presolvated Electron in Water: Can It Be Scavenged at Long Range?, *J. Phys. Chem. B*, 2004, **108**, 10509–10514.
95 W. J. Chase and J. W. Hunt, Solvation time of the electron in polar liquids. Water and alcohols, *J. Phys. Chem.*, 1975, **79**, 2835–2845.
96 G. A. Kenney-Wallace and C. D. Jonah, Picosecond spectroscopy and solvation clusters. The dynamics of localizing electrons in polar fluids, *J. Phys. Chem.*, 1982, **86**, 2572–2586.
97 C. D. Jonah, J. R. Miller and M. S. Matheson, The reaction of the precursor of the hydrated electron with electron scavengers, *J. Phys. Chem.*, 1977, **81**, 1618–1622.
98 J. E. Aldrich, M. J. Bronskill, R. K. Wolff and J. W. Hunt, Picosecond Pulse Radiolysis. III. Reaction Rates and Reduction in Yields of Hydrated Electrons, *J. Chem. Phys.*, 1971, **55**, 530–539.
99 A. Migus, Y. Gauduel, J. L. Martin and A. Antonetti, Excess electrons in liquid water: First evidence of a prehydrated state with femtosecond lifetime, *Phys. Rev. Lett.*, 1987, **58**, 1559–1562.
100 F. Wang, P. Archirel, Y. Muroya, S. Yamashita, P. Pernot, C. Yin, A. K. E. Omar, U. Schmidhammer, J.-M. Teuler and M. Mostafavi, Effect of the solvation state of electron in dissociative electron attachment reaction in aqueous solutions, *Phys. Chem. Chem. Phys.*, 2017, **19**, 23068–23077.
101 J. Ma, F. Wang, S. A. Denisov, A. Adhikary and M. Mostafavi, Reactivity of prehydrated electrons toward nucleobases and nucleotides in aqueous solution, *Sci. Adv.*, 2017, **3**, 1701669.
102 R. A. Crowell and D. M. Bartels, Multiphoton Ionization of Liquid Water with 3.0−5.0 eV Photons, *J. Phys. Chem.*, 1996, **100**, 17940–17949.
103 D. H. Son, P. Kambhampati, T. W. Kee and P. F. Barbara, Delocalizing Electrons in Water with Light, *J. Phys. Chem. A*, 2001, **105**, 8269–8272.
104 T. W. Kee, D. H. Son, P. Kambhampati and P. F. Barbara, A Unified Electron Transfer Model for the Different Precursors and Excited States of the Hydrated Electron, *J. Phys. Chem. A*, 2001, **105**, 8434–8439.
105 C. G. Elles, A. E. Jailaubekov, R. A. Crowell and S. E. Bradforth, Excitation-energy dependence of the mechanism for two-photon ionization of liquid H2O and D2O from 8.3 to 12.4 eV, *J. Chem. Phys.*, 2006, **125**, 044515.
106 R. Lian, D. A. Oulianov, I. A. Shkrob and R. A. Crowell, Geminate recombination of electrons generated by above-the-gap (12.4 eV) photoionization of liquid water, *Chem. Phys. Lett.*, 2004, **398**, 102–106.

107 C. L. Thomsen, D. Madsen, S. R. Keiding, J. Tho/gersen and O. Christiansen, Two-photon dissociation and ionization of liquid water studied by femtosecond transient absorption spectroscopy, *J. Chem. Phys.*, 1999, **110**, 3453–3462.
108 X. Chen and S. E. Bradforth, The Ultrafast Dynamics of Photodetachment, *Annu. Rev. Phys. Chem.*, 2008, **59**, 203–231.
109 S. E. Bradforth and P. Jungwirth, Excited States of Iodide Anions in Water: A Comparison of the Electronic Structure in Clusters and in Bulk Solution, *J. Phys. Chem. A*, 2002, **106**, 1286–1298.
110 J. Jortner, M. Ottolenghi and G. Stein, On the Photochemistry of Aqueous Solutions of Chloride, Bromide, and Iodide Ions, *J. Phys. Chem.*, 1964, **68**, 247–255.
111 F. Messina, O. Bräm, A. Cannizzo and M. Chergui, Real-time observation of the charge transfer to solvent dynamics, *Nat. Commun.*, 2013, **4**, 2119.
112 A. E. Bragg and B. J. Schwartz, The Ultrafast Charge-Transfer-to-Solvent Dynamics of Iodide in Tetrahydrofuran. 1. Exploring the Roles of Solvent and Solute Electronic Structure in Condensed-Phase Charge-Transfer Reactions, *J. Phys. Chem. B*, 2008, **112**, 483–494.
113 J. Gu, L. Yang, J. Ma, J. Jiang, J. Yang, J. Zhang, H. Chi, Y. Song, S. Sun and W. Q. Tian, Hydrated electron (eaq−) generation from p-benzoquinone/UV: Combined experimental and theoretical study, *Appl. Catal. B Environ.*, 2017, **212**, 150–158.
114 J. Gu, L. Yang, J. Jiang, J. Ma, W. Qiu, J. Yang, Y. Song and W. Q. Tian, Insights into the effects of alcohols on hydrated electron (eaq−) generation from the p-benzoquinone/UV process, *Appl. Catal. B Environ.*, 2018, **220**, 477–487.
115 W.-S. Sheu and P. J. Rossky, Electronic and Solvent Relaxation Dynamics of a Photoexcited Aqueous Halide, *J. Phys. Chem.*, 1996, **100**, 1295–1302.
116 N. Takahashi, K. Sakai, H. Tanida and I. Watanabe, Vertical ionization potentials and CTTS energies for anions in water and acetonitrile, *Chem. Phys. Lett.*, 1995, **246**, 183–186.
117 E. R. Barthel and B. J. Schwartz, Mapping out the conduction band under CTTS transitions: the photodetachment quantum yield of sodide (Na−) in tetrahydrofuran, *Chem. Phys. Lett.*, 2003, **375**, 435–443.
118 M. Shirom and G. Stein, Excited State Chemistry of the Ferrocyanide Ion in Aqueous Solution. I. Formation of the Hydrated Electron, *J. Chem. Phys.*, 1971, **55**, 3372–3378.
119 S. Pommeret, R. Naskrecki, P. van der Meulen, M. Ménard, G. Vigneron and T. Gustavsson, Ultrafast events in the electron photodetachment from the hexacyanoferrate(II) complex in solution, *Chem. Phys. Lett.*, 1998, **288**, 833–840.
120 M. C. Sauer, R. A. Crowell and I. A. Shkrob, Electron Photodetachment from Aqueous Anions. 1. Quantum Yields for Generation of Hydrated Electron by 193 and 248 nm Laser Photoexcitation of Miscellaneous Inorganic Anions, *J. Phys. Chem. A*, 2004, **108**, 5490–5502.
121 L. I. Grossweiner, G. W. Swenson and E. F. Zwicker, Photochemical Generation of the Hydrated Electron, *Science*, 1963, **141**, 805–806.
122 J. Feitelson, The Formation of Hydrated Electrons from the Excited State of Indole Derivatives, *Photochem. Photobiol.*, 1971, **13**, 87–96.
123 D. V. Bent and E. Hayon, Excited state chemistry of aromatic amino acids and related peptides. I. Tyrosine, *J. Am. Chem. Soc.*, 1975, **97**, 2599–2606.
124 J. Peon, G. C. Hess, J.-M. L. Pecourt, T. Yuzawa and B. Kohler, Ultrafast Photoionization Dynamics of Indole in Water, *J. Phys. Chem. A*, 1999, **103**, 2460–2466.
125 B. Winter and M. Faubel, Photoemission from Liquid Aqueous Solutions, *Chem. Rev.*, 2006, **106**, 1176–1211.
126 P. Jungwirth and D. J. Tobias, Ions at the Air/Water Interface, *J. Phys. Chem. B*, 2002, **106**, 6361–6373.
127 P. Jungwirth and D. J. Tobias, Specific Ion Effects at the Air/Water Interface, *Chem. Rev.*, 2006, **106**, 1259–1281.

128 Á. Madarász, P. J. Rossky and L. Turi, Excess electron relaxation dynamics at water/air interfaces, *J. Chem. Phys.*, 2007, **126**, 234707.
129 Y. Tang, Y. Suzuki, H. Shen, K. Sekiguchi, N. Kurahashi, K. Nishizawa, P. Zuo and T. Suzuki, Time-resolved photoelectron spectroscopy of bulk liquids at ultra-low kinetic energy, *Chem. Phys. Lett.*, 2010, **494**, 111–116.
130 Y. Yamamoto, Y.-I. Suzuki, G. Tomasello, T. Horio, S. Karashima, R. Mitríc and T. Suzuki, Time- and Angle-Resolved Photoemission Spectroscopy of Hydrated Electrons Near a Liquid Water Surface, *Phys. Rev. Lett.*, 2014, **112**, 187603.
131 M. Meyer, J. Stähler, D. O. Kusmierek, M. Wolf and U. Bovensiepen, Determination of the electron's solvation site on D2O/Cu(111) using Xe overlayers and femtosecond photoelectron spectroscopy, *Phys. Chem. Chem. Phys.*, 2008, **10**, 4932–4938.
132 U. Bovensiepen, C. Gahl, J. Stähler, M. Bockstedte, M. Meyer, F. Baletto, S. Scandolo, X.-Y. Zhu, A. Rubio and M. Wolf, A Dynamic Landscape from Femtoseconds to Minutes for Excess Electrons at Ice−Metal Interfaces, *J. Phys. Chem. C*, 2009, **113**, 979–988.
133 J. Stähler, J.-C. Deinert, D. Wegkamp, S. Hagen and M. Wolf, Real-Time Measurement of the Vertical Binding Energy during the Birth of a Solvated Electron, *J. Am. Chem. Soc.*, 2015, **137**, 3520–3524.
134 S. K. Bhattacharya, F. Inam and S. Scandolo, Excess electrons in ice: a density functional theory study, *Phys. Chem. Chem. Phys.*, 2014, **16**, 3103–3107.
135 H. Iglev, A. Trifonov, A. Thaller, I. Buchvarov, T. Fiebig and A. Laubereau, Photoionization dynamics of an aqueous iodide solution: the temperature dependence, *Chem. Phys. Lett.*, 2005, **403**, 198–204.
136 D. Andrews, *Molecular Photophysics and Spectroscopy*, Morgan & Claypool Publishers, 2014.
137 R. Menzel, *Photonics: Linear and Nonlinear Interactions of Laser Light and Matter*, Springer Science & Business Media, 2007.
138 R. Berera, R. van Grondelle and J. T. M. Kennis, Ultrafast transient absorption spectroscopy: principles and application to photosynthetic systems, *Photosynth. Res.*, 2009, **101**, 105–118.
139 T. Fiebig, C. Wan and A. H. Zewail, Femtosecond Charge Transfer Dynamics of a Modified DNA Base: 2-Aminopurine in Complexes with Nucleotides, *ChemPhysChem*, **3**, 781–788.
140 A. Maciejewski, R. Naskrecki, M. Lorenc, M. Ziolek, J. Karolczak, J. Kubicki, M. Matysiak and M. Szymanski, Transient absorption experimental set-up with femtosecond time resolution. Femto- and picosecond study of DCM molecule in cyclohexane and methanol solution, *J. Mol. Struct.*, 2000, **555**, 1–13.
141 F. Preda, V. Kumar, F. Crisafi, D. G. F. del Valle, G. Cerullo and D. Polli, Broadband pump-probe spectroscopy at 20-MHz modulation frequency, *Opt. Lett.*, 2016, **41**, 2970–2973.
142 F. Kanal, S. Keiber, R. Eck and T. Brixner, 100-kHz shot-to-shot broadband data acquisition for high-repetition-rate pump–probe spectroscopy, *Opt. Express*, 2014, **22**, 16965–16975.
143 B. I. Greene, R. M. Hochstrasser and R. B. Weisman, Picosecond transient spectroscopy of molecules in solution, *J. Chem. Phys.*, 1979, **70**, 1247–1259.
144 C. C. Gradinaru, J. T. M. Kennis, E. Papagiannakis, I. H. M. van Stokkum, R. J. Cogdell, G. R. Fleming, R. A. Niederman and R. van Grondelle, An unusual pathway of excitation energy deactivation in carotenoids: Singlet-to-triplet conversion on an ultrafast timescale in a photosynthetic antenna, *Proc. Natl. Acad. Sci.*, 2001, **98**, 2364–2369.
145 S. A. Kovalenko, N. P. Ernsting and J. Ruthmann, Femtosecond hole-burning spectroscopy of the dye DCM in solution: the transition from the locally excited to a charge-transfer state, *Chem. Phys. Lett.*, 1996, **258**, 445–454.
146 S. A. Kovalenko, A. L. Dobryakov, J. Ruthmann and N. P. Ernsting, Femtosecond spectroscopy of condensed phases with chirped supercontinuum probing, *Phys. Rev. A*, 1999, **59**, 2369–2384.

147 X. Chen, D. S. Larsen, S. E. Bradforth and I. H. M. van Stokkum, Broadband Spectral Probing Revealing Ultrafast Photochemical Branching after Ultraviolet Excitation of the Aqueous Phenolate Anion, *J. Phys. Chem. A*, 2011, **115**, 3807–3819.
148 C. Manzoni, R. Osellame, M. Marangoni, M. Schultze, U. Morgner and G. Cerullo, High-repetition-rate two-color pump–probe system directly pumped by a femtosecond ytterbium oscillator, *Opt. Lett.*, 2009, **34**, 620–622.
149 A. J. Ruggiero, N. F. Scherer, G. M. Mitchell, G. R. Fleming and J. N. Hogan, Regenerative amplification of picosecond pulses in Nd:YAG at repetition rates in the 100-kHz range, *J. Opt. Soc. Am. B*, 1991, **8**, 2061–2067.
150 L. A. Huston, K. Iwata, W. L. Weaver and T. L. Gustafson, Broadband picosecond transient absorption spectroscopy at MHz repetition rates, *Opt. Commun.*, 1992, **88**, 105–109.
151 Y.-Z. Ma, N. E. Holt, X.-P. Li, K. K. Niyogi and G. R. Fleming, Evidence for direct carotenoid involvement in the regulation of photosynthetic light harvesting, *Proc. Natl. Acad. Sci.*, 2003, **100**, 4377–4382.
152 M. Liebel, C. Schnedermann and P. Kukura, Sub-10-fs pulses tunable from 480 to 980 nm from a NOPA pumped by an Yb:KGW source, *Opt. Lett.*, 2014, **39**, 4112.
153 F. Preda, A. Perri, D. Viola, S. D. Silvestri, G. Cerullo, D. Polli and D. Polli, in *2017 European Conference on Lasers and Electro-Optics and European Quantum Electronics Conference (2017),* Optical Society of America, 2017.
154 R. W. Boyd, *Nonlinear Optics, Third Edition*, Academic Press, Amsterdam ; Boston, 3 edition., 2008.
155 P. Powers, *Field Guide to Nonlinear Optics*, SPIE Press, 2013.
156 E. Hecht, *Optics*, Addison Wesley, San Francisco ; London, 4th ed., 2002.
157 R. L. Fork, W. J. Tomlinson, C. V. Shank, C. Hirlimann and R. Yen, Femtosecond white-light continuum pulses, *Opt. Lett.*, 1983, **8**, 1–3.
158 R. Sjöback, J. Nygren and M. Kubista, Absorption and fluorescence properties of fluorescein, *Spectrochim. Acta. A. Mol. Biomol. Spectrosc.*, 1995, **51**, L7–L21.
159 L. Song, C. A. Varma, J. W. Verhoeven and H. J. Tanke, Influence of the triplet excited state on the photobleaching kinetics of fluorescein in microscopy, *Biophys. J.*, 1996, **70**, 2959–2968.
160 B. B. Collier, S. Awasthi, D. K. Lieu and J. W. Chan, Non-Linear Optical Flow Cytometry Using a Scanned, Bessel Beam Light-Sheet, *Sci. Rep.*, 2015, **5**, 10751.
161 A. Brodeur and S. L. Chin, Ultrafast white-light continuum generation and self-focusing in transparent condensed media, *J. Opt. Soc. Am. B*, 1999, **16**, 637–650.
162 K. Yokoyama, C. Silva, D. H. Son, P. K. Walhout and P. F. Barbara, Detailed Investigation of the Femtosecond Pump−Probe Spectroscopy of the Hydrated Electron, *J. Phys. Chem. A*, 1998, **102**, 6957–6966.
163 A. Kummrow, M. F. Emde, A. Baltuška, M. S. Pshenichnikov and D. A. Wiersma, Wave Packet Dynamics in Ultrafast Spectroscopy of the Hydrated Electron, *J. Phys. Chem. A*, 1998, **102**, 4172–4176.
164 J. Mialocq, J. Sutton and P. Goujon, Picosecond study of electron ejection in aqueous phenol and phenolate solutions, *J. Chem. Phys.*, 1980, **72**, 6338–6345.
165 F.-Y. Jou and G. R. Freeman, Temperature and isotope effects on the shape of the optical absorption spectrum of solvated electrons in water, *J. Phys. Chem.*, 1979, **83**, 2383–2387.
166 V. Lenchenkov, J. Kloepfer, V. Vilchiz and S. E. Bradforth, Electron photodetachment from [Fe(CN)6]4−: photoelectron relaxation and geminate recombination, *Chem. Phys. Lett.*, 2001, **342**, 277–286.
167 V. H. Vilchiz, J. A. Kloepfer, A. C. Germaine, V. A. Lenchenkov and S. E. Bradforth, Map for the Relaxation Dynamics of Hot Photoelectrons Injected into Liquid Water via Anion Threshold Photodetachment and above Threshold Solvent Ionization, *J. Phys. Chem. A*, 2001, **105**, 1711–1723.

168 D. Borgis and A. Staib, Quantum adiabatic umbrella sampling: The excited state free energy surface of an electron-atom pair in solution, *J. Chem. Phys.*, 1996, **104**, 4776–4783.
169 A. Staib and D. Borgis, Reaction pathways in the photodetachment of an electron from aqueous chloride: A quantum molecular dynamics study, *J. Chem. Phys.*, 1996, **104**, 9027–9039.
170 A. E. Bragg and B. J. Schwartz, Ultrafast Charge-Transfer-to-Solvent Dynamics of Iodide in Tetrahydrofuran. 2. Photoinduced Electron Transfer to Counterions in Solution, *J. Phys. Chem. A*, 2008, **112**, 3530–3543.
171 O. Shoshana, J. L. P. Lustres, N. P. Ernsting and S. Ruhman, Mapping CTTS dynamics of Na− in tetrahydrofurane with ultrafast multichannel pump–probe spectroscopy, *Phys. Chem. Chem. Phys.*, 2006, **8**, 2599–2609.
172 P. J. Nowakowski, D. A. Woods and J. R. R. Verlet, Charge Transfer to Solvent Dynamics at the Ambient Water/Air Interface, *J. Phys. Chem. Lett.*, 2016, **7**, 4079–4085.
173 J. A. Kloepfer, V. H. Vilchiz, V. A. Lenchenkov, A. C. Germaine and S. E. Bradforth, The ejection distribution of solvated electrons generated by the one-photon photodetachment of aqueous I− and two-photon ionization of the solvent, *J. Chem. Phys.*, 2000, **113**, 6288–6307.
174 D. V. Bent and E. Hayon, Excited state chemistry of aromatic amino acids and related peptides. I. Tyrosine, *J. Am. Chem. Soc.*, 1975, **97**, 2599–2606.
175 C. W. West, A. S. Hudson, S. L. Cobb and J. R. R. Verlet, Communication: Autodetachment versus internal conversion from the S1 state of the isolated GFP chromophore anion, *J. Chem. Phys.*, 2013, **139**, 071104.
176 C. R. S. Mooney, D. A. Horke, A. S. Chatterley, A. Simperler, H. H. Fielding and J. R. R. Verlet, Taking the green fluorescence out of the protein: dynamics of the isolated GFP chromophore anion, *Chem. Sci.*, 2013, **4**, 921–927.
177 P. Changenet-Barret, A. Espagne, N. Katsonis, S. Charier, J.-B. Baudin, L. Jullien, P. Plaza and M. M. Martin, Excited-state relaxation dynamics of a PYP chromophore model in solution: influence of the thioester group, *Chem. Phys. Lett.*, 2002, **365**, 285–291.
178 D. S. Larsen, M. Vengris, I. H. M. van Stokkum, M. A. van der Horst, F. L. de Weerd, K. J. Hellingwerf and R. van Grondelle, Photoisomerization and Photoionization of the Photoactive Yellow Protein Chromophore in Solution, *Biophys. J.*, 2004, **86**, 2538–2550.
179 M. Vengris, I. H. M. van Stokkum, X. He, A. F. Bell, P. J. Tonge, R. van Grondelle and D. S. Larsen, Ultrafast Excited and Ground-State Dynamics of the Green Fluorescent Protein Chromophore in Solution, *J. Phys. Chem. A*, 2004, **108**, 4587–4598.
180 J. Zhu, L. Paparelli, M. Hospes, J. Arents, J. T. M. Kennis, I. H. M. van Stokkum, K. J. Hellingwerf and M. L. Groot, Photoionization and Electron Radical Recombination Dynamics in Photoactive Yellow Protein Investigated by Ultrafast Spectroscopy in the Visible and Near-Infrared Spectral Region, *J. Phys. Chem. B*, 2013, **117**, 11042–11048.
181 C. W. West, J. N. Bull, A. S. Hudson, S. L. Cobb and J. R. R. Verlet, Excited State Dynamics of the Isolated Green Fluorescent Protein Chromophore Anion Following UV Excitation, *J. Phys. Chem. B*, 2015, **119**, 3982–3987.
182 P. Changenet-Barret, A. Espagne, P. Plaza, K. J. Hellingwerf and M. M. Martin, Investigations of the primary events in a bacterial photoreceptor for photomotility: photoactive yellow protein (PYP), *New J. Chem.*, 2005, **29**, 527–534.
183 J. C. Mialocq, E. Amouyal, A. Bernas and D. Grand, Picosecond laser photolysis of aqueous indole and tryptophan, *J. Phys. Chem.*, 1982, **86**, 3173–3177.
184 R. M. Noyes, Kinetics of Competitive Processes when Reactive Fragments are Produced in Pairs, *J. Am. Chem. Soc.*, 1955, **77**, 2042–2045.
185 R. A. Crowell, R. Lian, I. A. Shkrob, D. M. Bartels, X. Chen and S. E. Bradforth, Ultrafast dynamics for electron photodetachment from aqueous hydroxide, *J. Chem. Phys.*, 2004, **120**, 11712–11725.

186 R. Lian, D. A. Oulianov, R. A. Crowell, I. A. Shkrob, X. Chen and S. E. Bradforth, Electron Photodetachment from Aqueous Anions. 3. Dynamics of Geminate Pairs Derived from Photoexcitation of Mono- vs Polyatomic Anions, *J. Phys. Chem. A*, 2006, **110**, 9071–9078.
187 J. Feitelson and G. Stein, Wavelength and Temperature Dependent Effects on Hydrated Electron Formation and Fluorescence of β-Naphtholate, *J. Chem. Phys.*, 1972, **57**, 5378–5382.
188 A. Matsuzaki, T. Kobayashi and S. Nagakura, Picosecond time-resolved spectroscopic study of solvated electron formation from the photoexcited .beta.-naphtholate ion, *J. Phys. Chem.*, 1978, **82**, 1201–1202.
189 F. Saito, S. Tobita and H. Shizuka, Photoionization mechanism of aniline derivatives in aqueous solution studied by laser flash photolysis, *J. Photochem. Photobiol. Chem.*, 1997, **106**, 119–126.
190 C. S. Anstöter, C. R. Dean and J. R. R. Verlet, Chromophores of chromophores: a bottom-up Hückel picture of the excited states of photoactive proteins, *Phys. Chem. Chem. Phys.*, 2017, **19**, 29772–29779.
191 M. H. Elkins, H. L. Williams, A. T. Shreve and D. M. Neumark, Relaxation Mechanism of the Hydrated Electron, *Science*, 2013, **342**, 1496–1499.
192 A. E. Bragg, J. R. R. Verlet, A. Kammrath, O. Cheshnovsky and D. M. Neumark, Hydrated Electron Dynamics: From Clusters to Bulk, *Science*, 2004, **306**, 669–671.
193 H.-T. Liu, C.-G. Ning, D.-L. Huang, P. D. Dau and L.-S. Wang, Observation of Mode-Specific Vibrational Autodetachment from Dipole-Bound States of Cold Anions, *Angew. Chem. Int. Ed.*, 2013, **52**, 8976–8979.
194 J. N. Bull and J. R. R. Verlet, Observation and ultrafast dynamics of a nonvalence correlation-bound state of an anion, *Sci. Adv.*, 2017, **3**, e1603106.
195 J. N. Bull, C. W. West and J. R. R. Verlet, Ultrafast dynamics of formation and autodetachment of a dipole-bound state in an open-shell π-stacked dimer anion, *Chem. Sci.*, 2016, **7**, 5352–5361.
196 J. P. Rogers, C. S. Anstöter and J. R. R. Verlet, Evidence of Electron Capture of an Outgoing Photoelectron Wave by a Nonvalence State in (C6F6)n–, *J. Phys. Chem. Lett.*, , DOI:10.1021/acs.jpclett.8b00739.
197 P. A. Franken, A. E. Hill, C. W. Peters and G. Weinreich, Generation of Optical Harmonics, *Phys. Rev. Lett.*, 1961, **7**, 118–119.
198 R. L. Byer, Nonlinear Optical Phenomena and Materials, *Annu. Rev. Mater. Sci.*, 1974, **4**, 147–190.
199 G. N. Lewis, D. Lipkin and T. T. Magel, Reversible Photochemical Processes in Rigid Media. A Study of the Phosphorescent State, *J. Am. Chem. Soc.*, 1941, **63**, 3005–3018.
200 T. H. Maiman, Stimulated Optical Radiation in Ruby, *Nature*, 1960, **187**, 493–494.
201 A. Warwick, Frequency, Theorem and Formula: Remembering Joseph Larmor in Electromagnetic Theory, *Notes Rec. R. Soc. Lond.*, 1993, **47**, 49–60.
202 P. Guyot-Sionnest and Y. R. Shen, Bulk contribution in surface second-harmonic generation, *Phys. Rev. B*, 1988, **38**, 7985–7989.
203 P. Guyot-Sionnest and Y. R. Shen, Local and nonlocal surface nonlinearities for surface optical second-harmonic generation, *Phys. Rev. B*, 1987, **35**, 4420–4426.
204 P. Guyot-Sionnest, W. Chen and Y. R. Shen, General considerations on optical second-harmonic generation from surfaces and interfaces, *Phys. Rev. B*, 1986, **33**, 8254–8263.
205 T. F. Heinz and D. P. DiVincenzo, Comment on ``Forbidden nature of multipolar contributions to second-harmonic generation in isotropic fluids'', *Phys. Rev. A*, 1990, **42**, 6249.
206 Y. R. Shen, Surface properties probed by second-harmonic and sum-frequency generation, *Nature*, 1989, **337**, 519–525.
207 J. Rudnick and E. A. Stern, Second-Harmonic Radiation from Metal Surfaces, *Phys. Rev. B*, 1971, **4**, 4274–4290.

208 F. Brown and M. Matsuoka, Effect of Adsorbed Surface Layers on Second-Harmonic Light from Silver, *Phys. Rev.*, 1969, **185**, 985–987.
209 T. F. Heinz, M. M. T. Loy and W. A. Thompson, Study of Si(111) Surfaces by Optical Second-Harmonic Generation: Reconstruction and Surface Phase Transformation, *Phys. Rev. Lett.*, 1985, **54**, 63–66.
210 H. W. K. Tom, C. M. Mate, X. D. Zhu, J. E. Crowell, T. F. Heinz, G. A. Somorjai and Y. R. Shen, Surface Studies by Optical Second-Harmonic Generation: The Adsorption of O2, CO, and Sodium on the Rh(111) Surface., *Phys. Rev. Lett.*, 1984, **52**, 348–351.
211 H. W. K. Tom and G. D. Aumiller, Observation of rotational anisotropy in the second-harmonic generation from a metal surface, *Phys. Rev. B*, 1986, **33**, 8818–8821.
212 N. Bloembergen and P. S. Pershan, Light Waves at the Boundary of Nonlinear Media, *Phys. Rev.*, 1962, **128**, 606–622.
213 T. Heinz, Ph.D. Thesis, California Univ., Berkeley. Lawrence Berkeley Lab. Dept. of Physics., 1982.
214 T. F. Heinz, in *Nonlinear surface electromagnetic phenomena*, eds. H. E. Ponath and G. I. Stegeman, North-Holland Publ., 1991.
215 R. Feynman and Leighton, *Feynman Lectures on Physics, Vol. II: 2*, Basic Books, revised 50th anniverary ed edition., 2011.
216 R. M. Corn and D. A. Higgins, Optical second harmonic generation as a probe of surface chemistry, *Chem. Rev.*, 1994, **94**, 107–125.
217 V. Mizrahi and J. E. Sipe, Phenomenological treatment of surface second-harmonic generation, *J. Opt. Soc. Am. B*, 1988, **5**, 660.
218 A. A. T. Luca, P. Hébert, P. F. Brevet and H. H. Girault, Surface second-harmonic generation at air/solvent and solvent/solvent interfaces, *J. Chem. Soc. Faraday Trans.*, 1995, **91**, 1763–1768.
219 Q. Du, R. Superfine, E. Freysz and Y. R. Shen, Vibrational spectroscopy of water at the vapor/water interface, *Phys. Rev. Lett.*, 1993, **70**, 2313–2316.
220 W. Zhang, D. Zheng, Y. Xu, H. Bian, Y. Guo and H. Wang, Reconsideration of second-harmonic generation from isotropic liquid interface: Broken Kleinman symmetry of neat air/water interface from dipolar contribution, *J. Chem. Phys.*, 2005, **123**, 224713.
221 S. Yamaguchi, K. Shiratori, A. Morita and T. Tahara, Electric quadrupole contribution to the nonresonant background of sum frequency generation at air/liquid interfaces, *J. Chem. Phys.*, 2011, **134**, 184705.
222 K. Shiratori, S. Yamaguchi, T. Tahara and A. Morita, Computational analysis of the quadrupole contribution in the second-harmonic generation spectroscopy for the water/vapor interface, *J. Chem. Phys.*, 2013, **138**, 064704.
223 Y. R. Shen, Surface nonlinear optics: a historical perspective, *IEEE J. Sel. Top. Quantum Electron.*, 2000, **6**, 1375–1379.
224 R. E. Pool, J. Versluis, E. H. G. Backus and M. Bonn, Comparative Study of Direct and Phase-Specific Vibrational Sum-Frequency Generation Spectroscopy: Advantages and Limitations, *J. Phys. Chem. B*, 2011, **115**, 15362–15369.
225 P. Thiansathaporn and R. Superfine, Homodyne surface second-harmonic generation, *Opt. Lett.*, 1995, **20**, 545.
226 Y. R. Shen, Wave mixing spectroscopy for surface studies, *Solid State Commun.*, 1997, **102**, 221–229.
227 J. A. McGuire, W. Beck, X. Wei and Y. R. Shen, Fourier-transform sum-frequency surface vibrational spectroscopy with femtosecond pulses, *Opt. Lett.*, 1999, **24**, 1877.
228 E. W. M. van der Ham, Q. H. F. Vrehen and E. R. Eliel, Self-dispersive sum-frequency generation at interfaces, *Opt. Lett.*, 1996, **21**, 1448.
229 J. H. Hunt, P. Guyot-Sionnest and Y. R. Shen, Observation of C-H stretch vibrations of monolayers of molecules optical sum-frequency generation, *Chem. Phys. Lett.*, 1987, **133**, 189–192.

230 T. F. Heinz, C. K. Chen, D. Ricard and Y. R. Shen, Spectroscopy of Molecular Monolayers by Resonant Second-Harmonic Generation, *Phys. Rev. Lett.*, 1982, **48**, 478–481.
231 P. Guyot-Sionnest, J. H. Hunt and Y. R. Shen, Sum-frequency vibrational spectroscopy of a Langmuir film: Study of molecular orientation of a two-dimensional system, *Phys. Rev. Lett.*, 1987, **59**, 1597–1600.
232 Q. Du, E. Freysz and Y. R. Shen, Vibrational spectra of water molecules at quartz/water interfaces, *Phys. Rev. Lett.*, 1994, **72**, 238–241.
233 Q. Du, E. Freysz and Y. R. Shen, Surface Vibrational Spectroscopic Studies of Hydrogen Bonding and Hydrophobicity, *Science*, 1994, **264**, 826–828.
234 C. D. Stanners, Q. Du, R. P. Chin, P. Cremer, G. A. Somorjai and Y.-R. Shen, Polar ordering at the liquid-vapor interface of n-alcohols (C1-C8), *Chem. Phys. Lett.*, 1995, **232**, 407–413.
235 R. Superfine, J. Y. Huang and Y. R. Shen, Nonlinear optical studies of the pure liquid/vapor interface: Vibrational spectra and polar ordering, *Phys. Rev. Lett.*, 1991, **66**, 1066–1069.
236 L. J. Richter, T. P. Petralli-Mallow and J. C. Stephenson, Vibrationally resolved sum-frequency generation with broad-bandwidth infrared pulses, *Opt. Lett.*, 1998, **23**, 1594.
237 C. S. Tian and Y. R. Shen, Recent progress on sum-frequency spectroscopy, *Surf. Sci. Rep.*, 2014, **69**, 105–131.
238 J. E. Sipe, V. Mizrahi and G. I. Stegeman, Fundamental difficulty in the use of second-harmonic generation as a strictly surface probe, *Phys. Rev. B*, 1987, **35**, 9091–9094.
239 G. Lüpke, G. Marowsky and R. Steinhoff, Phase-controlled nonlinear interferometry, *Appl. Phys. B*, 1989, **49**, 283–289.
240 R. Superfine, J. Y. Huang and Y. R. Shen, Phase measurement for surface infrared–visible sum-frequency generation, *Opt. Lett.*, 1990, **15**, 1276.
241 R. K. Chang, J. Ducuing and N. Bloembergen, Relative Phase Measurement Between Fundamental and Second-Harmonic Light, *Phys. Rev. Lett.*, 1965, **15**, 6–8.
242 Y. R. Shen, Phase-Sensitive Sum-Frequency Spectroscopy, *Annu. Rev. Phys. Chem.*, 2013, **64**, 129–150.
243 S. Baldelli, C. Schnitzer, M. J. Shultz and D. J. Campbell, Sum Frequency Generation Investigation of Water at the Surface of H2O/H2SO4 Binary Systems, *J. Phys. Chem. B*, 1997, **101**, 10435–10441.
244 W. Gan, D. Wu, Z. Zhang, R. Feng and H. Wang, Polarization and experimental configuration analyses of sum frequency generation vibrational spectra, structure, and orientational motion of the air/water interface, *J. Chem. Phys.*, 2006, **124**, 114705.
245 M. Sovago, R. K. Campen, G. W. H. Wurpel, M. Müller, H. J. Bakker and M. Bonn, Vibrational Response of Hydrogen-Bonded Interfacial Water is Dominated by Intramolecular Coupling, *Phys. Rev. Lett.*, 2008, **100**, 173901.
246 L. M. Levering, M. R. Sierra-Hernández and H. C. Allen, Observation of Hydronium Ions at the Air−Aqueous Acid Interface: Vibrational Spectroscopic Studies of Aqueous HCl, HBr, and HI, *J. Phys. Chem. C*, 2007, **111**, 8814–8826.
247 R. Stolle, G. Marowsky, E. Schwarzberg and G. Berkovic, Phase measurements in nonlinear optics, *Appl. Phys. B*, 1996, **63**, 491–498.
248 S. Nihonyanagi, R. Kusaka, K. Inoue, A. Adhikari, S. Yamaguchi and T. Tahara, Accurate determination of complex χ(2) spectrum of the air/water interface, *J. Chem. Phys.*, 2015, **143**, 124707.
249 K. Kemnitz, K. Bhattacharyya, J. M. Hicks, G. R. Pinto, B. Eisenthal and T. F. Heinz, The phase of second-harmonic light generated at an interface and its relation to absolute molecular orientation, *Chem. Phys. Lett.*, 1986, **131**, 285–290.
250 T. F. Heinz, H. W. K. Tom and Y. R. Shen, Determination of molecular orientation of monolayer adsorbates by optical second-harmonic generation, *Phys. Rev. A*, 1983, **28**, 1883–1885.

251 H. W. K. Tom, T. F. Heinz and Y. R. Shen, Second-Harmonic Reflection from Silicon Surfaces and Its Relation to Structural Symmetry, *Phys. Rev. Lett.*, 1983, **51**, 1983–1986.
252 H. W. K. Tom, Ph.D. Thesis, California Univ., Berkeley. Lawrence Berkeley Lab. Dept. of Physics., 1984.
253 G. Berkovic, G. Marowsky, R. Steinhoff and Y. R. Shen, Interference between second-harmonic generation from a substrate and from an adsorbate layer, *J. Opt. Soc. Am. B*, 1989, **6**, 205.
254 N. Ji, V. Ostroverkhov, C.-Y. Chen and Y.-R. Shen, Phase-Sensitive Sum-Frequency Vibrational Spectroscopy and Its Application to Studies of Interfacial Alkyl Chains, *J. Am. Chem. Soc.*, 2007, **129**, 10056–10057.
255 I. V. Stiopkin, H. D. Jayathilake, A. N. Bordenyuk and A. V. Benderskii, Heterodyne-Detected Vibrational Sum Frequency Generation Spectroscopy, *J. Am. Chem. Soc.*, 2008, **130**, 2271–2275.
256 K. J. Veenstra, A. V. Petukhov, A. P. de Boer and T. Rasing, Phase-sensitive detection technique for surface nonlinear optics, *Phys. Rev. B*, 1998, **58**, 16020–16023.
257 P. T. Wilson, Y. Jiang, O. A. Aktsipetrov, E. D. Mishina and M. C. Downer, Frequency-domain interferometric second-harmonic spectroscopy, *Opt. Lett.*, 1999, **24**, 496.
258 V. Ostroverkhov, G. A. Waychunas and Y. R. Shen, New Information on Water Interfacial Structure Revealed by Phase-Sensitive Surface Spectroscopy, *Phys. Rev. Lett.*, 2005, **94**, 046102.
259 S. Yamaguchi and T. Tahara, Heterodyne-detected electronic sum frequency generation: “Up” versus “down” alignment of interfacial molecules, *J. Chem. Phys.*, 2008, **129**, 101102.
260 S. Nihonyanagi, S. Yamaguchi and T. Tahara, Direct evidence for orientational flip-flop of water molecules at charged interfaces: A heterodyne-detected vibrational sum frequency generation study, *J. Chem. Phys.*, 2009, **130**, 204704.
261 S. Nihonyanagi, J. A. Mondal, S. Yamaguchi and T. Tahara, Structure and Dynamics of Interfacial Water Studied by Heterodyne-Detected Vibrational Sum-Frequency Generation, *Annu. Rev. Phys. Chem.*, 2013, **64**, 579–603.
262 I. V. Stiopkin, H. D. Jayathilake, C. Weeraman and A. V. Benderskii, Temporal effects on spectroscopic line shapes, resolution, and sensitivity of the broad-band sum frequency generation, *J. Chem. Phys.*, 2010, **132**, 234503.
263 L. Velarde, X. Zhang, Z. Lu, A. G. Joly, Z. Wang and H. Wang, Communication: Spectroscopic phase and lineshapes in high-resolution broadband sum frequency vibrational spectroscopy: Resolving interfacial inhomogeneities of “identical” molecular groups, *J. Chem. Phys.*, 2011, **135**, 241102.
264 L. Fu, S.-L. Chen and H.-F. Wang, Validation of Spectra and Phase in Sub-1 cm–1 Resolution Sum-Frequency Generation Vibrational Spectroscopy through Internal Heterodyne Phase-Resolved Measurement, *J. Phys. Chem. B*, 2016, **120**, 1579–1589.
265 Heterodyne | Define Heterodyne at Dictionary.com, http://www.dictionary.com/browse/heterodyne, (accessed May 14, 2016).
266 heterodyne, adj. and n., http://www.oed.com/view/Entry/86444, (accessed May 14, 2016).
267 homo-, comb. form, http://www.oed.com/view/Entry/87990, (accessed May 14, 2016).
268 X. Wei and Y. R. Shen, Motional Effect in Surface Sum-Frequency Vibrational Spectroscopy, *Phys. Rev. Lett.*, 2001, **86**, 4799–4802.
269 H. Arnolds and M. Bonn, Ultrafast surface vibrational dynamics, *Surf. Sci. Rep.*, 2010, **65**, 45–66.
270 D. Zimdars, J. I. Dadap, K. B. Eisenthal and T. F. Heinz, Anisotropic Orientational Motion of Molecular Adsorbates at the Air−Water Interface, *J. Phys. Chem. B*, 1999, **103**, 3425–3433.

271 A. Castro, E. V. Sitzmann, D. Zhang and K. B. Eisenthal, Rotational relaxation at the air/water interface by time-resolved second harmonic generation, *J. Phys. Chem.*, 1991, **95**, 6752–6753.
272 R. Antoine, A. A. Tamburello-Luca, P. Hébert, P. F. Brevet and H. H. Girault, Picosecond dynamics of Eosin B at the air/water interface by time-resolved second harmonic generation: orientational randomization and rotational relaxation, *Chem. Phys. Lett.*, 1998, **288**, 138–146.
273 J. Sung and D. Kim, Fast Motion of the Surface Alcohol Molecules Deduced from Sum-Frequency Vibrational Spectroscopy, *J. Phys. Chem. C*, 2007, **111**, 1783–1787.
274 X. Shi, E. Borguet, A. N. Tarnovsky and K. B. Eisenthal, Ultrafast dynamics and structure at aqueous interfaces by second harmonic generation, *Chem. Phys.*, 1996, **205**, 167–178.
275 J. A. McGuire and Y. R. Shen, Ultrafast Vibrational Dynamics at Water Interfaces, *Science*, 2006, **313**, 1945–1948.
276 D. E. Wilcox, M. E. Sykes, A. Niedringhaus, M. Shtein and J. P. Ogilvie, Heterodyne-detected and ultrafast time-resolved second-harmonic generation for sensitive measurements of charge transfer, *Opt. Lett.*, 2014, **39**, 4274.
277 S. Nihonyanagi, P. C. Singh, S. Yamaguchi and T. Tahara, Ultrafast Vibrational Dynamics of a Charged Aqueous Interface by Femtosecond Time-Resolved Heterodyne-Detected Vibrational Sum Frequency Generation, *Bull. Chem. Soc. Jpn.*, 2012, **85**, 758–760.
278 G. Licari, P.-F. Brevet and E. Vauthey, Fluorescent DNA probes at liquid/liquid interfaces studied by surface second harmonic generation, *Phys. Chem. Chem. Phys.*, 2016, **18**, 2981–2992.
279 D. M. Sagar, C. D. Bain and J. R. R. Verlet, Hydrated Electrons at the Water/Air Interface, *J. Am. Chem. Soc.*, 2010, **132**, 6917–6919.
280 K. Matsuzaki, R. Kusaka, S. Nihonyanagi, S. Yamaguchi, T. Nagata and T. Tahara, Partially Hydrated Electrons at the Air/Water Interface Observed by UV-Excited Time-Resolved Heterodyne-Detected Vibrational Sum Frequency Generation Spectroscopy, *J. Am. Chem. Soc.*, 2016, **138**, 7551–7557.
281 F. Uhlig, O. Marsalek and P. Jungwirth, Electron at the Surface of Water: Dehydrated or Not?, *J. Phys. Chem. Lett.*, 2013, **4**, 338–343.
282 P. J. Nowakowski, Ph.D. Thesis, Durham University, 2016.
283 P. J. Nowakowski, D. A. Woods, C. D. Bain and J. R. R. Verlet, Time-resolved phase-sensitive second harmonic generation spectroscopy., *J. Chem. Phys.*, 2015, **142**, 084201.
284 Refractive index database, https://refractiveindex.info/?shelf=main&book=H2O&page=Hale, (accessed June 29, 2017).
285 D. S. Correa, L. D. Boni, A. J. G. Otuka, V. Tribuzi and C. R. Mendonça, in *Polymerization*, INTECH, 2012.
286 CCD Spatial Resolution - Understanding spatial resolution | Andor, http://www.andor.com/learning-academy/ccd-spatial-resolution-understanding-spatial-resolution, (accessed March 8, 2018).
287 M. Graham, Excel_FFT, http://physics.oregonstate.edu/~grahamat/COURSES/ph421/Excel_FFT.pdf, (accessed March 22, 2018).
288 A. Punzi, G. Martin-Gassin, J. Grilj and E. Vauthey, Effect of Salt on the Excited-State Dynamics of Malachite Green in Bulk Aqueous Solutions and at Air/Water Interfaces: a Femtosecond Transient Absorption and Surface Second Harmonic Generation Study, *J. Phys. Chem. C*, 2009, **113**, 11822–11829.
289 K. B. Eisenthal, Liquid Interfaces Probed by Second-Harmonic and Sum-Frequency Spectroscopy, *Chem. Rev.*, 1996, **96**, 1343–1360.
290 F. M. Geiger, Second Harmonic Generation, Sum Frequency Generation, and χ(3): Dissecting Environmental Interfaces with a Nonlinear Optical Swiss Army Knife, *Annu. Rev. Phys. Chem.*, 2009, **60**, 61–83.

291 S. Nihonyanagi, S. Yamaguchi and T. Tahara, Ultrafast Dynamics at Water Interfaces Studied by Vibrational Sum Frequency Generation Spectroscopy, *Chem. Rev.*, 2017, **117**, 10665–10693.
292 P. L. Geissler, Water Interfaces, Solvation, and Spectroscopy, *Annu. Rev. Phys. Chem.*, 2013, **64**, 317–337.
293 M. S. Fee, K. Danzmann and S. Chu, Optical heterodyne measurement of pulsed lasers: Toward high-precision pulsed spectroscopy, *Phys. Rev. A*, 1992, **45**, 4911–4924.
294 K. Inoue, S. Nihonyanagi, P. C. Singh, S. Yamaguchi and T. Tahara, 2D heterodyne-detected sum frequency generation study on the ultrafast vibrational dynamics of H2O and HOD water at charged interfaces, *J. Chem. Phys.*, 2015, **142**, 212431.
295 P. Mathi, B. N. Jagatap and J. A. Mondal, Heterodyne-Detected Sum Frequency Generation Study of Adsorption of I– at Model Paint–Water Interface and Its Relevance to Post-Nuclear Accident Scenario, *J. Phys. Chem. C*, 2017, **121**, 7993–8001.
296 J. A. Mondal, S. Nihonyanagi, S. Yamaguchi and T. Tahara, Structure and Orientation of Water at Charged Lipid Monolayer/Water Interfaces Probed by Heterodyne-Detected Vibrational Sum Frequency Generation Spectroscopy, *J. Am. Chem. Soc.*, 2010, **132**, 10656–10657.
297 H. Vanselous and P. B. Petersen, Extending the Capabilities of Heterodyne-Detected Sum-Frequency Generation Spectroscopy: Probing Any Interface in Any Polarization Combination, *J. Phys. Chem. C*, 2016, **120**, 8175–8184.
298 I. Hughes, *Measurements And Their Uncertainties: A practical guide to modern error analysis*, Oxford University Press, U.S.A., Oxford, 2009.
299 Pressure, http://hyperphysics.phy-astr.gsu.edu/hbase/ppois.html, (accessed June 18, 2016).
300 F. Wooten, *Optical properties of solids*, Academic Press, New York, 1972.
301 P. Brevet, *Surface second harmonic generation*, PPUR, 1996.
302 R. J. D. Tilley, *Colour and the Optical Properties of Materials: An Exploration of the Relationship Between Light, the Optical Properties of Materials and Colour*, John Wiley & Sons, 2010.
303 P. Atkins, *By Peter Atkins - Molecular Quantum Mechanics: 4th (fourth) Edition*, Oxford University Press, USA, 21923rd edition., 2006.
304 K. D. Singer, M. G. Kuzyk and J. E. Sohn, Second-order nonlinear-optical processes in orientationally ordered materials: relationship between molecular and macroscopic properties, *J. Opt. Soc. Am. B*, 1987, **4**, 968.
305 S. Kielich, Optical second-harmonic generation by electrically polarized isotropic media, *IEEE J. Quantum Electron.*, 1969, **5**, 562–568.
306 C. Giacovazzo, *Fundamentals of Crystallography*, Oxford University Press, 2002.
307 D. L. Mills, *Nonlinear Optics: Basic Concepts*, Springer Science & Business Media, 2012.
308 E. A. Raymond, T. L. Tarbuck and G. L. Richmond, Isotopic Dilution Studies of the Vapor/Water Interface as Investigated by Vibrational Sum-Frequency Spectroscopy, *J. Phys. Chem. B*, 2002, **106**, 2817–2820.
309 A. Morita, Improved Computation of Sum Frequency Generation Spectrum of the Surface of Water, *J. Phys. Chem. B*, 2006, **110**, 3158–3163.
310 M. G. Brown, E. A. Raymond, H. C. Allen, L. F. Scatena and G. L. Richmond, The Analysis of Interference Effects in the Sum Frequency Spectra of Water Interfaces, *J. Phys. Chem. A*, 2000, **104**, 10220–10226.
311 E. A. Raymond, T. L. Tarbuck, M. G. Brown and G. L. Richmond, Hydrogen-Bonding Interactions at the Vapor/Water Interface Investigated by Vibrational Sum-Frequency Spectroscopy of HOD/H2O/D2O Mixtures and Molecular Dynamics Simulations, *J. Phys. Chem. B*, 2003, **107**, 546–556.

312 N. Ji, V. Ostroverkhov, C. S. Tian and Y. R. Shen, Characterization of Vibrational Resonances of Water-Vapor Interfaces by Phase-Sensitive Sum-Frequency Spectroscopy, *Phys. Rev. Lett.*, 2008, **100**, 096102.
313 C.-S. Tian and Y. R. Shen, Isotopic Dilution Study of the Water/Vapor Interface by Phase-Sensitive Sum-Frequency Vibrational Spectroscopy, *J. Am. Chem. Soc.*, 2009, **131**, 2790–2791.
314 T. Ishiyama and A. Morita, Vibrational Spectroscopic Response of Intermolecular Orientational Correlation at the Water Surface, *J. Phys. Chem. C*, 2009, **113**, 16299–16302.
315 S. Nihonyanagi, T. Ishiyama, T. Lee, S. Yamaguchi, M. Bonn, A. Morita and T. Tahara, Unified Molecular View of the Air/Water Interface Based on Experimental and Theoretical χ(2) Spectra of an Isotopically Diluted Water Surface, *J. Am. Chem. Soc.*, 2011, **133**, 16875–16880.
316 P. A. Pieniazek, C. J. Tainter and J. L. Skinner, Interpretation of the water surface vibrational sum-frequency spectrum, *J. Chem. Phys.*, 2011, **135**, 044701.
317 G. R. Medders and F. Paesani, Dissecting the Molecular Structure of the Air/Water Interface from Quantum Simulations of the Sum-Frequency Generation Spectrum, *J. Am. Chem. Soc.*, 2016, **138**, 3912–3919.
318 S. Yamaguchi, Development of single-channel heterodyne-detected sum frequency generation spectroscopy and its application to the water/vapor interface, *J. Chem. Phys.*, 2015, **143**, 034202.
319 M. Flörsheimer, M.-T. Bootsmann and H. Fuchs, Second-harmonic imaging of the absolute polar molecular orientation at interfaces, *Phys. Rev. B*, 2002, **65**, 125406.
320 R. Superfine, J. Y. Huang and Y. R. Shen, Experimental determination of the sign of molecular dipole moment derivatives: an infrared—visible sum frequency generation absolute phase measurement study, *Chem. Phys. Lett.*, 1990, **172**, 303–306.
321 C. D. Wick, I.-F. W. Kuo, C. J. Mundy and L. X. Dang, The Effect of Polarizability for Understanding the Molecular Structure of Aqueous Interfaces, *J. Chem. Theory Comput.*, 2007, **3**, 2002–2010.
322 X. Chen, W. Hua, Z. Huang and H. C. Allen, Interfacial Water Structure Associated with Phospholipid Membranes Studied by Phase-Sensitive Vibrational Sum Frequency Generation Spectroscopy, *J. Am. Chem. Soc.*, 2010, **132**, 11336–11342.
323 S. Strazdaite, K. Meister and H. J. Bakker, Orientation of polar molecules near charged protein interfaces, *Phys. Chem. Chem. Phys.*, 2016, **18**, 7414–7418.